Slope Movement Monitoring of The Ciloto Landslides Area Using InSAR Techniques

Von der
Fakultät Architektur, Bauingenieurwesen und Umweltwissenschaften
der Technischen Universität Carolo-Wilhelmina
zu Braunschweig

zur Erlangung des Grades einer
Doktoringenieurin (Dr.-Ing.)

genehmigte

Dissertation

von
Noorlaila Hayati
geboren am 03.06.1990
aus Banjarmasin, Indonesien

Eingereicht am:	14. Oktober 2019
Disputation am:	20. Januar 2020
Berichterstatter	Prof. Dr.-Ing. habil. Wolfgang Niemeier
	Prof. Dr.-Ing. Uwe Sörgel

2020

Printed and/or published with the support of the German Academic Exchange Service (DAAD)

Abstract

Landslides are one of the natural hazards that occur annually in Indonesia, not only destroying infrastructure and environment but usually causing the deaths of many people. A continuous geodetic observation in the landslide prone areas is essential to support precautionary measures. Because of its steep topography, torrential rainfall, and landslide events, the Ciloto district in West-Java, Indonesia has suffered from this type of ground movement phenomenon since 1984. Being known for its touristic and agricultural activities, Ciloto has gained further economic importance through the highway connecting the three big cities Jakarta, Bogor, and Bandung.

In my doctoral work, the InSAR techniques are applied to detect the ground movement phenomenon and to assess the InSAR result geometrically in the Ciloto area. Mainly, one of those techniques, the SB-SDFP algorithm, overcomes the limitations of conventional InSAR in monitoring rural and agricultural areas and can observe extremely slow landslides. Although ground or *in-situ* measurements can provide more detail in investigating the landslide types and processes, the InSAR strategy is positively known as a promising option to detect and quantify the kinematics of active landslides on a large areal scale. Furthermore, multi-interferograms techniques have been developed in recent years in purpose to increase the accuracy of InSAR products and compare well with other geodetic tools.

To minimize the bias of the InSAR displacement result, the correction of the tropospheric phase delay was carried out in a first step. This procedure is demonstrated in experiments both in the small study area in Ciloto and in a larger area. The latter is an area located in Northern Baja California, Mexico and is dominated by tectonic activity as well as groundwater-induced subsidence. A detailed investigation of the slope movement's behavior in the Ciloto district was conducted utilizing multi-temporal and multi-band SAR data from ERS1/2 (1996-1999), ALOS PALSAR (2007-2009) and Sentinel-1 (2014-2018) satellites. The region was successfully identified as a permanent active landslide prone area, especially in the vicinity of the Puncak Pass and Puncak Highway. The full 3D velocity field and the displacement time series were estimated using the inversion model. Therefore data from the two pass directions (ascending and descending tracks) was used and the slope aspect assumption derived from a digital elevation model was implemented. The velocity rate was classified from extremely slow to slow movement.

To comprehend the landslide's behavior, a further examination of the relationship between InSAR results and physical characteristics of the area was carried out. For the long period of a slow-moving landslide, the relationship between precipitation and displacement trend shows a weak correlation. It is concluded that the extremely slow to slow deformation is not directly influenced by the rainfall intensity, yet it effectuates the subsurface and the groundwater flow. The run-off process with rainfall exceeding a soil's infiltration capacity was suspected as the main driver of the slow ground movement phenomenon. However, when analyzing rapid and extremely rapid landslide events at Puncak Pass, a significant increase in the correlation coefficient between precipitation and displacement rate could be observed.

Zusammenfassung

Hangrutschungen sind eine der Naturgefahren in Indonesien, welche jährlich zu großen Schäden an Infrastruktur und Umwelt führen sowie die Leben zahlreicher Menschen fordern. Ein kontinuierliches geodätisches Monitoring ist notwendig, um Präventions- und Sicherheitsmaßnahmen in den gefährdeten Gebieten zu unterstützen. Das Gebiet Ciloto in West- Java, Indonesien, hat eine lange Historie an Hangrutschungen und ist durch seine unebene, gebirgige Topographie und die Starkniederschläge in der Regenzeit seit langer Zeit von diesem Phänomen der Bodenbewegungen betroffen. Ciloto ist berühmt für Tourismus und Landwirtschaft. Durch die Autobahn, welche die drei großen Städte Jakarta, Bogor und Bandung verbindet, kommt der Region eine hohe wirtschaftliche Bedeutung zu.

In dieser Doktorarbeit wird die Anwendung von erweiterten Verarbeitungsstrategien von InSAR Daten zur Erkennung und geometrischen Bewertung der Bodenbewegungen im Ciloto dargestellt. Dieser Ansatz überwindet die Beschränkungen konventioneller SAR-Interferometrie und ermöglicht sowohl ein kontinuierliches Monitoring dieses landwirtschaftich geprägten Gebietes als auch die Erfassung extrem langsamer Hangrutschungen. Neben in-situ Messungen zur Untersuchung von Hangrutschungstypen und -prozessen ist die Radarinterferometrie als einzigartige Möglichkeit bekannt, flächenhaft aktive Hangrutschungen zu erkennen und zu quantifizieren. Darüber hinaus wurden in den letzten Jahren multi-interferometrie Techniken entwickelt, welche die Qualität der InSAR Produkte gegenüber anderen geodätischen Werkzeugen deutlich verbessert haben.

Um eine Verzerrung der InSAR Deformationsergebnisse zu minimieren, wurde zunächst eine Korrektur der troposphärischen Phase durchgeführt. Diese neuartige Strategie wird sowohl im Forschungsgebiet Ciloto als auch an einem größeren Gebiet demonstriert. Bei letzterem handelt es sich um einen Küstenstreifen im nördlichen Niederkalifornien, Mexiko, welcher durch hohe tektonische Aktivität und grundwasserinduzierte Landsetzungen charakterisiert ist. Die detaillierte Untersuchung des Verhaltens von Hangrutschungen im Ciloto erfolgte durch die Verarbeitung multi-temporaler SAR-Daten unter Nutzung verschiedener Frequenzbänder, darunter ESR1/2 (1996-1999), ALOS PALSAR (2007-2009) und Sentinel-1 (2014-2018) Daten. Die Region konnte erfolgreich als permanent aktives Hangrutschungsgebiet identifiziert werden, wobei der Puncak Pass und der Puncak Highway ein erhöhtes Gefahrenpotential aufweisen. Ein 3D- Geschwindigkeitsfeld der Deformation und die zugehörigen Zeitreihen wurden mit dem Inversionsmodell berechnet. Hierfür wurden Daten des auf- als auch absteigenden Bahnbogens der Satelliten und die Annahme des aus dem digitalen Höhenmodell (DEM) abgeleiteten Steigungsaspekts verwendet. Die Geschwindigkeitsrate wurde als langsam bis extrem langsam klassifiziert.

Um das dynamische Verhalten der Hangrutschung zu verstehen wurde, in einer weiteren Untersuchung die Beziehung zwischen dem InSAR-Ergebnis und den physikalischen Begebenheiten im Forschungsgebiet analysiert. Hierbei konnte die schwache Korrelation zwischen Niederschlagsereignissen und dem Bewegungsverhalten gefunden werden. Es wird der Schluss gezogen, dass die langsame bis extrem langsame Verformung nicht direkt von der Niederschlagsintensität beeinflusst wird, diese sich aber auf den Untergrund und die Grundwasserströmung auswirkt. Es wird vermutet, dass der Oberflächenablauf, welcher die Infiltrationskapazität des Bodens übersteigt, ausschlaggebend für das Phänomen der langsamen Bodenbewegung ist. Für die schnellen und extrem schnellen Hangrutschungen jedoch konnte eine signifikante Erhöhung des Korrelationskoeffizienten zwischen Niederschlag und Verschiebungsrate bei Untersuchungen der Hangrutschung am Puncak-Pass nachgewiesen werden.

Acknowledgements

First and foremost, I would like to thank my advisor Prof. Dr-Ing. Wolfgang Niemeier who supported, guided and gave me great encouragement during the four years of my doctoral program at the Institute of Geodesy and Photogrammetry (IGP), Technische Universität Braunschweig. Special thanks to Prof. Dr.-Ing. Uwe Sörgel as my second supervisor and Prof. Dr. sc. Antje Schwalb as my examiner for participating in my defense committee team. I express my gratitude to Dr.-Ing. Björn Riedel, who gave me many technical supports and guidance while conducting this PhD research and Prof. Dr.-Ing. Markus Gerke as the head of IGP who supported me very well. Many thanks also go to Dr. Vera Sadarviana from Institut Teknologi Bandung who always provides me the detail information and investigations of my case study, the Ciloto region, Indonesia.

I have been a pleasure to be part of the radar research group at IGP, and I am indebted to all of my colleagues for their help, friendship, and advice throughout the years. In particular, I thank Anika Riedel, Christine Schotmüller, Christa Homann, Eike Reinosch, Yahya Ghoussan, and other IGP members who were always available to support and help me for discussion of my works and lives.

Finally, I dedicate this work to my mother and my big family for their understanding, encouragement, and unconditional support during my residence in Germany, with a special dedication of the memory of my father.

Funding for this research was provided by the German Academic Exchange Service (DAAD) through the research grant - doctoral program. The SAR data were acquired by the European Space Agency (ESA), through EO data resources and Copernicus open access hub, and the Japanese Aerospace and Exploration Agency (JAXA) which the data were made available through the Alaska Satellite Facility data portal. The supporting data for the Ciloto environment were provided by the Center of Volcanology and Geological Hazard Mitigation (PVMBG) and the Regional Disaster Management Authority (BPBD), Indonesia.

Contents

List of Figures

List of Tables

List of Abbreviations

2D	**2D**imensions, vertical and east-west direction
3D	**3D**imensions, vertical, east-west, and north-south direction
ACE	**A**lternating **C**onditional **E**xpectations
ADD	**A**mplitude **D**ifference **D**ispersion
ADI	**A**mplitude **D**ispersion **I**ndex
ALOS	**A**dvanced **L**and **O**bserving **S**atellite
ALS	**A**irborne **L**aser **S**canner
AMI	**A**ctive **M**icrowave **I**nstrument
APS	**A**tmospheric **P**hase **S**creen
ASAR	The **A**dvanced **S**ynthetic **A**perture **R**adar
AVNIR	**A**dvanced **V**isible and **N**ear-**I**nfrared **Radiometer**
DC	**D**oppler **C**entroid
DS	**D**istributed **S**catters
DEM	**D**igital **E**levation **M**odel
DORIS	**D**elft **O**bject-oriented **R**adar **I**nterferometric **S**oftware
ERA	ECMWF **R**e**A**nalysis
ERS	**E**uropean **R**emote **S**ensing
Envisat	**Envi**ronmental **S**atellite
EW	**E**xtra **W**ide mode
GIS	**G**eographic **I**nformation **S**ystem
FBD	**F**ine **B**eam **D**ouble
FBS	**F**ine **B**eam **S**ingle
GAM	**G**eneralized **A**dditive **M**odel
GB-InSAR	**G**round **B**ased **In**nterferometry **S**ynthetic **A**perture **R**adar
GLM	**G**eneralized **L**inear **M**odel
GLS	**G**eneralized **L**east **S**quare
GMT	**G**eneric **M**apping **T**ools
GOME	**G**lobal **O**zone **M**onitoring **I**nstrument
GPS	**G**lobal **P**ositioning **S**ystem
IDW	**I**nverse **D**istance **W**eighted
IW	**I**nterferometric **W**ideswath mode
InSAR	**In**nterferometry **S**ynthetic **A**perture **R**adar
MAI	**M**ultiple **A**perture **I**nterferometry
MCF	**M**inimum **C**ost **F**low
MERRA	**M**odern **ER**A-**R**etrospective **A**nalysis
MERIS	**ME**dium-spectral **R**esolution **I**maging **S**pectrometer
MODIS	**M**oderate **R**esolution **I**maging **S**pectroradiometer
MS	**M**icrowave **S**ounder
MSL	**M**ean **S**ea **L**evel
LEWS	**L**andsldie **E**early **W**arning **S**ystem
LiDAR	**Li**ght **D**etection **a**nd **R**anging
LOS	**L**ine **o**f **S**ight
OLS	**O**riginal **L**east **S**quare

PALSAR	**P**hased **A**rray **L**-Band **S**ynthetic **A**perture **R**adar
POE	**P**recise **O**rbit **E**phemeris
PS	**P**ersistent **S**catters
PRF	**P**ulse **R**epetition **F**requency
PRISM	**P**anchromatic **R**emote-sensing **I**nstrument for **Stereo Mapping**
RMSE	**R**oot **M**ean **S**quare **E**rrors
ROI	**R**egion **of** **I**nterest
ROIPAC	**R**epeat **O**rbit **I**nterferometry **P**ackage
SCLA	**S**patially **C**orrelated **L**ook **A**ngle
SB	**S**mall **B**aselines
SBAS	**S**mall **Ba**selines **S**ubsets
SCLA	**S**patially **C**orrelated **L**ook **A**ngle
SDFP	**S**lowly **D**ecorelating **F**ilter **P**hase
SHD	**S**lant **H**ydrostatic **D**elay
SLC	**S**ingle **L**ook **C**omplex
SM	**S**ingle **M**aster
SM	**S**tripmap **M**ode
SRTM	**S**huttle **R**adar **T**opography **M**ission
StaMPS	**Sta**nford **M**ethod for **P**ersistent **S**catters
STD	**S**lant **T**otal **D**elay
SULA	**S**patially **U**ncorrelated **L**ook **A**ngle
SVD	**S**ingular **V**alue **D**ecomposition
SWD	**S**lant **W**et **D**elay
TIN	**T**riangulated **I**rregular **N**etworks
TLS	**T**errestrial **L**aser **S**canner
TRAIN	**T**oolbox for **R**educing **A**tmospheric **In**SAR **N**oise
UAVSAR	**U**ninhabited **A**erial **V**ehicle **S**ynthetic **A**perture **R**adar
WLS	**W**eighted **L**east **S**quare
WRF	**W**eather **F**orecast **M**odels
WV	**W**a**V**e mode

List of Symbols

ϕ_{int}	The interferometric phase
ϕ_{disp}	The phase contribution due to earth's surface change occurring between two acquisitions
$\phi_{geometry}$	A baseline error due to the slightly different position of two images
ϕ_{topo}	The phase concerning the local topographic information
ϕ_{atm}	A part of phase caused by atmospheric patterns
d_{LOS}	The displacement in the line-of-sight
λ	The wavelength's sensor
σ_A	The temporal standard deviation of the amplitude
μ_A	The temporal mean of the amplitude
R_i	The calibration factor
μA_i	The mean amplitude of each image (i)
$calA_i$	The calibrated of each SLC image
D_A	The amplitude dispersion index
$D_{\Delta A}$	The amplitude difference dispersion index
$\phi_{disp,x,i}$	The deformation value
$\Delta\phi_{atmos}$	The uncorrelated atmospheric delay contribution
$\Delta\phi_{orb}$	The residual orbital error or phase ramp
$\Delta\phi_{\theta,x,i}$	The spatially correlated part of look angle error
$\Delta\phi_{noise,x,i}$	The residual spatially uncorrelated noise term
γ_x	The function to measure the phase noise level
$\psi_{x,i}$	The wrapped phase
$\tilde{\psi}_{x,i}$	The estimate of spatially correlated terms
$\Delta\hat{\phi}^u_{\theta,x,i}$	The estimate of the spatially-uncorrelated look angle error term
N	The refractivity
P	The total atmospheric pressure
T	The temperature
e	The partial pressure of water vapor
d_{tropo}	The tropospheric (slant) delay
$\Delta\phi_{tropo}$	The interferometric tropospheric phase
$K'_{\Delta\phi}$	The coefficient relating phase to topography with spatial and temporal variation
h_o	The power law reference height
α	The power law coefficient
d_U	The vertical displacement component
d_E	The west-east displacement component
d_N	The north-south displacement component
d_{tot}	The distance in three-dimensional
θ_{inc}	The incidence angle
α_h	The satellite platform heading angle - $3\pi/2$
R^2	The coefficient of determination
R	The correlation value
δT	The time between acquisition images

β	The angle between x axis and the across track ascending direction
α	The angle between across track ascending and descending
$\psi_{int,x,i}$	The wrapped interferogram phase
$\phi_{uw,x,i}$	The unwrapped value of $W\{\psi_{int,x,i} - \Delta\widehat{\phi}^{nc}_{\theta,x,i} - \widehat{\phi}^{m,nc}_{x}\}$
G	Matrix element for temporal SAR distribution
m	The incremental range change between SAR acquisitions
C	The range change time series
d	The range time change for all numbers (N) of interferograms in two-dimensional (i,j)

Chapter 1

Introduction

The discovery of phase change contribution to measuring surface deformation (Massonnet et al., 1993) from the ERS SAR mission (Sanchez et al., 1997) throwback in 1998 has opened an extensive opportunity to understand earth's surface change phenomena such as tectonics, earthquakes, volcanism, subsidence, and landslides using space-borne technology. The two most popular techniques of space geodetic observations to measure surface deformation are Global Navigation Satellite System (GNSS) and Interferometric Synthetic Aperture Radar (InSAR). InSAR has an ability to monitor seismic activity, volcanic process, subsidence affected either by nature or human-made and to quantify the kinematics of active landslides. This dissertation describes the application of InSAR techniques in active landslide areas. It presents the application of the time series InSAR analysis called the small baseline - slowly decorrelating filter phase (SB-SDFP) algorithm in the Ciloto district - West Java, one of the most landslide-prone regions in Indonesia. Furthermore, the result from an ongoing SAR product is corrected for the tropospheric delay, the main problem in analyzing InSAR result due to overprinting deformation signal.

The motivation to conduct the research is highly boosted by the landslide events which have occurred since 1984 in Ciloto, West Java (Sugalang, 1993). The lack of continuously geodetic monitoring installed in some principal spots was a crucial factor for the local government to prevent the slope failures with a well-organized precaution especially in the geotechnical aspect. Therefore, the detection of slope movement that will be a pre-failure indication of landslide event is inspected using the available multi-band SAR data as seen in Figure 1.1; ERS1/2, ALOS PALSAR and Sentinel-1 in order to understand more its behavior in a long period. This work introduces a method to estimate 3D-field motion generated from two different InSAR tracks and an assumption of motion in direction of the slope.

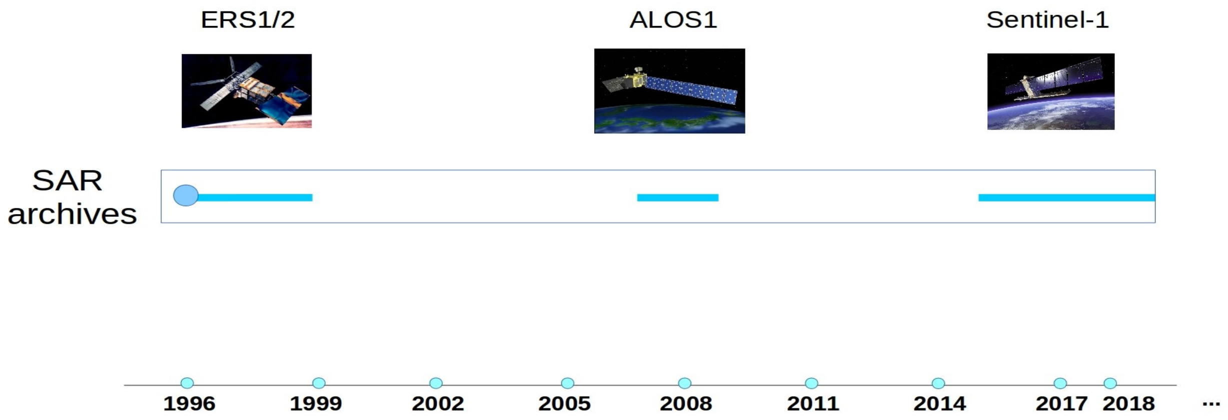

FIGURE 1.1: The available SAR archives to be applied on the multi-temporal InSAR analysis are ERS1/2 (C-Band), ALOS (L-Band), and Sentinel-1 (C-Band) in Ciloto.

Types of Landslide

Based on Varnes, 1978 the classification of mass movement considering the massive slide case is a rotational, translational and compound slide. However, Varnes also considered the type of movement viewed by soil materials, which are: falls, topples, lateral spreads, and flows.

- *Rotational slide*: soil and rock materials move along a curved concavely surface of rupture having a roughly rotational movement upward and transverse across a slide.
- *Translational slide*: soil and rock materials move along a roughly planar surface without big rotation and backward tilting happened.
- *Compound slide*: the type of movement that combines rotational and translational slides. It is also named a complex slide if there are two or more combination types of movement.
- *Falls*: masses from geologic material such as rocks and boulders are detached and fall freely, bouncing or rolling from the main body is also possible. Usually, it happens at cliffs or shore areas where a very extreme steep slope appears. It is influenced by gravity, the presence of interstitial water and weathering.
- *Topples*: with a great action of gravity, force, and fluids in the cracks, a segment of rock could fall at some pivotal point of the main body part.
- *Lateral Spreads*: They occur on a gentle slope and flat terrain. It is different from other slides because of liquefaction, a transformation from a solid into a liquefied state. The mass consists of saturated, loose and cohesionless sediment (USGS, 2004).
- *Flows*: The movement of material is greatly influenced by water. The velocity flow depends on a steep slope, water volume, water pressure, and others carried material. Five basic categories of flows are; debris flow, debris avalanche, earthflow, mudflow and creep (USGS, 2004). Debris flow usually happens in watershed and volcano areas and could flow about a thousand meters causing huge damage to residences and infrastructure. Meanwhile, creeps run slowly which their soil materials are mostly rough and small-scale. People do not recognize clearly this movement, but there is a shred of evidence from the human-made object close to the failure, for instance, houses are broken or cracked, power and telephone poles are not standing up straight, tree trunks are curved, and roadways move out of alignment.

If mass movement flows distinguished by the velocity (Ahnert, 1996), generally it is divided to 3 classes:

- *very slowly/slow*: the type for very slow to slow movement is called **creep** which based on soil materials is classified to:
    - **soil creep** contains rock (dry) materials
    - **debris creep** contains regolith, soil, alluvium, and water
    - **solifluction** contains materials of the debris creep and sediment
- *middle to fast*: it is named as **slip** which normally means a landslide phenomenon and refers to this class. It is divided to **slump** and **rock slide**. Another class is **flow** which are explained above.
- *very fast*: it is named as **fall** which based on soil materials is classified to:
    - **rock fall** contains rock (dry) materials

  - **debris avalanche** contains regolith, soil, alluvium, ion and water. It could also be considered as fall from volcanic eruption.
  - **mudslide** contains a mixture of detrital, sediment and water and mostly occurs in high mountain regions (Schuler, 2015).

Causes of Landslide

According to USGS, 2004, three sources influence the landslide phenomenon. Firstly, geological circumstances which are fragile and solid materials. The solid materials, however, could be altered in time if they are affected by physical and chemical weathering. Intensity rainfall is an influential external factor that has an impact on a geological condition. Beginning from dry season or summer, abundant water evaporation on the surface occurs and causes soil pore spaces and cracks on the land surface. Following in the rainy season, the intensity of rainfall increases and affects water content in the ground which is saturated in a short time (weathered materials). Hence, heavy rain could indirectly cause lateral movement since water could quickly enter the ground fissure and be cumulated along the slope of the surface of rupture.

Geo-morphologies such as tectonic or volcanic uplift, deposition loading slope or its crest, weathering and vegetation removal are the second parameter of slope instability. Highly steep slope usually have been formed due to river erosion. Furthermore, vegetation removal due to fire and drought could raise the groundwater level and unbalance the slope as well since it increases the rate of erosion and makes soil absorbs water greater.

The third source for landslides is human activities. It is recognized that deforestation, irrigation, artificial vibration, the change of land use, and mining give a significant role to the failure. The change of land use for crop, plantation, and irrigation make abundant water keep along the steep slope. Because crop and cultivation do not have firm roots, it makes soil becomes frail and saturated. The building of houses and villas and vehicle transportation add a heavy load and make more significant propulsive force along slope instability surface especially around the bend of a valley. The evidence usually could be seen as subsidence and cracking appearance with the motion's direction relatively toward the valley toe. Additionally, vibration or shaking in consequence of earthquake, explosive, heavy machine and transportation also brings a vulnerability to slope movement.

Hardiyatmo, 2012 described specifically the causes of natural slope failure as following:

a. Adding a burden on a slope. An additional load could come from new buildings, extra water containing infiltration to either soil pores or surface pools, and a dynamics burden sourced by plants and trees.

b. Excavation and cutting land on slope toe causing the increase of slope height on its sections.

c. Excavation which increases the gradient of the slope.

d. A rapid drawdown of groundwater table (on a dam or a river)

e. A rise of lateral water pressure (water will flow into a ground fissure and push the mash of land toward lateral direction).

f. Decreasing of slope shear resistance caused by increasing soil water content, pore water pressure, and material of soil which mostly contains clay which has the characteristic of shrinkage physics.

g. Vibrations due to an earthquake (seismic signals) or human activities.

Concepts of Landslide Monitoring

Existing conceptual approaches of landslide early warning system (LEWS) provided by Tiebes et al., 2016 explain the forecasting methodology and alerts that vary significantly depending on the scale on which the areas are investigated. For the global scale, the rainfall intensity and duration thresholds analyses are suggested to forecast a certain probability of landslides occurrence, see, e.g., Crosta et al., 2001; Wieczorek et al., 2005; and Guzzetti et al., 2007. However, some criticisms are mentioned that it is not the amount of precipitation but the amount of water that infiltrates and moves into the ground to cause failure (e.g., Caine, 1980; Reichenbach et al., 1998). Therefore, the rainfall thresholds are used to forecast the landslide occurrence only for the shallow landslides and debris flows based on continuous rainfall measurements (e.g., Aleotti, 2004; Godt et al., 2006; Guzzetti et al., 2008).

In the regional scale LEWS, the most frequently applied concepts are empirical rainfall thresholds in combination with rainfall measurements and quantitative rainfall forecasts. The monitoring ground stations, the meteorological, and the rainfall radar derive the quantitative rainfall forecasts. Some remarkable researches are the integration in overall landslide risk management with more than 100 automatic rainfall gauges and a set of different rainfall thresholds conducted by Dai et al., 2001; a GIS-based approach in spatially varying landslide susceptibility (e.g., Segoni et al., 2009; Isya et al., 2014); the combination of landslide susceptibility maps as a spatial forecast and rainfall thresholds as a temporal probability (Segoni et al., 2015); and a rainfall radar system to observe the real-time situation and to allow the emergency actions (Cheung et al., 2006).

The landslide monitoring systems on the local-scale LEWS using the ground geodetic observations (e.g., inclinometers, GNSS, total stations, piezometers) are generally well known by geotechnical engineers. The explorations of terrestrial laser scanning and radar interferometry techniques are in the last decade rising popularity due to a useful method to support the LEWS.

- Light detection (LiDAR)
  Jaboyedoff et al., 2012 has reviewed the advantages and limitations of LiDAR for landslide monitoring. LiDAR provides high-resolution point clouds of the topography. It creates an accurate and precise high-resolution (HR)DEM in raster grids and triangulated irregular networks (TINs). LiDAR is divided into two systems based on the position of the sensor: airborne-based laser scanner (ALS) and ground-based or terrestrial laser scanner (TLS). The main applications of TLS and ALS can be subdivided into 3 types; (1) Landslide detection and characterization (e.g., Corsini et al., 2009; Jaboyedoff et al., 2009); (2) Hazard assessment and susceptibility mapping and modelling (e.g. Dietrich et al., 2001; Jaboyedoff et al., 2004); and (3) Monitoring which requires at least two epochs of HRDEM acquisition (Baldo et al., 2009). For the TLS-based early warning, Canli et al., 2015 reported that the permanent 3D TLS system was established for Alpine hill-slope instabilities to monitor deliverables such as volumetric calculations, spatio-temporal movement patterns, predictions and alerting. The system offers a fully automated surface capture by integrated time functionality.

- Radar Interferometry
  Radar interferometry (InSAR) is divided into the ground- and satellite-based systems which both types have a high accuracy of the differential phase measurement in mm-range. For the satellite-based or spaceborne InSAR, the research of the landslide inventory has been conducted by Cascini et al., 2010 for ERS data and Notti et al., 2010 for TSX data. The landslide monitoring for a long period using ERS and Envisat data has been done by Herrera et al., 2009 and Rosi et al., 2013. The application increase to the landslide analysis and modeling using the big archive SAR data, see, e.g. Herrera et al., 2011; Bovenga et al., 2012; Cigna et al., 2013. A couple of researches have explored the ground-based (GB) InSAR technology for landslide monitoring (e.g., Casagli et al., 2003; Tarchi et al., 2003). Two radar antennas are installed on a linear rail and horizontally slide to create a synthetic aperture. The raw data

then converts into a SAR image containing the wave phases based on the target-sensor distance. The interferogram is generated by cross-correlated SAR images along the sight-line of the position of GB-InSAR (Antonello et al., 2004).

The advantages of InSAR techniques

In recent years, SAR data are improving well both in spatial and temporal resolution. This massive data could increase the possibility to measure an area suffered by decorrelation especially for a landslide case study which mostly located around dense vegetation and rural area. It is supported by the advanced InSAR methods overcoming the problems of the conventional InSAR, which are the atmospheric phase delay and phase decorrelation. The implementation is up to now not only limited to earth study applications with steady displacement rates where human-made structures are excessively exist indicated as bright scatters but also a study area in the absence of bright scatters and having non-steady deformation.

1.1 Contributions

The main focuses of this dissertation are the use of InSAR techniques in a landslide application using multi-band SAR data and the establishment of a 3D perspective view generated by the InSAR results. I summarize the main contribution of this works as follows:

1. The implementation of SB-SDFP classified as a Persistent Scatters algorithm in the active landslide area, Ciloto, Indonesia.
2. The implementation of the power-law algorithm in order to correct the tropospheric delay in interferograms.
3. The establishment between the generation of interferogram and advanced InSAR processing based on open-source softwares.
4. The slow movement landslides are detected in some parts of the Ciloto district. We found that there are places in the Puncak Highway that are constantly moving over a long period of time.
5. The relationship between the recorded precipitation near Ciloto and the time series InSAR result is observed as a weak linear correlation. However, the correlation coefficient increases significantly close to the mass movement event.
6. The development and implementation of InSAR results in a 3D perspective have been applied in the Puncak Pass and the Puncak Highway region.

1.2 Thesis Organization

Chapter 2 gives details of the Ciloto physical environment and previous works using other geodetic methods; terrestrial and GPS measurement.

Chapter 3 describes a brief theory of the InSAR and Persistent Scatter algorithm implemented by StaMPS (Hooper et al., 2012) and initially developed for PS applications in natural terrain such as rural and agricultural areas.

Chapter 4 is a detail explanation of the atmospheric phase screen that mostly overprints the deformation signal in the InSAR applications. We focus the correction into tropospheric delay using a power-law band filter. We tested the performance in two mountainous areas. It was applied in a small region of interest, Ciloto - Indonesia whereas for a large area in Northern Baja California, Mexico. The validation was assessed by the other observations which are the extensometer for the Ciloto study and the MERIS sensor for the Northern Baja California study. This chapter has been published in the conference proceeding: *Wissenschaftlich-Technische Jahrestagung der DGPF und PFGK18* (Isya et al., 2018).

Chapter 5 describes the result of time series InSAR generated from ERS1/2, ALOS PALSAR and Sentinel-1 data. PS points are examined on each sensor and further integrated to other geodetic measurements for evaluating the Ciloto ground movement in an extended period of time. A strong deformation signal is verified by the evidence of ground motion and landslide events occurred in the observed points. We found the relationship between InSAR result and precipitation as the main trigger of the mass movement in Puncak Pass for a short period of time.

Chapter 6 describes a method to estimate 3D vectors displacement by taking into account that the movement is parallel to down-slope. We created the experimental test of the purposed method in the Puncak Pass and Puncak Highway region, part of the Ciloto district, using Sentinel-1 ascending and descending data. We display the slow movement in the vertical and horizontal direction and locate the zone of depletion and accumulation in the Puncak Pass region. A part of this chapter has been published on The ISPRS Annals of the Photogrammetry, Remote Sensing and Spatial Information Sciences 2019 (Isya et al., 2019).

Chapter 7 provides a summary of this thesis and recommendations for future works.

Chapter 2

The Available Knowledge in The Ciloto District

A landslide is a mass movement of material which moves on a steep slope area along the detachment surface or relative to a shear strain zone. The early sign of a landslide is a crack on the original ground surface along the main scarp. This main scarp also shows the forms of a landslide which are a rotational, translational or compound slide. A landslide is driven by two main factors: The first factor is the controlling factor related to the physical material of sediment and slope geometry. It consists of the steepness of slope, stratigraphy, geologic structure, hydrogeology, and land use. The second, called an external factor, is the trigger of a landslide if the conditions exceed a limit calculation of the safety zone. The significant parameter is weather and climate which leads to an alteration of soil structure affecting corrosion, water volume fluctuation, and rainfall infiltration. Water volume induces major changes in the rock and soil morphologies. It decreases their cohesion as well.

Furthermore, the change in land use on slope areas is another external factor of a mass movement. If human activity changes the original biodiversity plant to harvesting crops along the slope area, it could increase both water infiltration passing through soil and pore water pressure. The establishment of infrastructure has also a big influence on the change of gradient slope. In addition, either a natural shock such as earthquakes and volcanic activities or the vibration of a heavy machine on the ground would produce a different oscillation to rock and soil which may change the sliding mechanism. As a consequence, the effect could lead to intrude of the slope stability due to an amendment pressure temporarily. Generally, the landslide processing is divided into three main steps; discharging, movement and settling of material. For the last step, the displaced materials bring along accumulative masses from the main scarp to the tip surface. Hence, the risk of human life is threatened when huge mass material falls to an urban residence located on the toe of surface rupture.

Indonesia is frequently suffered by the landslide hazard in upland areas which destroys not only the environment and its properties but also loss of lives. Landslides give a contribution to 1.1% of fatalities and 1.3% of people affected by this geological hazard (Cummins, 2017). Although the percent number of the landslide is relatively small in comparison to other natural hazards (e.g., earthquakes, tsunami, volcanic eruptions, mud volcanoes), it significantly occurs every year in mountainous areas of Indonesia. As mentioned in Abidin et al., 2007, landslides caused 1438 deaths during the period 1977-1987 while from 1987 to 1997 they resulted in the loss of 641 lives and 112 injuries, and the damage of 2116 ha of agricultural fields, 5155 houses, 771 public buildings, and 33 km of roads. Moreover, BNPB, 2018[1] reported that 74 landslides occurred and caused 18 deaths and 947 people losing their houses during the period of January-November 2018.

According to the map of potential ground movement areas in Indonesia, as shown in Figure 2.1, the province of West Java is categorized as the highest risk level of ground movement where 544 landslides occurred in 2018 (Sudrajat et al., 2019). One of these is situated in the Ciloto district. The Ciloto landslides have been active since 1984 (Sugalang, 1993; Abidin et al., 2015) and have

---

[1] Indonesia National Disaster Management Authority

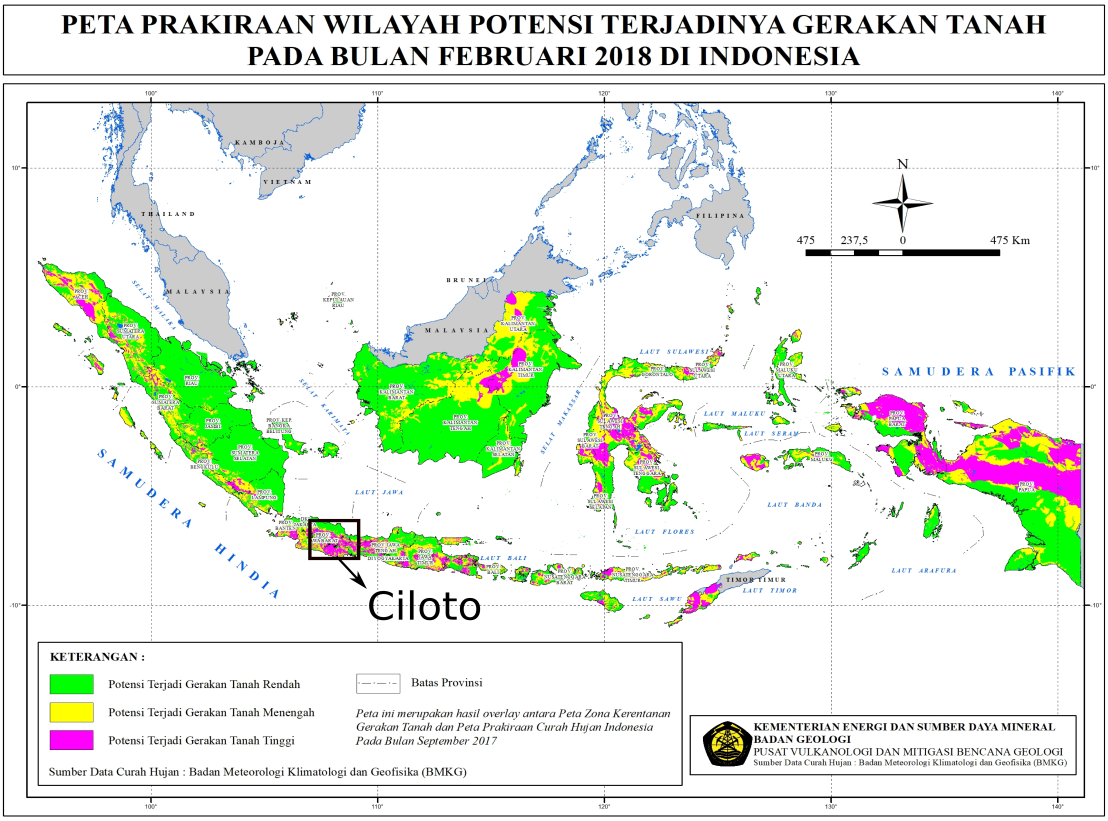

FIGURE 2.1: The potential areas of ground movement in Indonesia (PVMBG, 2018) with the location of the case study, the Ciloto district, West Java. The green color illustrates low-risk regions of the potential ground movement, the yellow color for the middle-risk level, while the purple color describes the high-risk level of the potential ground movement.

affected the economic and social factors due to the existence of the crucial highway connecting Jakarta and Bandung, two of big cities in Indonesia (Munarto et al., 2015). For this reason, it is worthwhile to investigate the Ciloto landslides.

2.1 The Physical Environment in Ciloto

Ciloto, West Java is one of the most landslide-prone areas in Indonesia. This region moves periodically and has a high risk of landslides when the physical conditions are over the limit of slope stability. The physical description of the Ciloto area includes morphology, lithology, and hydrology along with rainfall intensity as an external factor trigging higher soil water saturation. Geomorphology describes the landscape with its earth's surface features which influence landslide risk created by the physical, chemical or biological process. Lithology is the description of physical characteristics, such as the type, size, color, texture, and composition or mineralogy, of soil (include grain and clast) and rock. Furthermore, hydrology gives information about how water circulates according to surface water flow, groundwater, infiltration, soil moisture, and pore water pressure.

2.1.1 Morphology

The Ciloto landslide zone is located on the hilly ridges to a creek. The Cijember river flows in the middle of this area. The slope is mostly about 15^{o} - 25^{o} and on some parts there are steep slopes about 50°. This mountainous area was built to residence and agriculture. Cianjur-Puncak Highway lays between Kampung Baru Region and green space cutting the foothills on the location (Purnomo, 1993). Meanwhile, there is also a deep creek splitting along Kampung Baru become two main zones.

FIGURE 2.2: Spatial view for morphology classes in Ciloto area

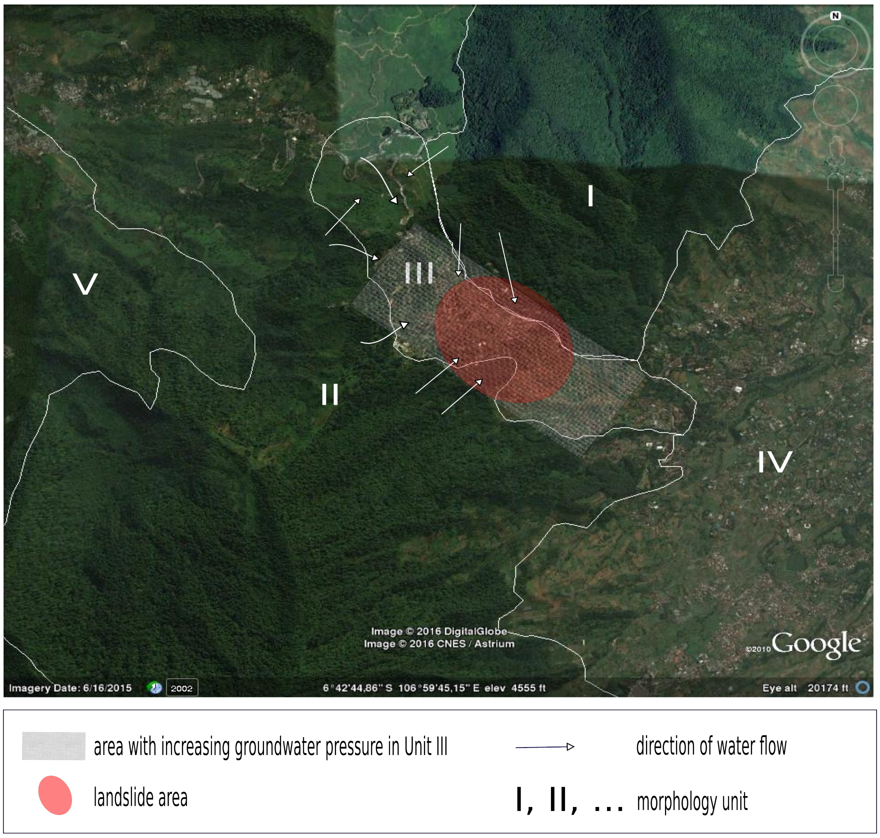

(A) the morphological unit of the Ciloto area is divided into five classes (Sugalang, 1989).

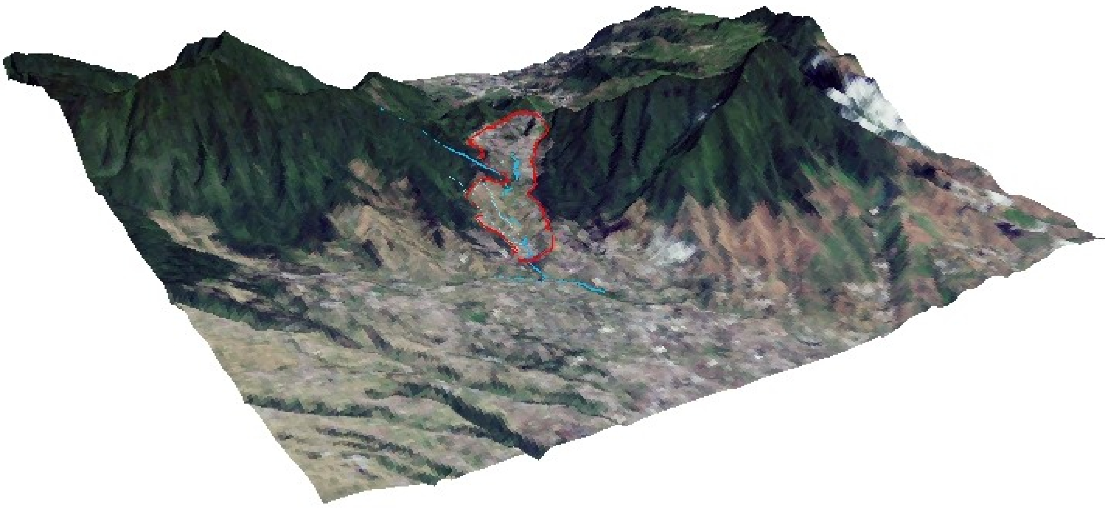

(B) The 3D modeling Ciloto prone landslide area with the blue lines as CiJember River. The optical image is generated by Landsat 8 with a color composite from the natural band (4,3,2) and the elevation model from SRTM 30 m.

Sugalang, 1989 described the geomorphology reason why Ciloto is risked by the landslide as seen in Figure 2.2. Based on water flow, The Ciloto is classified as five classes, which are:

- Unit I : Lemo Mountain area
- Unit II : Pondok Cikoneng area
- Unit III : Puncak, Jember and surrounding area
- Unit IV : Sindanglaya area
- Unit V: Foothills of Cempaka, Tugu and the surrounding area.

The unit I & II are acting as water infiltration and Unit III, IV & V as water flow area.

Rainfall on the unit I & II as infiltration area is higher than other units; hence both surface water flow and groundwater will be accumulated and increase pore water pressure on Unit III (Figure 2.2.a). The groundwater further infiltrates through a layer of permeable rock and reach Unit IV. Slope inclination of crown landslide Ciloto is about 15^{o} - 20^{o} and 7^{o} - 15^{o} on the middle. Namely, Unit III, IV and V become areas of water flow. For unit III, erosion was confirmed exist temporally at the steep valley of the Cijember River.

2.1.2 Geology

According to the geology map as shown in Figure 2.3, mostly the type of rock around Ciloto is quaternary volcanic sediments consisting of basalt and andesitic tuffs especially breccias (Sadarviana, 2006). Two geologist drill holes as seen in Figure 2.4 and a surface mapping were undertaken on the location. The first survey was held from 14 to 18 June 1988 with the height of 1319.18 m above MSL and the total depth of 11 m. The second survey was from 20 to 24 June 1988 with the height of 1281.48 m above MSL and the total depth of 18.6 m. Sugalang, 1993 divided the soil framework in Landslide Ciloto into several layers:

- Clay and Silt
  They are formed by weathering with characteristics of brown color, soft-firm constitution, and high plasticity. The thickness of this soil layer is about 3 m.
- Silty sand and sandy clay
  The characteristics of this layer are permeable, grey in color, soft-medium plasticity, fine to coarse-grained, and saturated with water. The unconsolidated sand was found in the ground depth of 4-7 m.
- Clay with a small number of pebbles
  Medium weathering, brown in color and unconsolidated quaternary volcanic product, high plasticity, stiff, rock fragments of andesitic origin formed this layer.
- Breccias
  Breccia is clastic sedimentary rocks composed of fragments of mineral such as andesite embedded in a fine-grained matrix of sand or tuff. The rocks feature a hard and compact texture with a grey color.
- Silt-clay
  A combination of silt and clay on this layer has grey and brownish grey color, a relatively soft texture, and contains wood or plants. The thickness was about 8 m found at the deepest part of the second drilling. The clay content was stiff and high plasticity. There was also a thin layer below the silt-clay layer consisting of sand with gravel and some wood pieces sourced from lake sediment.

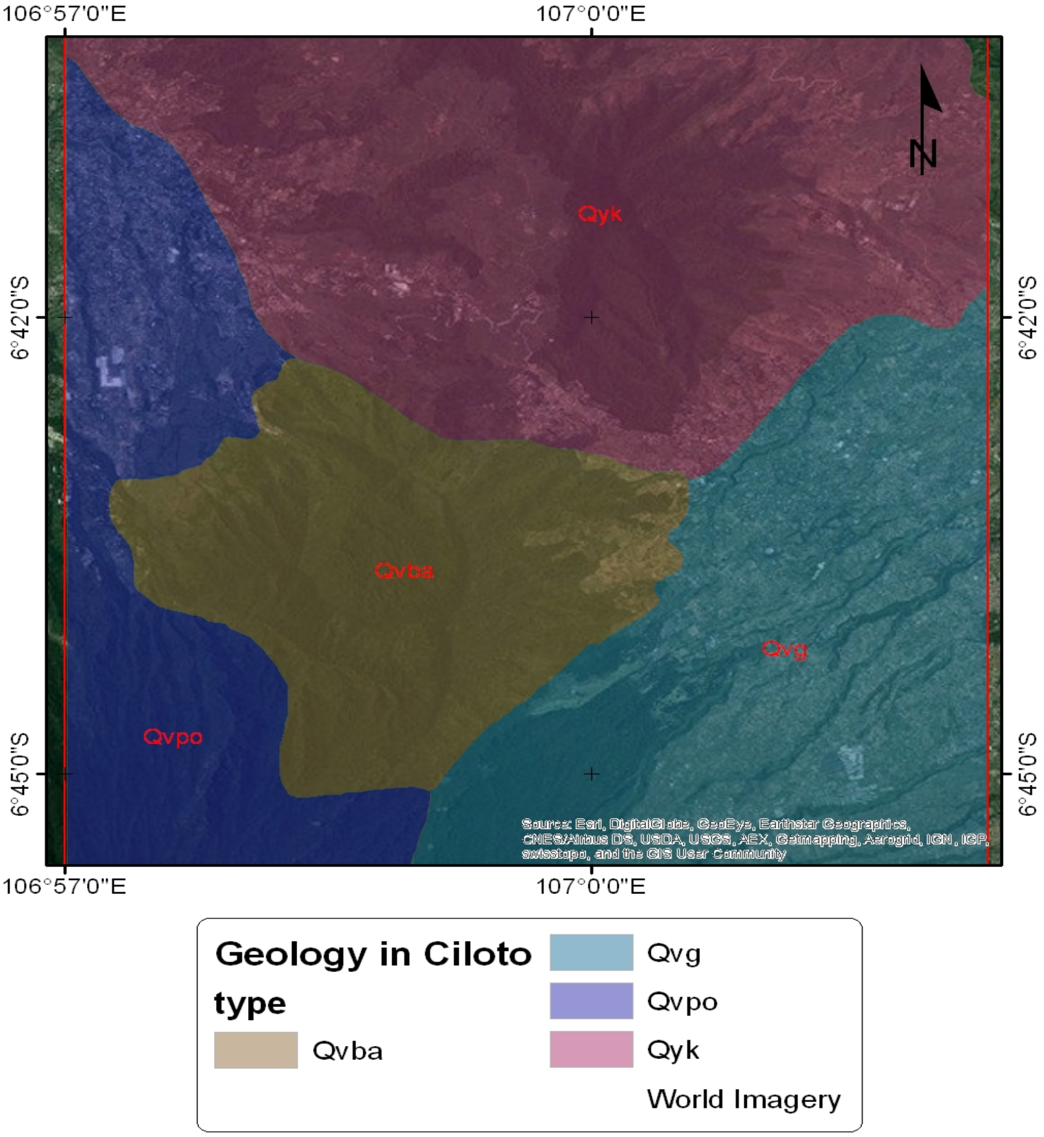

Qvpo = older deposits lahar & lava, andesitic basalt, with oligoclase-andesine labradorite, olivine, pyroxene, and hornblende
Qvba = basalt lava flow from Gegerbentang Mountain and local vents
Qyk = breccia and lava from local vents
Qyg = breccia and lahar from Gede Mountain
Source: Systematic Geologic Map, Java. Cianjur-Bogor Quadrangle. Geological Research and Development Center, Indonesia

FIGURE 2.3: The type of rocks in the Ciloto district

FIGURE 2.4: The drilling result of two points observation

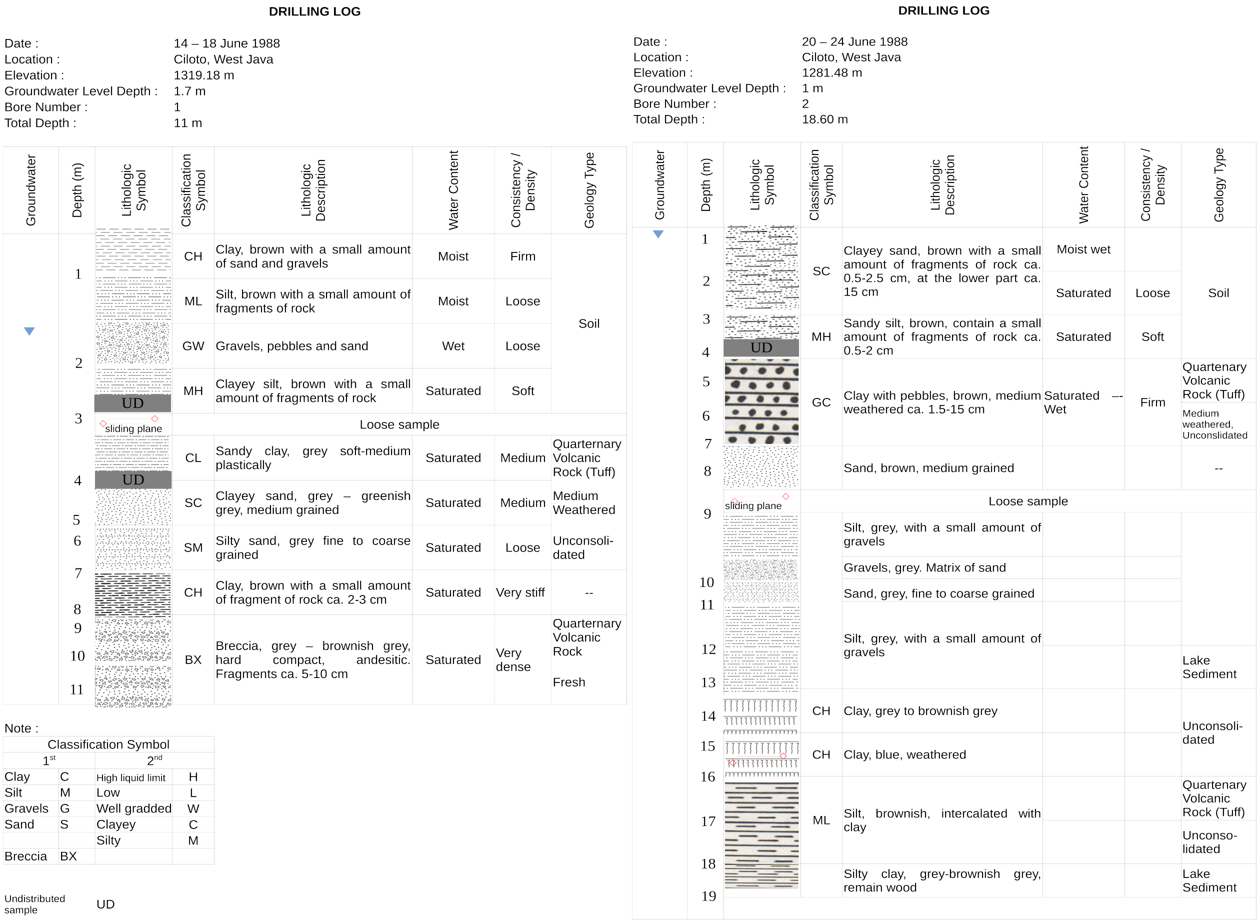

DRILLING LOG

Date : 14 – 18 June 1988
Location : Ciloto, West Java
Elevation : 1319.18 m
Groundwater Level Depth : 1.7 m
Bore Number : 1
Total Depth : 11 m

Groundwater	Depth (m)	Lithologic Symbol	Classification Symbol	Lithologic Description	Water Content	Consistency / Density	Geology Type
	1		CH	Clay, brown with a small amount of sand and gravels	Moist	Firm	Soil
			ML	Silt, brown with a small amount of fragments of rock	Moist	Loose	
▼			GW	Gravels, pebbles and sand	Wet	Loose	
	2	UD	MH	Clayey silt, brown with a small amount of fragments of rock	Saturated	Soft	
	3	sliding plane	Loose sample				
	4	UD	CL	Sandy clay, grey soft-medium plastically	Saturated	Medium	Quarternary Volcanic Rock (Tuff)
			SC	Clayey sand, grey – greenish grey, medium grained	Saturated	Medium	Medium Weathered
	5 6		SM	Silty sand, grey fine to coarse grained	Saturated	Loose	Unconsoli-dated
	7 8		CH	Clay, brown with a small amount of fragment of rock ca. 2-3 cm	Saturated	Very stiff	--
	9 10 11		BX	Breccia, grey – brownish grey, hard compact, andesitic. Fragments ca. 5-10 cm	Saturated	Very dense	Quarternary Volcanic Rock Fresh

Note :

Classification Symbol			
1st		2nd	
Clay	C	High liquid limit	H
Silt	M	Low	L
Gravels	G	Well gradded	W
Sand	S	Clayey	C
		Silty	M
Breccia	BX		

Undistributed sample UD

(A) Drilling Log I (Sugalang, 1989)

DRILLING LOG

Date : 20 – 24 June 1988
Location : Ciloto, West Java
Elevation : 1281.48 m
Groundwater Level Depth : 1 m
Bore Number : 2
Total Depth : 18.60 m

Groundwater	Depth (m)	Lithologic Symbol	Classification Symbol	Lithologic Description	Water Content	Consistency / Density	Geology Type
▼	1 2		SC	Clayey sand, brown with a small amount of fragments of rock ca. 0.5-2.5 cm, at the lower part ca. 15 cm	Moist wet Saturated	Loose	Soil
	3 4	UD	MH	Sandy silt, brown, contain a small amount of fragments of rock ca. 0.5-2 cm	Saturated	Soft	
	5 6 7		GC	Clay with pebbles, brown, medium weathered ca. 1.5-15 cm	Saturated — Wet	Firm	Quartenary Volcanic Rock (Tuff) Medium weathered, Unconslidated
	8			Sand, brown, medium grained			--
	9	sliding plane	Loose sample				
				Silt, grey, with a small amount of gravels			
				Gravels, grey. Matrix of sand			
	10 11			Sand, grey, fine to coarse grained			
	12 13			Silt, grey, with a small amount of gravels			Lake Sediment
	14		CH	Clay, grey to brownish grey			Unconsoli-dated
	15		CH	Clay, blue, weathered			
	16 17		ML	Silt, brownish, intercalated with clay			Quartenary Volcanic Rock (Tuff) Unconso-lidated
	18 19			Silty clay, grey-brownish grey, remain wood			Lake Sediment

(B) Drilling Log II (Sugalang, 1989)

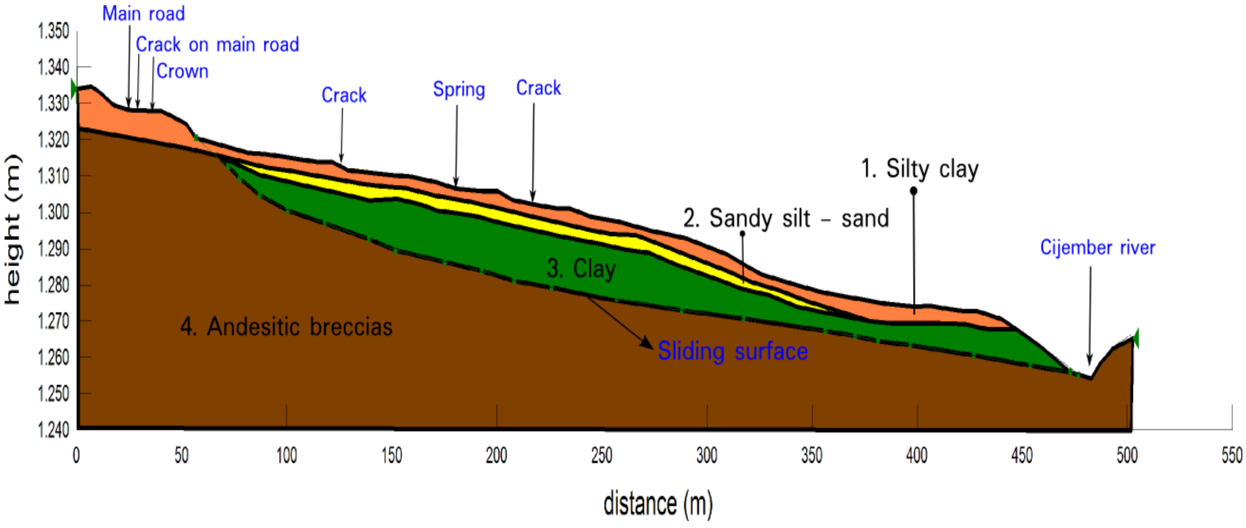

FIGURE 2.5: The landslide profile based on the assessment of GPS surveys, slope stability and geomorphology analysis, and the extraction of boreholes in Figure 2.4 (Sumaryono et al., 2015)

Considering soil mechanics data, a previous researcher (Sumaryono et al., 2015) mapped the profile model of the sliding surface in Puncak Highway, Ciloto. Figure 2. 5 shows a line profile starting from on the top layer to toe of the landslide body based on the drilling logs survey in Figure 2.4. Silty clay mostly covers the top layer and following to sandy silt - sand. The sliding surface lays between clay and andesitic breccias layer. Since andesitic breccias are volcanic rocks with cohesion value kg/cm^2, the layer is quite stable in condition no great weathering infiltrated into it. However, upon these volcanic rocks, there is a reposed clay layer having water content of 50.87% and cohesion of 0.104 kg/cm^2 which makes the border layer easily sliding to the lower elevation. As noted, this slope profile considered only one slide surface but the field surveys assessment indicates the movement as multiple sliding surfaces.

2.1.3 Hydrology

The Ciloto landslide is affected by both groundwater and surface water flow. Even though the flow and pressure of water and hydrological gradient depend on local geology conditions, it concludes that the great recharge of ground and surface water comes from rainfall (Kotchoni et al., 2019). Based on weather and climate data and average rainfall maps of East Java (1981-2010) produced by BMKG[2], the type of rainfall in Ciloto belongs to tropical monsoon climate which has extraordinarily rainy wet seasons and pronounced dry seasons. The wet season begins in November - April with intensity rainfall 235-334 mm/month and the dry season is in May - September with the number of rainfall about 71-167 mm/month. The average rainfall is about 1830 - 3000 mm/year.

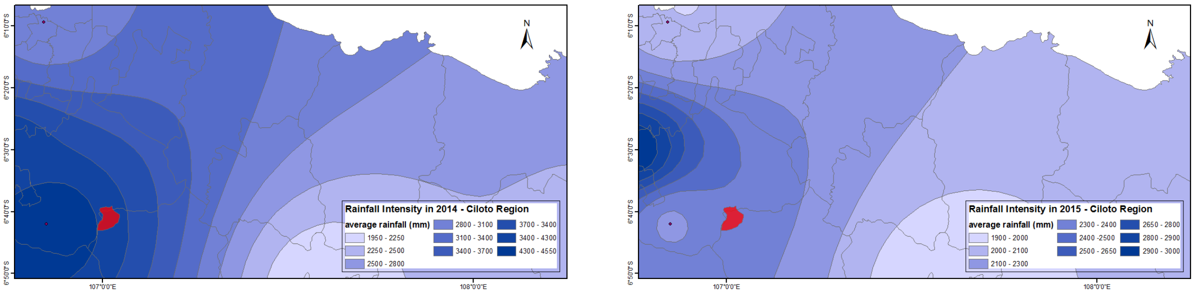

(A) 2014 (B) 2015

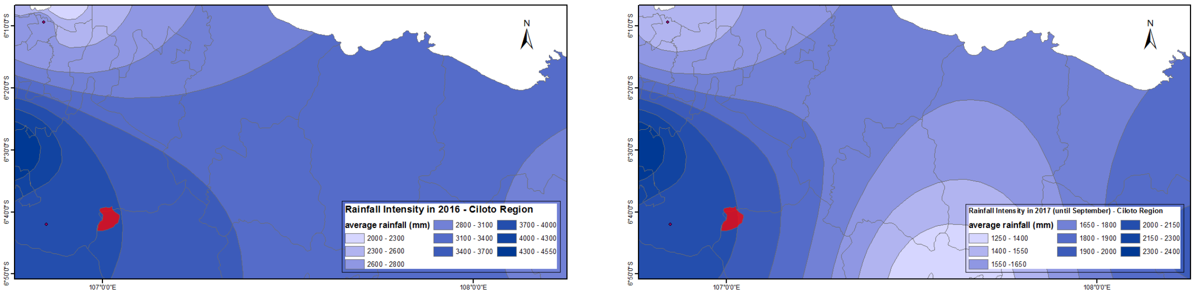

(C) 2016 (D) 2017

FIGURE 2.6: West Java rainfall map from weather stations bank data in Indonesia. The red polygon is marked as Ciloto region with the nearest meteorology station (Citeko) plot as red dot.

---

[2] Indonesian Agency for Meteorological, Climatological, and Geophysics

The actual rainfall for the three recent years in Ciloto does not have a significant difference to 1981-2010. We used the collective weather data from the rain gauge instrument installed on local meteorological stations around West Java which are Stasiun Geofisika Bandung, Stasiun Klimatalogi Darmaga, Stasiun Meteorologi Citeko, Stasiun Meteorologi Jatiwangi, Stasiun Meteorologi Kemayoran, and Stasiun Meteorologi Maritim Tanjung Priok. The total rainfall intensity in 2014, 2015, 2016 and until September 2017 were 3400 - 4300 mm, 2300 - 2400 mm, 3700 - 4000 and 1900 - 2000 mm, respectively. The interpolation of the rainfall map has been generated using the Inverse Distance Weighted (IDW) method shown in Figure 2.6.

Furthermore, the hydrological cycle also involves precipitation to surface runoff then subsurface infiltration processes. This cycle is considered as some important factors of ground movement in Ciloto. The rainwater flows to the CiJember river and through subsurface and overland flow. Not all of the rainwater is direct going to the stream channel, but partly it is infiltrated into groundwater. Merely due to gravity, groundwater flow transports from high to lower elevation and in the end either reaching to stream channels or accumulated as springs or purposely created as fish ponds.

Regarding Ciloto morphology, recharge zones are Unit I (Lemo Mountain) and Unit II (Pondok Cikoneng) and a discharge zone as Unit III (Ciloto region). Because of this interaction, shallow groundwater is found in the Ciloto region. It is proved by the drilling log data which groundwater level (water table) has been detected from the depth of 1.5 m with its layer of clay and silt.

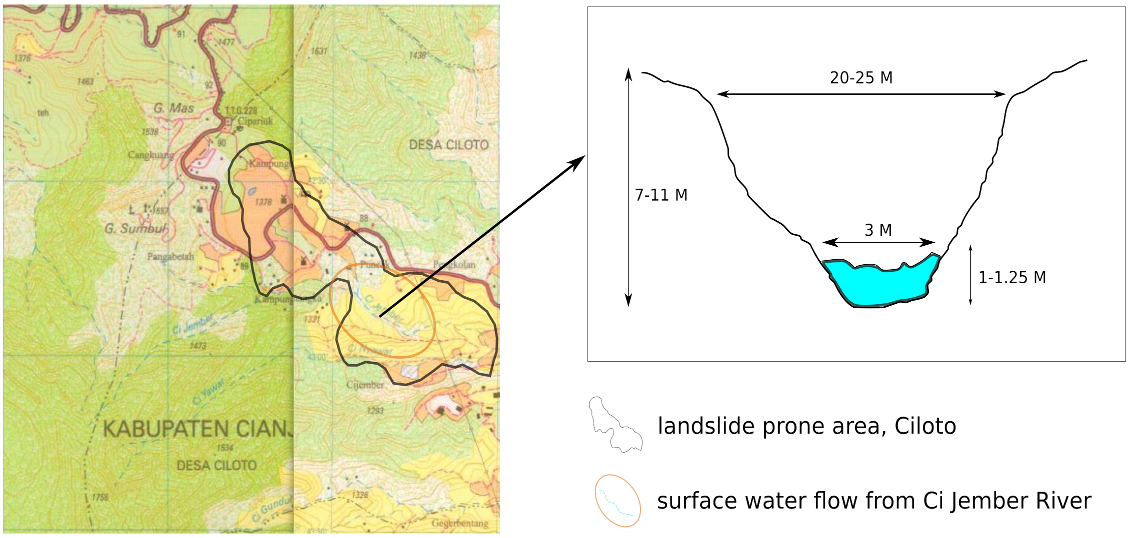

FIGURE 2.7: Profil of Cijember Basin ((Sadarviana, 2006) with modification)

Horizontal and vertical erosions driven by the Cijember river lead to slope instability because water sourced from the river leaks and infiltrates into the ground which has unconsolidated soil. Figure 2.7 describes the surface flow through the prone landslide Ciloto area. Several fishponds are found as well in the location and increase ground saturation since water from fishponds easily permeates into soil and rocks (Sadarviana, 2006). Wellspring is a natural condition where groundwater, from Unit I and II, flows from aquifer throughout surface (Unit III). The fluctuation in this area was almost 20 liters/second. However, Unit III belongs to the landslide risk zone, and if these wellsprings were not controlled well and let them flew abundantly on the surface, pore water pressure could increase, and hence it made the condition worse.

Pore Water Pressure

Pore water pressure is influenced by surface water flow, groundwater, porosity and permeability of soil and rock as illustrated in Figure 2.8. Infiltration is a circulation of water on the ground flowing beneath the surface. It means that water from the soil surface moves through the soil. The water redistribution is known as infiltrated water subsequently moving into the unsaturated and saturated zone of soil involving exfiltration, capillary rise, recharge, and interflow cases. The material and hydraulic properties of soils highly involve them. One of the hydraulic properties of soils is pore water pressure and shear stress.

Pore water pressure means a pressure of groundwater which has gaps between particles of soil and rock and measured by a piezometer. Abramson et al., 1995 explained that porosity is a percentage of total volume pores between particles and depends on the size and cohesion of the grains. On the other hand, permeability is an ability of soil layer or rock to proceed with the groundwater. The relationship between both of them is described as; the bigger percentage of porosity, the higher layer of soil and rocks could permeate the groundwater namely high permeability.

If effective stress slope stability would be applied in analysis, then the information of pore water pressure and effective shear strength parameters are very crucial. Day, 2010 assumed that pore water pressures are hard to determine and estimate although they have a significant impact on slope stability. There are three estimations concerning the pore water pressures, as follows:

- Zero pore water pressure
  This condition of a pore water pressure equal to zero could be applied if the slope or bench drains will be constructed by drainage devices or in case the soil layer is above groundwater table.

- Groundwater table
  Groundwater table is a hydrostatic level surface of water in the ground after replenished by source of surface water, for instance, precipitation, streams, and rivers.

- Pore water pressure ratio
  It is the common popular method to estimate pore water pressure. The pore water pressure ratio has been defined below:

  $$r_u = \frac{u}{\gamma_t.h} \quad , with\ \sigma_v = \gamma_t.h \tag{2.1}$$

  where:
  r_u = pore water pressure ratio
  u = pore water pressure (psf or KPa)
  γ_t = total unit weight of the soil (pcf or kN/m^3)
  h = depth below the ground surface (m)
  σ_v = total vertical subsurface soil stress at depth (kN/m^2)

From 1993 to 2001 pore water pressure has been measured in the Ciloto district by Pangabean et al., 1998 and Rachman et al., 2001 with 4.4 - 13.5 m depth. There are eight points of the piezometer measurement distributed in the area. Appendix A.1 shows the table of pore water pressure ratio in May 1993, August 1994, January 1995 and May 1995 around 0.3 - 0.5 which CP3 and CP5 points were the highest ratios. Due to the rainy season starting in August, the pore water pressure increased at point C2 and C4 with the depth of 7.35 and 9.3 m, respectively. Two years later, a significant rise in pore water pressure ratio to 0.4 - 0.65 has occurred. The possible reason is that the soil mechanics and the intensity of surface- and ground-water increase than a few years ago. Thus, the increase of pore water pressure ratio might be trigging a failure surface.

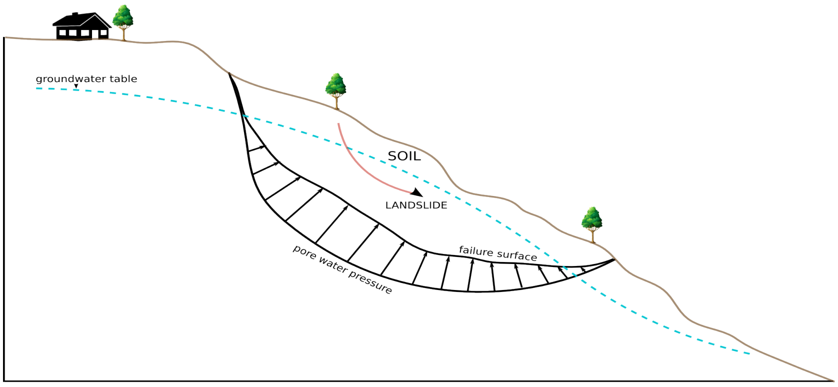

FIGURE 2.8: Pore water pressure along the slip surface

On the other hand, the total vertical subsurface soil stress has a similar pattern as rainfall intensity between May 1993 - July 2001 because there was an increment of rainfall between May to December 1997 as well. However, the resemblance was not found on all measured points (Table 2 in Appendix A.1) since subsurface soil stress is influenced not only by rainfall but also surface load, permeability, and human activities in Ciloto's environment.

2.2 The Field Survey in The Ciloto Landslides Prone Area

On 8 July 2017, the field trip to the Ciloto region was done to explore and comprehend the actual situation. Some documentation describing the environment was captured and plotted based on UTM coordinate. In the north of the observed area, the ground movements of 1-2 m at a resort hotel was reported in 2014. Since the incident, the swimming pool of the hotel is out of order. In the same year with a radius of 200 m from the first evidence, 33 families were evacuated from their houses since cracks have been found on several house's walls. Moreover, there was also an entire broken house as seen in Figure 2.9 which caused by not well-constructed buildings and easily getting destruction from the phenomenon. A soil sample was taken near to abandoned houses also initiated high moisture contained in soil fragment.

Afterward, the extensometer has been installed since November 2014 by BPPTKG[3] considering some clear evidence found in the area. The graphic (please see Figure 5.19 in Chapter 5) of displacement indicated no significant uplift and subsidence occurred after ground movement in 2014. However, the instrument has still recorded a ± 0.3 cm fluctuation vibrating in Kampung Puncak, Ciloto. In Chapter 4, this continuously ground measurement will be compared to the InSAR result since the duration's monitoring are in the same period.

Several landslides in the past occurred in Puncak highway located in the middle of the case study area. Indonesian National Board for Disaster Management (BNPB) recorded the two biggest landslide hazards that happened in Bandung and Bandung Barat, West Java on 23 February 2010 and 25 March 2013 with 33 deaths, 17 injured, 936 refugees and 14 death, 23 injured and 185 refugees, respectively. Even two single landslides occurred in the same region, Jl. Raya Puncak Km.81, close to the Bumi Aki restaurant. At first in 2015, the mass movement was placed next to the body of the Puncak highway and damaged the local infrastructure and plant field around the area. The second event happened in the rainy season of 2017. The mass movement was located on another side of the first event that occurred in 2015. This hazard belonged to a small type of mass wasting with the impact area of ± 25 x 25 m. However, the deposited debris was laid right into the Puncak highway (Jl. Raya Puncak Km.81) and disconnected one of the most crucial access

---

[3] Technical Research Center for Geological Hazard, Yogyakarta

FIGURE 2.9: A broken house due to the effect of ground movement located in the Puncak Pass, RW.6.

pathways between Bogor and Bandung city. Moreover, a few mass movements in recent years still threat Ciloto, Cipanas Regency which is briefly described in Table 2. 1.

TABLE 2.1: Mass movement occurred in Ciloto and surrounding

No	Date	Landslide Description
1	1 Jan 2012	Puncak Highway, Ciloto connecting between Bogor and Cianjur City was broken. All of the transportation movement was stopped.
2	17 Jan 2013	Ground movement about 1 m along 117 m occurred in Ciloto with evidence of cracks found at 11 houses. Twenty-five residences have been evacuated.
3	20 Jan 2014	Landslide occurred in the Ciloto area.
4	30 Jan 2014	Landslide occurred in the Ciloto area. There was a victim death crushed by debris or landslide materials.
5	21 Jan 2014	Landslide occurred on 8 m cliff at the side of Puncak Highway, Kampung Panimbangan, Cisarua. There was no victim but made long traffic due to the debris of the slide on the road.
6	9 Nov 2014	Two people died and two people injured because of landslide happened in the Puncak area, Cisarua. These people were workers to build a villa.
7	13 Jan 2016	A partly area of Puncak Highway, Cugenang was broken due to large landslide materials along 25 m with 5 m height on the road.

Furthermore, several fish ponds were still found at Ciloto. A fish pond had been seen near to a Kampung Puncak's hill and another one on the local citizen houses wherein the middle split by creek of CiJember river. Previous research from Schuler, 2015 stated that fish fonds and springs had caused surface water more easily saturated into underground soil/rock. According to the landslide profile analyzed by two drilling cores survey, surface water could penetrate three upper layers and accumulated to the clay fragment where slide surface also located on this layer marked as a symbol of sliding plane in Figure 2.4. Therefore, the abundant water contained from fish fond will increase the parameter of shear stress on slope instability. At the time of field survey, we did not find any spring but Sugalang, 1989 reported that several springs exist with one of them having a flux around 20 liters per minute. The adverse effect of springs, which are not controlled well, will contribute to the high of pore water pressure as well.

2.3 Previous Works Using Geodetic Methods

2.3.1 The Terrestrial Measurement

PVMBG[4] measured the Ciloto area using Electronic Distance Measurement (EDM) and the theodolite instrument. There are 18 measured points distributed on the location as shown in Figure 2.10. The landslide zone is generally divided into three segments:

- The top segment
  The distance of this zone is 0 - 245 m from the main scarp with the slope inclination 15^o - 20^o. It consists of M1, M2, M3, M4, M5, M19, M20, M21, M22, M27, M28, and M29.
- The middle segment
  The distance of this zone is 245 - 435 m from the main scarp with the slope inclination 7^o - 15^o. It consists of M6, M7, M8, M9, M10, M11, M12, M13, M14, and M15.
- The toe segment
  The distance of this zone is 435 - 590 m from the main scarp with the slope inclination $< 7^o$ and a relatively flat surface. It consists of M16, M17, M18, M23, M24, M25, and M26.

The duration of the terrestrial campaign was done from October 1993 to June 1997. Mostly points displaced from north-west to south-east direction (Sadarviana, 2006). There are a few measured points, M7 and M20, which has great cumulative displacements over 2 m. Point M20 is located on the top of the segment has greater horizontal movement than vertical one since the point is located close to the CiJember river wherein the duration of the terrestrial survey a debris slide occurred. Hence, it made the M20 Benchmark get forced to the river direction. Nevertheless, the M7 point was located in the middle of the segment laid not close to the river, but a great-scale displacement of 2 m still occurred. There is no description of what a real accident occurred at this point because M7 is not located near the river and yield not caused by an effect of debris slide.

The mean velocity displacement is created to visualize the motion in the Puncak Highway area using surface gridding by GMT software. The range of velocity is approximate -10 cm/year for the vertical and ± 5 cm/year for the horizontal component. The horizontal displacement was smaller in the top area than in the middle and bottom areas. On the other hand, the vertical displacement showed bigger motion in the middle than in the top and bottom area. Regarding this invented ground movement, minor scarp has existed at the steep surface of Puncak Highway. There are two spots in Figure 2.11 clearly showing subsidence toward a southern direction. These subsidence locations are near to the CiJimber river and reported that erosion and debris slide occurred along the stream's river. Overall, the Puncak Highway landslide is classified as a prolonged movement event with the velocity in the range of 15.8 mm/year. Nevertheless, some observed points located near to the river have greatly displaced values with a maximum of 1,58 m/year.

---

[4] Centre of Volcano and Geological Hazard Mitigation

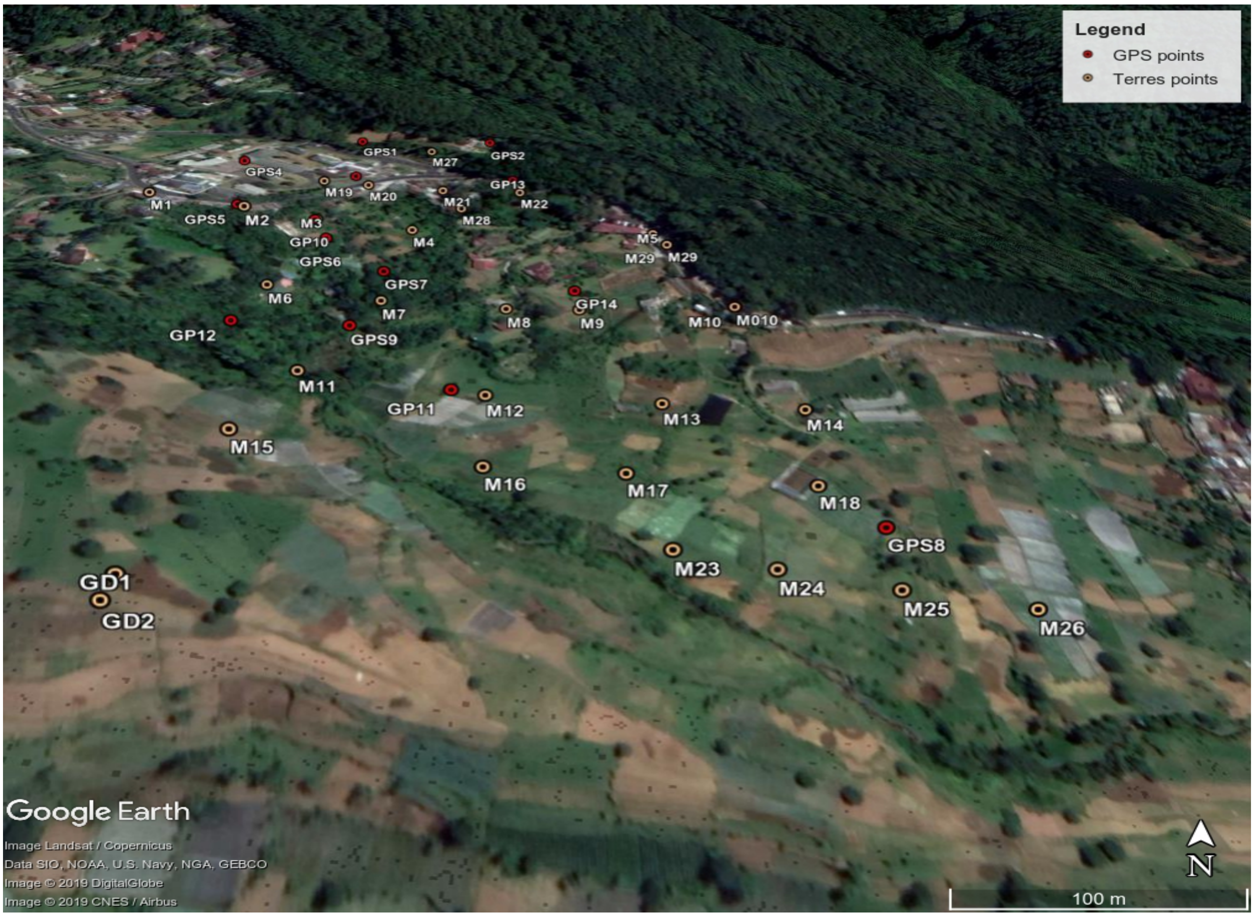

FIGURE 2.10: The terrestrial and GPS observation in the Puncak Highway area. Its detail information was described by (Sadarviana, 2006).

2.3.2 GPS Observation

ITB[5] and PVMBG conducted GPS measurements involving 17 observed points during 2002-2005. Furthermore, this campaign was continued in June 2012 - December 2012 held by the same institutes. Regarding the distance away from the main scarp, the distribution of GPS measured points (Figure 2.10) was divided into three main segments:

- The top segment
  The distance of this zone is 0 - 160 m. It consists of GPS1, GPS2, GPS3, GPS4, GP13 for the first GPS campaign and G01, G02, G03, G04, G06, BA1 for the second campaign.

- The middle segment
  The distance of this zone is 160 - 320 m. It consists of GPS5, GPS6, GPS7, GPS9, GP10, GP14, M10 and M28, BAT, BA2, G09, respectively.

- The toe segment
  The distance of this zone is 320 - 460 m. It consists of GPS8, GP11, GP12 and G08, G13, G27, respectively.

The first campaign assessed GPS measurement to statistic, kinematic and dynamic modeling in which the kinematic approach shows the best model to describe landslide movement in Ciloto since it had the closest approach with the model prediction. For GPS1, GPS2, GPS5, GPS8, GPS9,

---

[5] Bandung Institute of Technology

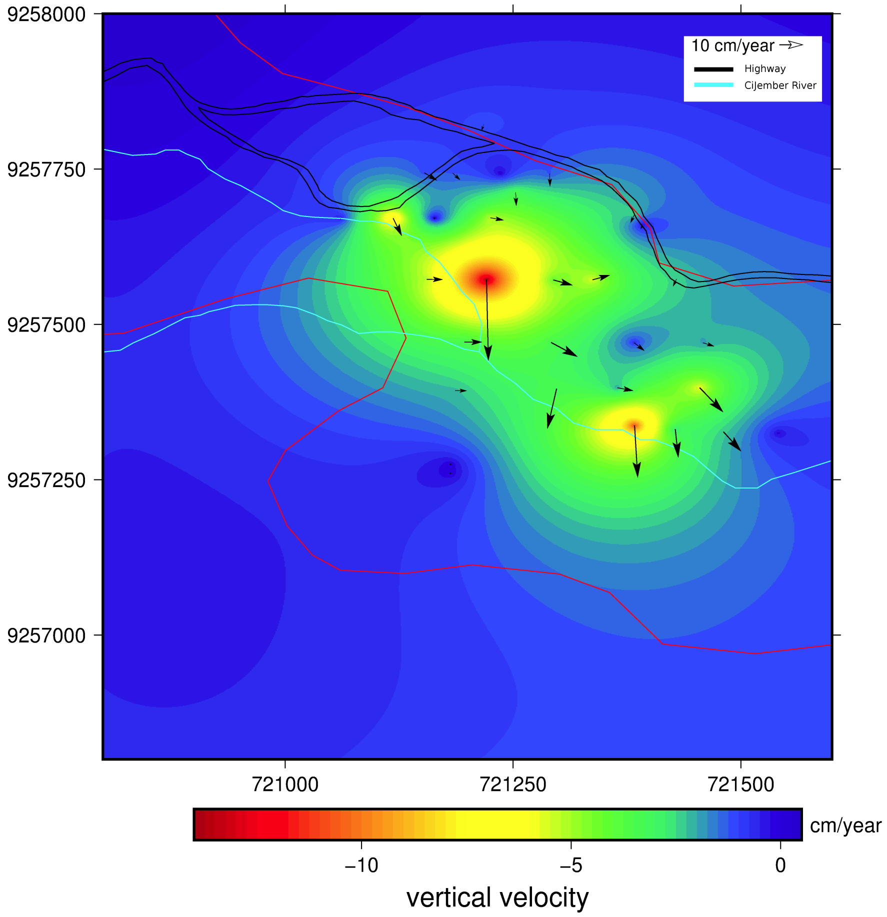

FIGURE 2.11: The mean velocity based on terrestrial observation in the Puncak Highway area.

GP10 and M10, the vertical displacement is much higher than horizontal displacement which could be interpreted that minor scarps found on these locations. As a pure representative of the movement behavior on a single slide, the displacement and velocity on the vertical direction are more fabulous than horizontal on the part of the head and toe. On the contrary, the horizontal displacement and velocity will be higher than the vertical ones on the middle part of the slide as illustrated in Figure 2.12 showing a correlation between the horizontal and vertical direction.

In December 2012, Sulaeman et al., 2013 found some curved slumps and cracks on Puncak roads. The slump was about 7 m length and vertically displaced about 10-15 cm. After the occurrence of heavy rainfall, new cracks appeared with a length and width of 4-6 m and 5-10 mm, respectively. The second campaign states that most of the measured points moved. The horizontal displacement on the crown body was 0.29 - 1.85 cm and vertically displaced -0.52 - -1.08 cm except for G2 point which uplifted to 1.48 cm. In the main body, the movement was about 0.45 - 11.41 cm horizontally and -0.30 - -3.95 cm vertically. Furthermore, the toe part had 1.32 - 13.65 cm horizontal shift and significantly uplifted 0.19 - 21.89 cm except for G27 point which subsided -13.82 cm. Generally, the horizontal velocity from Juni to December 2012 approximately was 6.2 mm/year - 12.4 cm/year with the direction toward southeastern. The table for the complete result of GPS measurement can be read from the article of Sulaeman et al., 2013.

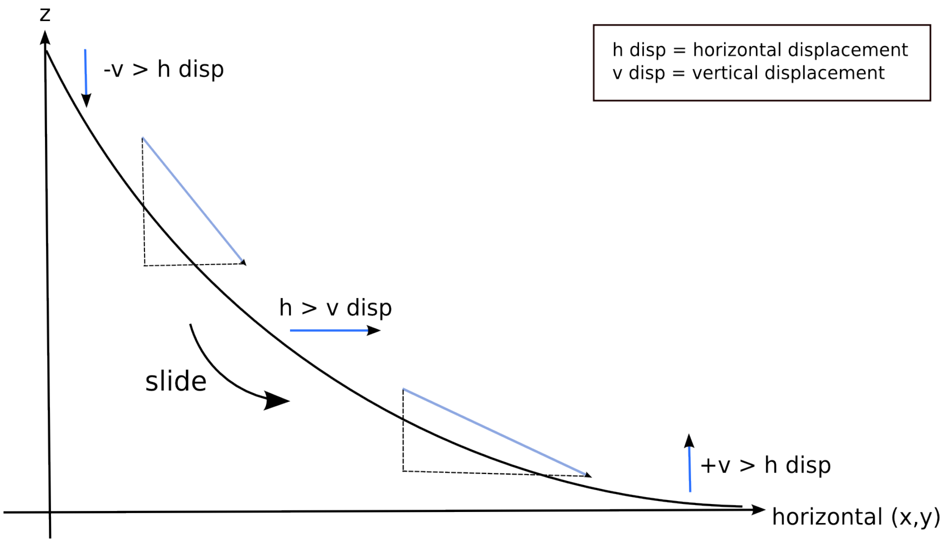

FIGURE 2.12: A simple illustration of slope displacement

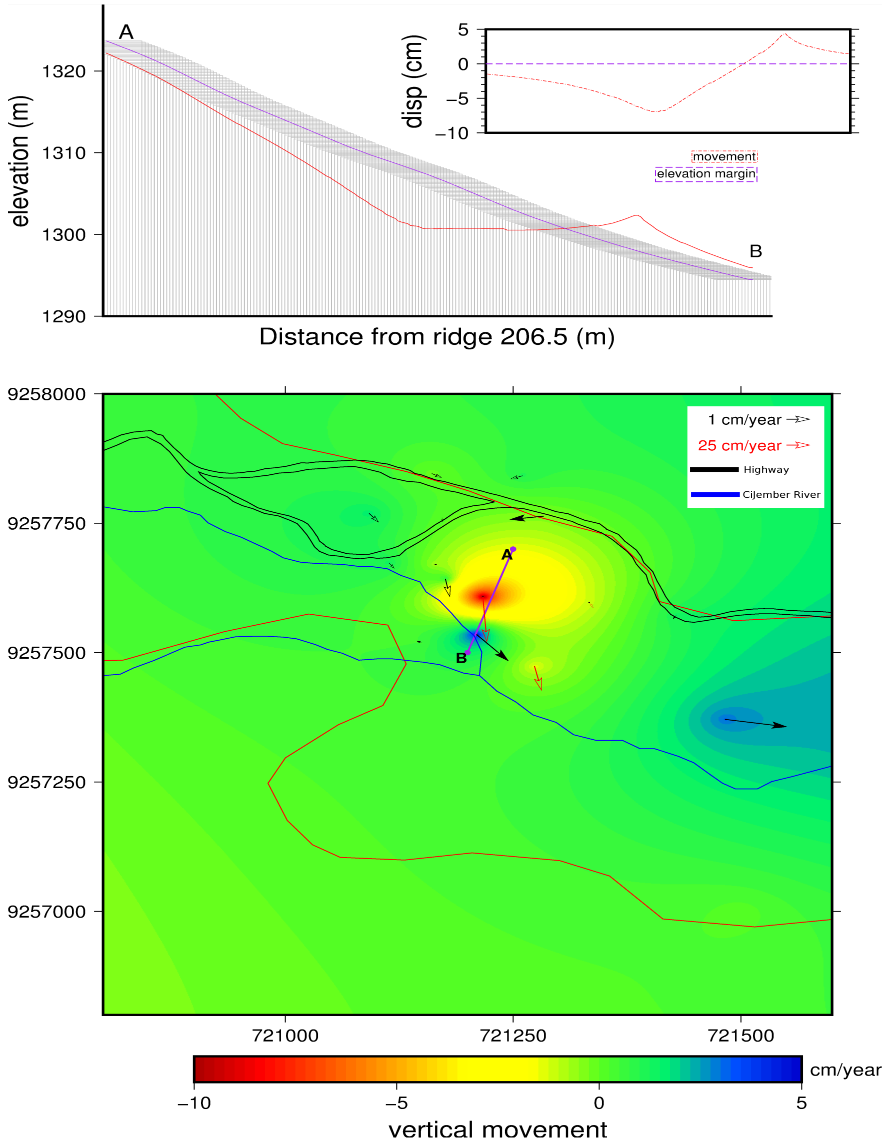

FIGURE 2.13: The mean velocity based on GPS observation in the Puncak Highway area.

Regarding Varnes, 1978 theory whether a mass movement exists or not, there are two simple tests to figure out the relationship between measured points and their reference points conducted by the GPS survey. The first evidence confirmed the distance between a monitored point and reference point should be usually shorter or longer by times and the second one is the consistency of displacement directions in the duration of observation times. As noted, the second theory is suitable only if the type of landslide is single-slide. It has a different direction along observation times if the landslide belongs to the compound slide (two or more slide). Abidin et al., 2007 tested the behavior of GPS survey points to Varney's Theory. The result proves that the type of landslide is multiple-slide because the displacement directions are not consistent in one way from the first survey to further surveys. This type of landslide agrees with previous research conducted by Sugalang, 1989.

We created the mean velocity displacement generated by GPS observation from 2002 to 2005 as the same gridding method as the terrestrial measurement. Figure 2.13 shows that the surface materials were still continuously displaced both in the horizontal and vertical components. However, the rate of velocity decreased comparing to the previous geodetic observation especially at the top of the area. There was a bulging found in the middle of the area caused by the accumulative of material pressure from the other observed GPS points and the increase of groundwater due to the infiltration of morphology 1 and the permeation of morphology 4. The profile between A and B explains the depleted and accumulated zone for three years. The vertical motion was displaced to -10 to 5 cm/year and ±1 cm/year. There were two points (GPS7 and GPS11) which moved about 55 and 30 cm/year horizontally since the points were located near to the CiJimber river. The GPS7, GPS8, and GPS11 were indicated as a retrogressive landslide in which the rupture surface extended in the direction opposite of the movement of displaced material (Sadarviana et al., 2010).

Chapter 3

The Basic Theory of InSAR

This chapter reviews the fundamental theory of Interferometry Synthetic Aperture Radar (InSAR) and Persistent Scatter (PSInSAR) which is the multi-temporal InSAR analysis using a stack of SAR data. It explains the development of PSInSAR briefly in recent years and then focuses on describing more to the PS and Small Baselines (SB) algorithm that is used to all of the processing data in the case studies. The interferogram is derived by SAR satellites. Generally, they are divided into different frequency bands; C (λ= 0.56 cm), Ka (λ= 0.85 cm), X (λ= 3 cm), and L-band (λ= 23.6 cm) which are commonly used by the InSAR society. The radar wavelength controls the ability of signal penetration below the ground surface. The depth of penetration increases with the wavelength λ (Dabbiru et al., 2014). It means that the L-band radar penetrates deeper than the C-band sensor. Hence, L-band can penetrate through parts of vegetation such as leaves and suitable to detect the surface's change in the vegetated region such as a landslide case study. Even though the C-band sensor has a lesser capability of penetration, the 12-day revisit cycle (for Sentinel-1 satellite) helps in supporting the performance of the time series InSAR algorithm to detect the persistent or distributed scatters.

3.1 Interferometry Synthetic Aperture Radar (InSAR)

Synthetic Aperture Radar Interferogram is two SAR images with slightly different look angles derived by either simultaneously two antennas mounted at the same satellite or at different times using repeated orbits on the same antenna. In terms of different times SAR image, namely master for the first acquisition and slave for the second acquisition, the interferogram is generated by cross-multiplying the first image with the complex conjugate of the second with a precise pixel-by-pixel after the co-registration process of both SAR images (Bamler et al., 1998). It contains both the total amplitude (interferogram amplitude) from the first amplitude image multiplied by the second and the phase difference (the interferometric phase) between the first and second phase values. It is one of the effective techniques to measure the Earth's surface changes utilizing the space-borne platform.

In the beginning, the basic principles of InSAR are dated back to the early 1970s (Graham, 1974). However, the first InSAR terrestrial application was introduced by Zebker et al., 1986 to obtain high-resolution topographic terrain maps from different simultaneous acquisitions based on slightly displaced antennas then continued by Gabriel et al., 1988 and Goldstein et al., 1989. The technique was explained in detail by Gabriel et al., 1989 in terms of mapping surface motion with the accuracy of 1 cm or less and over large areas ($\sim$ 50 km). It was applied in Imperial Valley, California using Seasat L-Band data. Furthermore, a general review of SAR interferometry has been explained, and the method was implemented to the observations of many geophysical phenomena such as deformations due to volcanoes, earthquakes and ice fields (e.g., Massonnet et al., 1993; Massonnet et al., 1995; Rosen et al., 2000). With the rising of the InSAR explorations, some research studies have identified seismic activities such as earthquake 's impact (Funning et al., 2005), subsidence due to over-exploitation of groundwater (Chen et al., 2016), oilfields (Liu et al., 2015) and relative sea-level rise (Bekaert et al., 2017), the behavior of volcanoes (Hooper et al., 2007a), and slow movement in landslide prone areas (Cascini et al., 2010).

For the case studies in this dissertation, the SAR data come from ERS-1/2, ALOS PALSAR and Sentinel-1 satellite. The European Remote Sensing satellite(ERS-1) was launched in July 1991 and the identical to ERS-1 with an extra instrument, ERS-2 was launched in April 1995. They were mainly operated in a 35-day repeat cycle with the different acquisition between ERS-1 and ERS-2 in a 1-day. The type of their orbit was near-circular, polar and sun-synchronous with 782 -785 km of the altitude. The ERS-1 and ERS-2 tandem by 1-day difference demonstrated the first time precise topographic information generated from space-data using SAR interferometry technique. ERS-1 was initially designed for maritime applications, but it produced very inspiring results for land applications (Klooster, 2011). The ERS-1 satellite carried five sensors: an Active Microwave Instrument (AMI) which consisted of a Synthetic Aperture Radar and a wind scatterometer in C-Band, a radar altimeter (RA), a radiometer (ATSR), a microwave sounder (MS) and range equipment (PRARE). Besides, the ERS-2 satellite carried the Global Ozone Monitoring Instrument (GOME)(ESA, 2019c). Envisat was launched in 2002 as a successor to ERS and to continue a series of earth observation missions from ESA. Envisat was operated in a 35-day repeat cycle as well, but it changed to a 30-day cycle in 2010 due to an extension of mission lifetime (ESA, 2019a). A complete geometric and radiometric specifications of ERS-1/2 and Envisat could be seen in Table 3.1.

TABLE 3.1: The geometric and radiometric specifications of ERS-1/2 and Envisat for SAR image mode (ESA, 2019b)

Geometric specifications		Radiometric specifications	
Spatial resolution	along track ≤30 m , across track ≤26.3 m	Frequency	5.3 GHz (C-band)
Swath width	102.5 km (telemetered), 80.4 km (full performance)	Wavelength	5.6 cm
Swath standoff	250 km to the right of the satellite track	Bandwidth	15.55±0.1 MHz
Localisation accuracy	along track ≤1 km , across-track ≤ 0.9 km	Polarization	VV for ERS-1/2; VV, HH, VV/HH, HV/HH or VH/VV for Envisat
Incidence angle	near swath 20.1°, mid swath 23°, far swath 25.9°	Peak sidelobe ratio	along track >20 dB, across-track > 18 dB
Incidence angle tolerance	≤0.5°	Spurious sidelobe ratio	along and across-track > 25 dB
		Integrated sidelobe ratio	>8 dB
		Radiometric resolution	≤2.5 dB at sigma-zero = -18 dB

The advanced Land Observing Satellite (ALOS) was launched in January 2006 and placed in a sun-synchronous orbit at 691 km. ALOS required 671 passes to cover a full global earth's surface with a 46-day repeat cycle. It carried three remote sensing instruments: the along-track 2.5 m resolution Panchromatic Remote-sensing Instrument for Stereo Mapping (PRISM), the 10 m resolution Advanced Visible and Near-Infrared Radiometer type 2 (AVNIR-2), and the variable-resolution polarimetric Phased Array L-Band Synthetic Aperture Radar (PALSAR) (Rosenqvist et al., 2007). The advantage of L-Band data is capable of penetration through vegetation and partially reaching the ground surface (Teshebaeva et al., 2015). Hence, the data is suitable for mapping the surface deformation in area covered by vegetation such as rural and agricultural places. The ALOS PALSAR characteristics is described in table 3.2.

Sentinel-1A has been launched since April 2014 while Sentinel-1B since April 2016. The main objective of these two satellite constellation is the land and ocean monitoring. The mission of Sentinel-1 is continue to provide C-Band SAR data following the retirement of ERS and Envisat (ESA, 2019d). The two-satellite constellation offers a 12-day repeat cycle and a conflict-free operation which is not requiring an official submit request to access the product. Sentinel-1 has

TABLE 3.2: The ALOS PALSAR instrument characteristics (Hamazaki, 1999)

Characteristic	ALOS PALSAR
Antenna size	8.9 m x 3.1 m
Centre frequency	1270 MHz / 23.6 cm (wavelength)
Chirp bandwidth	28 MHz (FBS, ScanSAR long burst) , 14 MHz (FBD, POL, ScanSAR short burst)
Image modes	Fine beam mode (FBS, FBD): Single Polarization (HH or VV) , Dual pol. (HH/HV or VV/VH) Polarimetric mode (POL): Quad-pol. (HH/HV/VH/VV) ScanSAR mode: Single pol. (HH or VV) , No. sub-beams: 3,4, or 5 , Short (14 MHz) or long (28 MHz) burst Direct Transmission mode (DT): FB single pol (14 MHz) , ScanSAR (14 MHz)
Swath width	70 km (FBS, FBD with 34.3° incidence angle 30 km (POL with 21.5° incidence angle
Ground resolution	10 x 10 m (FBS) and 20 x 10 m (FBD)

four operational modes (Attema et al., 2006), which are: stripmap mode (SM), interferometric wideswath mode (IW), extra wide swath mode (EW), and wave mode (WV). Table 3.3 explains the main characteristics of the Sentinel-1 for all modes.

TABLE 3.3: The main characteristics of the Sentinel-1 nominal measurement modes (Attema et al., 2010)

Parameter	SM mode	IW mode	EW mode	WV mode
Polarisation	Dual (HH+HV or VV+VH)	Dual (HH+HV or VV+VH)	Dual (HH+Hv or VV+VH)	Single (HH or VV)
Minimum incidence	20° - 45° (access range)	25°	20°	23° + 36.5°
Azimuth resolution	<5 m	<20 m	<40 m	<5 m
Ground range resolution	<5 m	<5 m	<20 m	<5m
Swath	>80 km	>250 km	>400 km	Vignette 20 x 20 km

3.2 The InSAR LOS Viewing Geometry

The InSAR technique observes the same area from slightly different look angles at different times by exploiting repeated orbits of the same satellite (Ferretti et al., 2007). The angle between the local zenith and the looking vector of the satellite called as the incidence angle (θ_{inc}) and the angle of satellite heading (α) define the viewing geometry of the satellite LOS. All of the available satellites are commonly acquired in a right-looking imaging geometry relative to heading as shown in Figure 3.1.

The incidence angle varies based on the image mode and the image extent from near-range to far-range (Fuhrmann et al., 2019). It makes LOS measurement has a different value according to its incidence angle. The farther sensor range (e.g., $\theta_{inc} = 46°$) is, the lesser the projection value of LOS measurement for an ascending pass heading and otherwise comes out. Regarding LOS projection to a ground coordinate system, the combination of SAR data from ascending and descending can estimate at least 2-dimensional fields which are vertical and east-west components. The result of the combination (2-D fields) can integrate better to other geodetic observations (Hu et al., 2014). Monitoring of ongoing surface displacement process requires knowledge for the applied satellite geometry as well as factors controlling the direction of movement such as gradient and aspect of the terrain, and orientation of controlling geological structures (Eriksen et al., 2017). A further discussion of this issue will be explained in Chapter 6.

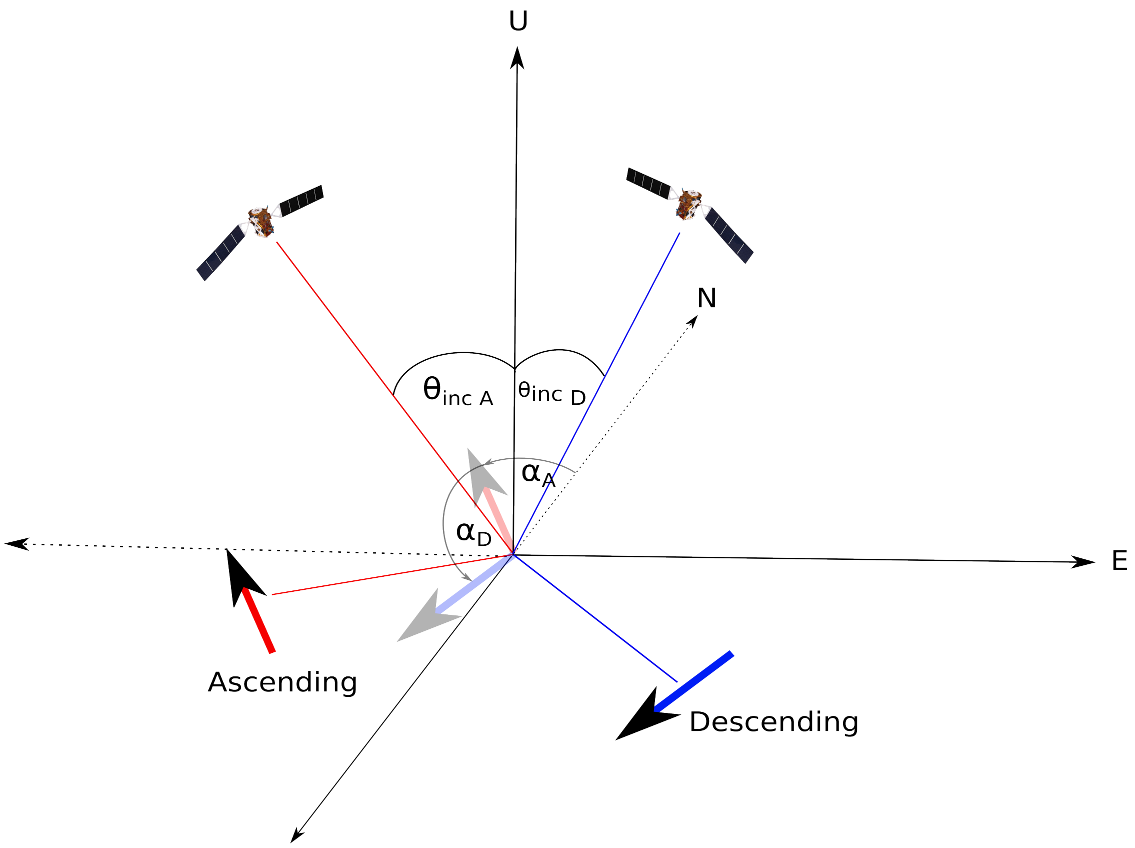

FIGURE 3.1: The imaging geometry of the right-looking SAR acquisition.

3.3 Interferometric Processing Chain

Interferometric processing is composed of several stages. It depends on the SAR product in which stage the processing starts. For this project, ERS1/2, ALOS PALSAR1 and Sentinel-1 products have been used. ALOS PALSAR data are provided from raw level 1.0 data which has to be focused firstly while ERS1/2 and Sentinel-1 are already in focusing format, as Single Look Complex (SLC) products. The process chain of the interferometric process as seen in Figure 3.3 is briefly discussed as following

- Focusing
  The process involves the coherent summation of range-aligned echoes over the length of the synthetic aperture. Since the range (R) varies with slow time (s) as measured by the precise orbit, it needs to calculate the range as a function of slow time. Each image will be focused to create the SLC format.

- Co-registration
  The precise orbital information is used to align the reference (master) and repeat (slave) image to sub-pixel accuracy in order to properly create the interferogram. It is accomplished by first using the orbital information to estimate the shift in range and azimuth coordinates. Furthermore, each image is divided into small patches to determine parameters of transformation using a cross-correlation algorithm needed to match the slave image into the reference one.

- Range and Azimuth Filtering
  The step processes the range spectral shift and the azimuth common bandwidth filtering in

purpose to keep the correlated phase between two images and remove the noise term or the uncorrelated phase. The process is also called as "phase co-registration" (Ferretti et al., 2007).

- Interferogram Generation
  The stage computes the phase difference between the two images. The interferometric phase is generated by the utilization of cross multiplication from the complex product between the single values of the pixels. Furthermore, if it is necessary to reduce noise in the interferogram, the filtering step might be processed by low-pass arcs such as Gaussian filter wavelength (Wei et al., 2010), Goldstein filter (Goldstein et al., 1998), adaptive windows (Wegmuller et al., 1998), and the boxcar (Lee et al., 2003). It decimates the real and imaginary components of the interferogram in both azimuth and range and computes final standard products of amplitude, phase, and coherence. Furthermore, the Differential InSAR step will be processed to remove fringes due to a topography effect using an external DEM.

3.3.1 Co-registration

One of the critical procedures in interferogram generation is ensuring that the range and azimuth pixels in both master and slave images are contributed as the same each ground target, called co-registration or image alignment. The procedure modifies the scales, rotations, and translations in a precise superimposition of two or more images to match the reference image. Two main steps of co-registration consist of 1) coarse co-registration, a matching process of two SAR images in pixel-level accuracy. 2) fine co-registration, a step to find subpixel tie points on two SAR images (Li et al., 2008). Although the primary purpose of co-registration is to compensate for the differing geometry due to different view angles caused by the parallax effect, it takes into account as well for effects due to orbit crossing/skewing, different sensor attitudes, different sampling rates and along- & across-track shifts.

Coarse co-registration is commonly assigned the master image as a reference and shifted the slave image on the reference grid of the master. It is approached by two-dimensional cross-correlation of hundreds of small sub-patches (Li et al., 1990). The average peak coordinates are computed to find the range and azimuth offsets between two SAR images after all patch pairs with good cross-correlation are completed. These offsets will shift the slave image.

Fine co-registration consists of searching for subpixel tie points and fitting transformation equations. Firstly, the cross-correlation is computed again with subpixel accuracy for some locations in the master to obtain sub-pixel offsets. Commonly, 1/10 pixel is widely accepted for fine co-registration (Hanssen et al., 1999). After this computation, the remaining offsets mostly exist in range direction because the parallel baseline component between two platforms varies almost linearly from near range to far range (Li et al., 1990). There are several approaches to find the parameter transformation.

For ERS sensor, the following four parameter transformation (Eq. 3.1) onto subpixel tie points is sufficient.

$$\begin{aligned} X &= x + ax + c \\ Y &= y + dx + f \end{aligned} \tag{3.1}$$

where (X,Y) is the coordinates of tie points in the slave image while (x,y) is the coordinates of corresponding points in master image. However, the highly distorted SAR images might occur. It is better to use the polynomial approach in following equation.

$$\begin{aligned} X &= ax^2 + bx + cy + d \\ Y &= ex^2 + fx + gy + h \end{aligned} \tag{3.2}$$

This approach applies the slave-image resampling in order to match the slant range and azimuth to the master geometry. The eight coefficients in Eq. 3.2 represent the following transformations, illustrated in Figure 3.2 :

- coefficient (d) is a fixed azimuth shift caused by different timing along the orbit.
- coefficient (h) is a fixed range shift caused by the perpendicular baseline component.
- coefficient (b) is a stretch in range due to the normal baseline variation with range and an azimuth stretch.
- coefficient (g) is a stretch in azimuth due to variation in PRF and or satellite velocity.
- coefficient (c,f) are a range and azimuth skew. They approximate an image rotation for small rotation angles.
- coefficient (a,e) as two-second order terms are used for processing large range swaths.

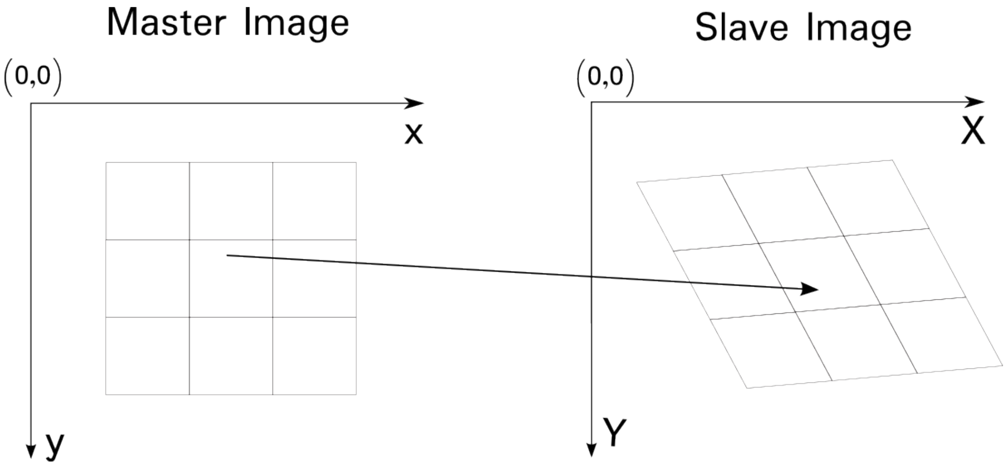

FIGURE 3.2: Transformation model to register the slave image on the reference grid of the master. The azimuth and range on the slave could be shifted, stretched and rotated (Source: Ferretti et al., 2007).

The dominant transformation depends on its sensor. For ERS and Envisat, azimuth and range shift are the major effects whereas the azimuth and range stretch are mostly small with a few pixels for a whole scene. On the other hand, the azimuth stretch might increase on the Envisat sensor in order to make it suitable for the pulse repetition frequency (PRF) variation in two acquisitions.

3.3.2 Range and Azimuth Filtering

The spectral shift filtering has an objective to maximize the coherence for each pixel of the interferogram. It is based on a Fourier Transform time-frequency analysis of the signals that are acquired. Preserving of the common overlapping frequency bands is needed to perform good coherence of an interferogram generation. Therefore, the phenomenon of non-overlapping spectral bands will be filtered by the spectral shift independently both in range and azimuth (ERDAS, 2010b).

- Range spectral shift filtering
  The ground spectra which are acquired by a master and a slave image are not the same due to the slight difference viewing geometries on the sloped terrain. The spectral shift firstly has been computed by Gatelli et al., 1994 for constant sloped terrain. The shift depends on among other parameters, both the looking angle and the local slope of the terrain. There are some possible filtering techniques to remove the uncorrelated spectral contributions, two of them are: a) standard range filtering, estimating the spectral shift from the acquisition geometry and a model of the flat earth, the ellipsoid; b) adaptive range filtering, a simulated

phase based on an external DEM will be processed to find the local frequency shift (ERDAS, 2010a).

- Azimuth common band filtering
  Because the azimuth spectral shift due to terrain slope is relatively small, the process can be ignored in full resolution SAR interferometry (Monti-Guarnieri et al., 2001). However, there is still an effect of spectral-shift due to a possible variation in the antenna pointing, e.g. the Doppler Centroid (DC) between the two acquisitions or a change in the squint angle. Doppler centroid, itself, is the linear relation between angles and frequencies due to particular SAR's time-frequency mapping (Ferretti et al., 2007). The larger the difference is in Doppler centroids between two images, the higher the decorrelation is in the interferogram (ERDAS, 2010a). To suppress this noise term, specific filters such as a band-pass filter can be used to extract only the frequency range common with a common DC and spectral band to both scenes for interferogram generation. Hence, the process is called the azimuth common band filtering.

3.3.3 Interferogram Formation

Interferogram is generated by multiplying the complex value of the master SAR image by the complex conjugate of the slave image as following

$$v_i = u_m \times u_s^* = A_m \times A_s e^{j(\phi_m - \phi_s)} \tag{3.3}$$

The purpose of generating an interferogram is to compute the phase difference of two acquisition images on a pixel by pixel basis. The process requires the product of two co-registered and spectral shift filtered images. It is still named as a raw interferogram since its phase is rather noisy and includes topography/flattening fringe patterns.

The real SAR interferograms could generate both for DEM reconstruction and the detection of the Earth's surface change. This chapter only describes how to detect the deformation signal using the SAR technique. The InSAR observation for monitoring surface deformation has some technical issues, which are; 1) the different baselines between two or more acquisitions contribute to the phase value (baseline-related phase), 2) phase noise and atmospheric effects might change the estimation of real displacement value in the area of interest.

For the first issue, if a digital elevation model (DEM) is available, the local topography effect could be reduced by generating *a differential interferogram*. This process estimates the baseline-related phase component. A synthetic DEM interferogram is generated using this estimation of the area of interest and information of satellite state vectors (the position and velocity of the satellite platform at different times) and further subtracted from the original SAR interferogram. It is noted that the satellite state vector's accuracy has improved in the last decade, for instance, the Sentinel-1 SAR sensor provides the precise orbit ephemeris (POE) as a sophisticated development of the orbit determination technique in order to reduce the impact of baseline error. The second issue is more complicated than the first one since there are many contributions from phase decorrelation, atmospheric effects, and difficulties related to phase unwrapping (Ferretti, 2014). The subject will be discussed in the next section on how to overcome the effect of phase decorrelation and phase unwrapping. Meanwhile, for the atmospheric disturbances, it will be explored in detail for the next chapter.

Interferometric Phase

The interferometric phase (ϕ_{int}) consists of a real deformation signal (if the area has deformed) and several contributions such as phase noise, atmospheric effects and orbit indetermination (baseline error) as described on following equation

$$\phi_{int} = \phi_{disp} + \phi_{geometry} + \phi_{topo} + \phi_{atm} + \phi_{error} \tag{3.4}$$

where ϕ_{disp} is the phase contribution due to earth's surface change occurring between two acquisitions, $\phi_{geometry}$ is a baseline error due to the slightly different position of two images, ϕ_{topo} is the phase concerning the local topographic information, ϕ_{atm} is a part of phase caused by atmospheric patterns, for example, inhomogeneities in temperature, pressure and water content in troposphere and variations of electron density in the ionosphere layer while ϕ_{error} is the contribution due to errors in different interferometric process chain and radiometric distortions.

The $\phi_{geometry}$ and ϕ_{topo} could be subtracted from ϕ_{int} since this systematic error could be estimated properly. If we ignore the decorellation and atmospheric effects, the remaining phase is a deformation signal of earth's surface change between two acquisitions,

$$\phi_{int} = -\frac{4\pi}{\lambda} \times d_{LOS} \tag{3.5}$$

where d_{LOS} is the displacement in the line-of-sight (LOS) viewed by satellite and λ is the wavelength's sensor. It was firstly found by Gabriel et al., 1989 and applied by Massonnet et al., 1993 and Zebker et al., 1994 to detect the ground displacement caused by Landers earthquake.

There are two decorrelation phenomena in SAR processing, which are: temporal and spatial decorrelation. Temporal decorrelation occurs when the interferometry losses its coherence since the scattering properties change with time. The reason for the change is mostly related to vegetated surfaces, weathers appreciably and snow coverage. Furthermore, the impact of variations in imaging geometry introduces spatial decorrelation. If the perpendicular baseline is non-zero, the difference in incidence angle alters the coherent sum of wavelets from the many small scattering elements within a resolution cell. Hence, the signal measurements are not appropriately repeated between two acquisitions. It is correspondent to the change of squint angle which alters the SAR Doppler frequency range leading to decorrelation (Hooper, 2006). The greater the perpendicular baseline is, the higher the spatial decorrelation effect is. Therefore, event though SAR data are regularly acquired in recent years, the possibility of pairing two SAR images is limited by both spatial and temporal decorrelation.

3.4 Persistent Scatters Algorithm

Two major sources of noises found on InSAR applications are phase decorrelation and atmospheric effects. The difficulty of conventional InSAR encountered by temporal and geometric decorrelation has a high impact on SAR interferograms over the non-urban and vegetated areas. Based on several years of InSAR exploitations, the atmospheric contribution also was significantly appeared in most of the interferograms especially in the tropical area characterized by high humidity values for most of the year (Ferretti, 2014) and the region with a significant temperature's change (Doin et al., 2009). This chapter explains the method to overcome the issue of the decorrelation signal while the next chapter will describe the second source of the noise.

A growing number of multi-temporal SAR data has been started since 1991 by ESA ERS-1 radar sensor following to Envisat sensor in 2001 then continues to the last update from Sentinel-1 since 2014. Multi-temporal InSAR has been widely used to monitor the earth's surface displacement and geophysics phenomena. One of these multi interferogram techniques is called Persistent Scatters (PS) which identifies stable scatters over long time intervals. In the first term of advanced InSAR studies, the highlight was exhibiting the high coherent pixels on human-made structures radar targets. However, it limits the application only to urban and non-vegetated study areas because the estimation needs a set of statistically homogeneous pixels and isolated point-wise but hardly detected in every single interferogram. Therefore overcoming the drawbacks, the primary objective of PS technique is nowadays to identify the good signal to noise ratio (SNR) corresponding to a possibility for exposing rocks or boulders out of a noisy background characterized by low coherence values.

Although Persistent Scatters approaches are varying in recent years, it represents the exploitation of multiple SAR images to separate the phase displacement (π_{disp}) from unwanted phase components. Crosetto et al., 2016 explained the development of the PS technique since the pioneer PS technique. Namely, The Permanent Scatters approach found by (Ferretti et al., 2001) then followed by several other contributions which are the Small Baselines (SBAS) technique from (Berardino et al., 2002) and (Schmidt et al., 2003); and the Persistent Scatters technique from (Hooper et al., 2004). Table 3. 4 explains the sequence development for the time series InSAR method.

TABLE 3.4: Characteristics of the main PSI approaches (Source: Crosetto et al., 2016 with a small modification)

PSI method reference	Baseline configuration	Pixel selection criterion	Deformation model
Ferretti et al. (2000, 2001)	Single master	Amplitude dispersion	Linear deformation in time
Berardino et al. (2002)	Small baselines	Coherence	Spatial smoothness
Mora et al. (2003)	Small baselines	Coherence	Linear deformation in time
Schmidt and Bürgmann (2003)	Small baselines	Coherence	Spatial and temporal smoothness
Werner et al. (2003)	Single master	Amplitude dispersion & Spectral phase diversity	Linear deformation in time
Duro et al. (2003) and Crosetto et al. (2008)	Small baselines	Amplitude dispersion, coherence, spectral coherence	Linear deformation in time
Kampes (2006)	Single master	Amplitude dispersion & Signal to clutter ratio	Different types of deformation models
Hooper et al. (2004, 2006)	Single master and Small baselines	Amplitude (difference) dispersion and phase criterion	Spatial smoothness
Crosetto et al. (2005)	Small baselines	Coherence	Stepwise linear function in time
Costantini et al. (2008)	Single master	Amplitude dispersion	Linear deformation in time
López-Quiroz et al. (2009)	Small baselines	Coherence	Spatial smoothness
Feretti et al. (2012)	Single master after triangulation	Statistical homogeneity test	Deformation model in time
Perissin and Wang (2012)	Target-dependent interferogram subset	Quasi-PS approach	Linear deformation in time
Hetland et al. (2012)	Small baselines	Coherence	Different types of deformation models
van Leijen (2014)	Single master	Amplitude dispersion	Different types of deformation models
Goel and Adam (2014)	Small baselines	Statistical homogeneity test	Linear deformation in time
Lv et al. (2014)	Single master	Statistical homogeneity test	Linear deformation in time
Devanthéry et al. (2014)	Small baselines	Amplitude dispersion and Cousin PS	Spatial smoothness

3.4.1 Criteria for Pixel Identification

Several reasons for pixels in the interferograms being decorrelated are due to the different angle or geometry at the observed resolution cell during two acquisitions, object scatters at the resolution cell moving inconsistently in time between two acquisitions, and error processing especially at the co-registration step. Those uncorrelated scatterers have to be eliminated to find dominant scatterers based on the phase stability on its pixels. Since they are mostly spatially surrounded by incoherent cluster's neighbor, the phase candidates would be characterized as a dominant signal with a superposition of the clutter. Furthermore, a distributed scattering mechanism also reduces the time computation because it restricts to pixels having this characteristic. Besides, this mechanism discourages the false alarm due to the probability of some random phase's pixels owning a good fit with the model yield presumed as a persistent candidate.

There are commonly three suggestions to detect dominant or persistent scatters, i.e., techniques based on the threshold of the amplitude, the signal to clutter ratio and the amplitude dispersion index (Kampes, 2006). Since the research work only uses the amplitude dispersion index to select points scatters, the following section will only describe it.

3.4.2 Amplitude Calibration and Dispersion

Before the temporal standard deviation of the amplitude (σ_A) and the temporal mean of the amplitude (μ_A) are calculated, the images are radiometrically calibrated using the ratio of the amplitude of each image to the mean amplitude of the entire set (Lyons et al., 2003) rather than a calibration factor from ESA. The calibration factor R_i is defined by,

$$R_i = \frac{\mu_{A_i}}{\left(\Sigma_{i=1}^{n}\, \mu_{A_i}\right)\Big/ n} \tag{3.6}$$

with μA_i is the mean amplitude of each image (i), and n is a number of images. The calibrated of each SLC image ($calA_i$) are computed by,

$$calA_i = \frac{A_i}{R_i} \tag{3.7}$$

The purpose of this calibration is to create an equalization of brightness between images; thus, σ_A and μ_A could be estimated fairly. Another calibration method is based on annotated parameters included in the header file. It takes into account for antenna pattern, range spreading loss and gain factors such as the sensor and acquisition time. However, SLC images might not be adequately calibrated because of incorrectly information of constant values in the annotated file.

For single master (SM) network time series InSAR analysis, likely called Permanent Scatters processing, the amplitude dispersion index (D_A) is applied. The main work yet implements another small baseline (SB) approach as introduced by Hooper, 2008 which takes the amplitude difference dispersion index ($D_{\Delta A}$), the standard deviation of the difference in amplitude between master and slave, instead of D_A. It is estimated in following,

$$D_{\Delta A} \equiv \frac{\sigma_{\Delta A}}{\mu_A} \tag{3.8}$$

where,

$$\sigma_{\Delta A} = \sqrt{\frac{\Sigma_{i=1}^{n}\, (calA_{master} - calA_{slave})^2}{n}} \tag{3.9}$$

and

$$\mu_A = \frac{\Sigma_{i=1}^{n}\, (calA_{master} + calA_{slave})}{n \times 2} \tag{3.10}$$

$D_{\Delta A}$ is an indication of phase stability viewed by the Gaussian scatter pixels. A threshold value of $D_{\Delta A}$ has to be set to reduce the size and time computation. It ranges between zero (0) to one (1), which lower number considered as an excellent correlated scatter. The relation between phase and amplitude assumes that a consistent or small different amplitude value expected to have a small phase dispersion as well. The result of this threshold is then called as Persistent Scatters (PS) candidate.

3.4.3 Pixel Selection

After the PS probability of each pixel is convergent, PS candidates will be selected by a threshold determined by the fraction of false positives with the threshold parameter defined by the user (*gamma change convergence*). Besides, the computation seeks the identified pixels with the criteria: only "*persist*" pixels in certain interferograms and dominated by scatterers in adjacent PS pixels and reject them. The brief steps to find selected PS pixels based on Hooper, 2006 explanation as following:

- Iterations take into account until the RMS in γ_x (please see section 3.5.2) falls below some threshold assuming that convergence has been reached.
- Because there is a correlation between amplitude variance and phase stability, the algorithm bins the pixels by the amplitude dispersion of the pixels ($\hat{D}_{A,x}$), ensures that every bin has at least 10^4 pixels, and finally generates a number of data probability distributions, $p(\gamma_x, \hat{D}_{A,x})$.
- Only pixels with γ_x above a threshold value, $\gamma^{thresh}(\hat{D}_{A,x})$, are selected with the number of those pixels considered as non-PS pixels given by

$$(1 - \alpha(\hat{D}_{A,x})) \int_{\gamma^{thresh}}^{1} pR(\gamma_x) d\gamma_x. \tag{3.11}$$

- The final PS pixels are then selected by the best-fitting κ using the least-square inversion for which $\gamma_x > \kappa \hat{D}_{A,x}$. κ is a constant linear relationship between the threshold value and the amplitude dispersion of the pixels, i.e. $\gamma^{thresh} = \kappa \hat{D}_{A,x}$.

Furthermore, the next step is weeding the selected pixels due to partially PS and multiple pixels PS. Partially PS means a signal contribution from neighboring ground resolution elements. The signal will be smoothed by windows in the time domain using the Gaussian-weighted piece linear fit algorithm. Meanwhile, multiple pixel PS could be a noise coming from dominating pixels due to look angle and squint angle error instead of corresponding to its physical location. Therefore, this PS algorithm, implemented on StaMPS software, recognizes the true "bright" pixels with expecting that they have the highest signal noise ratio (SNR). The SNR threshold parameter is taken from γ_x on every interferogram. If this condition does not fulfill, it will be dropped out.

3.5 Small Baselines Interferometry

3.5.1 A Theory of Small Baselines Approach

The small baselines subset (SBAS) multitemporal InSAR algorithm is firstly introduced by Berardino et al., 2002. The readers could explore further details of this algorithm in the referred article and Casu et al., 2006 article. The technique is developed initially to monitor large spatial scale displacement using the low-pass filter (multi-look) DInSAR interferograms (Lanari et al., 2007). To mitigate the decorrelation phenomena, the data pairs are selected adequately in particular spatial and temporal baselines. The effect of residual phase due to uncompensated topography is mitigated by exploiting the vector of perpendicular spatial baselines of the interferograms sequence concerning the radar line of sight. The atmospheric phase signals are then filtered out from the interferometric phase with the assumption that their signals are highly correlated in the space but poorly in time (Berardino et al., 2002). Nevertheless, the density of the coherence pixels is typically heterogeneous in a SAR scene, so that the decorrelated pixels might still impact. Thus, the SBAS technique mostly works only in urban and rocky areas having a homogeneous object's characteristic and providing spatially dense results.

In recent years, many Small Baselines Interferometry (SBI) approaches, besides the conventional SBAS algorithm, have developed, e.g., the New Small Baseline Subset (NSBAS) approach (Doin et al., 2011), the Multiscale InSAR time series (MInTS) method (Hetland et al., 2012), and the multi-temporal InSAR (MTI) approach which well known as the *SB-SDFP* algorithm (Hooper, 2008). Their strengths and limitations of four SBI processors are explained by Gong et al., 2016 as following:

- Applying the four processors to the urban area with proper temporal baselines shows similar performance and results.
- A predefined deformation model from NSBAS and MInTS provide a better constraint of time series deformation. On the other hand, SB-SDFP is a good option to preserve the non-linear deformation signal and generates good spatial coverages in natural environments.
- All of the processors provide extra atmospheric correction modules either by a phased-based correction or external atmospheric data.
- The identification of Distributed Scatters (DS) in SB-SDFP applies enhanced temporal coherence and amplitude difference dispersion analysis while NSBAS and MInTS are using the spatial coherence thresholding schemes. Therefore, the application containing the natural environment is recommended to utilize the SB-SDFP approach since NSBAS and MInTS will include decorrelated pixels and lead to noisy results. Otherwise, if there is a valid assumption about the temporal deformation model or prior knowledge of displacement pattern in an observed area, NSBAS and MInTS could be used in purpose to provide better constraints and reduce the error levels of the results.

The main point of SBI analysis is properly selected as the interferometric pairs with short temporal and geometry (perpendicular) baselines (Lanari et al., 2007). It is necessary to have redundant interferograms in the data stack to reduce systematic errors propagating through the interferograms network. For the connectivity between interferograms, SB-SDFP requires a single subset of a network in order to use the least-square adjustment for the determination of the pixel phase on each SAR image. The classical SBAS, NSBAS, and MInTS, otherwise, can invert an SBI stack containing disconnect clusters by using a singular value decomposition (SVD) approach with a minimum-norm criterion (Gong et al., 2016). For all works of the thesis, SB-SDFP is applied to produce the ground deformation temporal evolution. Therefore, the following sections will only explain the SBI method from SB-SDFP.

3.5.2 SBI Selection Criteria With The Phase Characteristic

The phase characteristic is identified by Slowly Decorrelating Filter Phase (SDFP) which is similar to PS algorithm (Hooper et al., 2007a) as explained in section 3.4. Stanford Method for Persistent Scatterers (StaMPS), a non-commercial statistical InSAR software, fully implements both of those algorithms. The main purpose of SDFP is able to detect dominant scatterers like the principle of Persistent Scatter (PS) in rural and agricultural areas. It operates many master-slave pairs configuration by generating interferograms with small perpendicular baselines and short time intervals, commonly named as Small Baselines (SB). In general, the following steps for selecting PS are:

a Identifying PS stability on every pixel using phase analysis in which the band-pass filter, an adaptive filter combined with a low-pass filter (CLAP), is implemented to estimate the phase noise correlated spatially. The inversion method is used for the look angle estimation error correlated to the perpendicular baseline. The function to measure this phase noise level, as an indicator to be accepted as PS pixel, is

$$\gamma_x = \frac{1}{N} \mid \sum_{i=1}^{N} exp\{\sqrt{-1}(\psi_{x,i} - \tilde{\psi}_{x,i} - \Delta\hat{\phi}^{u}_{\theta,x,i})\} \mid, \tag{3.12}$$

where $\psi_{x,i}$ is the wrapped phase, $\tilde{\psi}_{x,i}$ is the estimate of spatially correlated terms, $\Delta\hat{\phi}^{u}_{\theta,x,i}$ is the estimate of the spatially-uncorrelated look angle error term with pixel x of every ith interferogram and N is the number of interferograms. Furthermore, a statistical analysis takes place to determine the fit convergence and stopping the iteration. This distribution threshold value $\gamma_x^{thresh}(D_{\Delta A})$ set by default value, 0.005.

b Selecting PS pixels on the basis of their noise characteristic γ_x are determined by the fraction of false positives. StaMPS has two probability density method, the density (per km^2) rand and the percent rand for estimating the percentage of random (non-PS) pixels. In other words, the numbers of selected PS depends on the value given by this density or percent parameter. The higher the value of density or percent rand is given, the more PS pixels could be selected. Nevertheless, it arises the random phase either.

These candidates of PS points still contain the deformation phase, the atmospheric phase delay, the orbit error phase, the residual DEM error phase and the noise phase (Tao et al., 2018). As PS algorithm with a single master network, Hooper et al., (2007a) determined the character of those unwanted signals utilizing the amplitude (please see Section 3.4.2) and the phase analysis. Those phases of interferograms are correlated spatially, which are; the signal associated with the isolated movement of individual brightness considered as noise, the variation in atmospheric delay between two acquisitions, the orbital errors in azimuth, and the residual orbit error term in range due to a consequence of interferometric processing. Moreover, the look angle error is also partly spatially correlated and thus, a part of the residual DEM error phase. The estimation of spatial correlation for the four terms and part of the fifth term could be subtracted from the interferograms. Also, the spatially uncorrelated look angle (SULA) error phase, as a part of the residual DEM error phase as well, and the noise phase are estimated and filtered by utilizing a low-pass and adaptive filter. The next process is the estimation of the phase stability indicator for each of the initial candidate SDFP pixels, then the selection of SDFP pixels is done in the last step of processing. The processing flow chart of the SDFP module is illustrated in Figure 3.3.

Figure 3.3 shows the processing procedure of InSAR techniques. Generally, it divides into three main steps. The first step is the interferometric chain described in Section 3.3. On this step, the amplitude calibration and difference dispersion are computed as prior knowledge for the amplitude analysis of the SB-SDFP approach. The second milestone is the small baseline interferometry applied by the SB-SDFP algorithm. The wrapped interferometry product is unwrapped by the 3D phase unwrapping method, and the phase error will be removed including the atmospheric phase error. The last step is retrieving LOS deformation into 3D vectors displacement. This topic is discussed separately in Chapter 6.

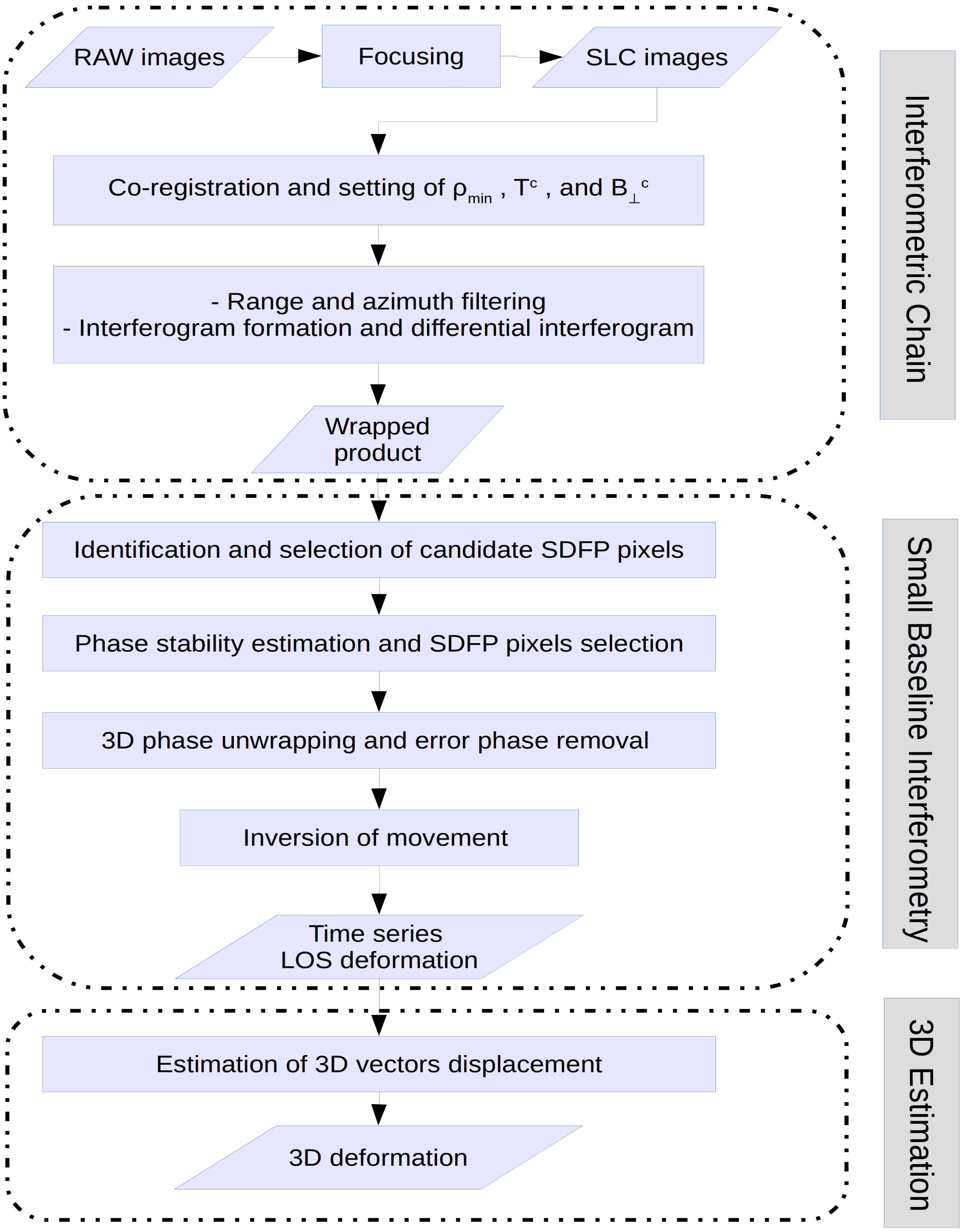

FIGURE 3.3: The processing flow chart of the SBI module. The procudure is a modified version from Gong et al., 2016 and Tao et al., 2018.

3.6 The Estimation of Deformation

The selected PS pixels from SB-SDFP algorithm are originally still on the wrapped interferogram phase ($\psi_{int,x,i}$) describe in Equation 3.13. Hence, the phase has to be unwrapped and other estimations of nuisance terms need to be removed in order to retrieve only the deformation phase.

$$\psi_{int,x,i} = W\left\{\phi_{disp,x,i} + \Delta\phi_{orb,x,i} + \Delta\phi_{\theta,x,i} + \Delta\phi_{noise,x,i}\right\} \quad (3.13)$$

where $\phi_{disp,x,i}$ is the deformation value, $\Delta\phi_{atmos}$ is the uncorellated atmospheric delay contribution, $\Delta\phi_{orb,x,i}$ is the residual orbital error or phase ramp, $\Delta\phi_{\theta,x,i}$ is the spatially correlated part of look angle error (SCLA), and $\Delta\phi_{noise,x,i}$ is the residual spatially uncorellated noise term.

Phase unwrapping is a reconstruction of absolute phase which is known only modulo 2π on a finite grid of points (Agram, 2010). An approach for unwrapping SAR interferogram was firstly developed by Hunt, 1979 and further improved by Goldstein et al., 1988. The method applies regular samples of two-dimensional data sets and estimates the phase gradient between two adjacent samples. The underlying continuous unwrapped phase function is assumed well sampled in every dimension so that the wrapped phase could be reconstructed except at a finite, relatively small, number of discontinuities.

The early commonly phase unwrapping approach is the branch cut algorithm and its derivatives (Goldstein et al., 1988) because of easy implementation. For the conventional InSAR processing, an approach from Chen et al., 2000 is popular on the InSAR community since the algorithm is widely available for an open-source project named as SNAPHU (Chen et al., 2002). SNAPHU is the network-flow-programming-based unwrapping algorithms for 2D data set by the development of an iterative L_o norm approximation algorithm with a combination of statistical cost functions. It incorporates three built-in statistical models, for topography data, deformation data, and smooth generic data as a solution of a different measured quantity (Chen et al., 2001). However, there is a drawback of the 2D phase unwrapping to be used in multi-temporal InSAR analysis. The generated wrapped product is not unwrapped properly since time-series interferograms are mostly irregularly sampled spatially and temporally. Thus, the extended development of the shortest branch cut to 3D phase unwrapping (Hooper et al., 2007b) is one of the solutions to reconstruct the wrapped phase in time series analysis.

3.6.1 3D Phase Unwrapping

The step is correcting the phase values of final SDFP pixels into an appropriate number of 2π cycles because the selected pixels are still wrapped to modulo 2π. It applies the three-dimensional phase unwrapping (Hooper et al., 2007b) which will perform the initial phase difference of SDFP pixels. This 3D unwrapping method performs the residues in space-space (two spatial), likely a phase unwrapped approach on conventional InSAR, and space-time (one temporal). Namely, the unwrapping is a series of 2D problems and sufficient to map slow deformation over time. It generates the unwrapped phase time series for each PS, concerning the reference PS (Hooper et al., 2004). The temporal phase differences for each PS are firstly computed, and then an iterative least square method takes into account for unwrapping spatially from a reference PS. The algorithm also has an option to apply the minimum cost flow (MCF) approach (Costantini, 1998) for three dimensions.

This following description of 3D phase unwrapping is a summary from Hooper, 2006 dissertation. Before the process of phase unwrapping is being executed, the wrapped interferogram is subtracted by two estimated errors in order to optimize a data set for unwrapping. To have an accurate unwrapping result, it requires the absolute difference in phase between neighboring PS which generally less than π. Due to non-spatially correlated part of the signal, the absolute difference in phase, however, can still be greater than π. Thus, the significant contributions of the non-spatially correlated part from the look angle error ($\Delta\widehat{\phi}_{\theta}^{nc}$) and the master or reference image ($\widehat{\phi}_{x}^{m,nc}$) are removed before unwrapping, yielding

$$W\left\{\psi_{int,x,i} - \Delta\widehat{\phi}_{\theta,x,i}^{nc} - \widehat{\phi}_{x}^{m,nc}\right\} = W\left\{\phi_{disp,x,i} + \Delta\phi_{atmos,x,i} + \Delta\phi_{orb,x,i} + \Delta\phi_{\theta,x,i}^{corr} + \Delta\phi_{noise,x,i}\right\} \quad (3.14)$$

where $\Delta\phi^{corr}_{\theta,x,i}$ is the correlated part of $\Delta\phi_{\theta,x,i}$ and $\Delta\phi_{noise,x,i}$ is the residual spatially uncorrelated noise term ($\phi_{noise,x,i} - \widehat{\phi_x}^{m,nc}$).

The result of three-dimensional unwrapping value regarding to the phase data, two in space and one in time, is summarized as

$$\phi_{uw,x,i} = \phi_{disp,x,i} + \Delta\phi_{atmos,x,i} + \Delta\phi_{orb,x,i} + \Delta\phi^{corr}_{\theta,x,i} + \Delta\phi_{noise,x,i} + 2k_{x,i}\pi \tag{3.15}$$

where $\phi_{uw,x,i}$ is the unwrapped value of $W\{\psi_{int,x,i} - \Delta\widehat{\phi}^{nc}_{\theta,x,i} - \widehat{\phi_x}^{m,nc}\}$ with the remaining variable as unknown integer ambiguity ($k_{x,i}\pi$). It will have a constant value if the unwrapping process is generally accurate. The reason is that $k_{x,i}\pi$ are the same integer for most x in any given interferogram i.

Two main approaches of phase unwrapping are **quasi-L^∞-norm 3D** and **pseudo 3D algorithm**. The quasi-L^∞-norm 3D algorithm requires no multi-loop discontinuity surfaces in a dataset, namely, bounded by only one loop as described in Chen et al., 2001. For each loop, a phase discontinuity surface, which is a minimal surface, equivalent to the surface formed by an equilibrium soap film in zero-gravity is selected by the algorithm. Generally, there are five stages to perform this approach as follows:

- Residue identification
  The 3-D data divides into several faces with a data point at each vertex. The difference in phase along arcs between adjacent vertices is computed and wrapping the difference into the interval $-\pi$ to π. It integrates the differences around the face. The three orthogonal orientations method is used to divide the data into rectangular faces if the data are regularly sampled. On the other hand, the InSAR data set is mostly irregularly sampled (sparse). Thus, Delaunay triangulation (Costantini et al., 1999) is applied in two spatial dimensions. For the time dimension, Each sample in time is already sampled the same as every point in two spatial dimensions.

- Linking residues
  Residues are linked by tracing the loops through each wedge element in turn until the loop either a data volume boundary is reached or closes on itself.

- Processing closed residue loops
  Surface evolver created by Brakke, 1992 is applied to find an approximation to the surface for each closed residue loop through iterative computation.

- Processing truncated residue loops
  Truncation might occur for the associated residue loops at the data volume boundary since some residue loops may lie partially outside the data volume. Regarding this issue, two possible solutions are the linking of multiple loops to minimize the total surface area of the surface formed and the linking of ends that are truncated by different volume boundaries.

- Integration of phase
  The last step identifies the intersected arcs due to discontinuity surfaces. A flood-fill algorithm is taking into account to integrate the phase in which the intersected arcs become barriers to flow.

Secondly, the pseudo 3-D algorithm is an alternative if multiple-loop discontinuity surfaces exist in the data set. It unwraps the data in one dimension temporally, then the result will be used as an initial solution for the other two dimensions performance. Namely, the algorithm is mentioned as a pseudo due to not strictly a 3-D solution of unwrapping but a fusion between 1-D unwrap in time and 2-D unwrapping routines, e.g. MCF (Costantini, 1998), statistical-cost-network-flow (Chen et al., 2000), and iterative weighted least-square.

The first step of 1-D unwrapping in time is the removal of atmospheric delay between acquisitions by applying delaunay triangulation computation to define arcs connecting pixels and to calculate the phase difference for each arch in each interferogram. The unwrapping process is run by low-pass filtering the multi-temporal phase difference in the frequency domain using a Gaussian window. The filtered result is then calculated and wrapped between $-\pi$ and π and integrated. The second step is to unwrap the sparse data set using an iterative weighted least-squares method. Each interferogram is inverted to give the phase at each pixel using the weighted least-square (WLS) method. The weighting comes from the inverse of the standard deviation of the difference between the original arc time series and the filtered arc time series. Furthermore, it calculates the residuals between the arc phase differences in time and the arc phase differences predicted by the model. The process is repeated until all residuals are zero and the most significant residuals are removed.

The unwrapped result either using quasi-L^{∞}-norm 3D or pseudo 3D algorithm is further corrected by subtracting the spatially correlated term errors which were already estimated on PS/SB-SDFP analysis. SCLA ($\Delta\phi_{\theta,x,i}$) is calculated to correct an error from the quality of DEM itself or incorrect of making simulation DEM in radar coordinates. Namely, it could be called as spatially correlated DEM error correction. Moreover, the orbital error ($\Delta\phi_{orb}$) has been estimated too as phase ramps for each interferogram although we assume this effect will be low due to the use of POE and C-Band data. After subtracting two error estimation described above, the signal leaves for the information of deformation, an uncorrelated part of nuisance terms or noise ($\Delta\phi_{noise,x,i}$). Although the atmospheric phase component has been evaluated and subtracted from the estimated phase signal, the possibility of remained uncorrelated atmospheric artifacts ($\Delta\phi_{atmos,x,i}$) might still exist especially for the tropospheric phase delay which is next discussed in Chapter 4. Hence, the final result of unwrapping ($\bar{\phi}_{x,i}$) process yielding

$$\bar{\phi}_{x,i} = \phi_{disp,x,i} + \Delta\phi_{atmos,x,i} + \Delta\phi_{noise,x,i}. \tag{3.16}$$

3.6.2 Time Series Displacement

The unwrapped phase result based on SB-SDFP interferograms needs to be inverted for deriving the time series displacement values regarding the range changes between SAR scene acquisition. The conventional SBAS approach (Usai, 2001) commonly uses a singular value decomposition approach (Berardino et al., 2002) with a requirement of a priori knowledge about the temporal behavior of the deformation. For a case study without any prior deformation knowledge, the least square technique (Schmidt et al., 2003) is applied to generate the approach displacement value in a sequence period inverted by all unwrapped interferograms. It requires no extra constraint deformation; however, the cluster of interferograms is limited to only one.

The common notation to generate time series of range change is shown in Equation 3.17 as the linear least square method which the definition of parameters are illustrated in Figure 3.4.

$$\begin{aligned} &Gm = d \\ &m = (G^{t}G)^{-1}G^{t}d \end{aligned} \tag{3.17}$$

where m is the incremental range change between SAR acquisitions, G corresponds to matrix element for temporal SAR distribution, d is the generalization of unwrapped phase change for 1 scene, and C is the range change time series which calculated by summing of all preceding time steps on SAR distribution, yielding

$$C_t = \sum_{k=1}^{t} mk \tag{3.18}$$

The temporal distribution of the SAR scene acquisitions constructs the G design matrix. An arbitrary reference pixel and master image are used for referencing the range change in every

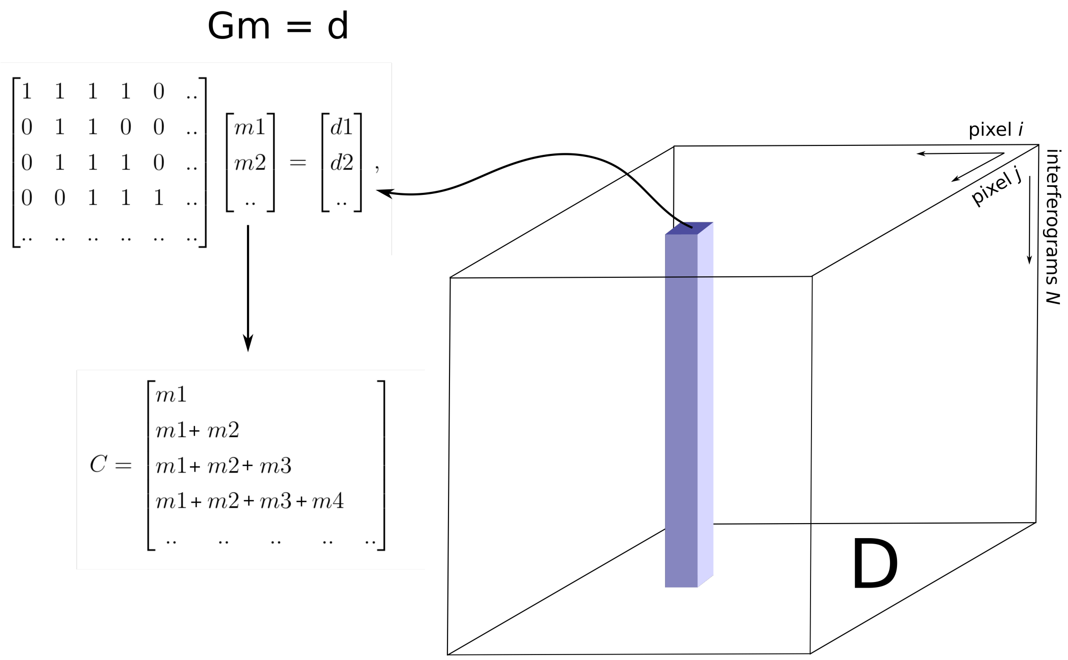

FIGURE 3.4: The relationship between data and model matrices in the inversion (source: Schmidt et al., 2003)

.

interferogram to ensure that all deformation is measured relative to a common location. The three-dimensional matrix $D_{i,j}$ as seen in Figure 3.4 is the *(i,j)* pixel of the kth interferogram. Thus, the vector d consist of the range time change for all numbers (N) of interferograms in two-dimensional (i, j),

$$d = \begin{bmatrix} D_{ij1} \\ .. \\ .. \\ D_{ijN} \end{bmatrix} \tag{3.19}$$

The inversion is computed repeatedly at each pixel location of PS or SB-SDFP points. Besides, the inversion performance depends on the acquisition rate of SAR scenes (temporal resolution) and the number and distribution of interferograms. The narrow revisit time-cycle improves the temporal resolution of the final time series while the numbers of interferograms determine the model and data resolution of the inversion (Schmidt et al., 2003).

The conventional PS method will eliminate the non-linear phase change signal carefully keeping the trend or model of expected deformation. It is different from the StaMPS algorithm which keeps the non-linear trend of displacement. The deformation model is retrieved by the phase of each pixel relative to an arbitrary reference pixel and master image. Besides, controlling consistent values for all SB interferograms contributing to each final single-master interferogram, StaMPS computes the residual phase between the SB interferograms and the predicted phase by the model SM interferograms. The residual up to 2π might indicate local phase-unwrapping error (Hooper, 2008). Two options could be chosen for this issue; either to more carefully process the phase unwrapped again if there is a manifestation of spatially-correlated residuals assumed as systematic phase-unwrapping errors or to drop the inversion if the network of interferogram pairs does not create an isolated cluster of interferograms.

Chapter 4

The Mitigation of Atmospheric Delay Effects

In this chapter, an application of tropospheric delay correction in InSAR both at a small and large area is presented. This work is an early result from the Sentinel-1 product for the Ciloto case study and additionally Envisat product for northern Baja California or neighboring valleys of Ensenada, the Mexico case study. We tested the performance of the power-law technique in both areas to find a significant result before and after the correction in multi-temporal InSAR processing. Our assessment finds that the tropospheric correction using power law has a better performance in a large area than a small area since there is a limit of spatial resolution and the influence from local weather to be applied in the small region. However, the validation between the InSAR result and the extensometer provides statistical confidence that the correlation of them is increased after the interferograms have been corrected for the tropospheric phase delay.

4.1 The Theory of Atmospheric Phase Delay

Permanent Scatter (PS) (Ferretti et al., 2001) and SBAS techniques (Berardino et al., 2002) are the advanced InSAR methods to generate real deformation and reduce unwanted signals coming from orbit and topographic errors, atmospheric effects, and noises. Some spatially correlated terms, orbit to height errors, could be removed from interferogram considering the use of abundant SAR imageries and finding out the stable scatters. Previously, atmospheric terms could be filtered out as well when we consider that atmospheric signals are random in time (e.g., Ferretti et al., 2001; Berardino et al., 2002). However, a recent study proved that they are also temporally correlated to stratified tropospheric delays (Doin et al., 2009). Thus, removing the atmospheric phase screen especially for tropospheric delay patterns using low-pass filtering might be a miss interpretation of specific deformation signals as noise or otherwise. If we observe some high rate deformations of large scale unit (cm to m) at a relatively small area, we could neglect the effect of atmospheric phase screen considering the accuracy of phase characteristics between pixels. Nevertheless, the monitors of crustal deformation, subsidence and slope movement could be considered as a very low rate displacement (mm to cm) whose InSAR practicals have to pay attention to atmospheric artifacts in order to perform more accurate results of displacements.

Two atmospheric layers that mostly affect microwave signals are propagating through the ionosphere and troposphere. The ionospheric delay mostly finds on the L-band sensor, ALOS PALSAR, and will be neglected on the processing procedure. The focused study is correcting the tropospheric delay using power-law function (Bekaert et al., 2015a) on the InSAR process and how the correction impacts the results of displacement value both in Indonesia and Mexico areas. For the Indonesia case, we observe slow movement in Ciloto, West Java, where the area has a high risk of landslide hazard using 50 SAR images of Sentinel 1A ascending orbit. Furthermore, we attempt to detect crustal deformation near to Agua Blanca Fault and additionally subsidence around the agricultural area in Manaedero Valley using 44 images of Envisat descending orbit.

4.1.1 Atmospheric Effects on InSAR and Their Mitigation

Hanssen, 2001 distinguish two types of the atmospheric signal based on their physical origin. The first one, turbulent mixing, is caused by a turbulent process in the atmosphere. A turbulent delay could affect both flat and mountain terrain. It creates phase artifacts on the interferogram due to spatial heterogeneity in the refractivity. Secondly, the vertical stratification is mostly correlated to topography and only affects mountainous terrain (Massonnet et al., 1998). This vertical stratification is caused by different vertical refractivity profiles between master-slave SAR acquisitions considered as no heterogeneities within the horizontal layers. Estimation of tropospheric delay might be described with a mathematical model which is generally divided as a systematic and stochastic component. Figure 4.1 explains shortly the scheme of atmospheric delay that most recent atmospheric studies categorize the types of delay estimation.

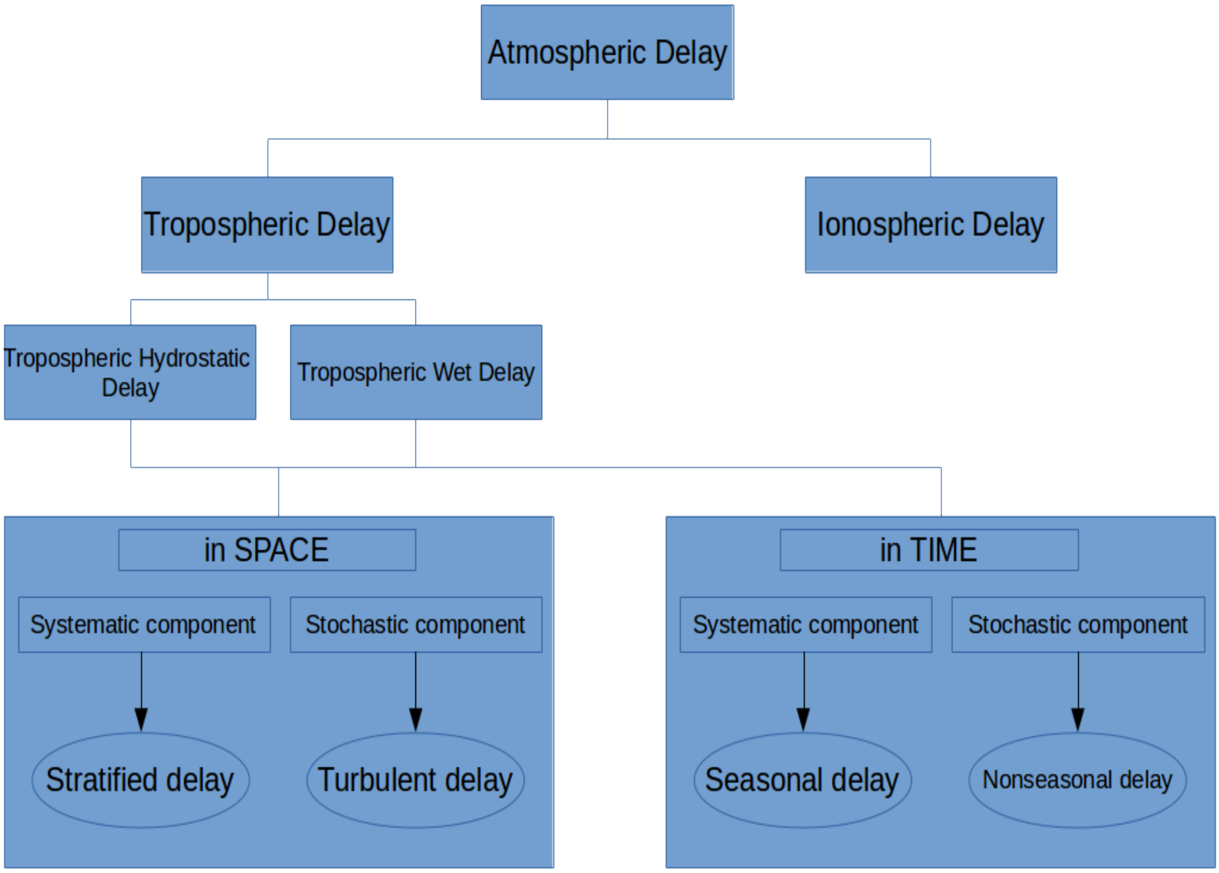

FIGURE 4.1: The scheme of atmospheric delay that might influence interpretation between SAR acquisitions.

4.1.2 Estimation of Tropospheric Phase Delay

According to the troposphere layer, it contains of hydrostatic delay and wet delay. The determined parameters of hydrostatic delay are the refractivity from dry air (atmospheric pressures and temperature) and of wet delay from wet air (partial pressure of water vapor and temperature). Smith et al., 1953 characterized the phase delay through atmosphere using the refractivity (N), with

$$N = (k_1 \frac{P}{T})_{hydro} + (k_2' \frac{e}{T} + k_3 \frac{e}{T_2})_{wet} \tag{4.1}$$

where P = total atmospheric pressure, T = temperature and e = partial pressure of water vapor, k1, k′2, k3 are constants parameter with 77.6 K hPa-1, 23.3 K hPa-1 and 3.75.105 K2 hPa-1, respectively (Thayer, 1974). Furthermore, if we consider tropospheric phase delay (ϕ_{tropo}) between pixels (p,q) and SAR acquisitions along radar line of sight (Hanssen, 2001), it can be defined as

$$d_{tropo} = 10^{-6}(cos\theta)^{-1}\left[\int_{h_p}^{h_{top,p}} N(h)dh - \int_{h_q}^{h_{top,q}} N(h)dh\right] \tag{4.2}$$

$$\phi_{tropo} = \frac{-4\pi}{\lambda} d_{tropo} \tag{4.3}$$

where d_{tropo} = the tropospheric (slant) delay, θ = the incidence angle, λ = the radar wavelength and h = height corresponds to the integration of the refractivity between h and the top of the troposphere (h_{top}).

Several main approaches to estimate tropospheric delay have been conducted to correct InSAR results (Fig. 4.2). Three main source models are; firstly, the numerical weather model, for instance, (i) high spatial and temporal resolution weather forecast models (WRF) (Jung et al., 2014), (ii) global atmospheric reanalysis models with low spatial and temporal resolution ERA-1 (80 km), MERRA2 (55 km) from the European Centre for Medium-Range Weather Forecasts, and (iii) Generic Atmospheric Correction Online Service for InSAR (Yu et al., 2018). The second one is from satellite spectrometers, which use observations of atmospheric water vapor from Moderate Resolution Imaging Spectroradiometer (MODIS) and Medium-Resolution Imaging Spectrometer onboard Envisat (MERIS) (Li et al., 2009). The third strategy is using a phase-based model itself with the main purpose to reduce stratified delay correlated with topography variations. A former method of phase-based use linear relation between tropospheric phase delay and topography and recently improved by using a spatially variable power law approach (Bekaert et al., 2015a). In this chapter, we assess only a power-law method and test the tropospheric correction at a small area in Ciloto and a large area in northern Baja California.

4.1.3 Correction of Tropospheric Delay

The power law method accounts variations spatially and temporally at tropospheric properties and belongs to phase-based tropospheric delays. It corrects only the stratified delay yet the turbulent mixing remains. The interferometric tropospheric phase $\Delta\phi_{tropo}$ could be estimated using the relationship between the interferometric phase and the topography described by Bekaert et al., 2015a as

$$\Delta\phi_{tropo} = K^{'}_{\Delta\phi}(h_o - h)^{\alpha} \; with \, h < h_o \tag{4.4}$$

where $K^{'}_{\Delta\phi}$ = the coefficient relating phase to topography with spatial and temporal variation, h_o = the power law reference height, α = the power law coefficient. α is an empirically constant calculated from balloon sounding data provided by *International Upper Air* network data, the Department of Atmospheric Science of the University of Wyoming. We used WIII Jakarta Station (106.65° ; -6.11° ; Number 96749) approximately 78 km away from Ciloto, Indonesia and NKX Sand Diego Station (-117.12° ; 32.85° ; Number 72293) approximately 130 km away from Baja California, Mexico. These sounding measurements provide atmospheric properties, such as, pressure, temperature, relative humidity and wind speed, to calculate the refractivity (Eq. 4.1), tropospheric delay (Eq. 4.2 & 4.3) hence the relative tropospheric delay with $\Delta d_{tropo} = d_{tropo}(t_{master}) - d_{tropo}(t_{slave})$.

The power-law exponent α could be found from the slope of linear fit by plotting the log-log relationship between the mean tropospheric delay d_{tropo} and relative height $(h_o - h)$. h_o was set to the altitude with the estimation of no relative delay ($\Delta d_{tropo} \approx 0$) between acquisitions as illustrated in Figure 4.3. Furthermore, $K^{'}_{\Delta\phi}$ is estimated in local windows using a band-filtered phase according to the pixel values between the interferometric filter phase $\Delta\phi_{filter}$ and the power-law

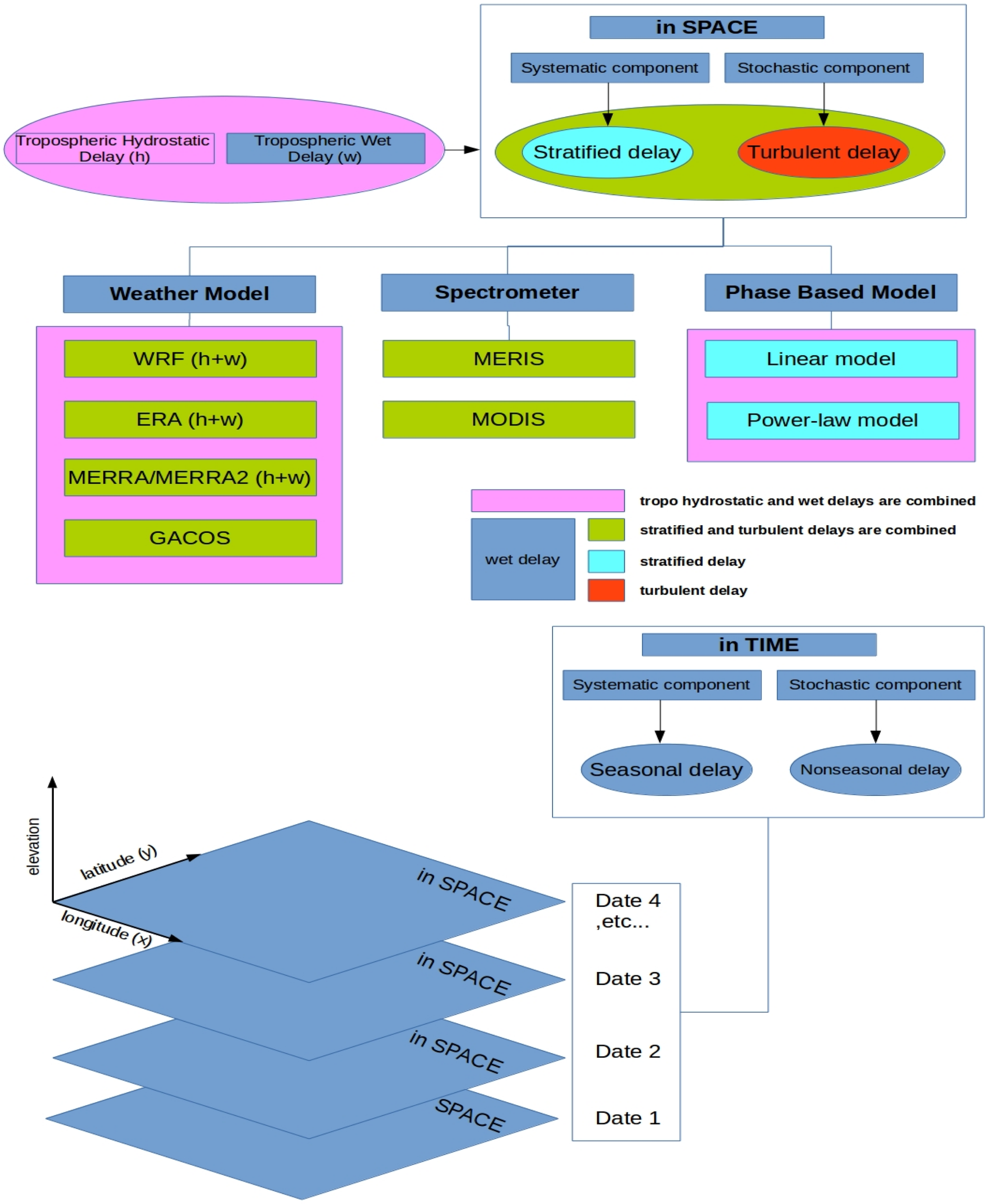

FIGURE 4.2: Different sources and strategies for estimating tropospheric delay in space (top) and in time (bottom).

scaled heights $(h_o - h)^{\alpha}$. We set the parameter of the power-law spatial band to 1000 - 1100 m in Ciloto and 4000 – 12000 m in Ensenada assuming the suitable-fit band filters excluding the deformation signal on those areas. The number of windows for local estimation depends on the size area. We set 50 windows with overlap 50% in the Baja California case and two windows with overlap 10% in the Ciloto case because the small location does not have extremely varying topography at certain lengths.

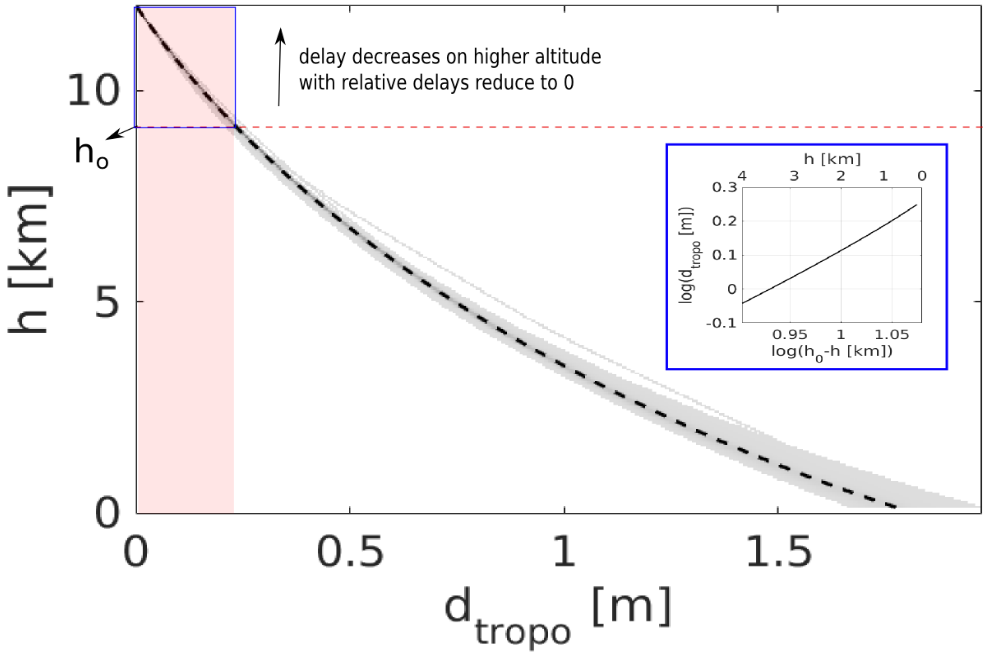

FIGURE 4.3: Tropospheric delay in Northern Baja California, Mexico computed from upper-air sounding data at San Diego Station, 72293 located $\sim$ 130 km away from the observed study area with the blue rectangle line described as log-log relationship indicating power-law relationship assumed as a linear model. The red color shows the interferometric delay at this reference height is approximately zero and will be neglected in the tropospheric correction.

4.2 The Application of Tropospheric Delay Correction

4.2.1 Ciloto, West Java, Indonesia

We demonstrate the temporal variation of the hydrostatic delay and wet delay as shown in Figure 4.4 between two pixel p [106.9976° ; -6.6851°] located on a hilly area and pixel q [107.0343° ; -6.7299°] located on a flat area. The length between the two pixels is about 6.5 km and 380 m elevation differences. Since the SAR scene was cropped to the small coverage evaluating only at the prone landslide region, we do not attempt to figure out the behavior of tropospheric phase delay in such a large area.

The temporal variation of hydrostatic and wet delay is calculated during the Sentinel 1A SAR acquisitions from October 2014 – September 2017 at 11:00 – 12:00 hour using weather model from ERA-1 Interim. Figure 4.5 describes the effect of slant hydrostatic delay (SHD) and slant wet delay (SWD) between these two pixels. The seasonal component is assumed to a periodic signal described as Fourier series model, a summation of sine and cosine functions with annual and biannual components (Fattahi et al., 2015) using the following function

$$SHD\ or\ SWD = a_o + \sum_{i=1}^{2} a_i cos(2\pi it) + b_i sin(2\pi it) \tag{4.5}$$

$$STD = SHD + SWD \tag{4.6}$$

where a_o = intercept, a_1,b_1 = the coefficients of annual components, a_2,b_2 = the coefficients of semi-annual components, t = period (every day in the the period of SAR taken acquisitions) and STD = Slant Total Delay. We assume that the stochastic components of the time series of

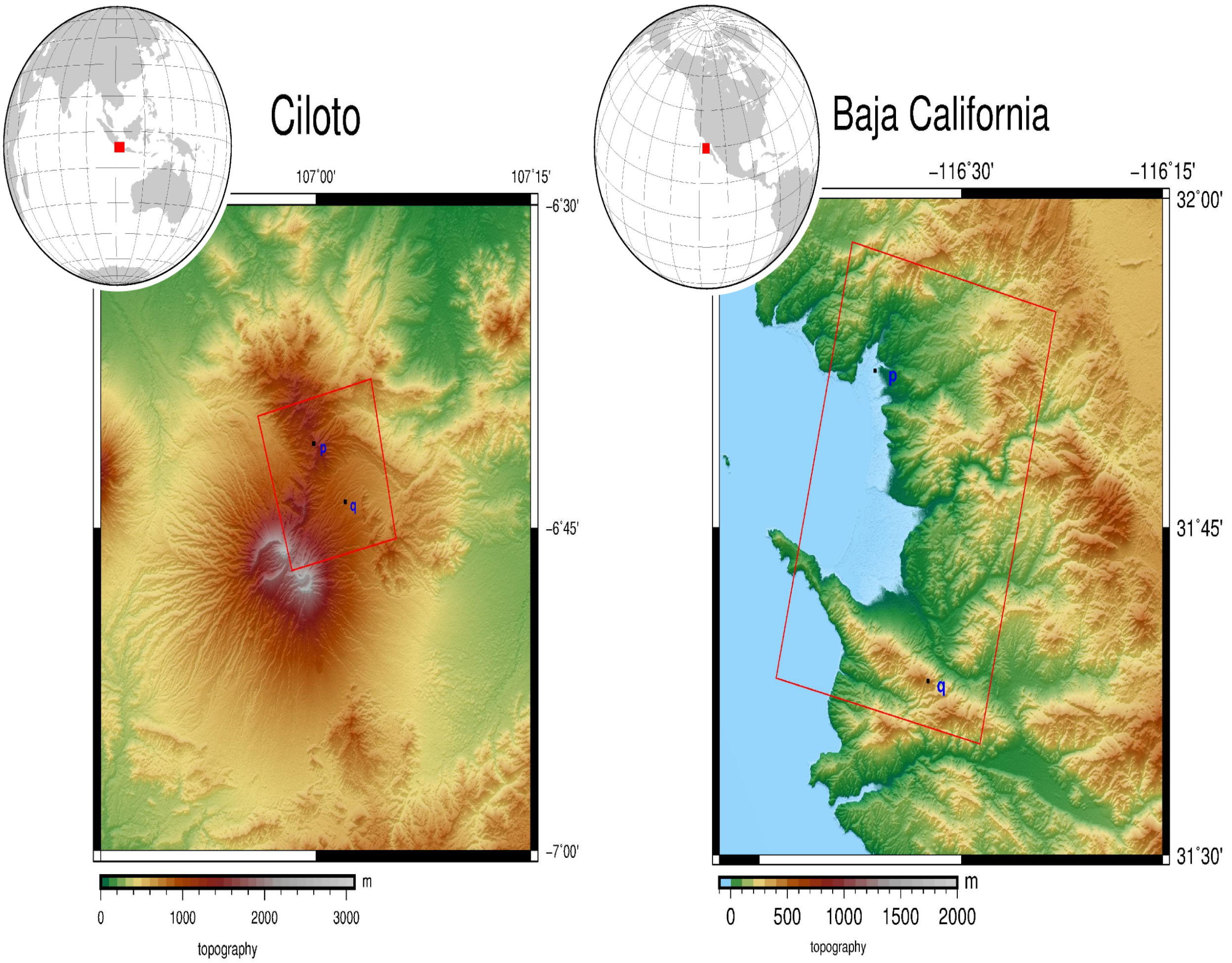

FIGURE 4.4: Study areas: (left) Ciloto, West Java, Indonesia with the red rectangle line showing Sentinel-1A ascending scene borders (Long E:105.5° – 108.5° and Lat S: -5.5° - 7.5°) and (right) Northern Baja California, Ensenada, Mexico with the red rectangle line showing Envisat descending scene borders (Long W: 117.5° – 115.5° and Lat N: 30.5° – 32.5°). Pixel p and q refer to different phase delays showed in Fig. 4.5 and Fig. 4.6.

relative delays are the residual of ERA-1 and best fitted seasonal. The relative delay and seasonal component could be plotted as Gaussian distribution in which the standard deviations of SHD, SWD, SHD are 0.0342, 0.4545, 0.4438, respectively. The highest and lowest peak of SHD is -14.6630 cm and -14.4246 cm, for SWD is -6.6920 cm and -3.7747 cm, respectively. The interval delay for SHD and SWD is 0.2385 cm and 2.9173 cm for three years. Hence, we could find out the interval between the highest and lowest peak of STD about 2.9659.

4.2.2 Northern Baja California, Ensenada, Mexico

The other second study area is located in an arid coastal region in the northern part of the Peninsula of Baja California, 110 km south from the US-México borderline (Figure 4.4). The region is morphologically characterized by coastal and alluvial flatlands, where the city of Ensenada and the croplands of Maneadero are located. These flatlands are surrounded by the Guadalupe and Ojos Negros, a series of intermountain valleys. The Agua Blanca fault is the southern border of our study area and extends from NW to SE as a 120 km length of the dextral strike-slip fault.

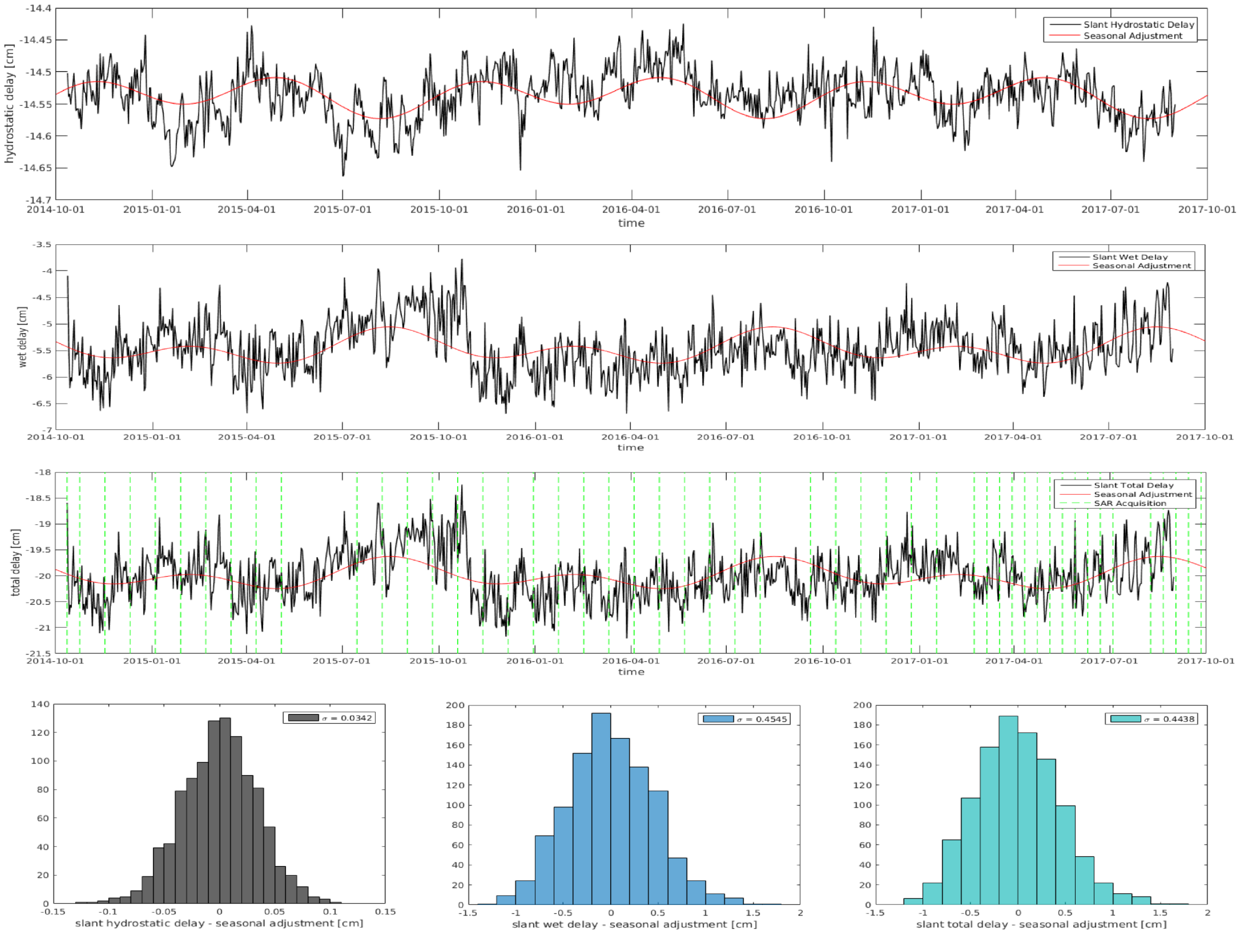

FIGURE 4.5: (The top rows) Time series of relative slant hydrostatic delay (top), slant wet delay (middle) and slant total delay (below) from ERA-1 with the seasonal model for each delay between pixels [p,q] in Ciloto region. The green line is Sentinel-1A date acquisitions. (The bottom row) Non-seasonal component with Gaussian distribution.

The geological background of this area was explained more at previous works (Dixon et al., 2002; Riedel et al., 2018).

Northern Baja California has a big possibility to observe the Earth's surface change, for example, crustal deformation due to tectonic activity and subsidence due to over-exploitation through water pumping in agricultural areas like in Maneadero Valley. The region has various terrains from flat areas in El Bajio and Maneadero Valley to a mountainous area in Punta Banda Ridge. Therefore, the atmospheric phase screen could affect microwave propagating signal especially through tropospheric layers in this region and make a dominant stratified delay in the interferograms.

Like the previous section, we also demonstrate the temporal variation of the hydrostatic delay and wet delay between two pixels; p [-116.6069°; 31.8690°] located on flat terrain and pixel q [-116.5410°; 31.6327°] located on mountainous terrain. The height difference between pixels is 910 m with the length of 29 km. The calculation of seasonal and non-seasonal delay is the same as what we applied in the Ciloto region. The relative delay and seasonal component could be plotted as Gaussian distribution in which the standard deviations of SHD, SWD, SHD are 0.2686, 1.1351, 1.2026, respectively. The highest and lowest peak of SHD is 22.2033 cm and 24.6427 cm, for SWD is 0.7407 cm and 9.2680 cm, respectively. The interval delay for SHD and SWD is 2.4214

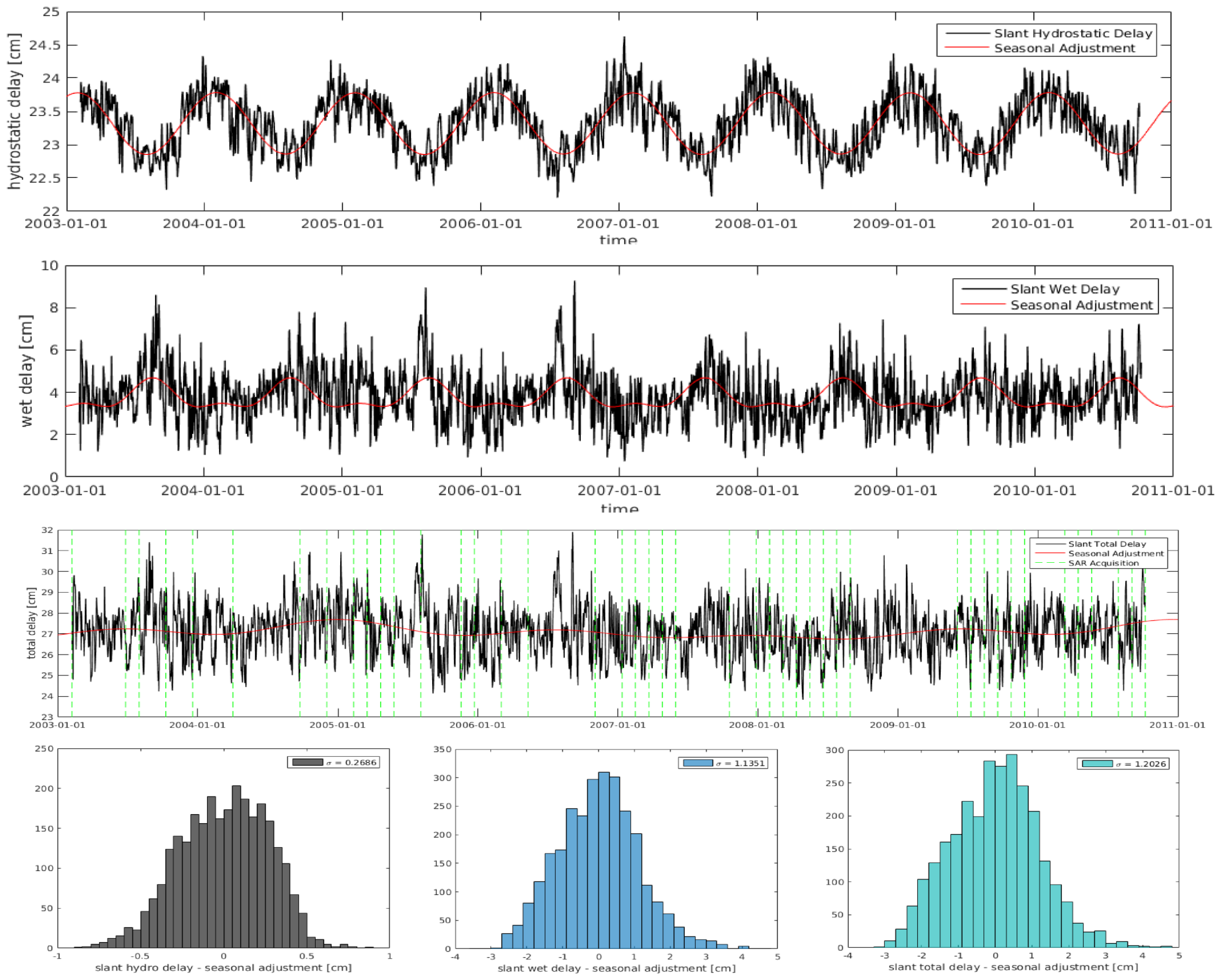

FIGURE 4.6: (The top rows) Time series of relative slant hydrostatic delay (top), slant wet delay (middle) and slant total delay (below) from ERA-1 with the seasonal model for each delay between pixels (p,q) in Ensenada region. The green line is Envisat acquisition dates. (The bottom row) The non-seasonal component with Gaussian distribution.

cm and 8.5274 cm for eight years. Hence, we could find out the interval between the highest and lowest peak of STD about 8.0610 cm. According to Figure 4.6, the seasonal model with the same summation of sine and cosine functions is not best fitted to STD since the periodic harmony between SHD and SWD in Ensenada is quite different and clearly shows greater range interval delay (8.06 cm) than range interval delay in Ciloto (2.96 cm). The high peak of seasonal delay for SHD occurs on every October-November annually. On the other hand, SWD has a high peak of it on every January - March annually.

4.3 Result and Analysis of Tropospheric Delay Mitigation

4.3.1 The Ciloto District, Indonesia

SAR images from Sentinel-1A ascending orbit were processed and generated 269 interferograms. We dropped out 19 interferograms for further time series computation since the residuals between small baselines (SB) network and inverted to single master (SM) network are more than 2π in magnitude indicating unwrapping problem (Hooper, 2008). The phase unwrapped results were further processed on the Toolbox for Reducing Atmospheric InSAR Noise (TRAIN) created by Bekaert et al., 2015b which implements this power-law method.

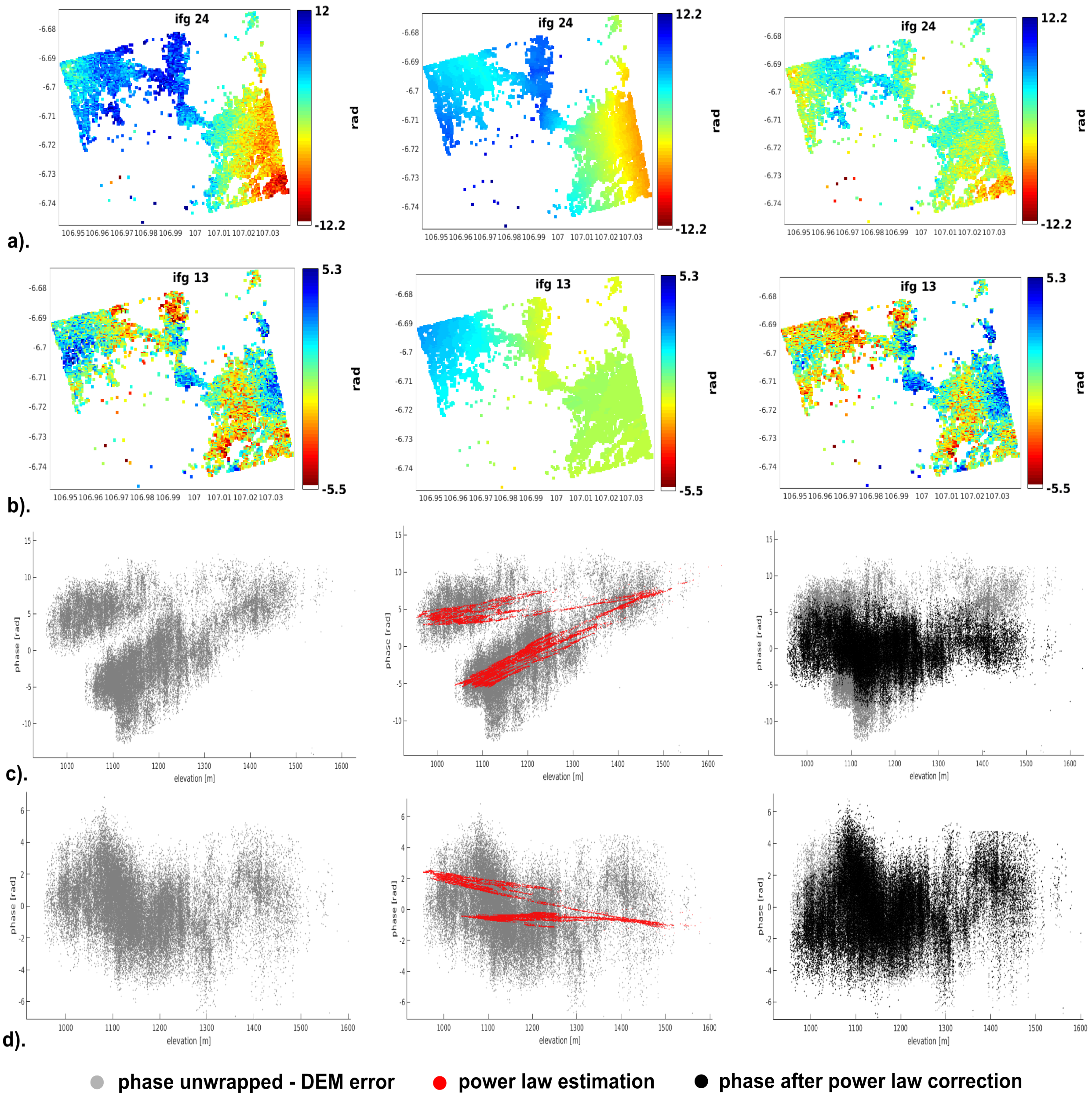

FIGURE 4.7: The left images are original phase unwrapped including DEM error correction, the middles are the estimation of power-law phase delay, and the rights are the corrected phase using the power-law procedure. Picture (a) and (b) refer to a sample of successful and unsuccessful corrected interferograms with (c) and (d) showing the relationship between phase and topographic height in Ciloto, Indonesia.

The tropospheric phase delay based on the power-law method was corrected on 250 interferograms. The success of applying this method depends on the relationship between phase and topography assuming APS dominant by the stratified delay. Thus, the estimated delay is appropriate for the power-law function. We compare some interferograms which have high and low correlations between the phase and elevation value. Figure 4.7.a shows an example of interferogram (20150317 – 20150808, ifg 24) where the stratified delay clearly appears on phase unwrapped result. On the contrary, an interferogram (20141211 – 20150128, ifg 13) does not have a good correlation to topography terrain as shown in Figure 4.7.d. The graphic at the bottom right refers to the power-law method not successful for mitigating the phase delay. Consequently, this correction could make the final phase interferogram having another bias than the original interferogram. Overcoming the problem that might appear in some interferograms, we smooth the corrected phase in the time series analysis by low-pass filtering which we predict the bias as spatially correlated noise due to either turbulent mixing or phase unwrapped error.

The time series displacement and assessment

250 interferograms with SB network will be inverted using least square to SM network (Schmidt et al., 2003) in purpose to calculate the time series displacement and mean velocity each PS pixels. The final interferometric phase $\Delta\phi_{depo}$ is PS scatters after a subtraction from DEM error (δ_{topo}), phase ramp (δ_{orbit}), stratified tropospheric delay ($\delta_{tropo,strat}$) and spatial correlated noise ($\delta_{corr.noise}$), which is described as

$$\Delta\phi_{depo} = \Delta\phi - \delta_{topo} - \delta_{orbit} - \delta_{tropo,strat} - \delta_{corr.noise} \tag{4.7}$$

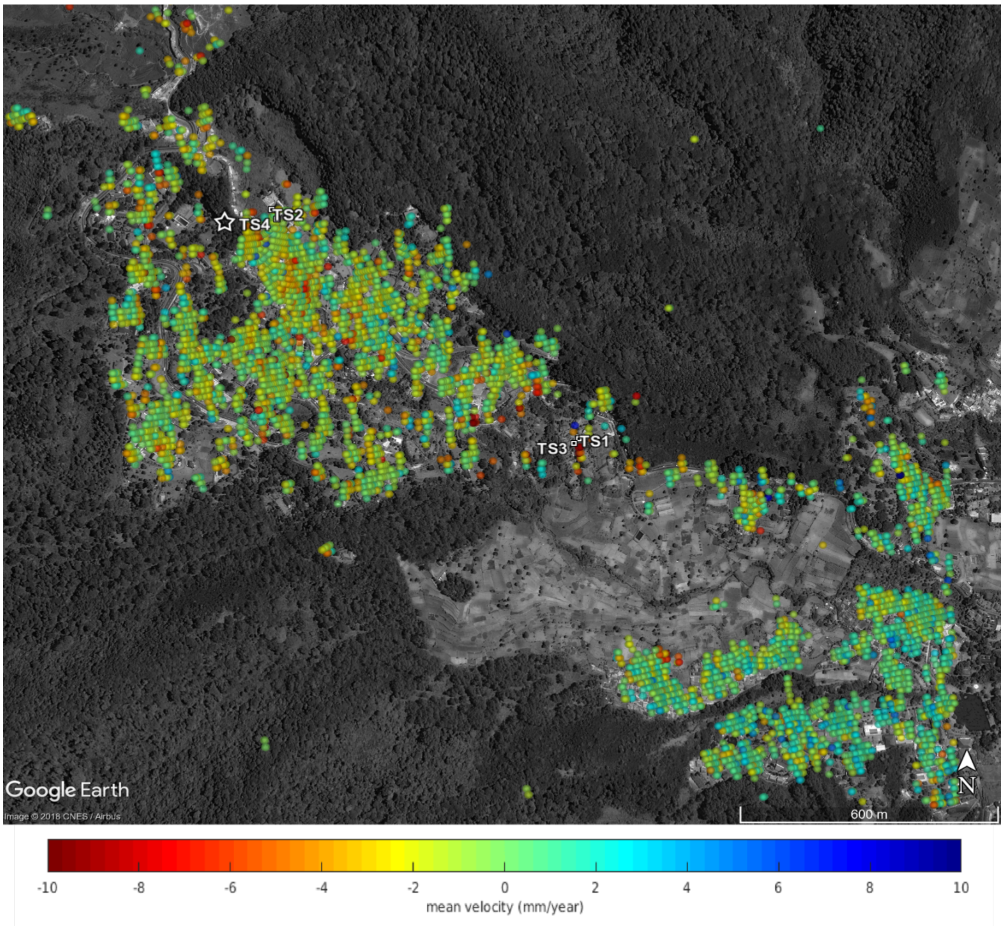

FIGURE 4.8: The mean velocity of slope movement -10 – +10 mm/year in the Ciloto landslide prone area. The type of movement is considered as a slow rate displacement with the high signal deformation is found in the middle of the study area. TS2 and TS4 are a sample of time series displacement near to the extensometer location (the star symbol). TS1 and TS3 are located to the main body of Landslide Ciloto which a few active landslides occurred in recent years.

The mean velocity was computed by the general least-square (GLS) from October 2014 – September 2017 in the Ciloto district as shown in Figure 4.8. It was calculated with the assumption that the displacement on every range of SAR acquisitions is a linear regression model. Moreover, it accounts only for a depiction of Ciloto's surface change for three years in order to visualize the change of displacement rate through PS points. It considers that -10 – +10 mm/year slow rate displacement occurred in Ciloto. There are a few PS scatters having high deformation signals in the top (Puncak Pass) and the middle (Puncak Highway) of the case both study where the previous geological research (Sumaryono et al., 2015) described the location as an active landslide zone. The scatters with a high displacement value are also located near to Puncak Highway Km. 81 where the small size landslides occurred in the area in 2015 and 2017. However, PS results cannot detect obviously the movement's behavior because only a few scatter left regarding the limitation of SAR resolution and lack of the exist-able for high correlated pixels.

Viewing on the main body of prone landslide zone, sample points TS1 and TS3 have detected the languid ground movement -4.3 mm/year and -1.96 mm/year, respectively. TS1 refers to a sample for conventional InSAR processing and TS3 after the corrected tropospheric phase delay. Figure 4.9 shows that PS scatters found on radius 25 m from TS1 and TS3. There are only a few scatter left on the area since it was difficult to find persistent objects in the agricultural area. Simply a linear model to figure out the mean velocity has been conducted using the ordinary least square method described as

$$disp_{TS1} = -0.0207t - 3.8072 \pm 0.31$$
$$disp_{TS2} = -0.0223t - 5.7450 \pm 0.39$$

The mean velocity of TS1 and TS2 are -7.5437 ± 2.22 and -8.1615 ± 2.79 mm/year, respectively. The model exaggerates the average time series values 0.0087 and 0.0169 /day accumulating to 3.2051 and 6.1959 /year.

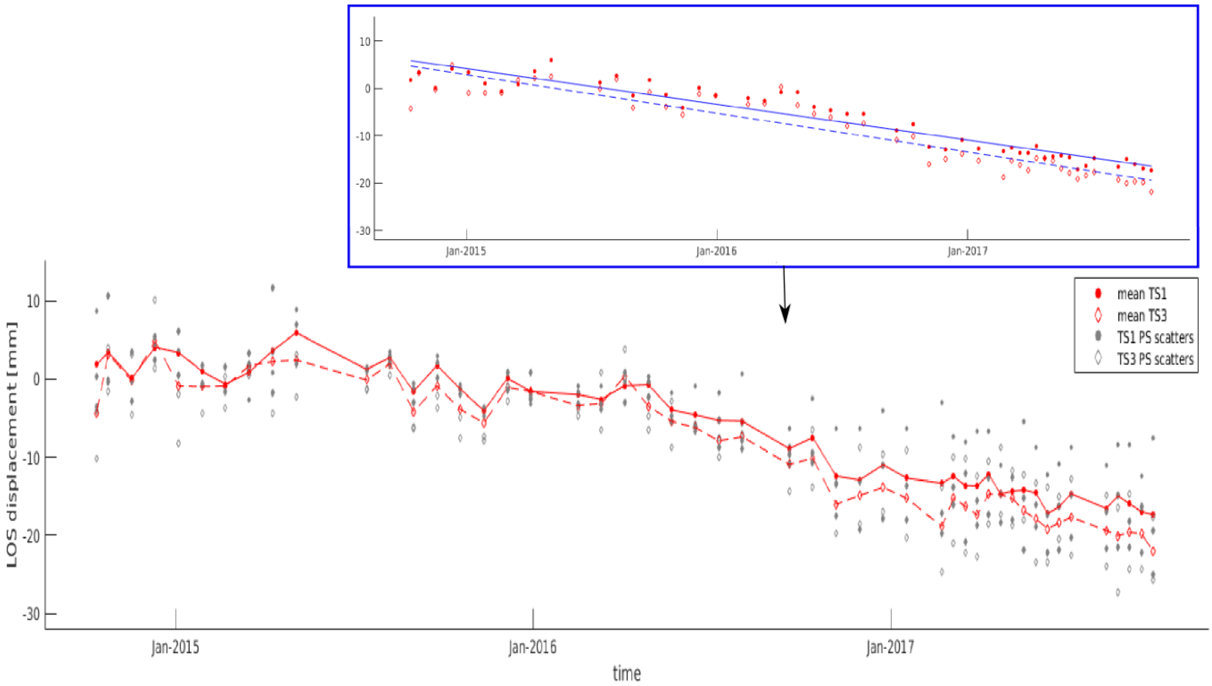

FIGURE 4.9: Time series displacements of TS1 and TS3 point (107.0021° E, -6.7119° S) located on Jl. Raya Puncak Km. 81, Ciloto. The blue box indicates the linear model movements both from InSAR results before (solid blue line) and after the power-law correction (dash blue line).

Furthermore, the result of the InSAR processing series needs to be compared to the ground measurement installed in the study area in order to quantify the InSAR result before and after the corrected tropospheric delay. BPPTKG[1], The Ministry of Energy and Mineral Resources of the Republic of Indonesia has built the 3G Track Extensometer, Cipanas Station, located at Kampung Puncak RT06/01 Desa Ciloto, 106°59″41.90″ E and 6°42′ 26.3″ S. The real-time updates of recorded extensometer could be browsed online via BPPTKG's official website. They installed a rain-gauge sensor also at the station, but unfortunately, it did not work since there was no data rainfall intensity recorded on the server's station.

We divide the recorded period of the extensometer into two sections based on the reference height of displacement in raw data due to the re-installment of the wire. The displacement trend from the first part was corrected to the trend showed in Figure 4.10.a because we found systematic error + 0.14 cm. Since the verified raw data need to be discussed with BPPTKG directly, we only assess the correlation from the second part which we do not find any systematic error, presuming that the wire worked properly. TS2, regular InSAR processing, and TS4, corrected tropospheric phase delay InSAR processing, are located at 106.9959° E, -6.707° S. The mean time series displacements for 28 scatters could be seen in Figure 4.10.a with ± 50 m the spatial length difference between PS scatters and the extensometer location. Figure 4.10.b indicates a correlation between the extensometer and the InSAR result before and after the tropospheric phase delay. It uses linear Pearson's correlation using a Student's t distribution for the correlation's transformation to quantify the measurements. The correlation value before the tropospheric delay is 0.7674 and after 0.8125. There is a small better accuracy after the power-law correction. In other words, it increases 0.0451.

4.3.2 The Northern Baja California, Mexico

SAR images from Envisat descending orbit were processed and generated 87 interferograms. Like the previous case, we correct the tropospheric delay for each interferogram. The terrain in Northern Baja California mostly mountainous area with the flat terrain found near to the coast area. The stratified delay causing the atmospheric phase screen is more dominant than turbulent mixing regarding the diverse topographic range and the demonstration of propagating delay from ERA-1 data. An example from an interferogram (18th Nov 2015 – 23rd Dec 2005 with B⊥ -165m) having a high atmospheric artifact could be seen in Figure 4.11.a. The high correlation accounts for the power-law function mitigating the propagation effect properly. Nonetheless, a problem may appear if a region is affected by either subsidence or uplift correlated to topography. Hence, the band-filter performance makes the deformation signal accidentally filter out as well. This issue is a drawback of the power-law method that we should concern for choosing the right band filtering to estimate constant coefficients of $K'_{\Delta\phi}$.

Not all interferograms are properly working to the power-law function. Some interferograms may have a partial success tropospheric correction or unsuccessful whether phase delay is fully not correlated to topography or the band filter is chosen incorrectly. One solution deciding the right band filter is trying some windows size and compares the result to weather model or non-deformed regions. The bandwidth is limited to the spatial extent of the study area for the largest window size and the resolution of resampling size for the smallest one (Bekaert et al., 2015a). We tried four power-law spatial bands, 2000 – 8000; 4000 – 10000; 4000 - 12000; 4000 – 14000 m, and selected [4000 12000] m as briefly discussed in Section 4.1.3 with a reason that most estimated tropospheric delays have scale range value similar to original interferograms. Figure 4.11.b refers to a corrected interferogram (19 Oct 2007 – 16 May 2008 with B⊥ 45 m) partially mitigating the propagating delay. The right picture in Figure 4.11.b declares explicitly that the power-law method had an over-estimation phase delay creating visible artifacts in La Bufadora and Punta Banda regions (the southwestern part from the study area).

We statistically compared the power-law method to MERIS computation. Because ASAR and this spectrometer instrument are operated on the same onboard Envisat Satellite, there is no time

---

[1] Balai Penyelidikan dan Mitigasi Bencana Geologi

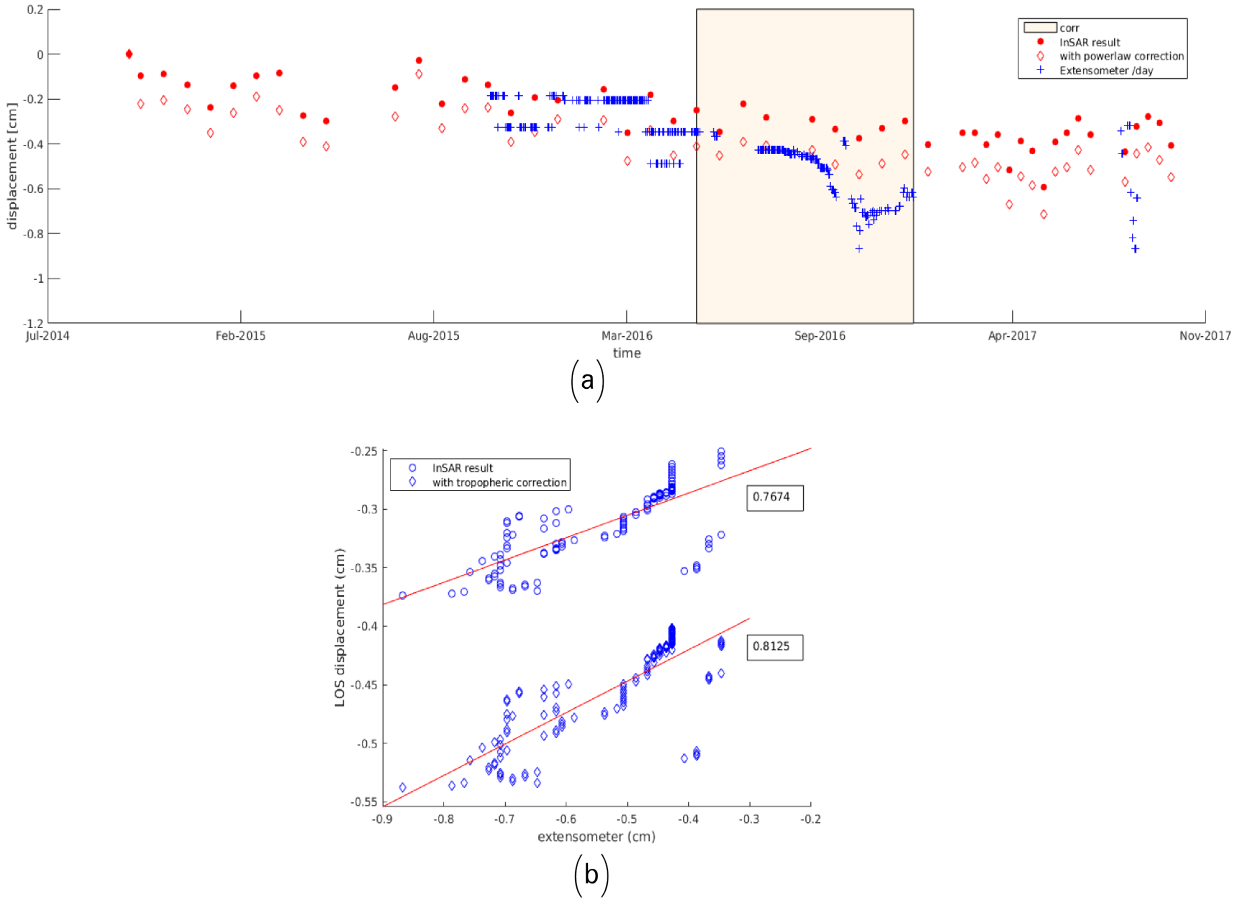

FIGURE 4.10: (a) Time series LOS displacement samples from TS2 point (before the power-law correction) and TS4 point (after the power-law correction) compare to the extensometer displacement (a local geometry). (b) A correlation between the extensometer and the LOS displacement from 22 May 2016 to 02 Jan 2017 (a corr. rectangle box).

delay to estimate an atmospheric delay for each SAR acquisition. However, the drawback of applying MERIS data is the daily varying cloud coverage. It makes the success of estimation depending on how much free cloud exist while the sensor is capturing the earth's surface. We tested the free-cloud coverage threshold of 50% and 90% which the results are 29 and 14 out of 44 SAR images, respectively. The mean correlation value between the phase-based power law and spectrometer MERIS is 0.52 for the threshold of 50% and 0.53 for the threshold of 90% with the selected number of interferograms shown in Figure 4.12.

If we consider 15 interferograms from the threshold of 90% as the appropriate comparison to quantify power-law method, 10 out of 15 have a high correlation (the mean correlation = 0.7) while interferograms 25, 28, 32, 33, and 41 show a low correlation (the mean correlation = 0.2). Despite an inaccurate surface interpolation for the gaps filled with cloud mask, the different correlation values are caused by the type of source delay estimated from the spectrometer and phase-based method. The MERIS correction generates an estimation coming from a wet delay which includes stratify and turbulent components. On the other hand, a phase-based estimation takes into account only from a stratified component but combining hydrostatic and wet delay. A hydrostatic component could be added to the MERIS result using the weather model, such as ERA-1 data. However, the mean correlation after adding the hydrostatic term from ERA-1 does not increase significantly (0.52 for 50% threshold) since a low coarse resolution (≈ 80 km) of ERA1-1 limits the varying hydrostatic delay in spatial. Another reason supposes that some interferograms do not

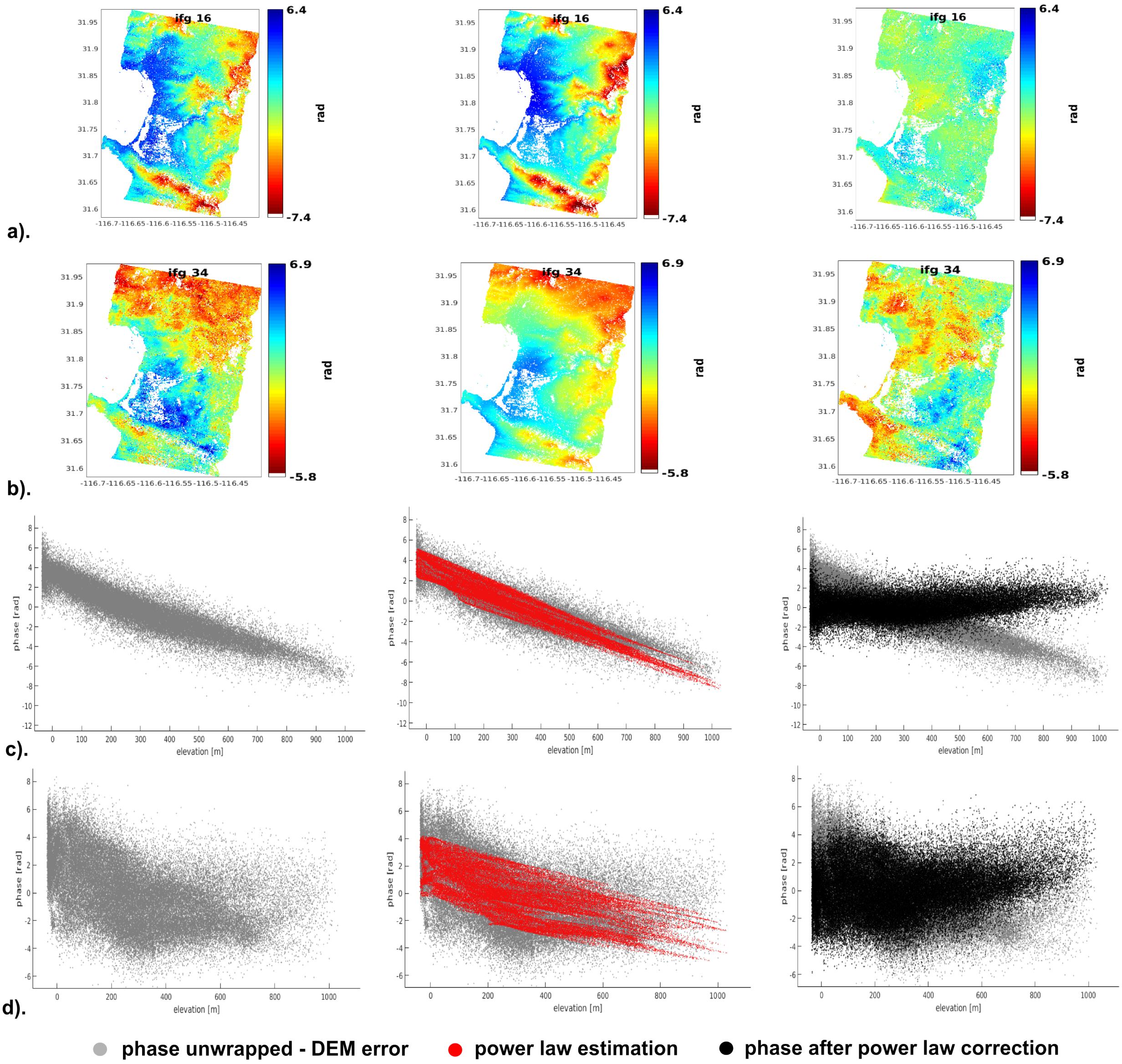

FIGURE 4.11: The left images are the original phase unwrapped including DEM error correction, the middles are the estimation of power-law phase delay, and the rights are the corrected phase after the power-law correction. Picture (a) and (b) refer to a sample of successful and unsuccessful corrected interferograms with (c) and (d) showing the relationship between phase and topographic height in Northern Baja California, Mexico.

have a high impact on the stratified delay examined by five low correlated interferograms. Their correlations to the terrain elevation encourage the point of view that only interferogram 33 has a high correlation (the correlation value = 0.79) with the other rest numbers 25,28,32,41 showing low correlation -0.44, 0.54, 0.11, -0.58, respectively. Particularly, the source of phase delay could be from a turbulent component, dynamic local weather, or unknown noise error that occurred at some acquisition dates.

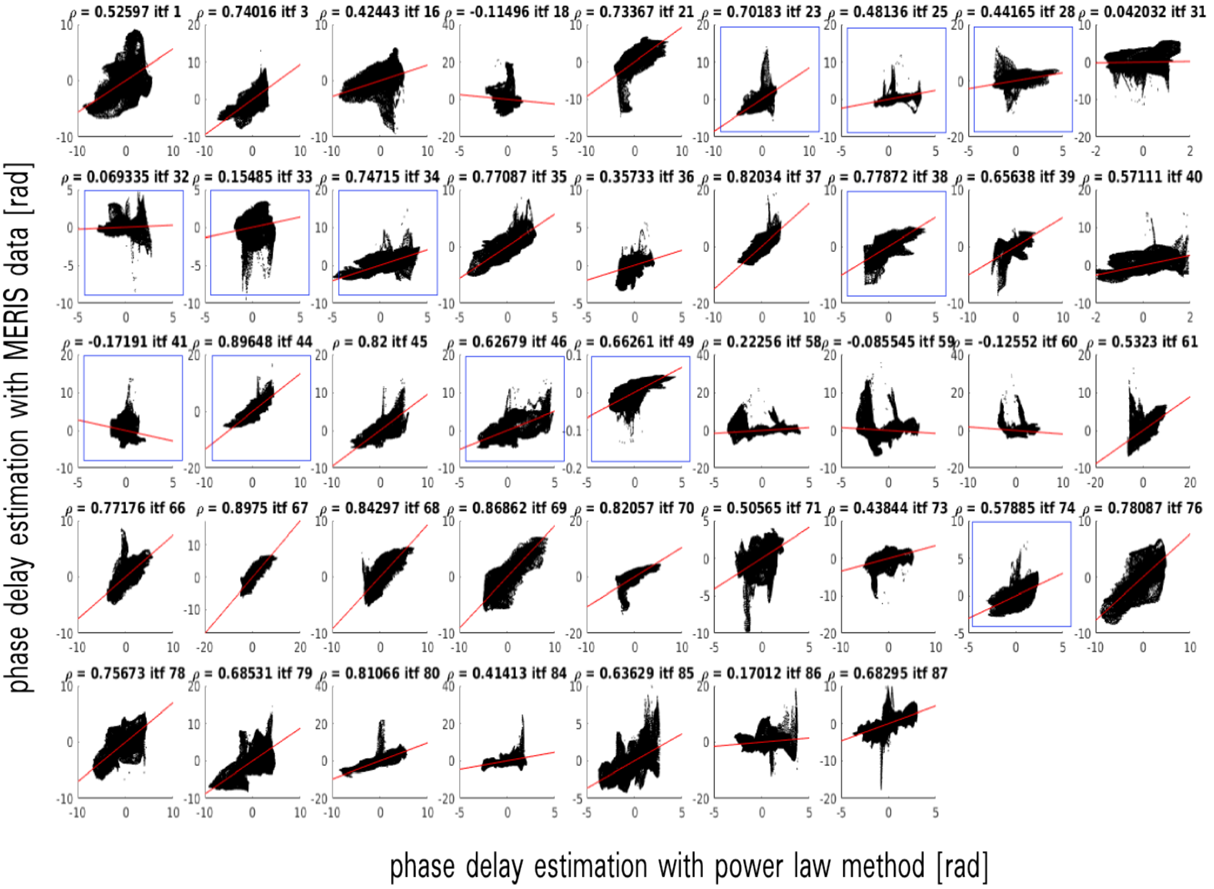

FIGURE 4.12: The correlation of estimated phase delay between the phase-based, power-law, and the spectrometer - MERIS method with 50% threshold of free cloud coverage while the blue line box refers to 90% threshold of it.

The time series displacement and assessment

The northern part of the Peninsula of Baja California (Mexico), south of Ensenada at the Pacific Ocean has mountain ranges up to 1000 m above MSL and arable land in the valleys. The morphology in those areas created some environmental issues due to either concessive natural or human activities. The Agua Blanca fault strikes from northwest to southeast and is a right-lateral strike-slip fault, which was reactivated during the development of the San Andreas fault. Moreover, the excessive use of groundwater for agricultural, urban, commercial, and touristic infrastructure put significant pressure on the aquifers with loss of groundwater supply and quality. Therefore, an investigation needs to be conducted in purpose to support the technical decision policy.

For the first observation, we seek a long-term fault slip along Agua Blanca fault using the InSAR time series from Envisat descending data for eight years. The propagating delay could mask out the sensitivity of InSAR performance for detecting the real signal of deformation, especially for the case of Agua Blanca fault surrounded by mountainous terrain with the most extreme height difference of 1 km. The mean velocity using a general least-squares method and Envisat oscillator correction (Marinkovic et al., 2015) has been generated to overview surface changes in which there are significant artifacts clearly shown by a conventional InSAR SB network in Figure 4.13.a. Although the inversion SM (Fig. 4.13.b) network has been done to reduce the noise, it still appears in the southeast observed area. Therefore, in the following paragraphs, we examine the result of the corrected tropospheric delay time series (TS) InSAR (Fig. 4.13.c) categorized into three groups. The first group explains a few TS points (TS1; TS2; TS3) along Agua Blanca fault to infer a slip rate displacement. The second one (TS4) is exploring Manaedero Valley where an environment issue arose in recent years due to over-exploitation water pumping. The last group (TS5; TS6) is a general resemblance between two TS points and GPS points (CICE, FILO) located on the covered area.

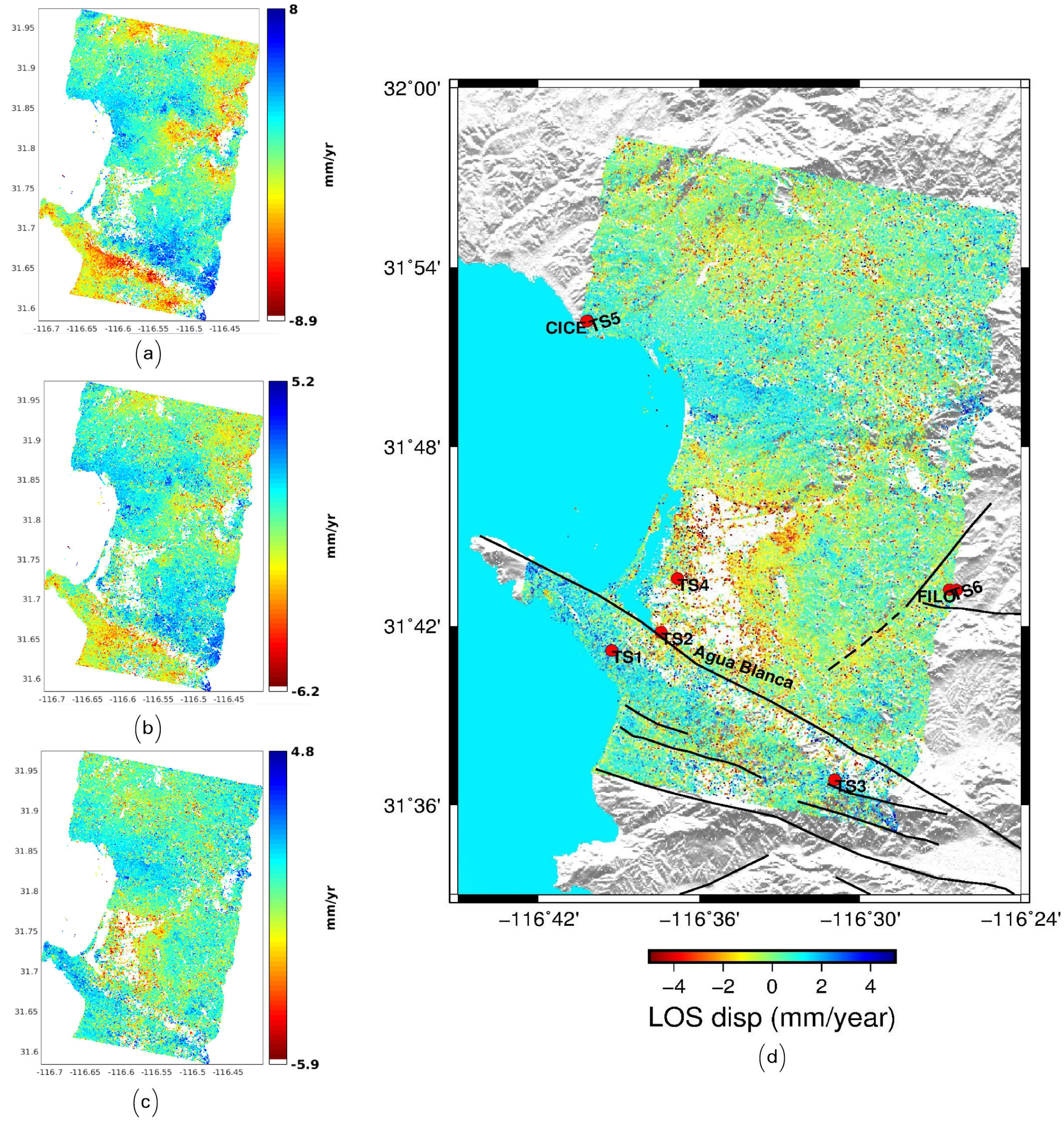

(a)

(b)

(c)

(d)

FIGURE 4.13: (a) The mean velocity generated from (a) conventional time series InSAR SB network, (b) with inversion to SM network and (c) after tropospheric delay has been corrected using the power-law method. (d) The mean velocity for final InSAR results overlaying on SRTM with sample time series points located at Agua Blanca strike-slip fault, Maneadero and GPS locations.

According to Figure 4.14, the mean velocity of TS1, TS2, TS3 using a linear model as written in Section 3.2 are 1.832±0.87, -2.688±0.43, 1.34±1.02 mm/year, respectively and considered as a slow rate motion. Dixon et al., 2002 suggested that the fault is active but seismically quiet. There is a similar uplift pattern between TS1 & TS3 that might assume the points placed on "tectonic block". These results agree to the previously conducted research from Riedel et al., 2018 which described the southern part of Aqua Blanca fault laid on the same block and having a similar movement behavior. Although the range TS1 and TS3 are approximately 15 km away assumed as a major right lateral strike-slip (Allan et al., 1960), we cannot determine whether it is a total offset along the fault. The reasons are; we do not retrieve the horizontal components, noise scatters are existing in the middle of Agua Blanca fault, and some parts have been masked out due to high decorrelation. On the other hand, TS2 acts differently to TS1 and TS3 where the area found depressed or down lift to -2.688 mm/year. Therefore, not only verification of this behavior motion needs to be compared to ground observation but also a geometry relationship between the ground and LOS direction is highly recommended in the future.

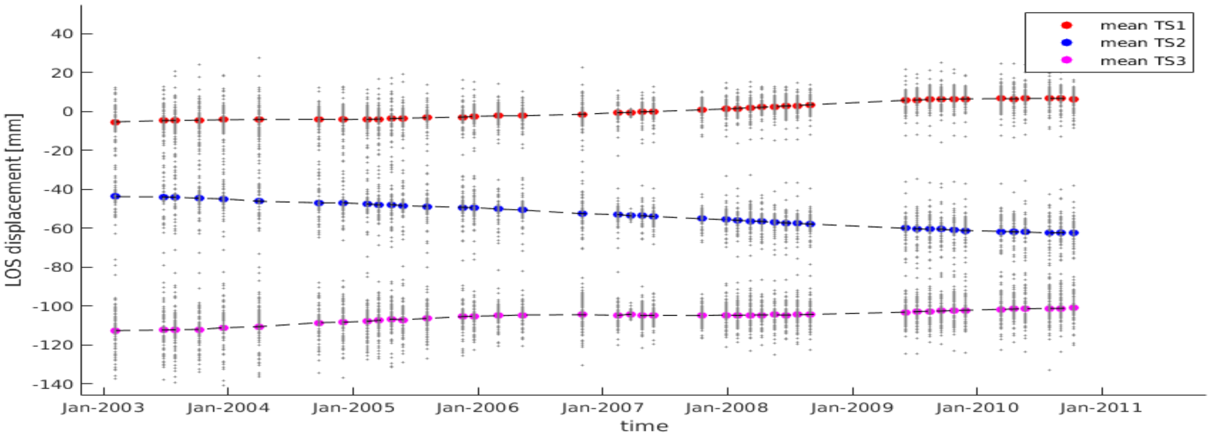

FIGURE 4.14: Time series displacement TS1 (-116.6546°, 31.6862°), TS2 (-116.6239°, 31.6964°), TS3 (-116.5158°, 31.6141°). The average movement is calculated from PS scatters found in radius of 500 m at each point. The figure has been shifted in y axis aiming for a visualization.

We further investigate in general Maneadero Valley where the region has been actively exploited for groundwater to support agriculture liveliness. Unfortunately, there are not enough PS points left in the middle of the region due to a decorrelated characteristic for vegetation cover. Near to the coastal dunes, the mean velocity of InSAR reveals that the surface's level around San Miguel decreases to -2.41±0.76 mm/year using a linear approach of time series displacement for eight years shown in Figure 4.15. The graphic presents the downward movement which is likely occurred because of soil degradation. Wind and water highly contribute to soil erosion. In fact, the area ecologically belongs to a sandspit or a coastal landform occupied by urban agriculture (Martinez et al., 2007). Since it is salt marshes located close enough to the shoreline, the motion easily gets influenced by wind-driven currents, tidal currents, wave action, and seasonal weather, especially during winter. Regarding the assumption of sinking land level at a developing salt marsh, there should be an area with the rate of sediment build-up (Rafferty, 2011) and it is seen in the southwest from San Miguel (TS4 mark) which PS scatters showing an uplift movement. Furthermore, the InSAR results are not significantly detecting any subsidence signal in the Maneadero City. Hence, we consider the region is more stable sustained by the geological structure of volcanic and sediment rocks than Manaedero Valley with the alluvial material structure.

Based on the previous research using GPS observation from 1993 to 1998 (Dixon et al., 2002), the mean velocity is about 5 mm/year across the Agua Blanca and San Miguel Vallecitos faults. Our location only covers the small part of a whole long-term slip rate area across these two faults. Therefore, we only discuss two GPS points, CICE, northwestern direction, and FILO, western direction, at northern Baja California. The sample of TS5 and TS6 represents to GPS locations where 69 and 59 PS scatters found in radius 500 m from the center of TS5 and TS6. We focus only to the vertical components generated from GPS because of unavailability the horizontal component

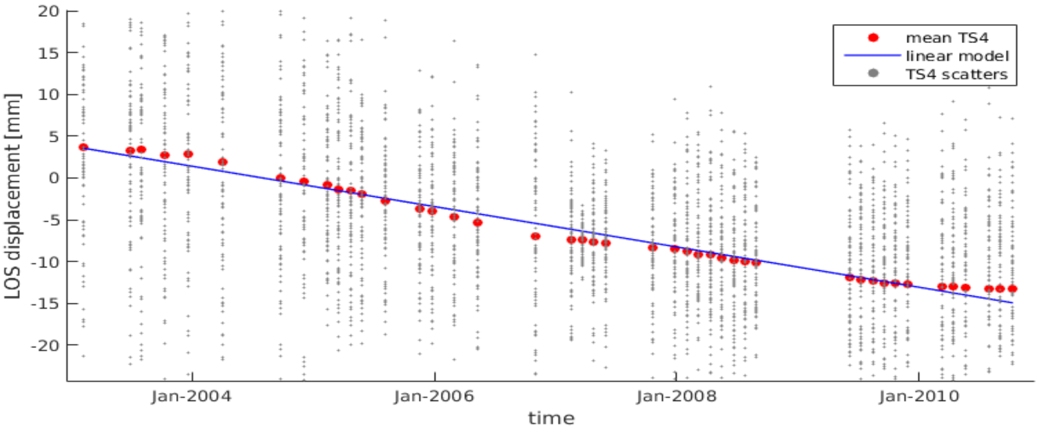

FIGURE 4.15: Time series displacement TS4 (-116.6137°, 31.7264°) located around San Miguel, Baja California. The mean movement is calculated from 81 PS scatters found at radius 500 m. The surface's level is sinking likely due to soil degradation.

from InSAR results since we processed only one track, the descending orbit. The condition is hardly possible to retrieve the full displacement vector (dz, de, dn) even if we use both ascending and descending interferograms because the slant range is more sensitive to vertical and west-east than north-south direction. The velocities generated both by GPS relative to ITRF-96 from 1993 to 1998 and SBAS InSAR from 2003 to 2011 could be seen in table 4.1. We projected the LOS displacement to a vertical component using the look angle information on selected PS pixels. Furthermore, the mean vertical velocity of InSAR results are calculated based on weighted least squares – linear line fit.

TABLE 4.1: GPS velocities relative to ITRF-96 for CICE and FILO station (Source: Dixon et al., 2002) and InSAR velocities samples for TS5 and TS6 points generated by 44 Envisat descending images.

Point	Lat (°)	Long (°)	Velocity East	(mm/yr) West	Vertical	Duration
CICE	31.87	-116.67	17.5±0.6	-38±0.9	1.5±2	1993-1998
TS5	31.87	-116.67	-	-	0.9±1.8	2003-2011
FILO	31.72	-116.44	17.3±1.1	-39.5±1.7	1.4±3.2	1993-1998
TS6	31.72	-116.44	-	-	-0.5±0.6	2003-2011

CICE station has the same behavior to TS5 considering that the area moved up 1.5±2.0 and 0.91±1.8 mm/year. Nevertheless, TS6 acted differently to the movement recorded at FILO station. The FILO records showed uplift to 1.4±3.2 on the contrary TS6 down lift to -0.47±0.6 mm/year. Figure 4.16 describes the time series displacements of TS5 and TS6. There are a few reasons that the vertical components between GPS and InSAR projected results acted differently. In point of geometric reason, GPS is the most insensitive measurement to the vertical component. Otherwise, the slant-range of SAR has the most insensitivity decomposition to the north-south component. Hence, the fault belongs to a strike-slip type in which horizontal displacements are more taking into account than the vertical one. Moreover, considering the processing strategies, a few concerns due to this bias InSAR result are; firstly, the band-filter process in tropospheric delay correction could accidentally remove a deformation signal because of the parallel movement direction to the terrain. Secondly, the unsuccessful corrected tropospheric delay and a random noise might remain. Moreover, FILO station was located at steep terrain which retrieving the side-looking displacement is a challenge due to geometric distortions in the SAR image.

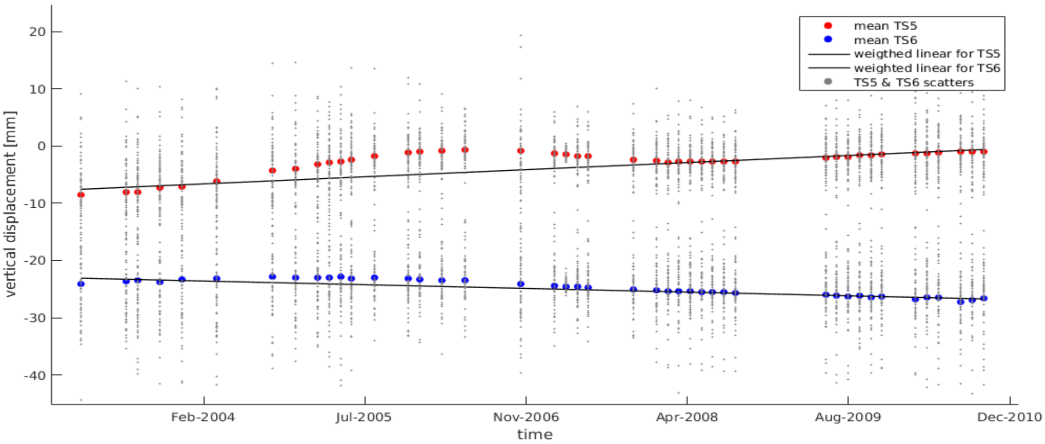

FIGURE 4.16: Time series displacement TS5 (-116.67°, 31.877°) and TS6 (-116.44°, 31.72°) located at CICE and FILO marks from GPS observation. The mean time series displacements are calculated from 69 and 59 PS scatters found at the radius of 500 m. The figure has been shifted in y-axis aiming for a visualization.

4.4 Conclusions of Tropospheric Phase Delay Mitigation

We conducted the performance of the power-law method to mitigate the tropospheric delay over Ciloto, Indonesia and Baja California, Mexico. The correction allows estimating locally varying interferometric phase delay signals in spatial and temporal. We tested the method on mountainous terrains in small and large areas. Although the validation to the ground measurement, the extensometer, showed an increased correlation before and after tropospheric delay correction, the performance is way better to be applied at large areas in condition to the dominant delay's source from a stratified term. The reason is that the spatial scales over these areas change significantly in pressure, temperature and relative humidity. However, the power-law method is principally successful when the study areas have relative delays appropriate to the power-law function. If it is not, it might introduce incorrect signals because of under or over tropospheric signal estimation subjecting to turbulent variations and local weather. Furthermore, we suggest that the tropospheric mitigation needs to use the combination method of phase-based, spectrometer and weather model phenomena with the development of optimization of algorithm to select the most accurate strategy of phase delay correction applied to each interferogram.

The quality of slow rate displacement time series InSAR could be improved with the stratified tropospheric delay correction. It removes the sampling biases of time series because the stratified delay is systematically presenting seasonal fluctuations and correlated to topography. Especially for the Mexico study area, the hydrostatic delay has to be taken into account when there is more than 10°C different surface temperature in a year (Doin et al., 2009). Nevertheless, the displacement's value remains still in a slant-range direction which in the next step of our work, we will perform both satellite's orbits for the Ciloto study area and assess the displacement's geometry projected from LOS to the ground surface direction.

Chapter 5

The LOS-Displacements in The Ciloto District Using InSAR Techniques

This chapter describes the interferometric processing and the LOS-displacements result of multi-band SAR datasets available in the Ciloto district. All of SAR data are processed by the SB-SDFP algorithm implemented on STaMPS, open-source software for InSAR time series analysis. The derived displacement results from ERS1/2, ALOS PALSAR and Sentinel-1 data are integrated to evaluate the movement's behavior in the Ciloto active landslide zones. The comparison of the velocity rate between InSAR and ground observations (e.g., terrestrial measurement, GPS, and extensometer) is conducted on specific locations both in the spatial and the temporal perspective. Furthermore, the relationship between the detected surface movement and the Ciloto physical environment is discussed descriptively to comprehend the behavior of Ciloto landslides for decades.

5.1 ERS1/2 C-Band Data (1996 - 1999)

ERS1/2 SAR data from April 1996 to 1999 with VV polarization and descending orbit were processed. The scenes available for the Ciloto area were from track 175 and frame 3744. ERS-1 and -2 have similar polar orbit so that we could combine those satellites for InSAR processing. The ERS tracks cover the Ciloto area listed in Table 5.1 and every track for SB configuration was combined using the minimum coherence parameter based on both the temporal and perpendicular baselines (Hooper, 2008). The arrangement of the perpendicular baseline was calculated with a reference scene from the 1998-11-07 acquisition date as a master scene for aligning co-registration. The region of interest (ROI) is about 2.5 km x 0.75 km where the surrounding location study is mostly covered by vegetation.

The ERS satellite is C-band with 5.6 cm wavelength and the orbit information at every acquisition date uses precise orbit ephemeris (POE) provided by ESA and TU Delft (Scharroo et al., 1998) with a gravity model from DGM-E04. The use of POE will minimize the orbital error artifact or phase ramp on the interferograms. The mission of the ERS1 satellite ended in 2000 and ERS2 fully retired in 2011. ERS mission was continued by the Envisat satellite until shutting down in 2012. The mission is further being continued by Sentinel-1 from 2014 until present with enhancements in terms of revisit, coverage, and timeliness. For Envisat data, we can not detect any proper deformation signal since there was no sufficient number of SAR data to identify persistent scatters objects in the observed area. Therefore, the Envisat result is not including in this dissertation.

5.1.1 Multi Temporal Interferometric Generation

Interferometric processing was done using Delft Object-oriented Radar Interferometric Software (Doris) (Kampes et al., 2003) while the focusing of SAR images was performed by Repeat Orbit Interferometry Package (ROIPAC) (Rosen et al., 2004). The configuration of master-slave interferometry depended on the following parameters; 0.3 for minimum coherence, 365 days for maximum temporal and 430 m for the perpendicular baseline. For an example of high coherences

TABLE 5.1: ERS data for Ciloto, Cipanas regency

No	Acq. Date	Sensor	Orbit	⊥Baseline(m)
1	19960406	ERS1	24712	162.8
2	19960407	ERS2	5039	50.9
3	19960512	ERS2	5540	390.1
4	19960929	ERS2	7544	-358.2
5	19961103	ERS2	8045	904.1
6	19970706	ERS2	11552	-376.1
7	19980725	ERS1	36736	619.7
8	19980726	ERS2	17063	52.8
9	19981004	ERS2	18065	534.4
10	19981107	ERS1	38239	0
11	19981108	ERS2	18566	320.4
12	19990117	ERS2	19568	-183.4
13	19990220	ERS1	39742	1119.5
14	19990221	ERS2	20069	714.3
15	19990328	ERS2	20570	-847.8
16	19990502	ERS2	21071	-274.5
17	19990606	ERS2	21572	334
18	19990711	ERS2	22073	-615.1
19	19990815	ERS2	22574	801.3
20	19990919	ERS2	23075	366.3

of an interferogram in the Ciloto area, Figure 5.1 shows a raw interferogram generated by a pair of SAR images between 06.04.1996 and 07.04.1996 acquisition time. The coherence values are mostly >0.6 which means it is sufficient to generate interferometry images in the case study area. However, because of the location placed on the mountainous and agriculture area, some SAR images had high total decorrelated and lost much back-scattering power on its way back to the sensor. In consequence, they were not selected for further interferometric processing. For instance, two acquisition dates, 19.10.1997 and 07.11.1998, SAR images even failed for the co-registration process with the coherence values of almost all pixels being <0.2 and two acquisition dates, 10.02.2002 and 17.11.2002, have long temporal baselines.

Therefore, four master-slave pairs were eliminated because of high decorrelated and having long temporal baselines. Excluding them, all raw interferograms continue to be processed for geometric phase which is called the differential interferometry with the simulation topography or digital elevation model (DEM) was taken from the external SRTM 30 m and 2-pass interferometry from the phase to the height elevation value generated by the 19960406-19960407 scene pair. For the information, the final SB InSAR processing result uses SRTM data (also for ALOS and Sentinel-1 data processing) since the topography simulation generated by 2-pass interferometry is densely noise hence some areas should be masked to avoid the effect of unwrapping error on final interferogram. Because of this issue, the DEM result of 2-pass interferometry can not be represented as an alternative option to correct a raw interferogram from the real topography phase effect and the phase component due to the variation of the range distance across the image, i.e,

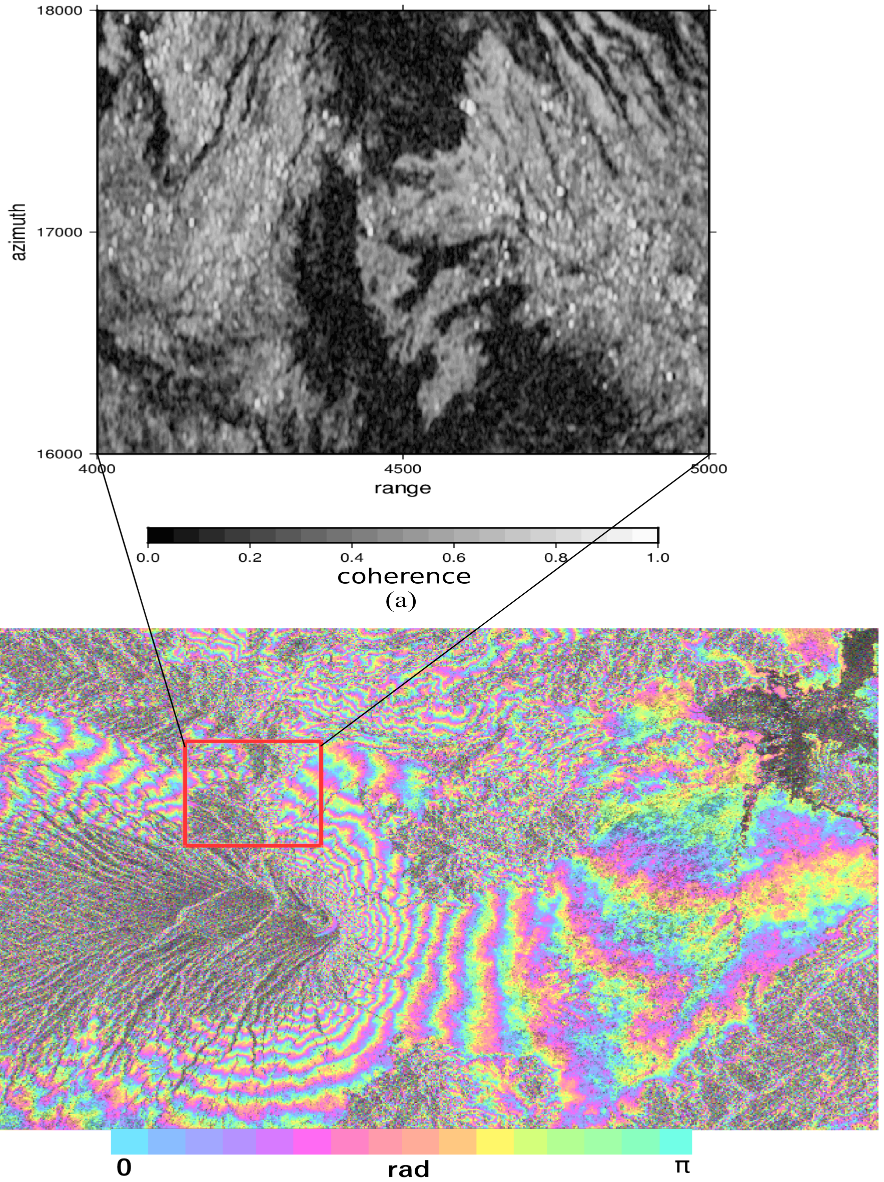

(a)

(b)

FIGURE 5.1: (a) The high coherence between 06.04.1996 & 07.04.1996 of ERS1/2 tandem scene and corresponds to (b) the raw interferogram with the effect of topo-fringes.

$\phi_{curved\,Earth}$. Furthermore, the height profiles between SRTM and ERS InSAR DEM show a different elevation pattern. Particularly, it is still unclear whether the elevation values generated by the ERS sensor represent the real surface topography or a geometric error (Figure 5.2). We suggest that 2-pass DEM generation from ERS1/2 should be studied in detail separately before it could be used widely for the SB InSAR method, as the low quality of the DEM will cause more errors in two terms, both look and squint angle.

A conventional PS method requires one master to many slaves (the star graph network). In our case study, a rural and agricultural area, the application of the original PS method is difficult. Finding a dominant scatterer is problematic since the signals are easily decorrelated especially for the long temporal and perpendicular baseline configurations. To overcome this issue, SB-SDFP introduces a selection to an underlying signal by forming interferograms only with small perpendicular baseline, short time interval and small difference between the Doppler centroids of

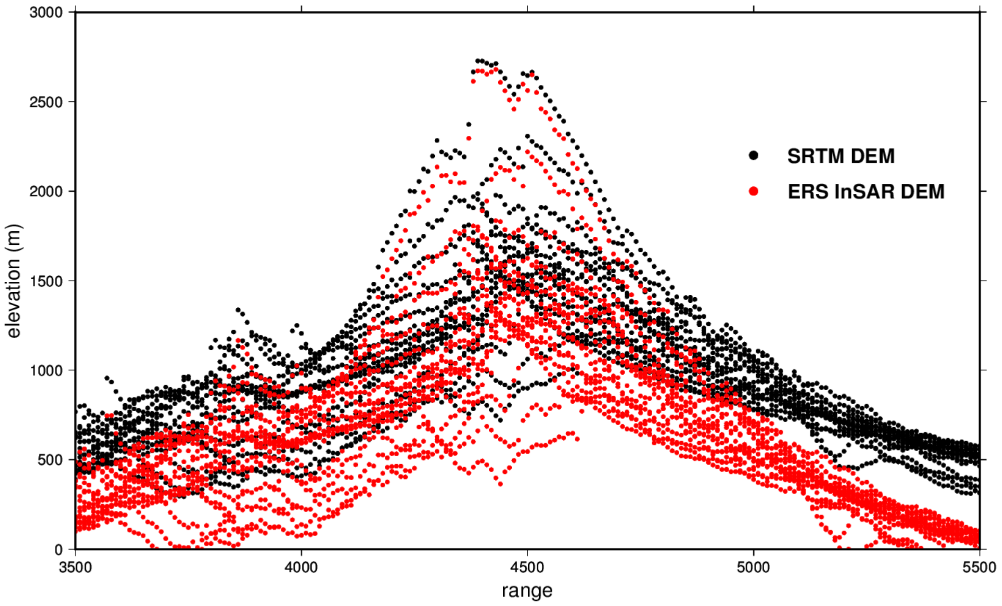

FIGURE 5.2: Comparison between SRTM DEM (black dot) and ERS InSAR TanDEM (red dot).

acquisition pairs. The result of the SB configuration can be seen in Figure 5.3. Before going to the SDFP selection step, the one-look interferograms were filtered both in azimuth and range to keep only overlapping the Doppler spectrum and to reduce the influence of geometric decorrelation.

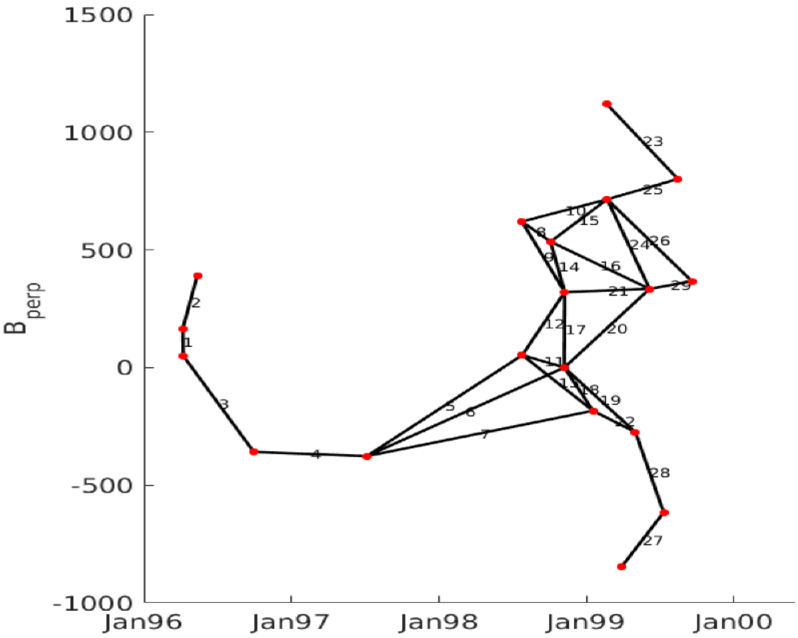

FIGURE 5.3: SB configuration for ERS1/2 data sets

SDFP pixel selection was performed on the highest resolution of SAR images in order to identify more pixels as PS candidates. Hence, the multi-look step during the resampling process is not done. Due to reducing high computation memory, pixels firstly were selected by the analysis of amplitudes using the amplitude difference dispersion introduced by Ferretti et al., 2001 and modified by Hooper, 2008. We subsequently performed bandpass filtering of surrounding pixels to estimate the spatially-correlated contribution to the interferometric phase for small baselines networks.

5.1.2 The LOS Displacement Result

29 interferograms of 16 scenes were generated from descending orbit, track 175. Meanwhile, we could not detect a good deformation signal for the ascending orbit due to insufficient data for processing with the SB-SDFP algorithm. We realize that the misregistration from coregistration and Doppler centroid separation may exist and contribute to error and noise in the phase values. However, they might be correlated spatially. Thus, the chance to eliminate these propagation errors is promising. While applying SB-SDFP to detect slow deformation in Ciloto, we figured out which parameters were suitable to the application since it was quite challenging to identify the signal with both a high coherence and a stable phase in such a heterogeneous place. We changed some parameters on StaMPS and Table 5.2 shows in detail the specific parameters used in the processing. These altered parameters are considered to be the most suitable values after much trial processing in the Ciloto's environmental conditions.

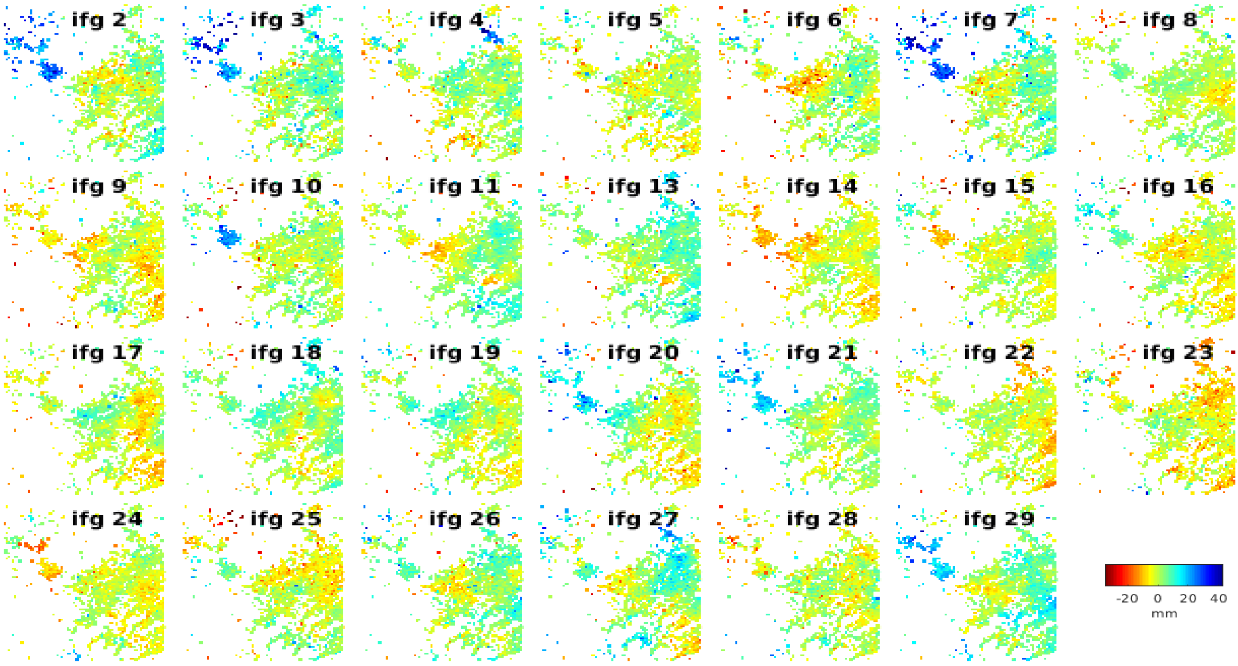

FIGURE 5.4: The unwrapped interferograms from ERS data in the Ciloto area

Furthermore, unwrapping 29 interferograms using a 3D approach helped to reduce the unwrapping error spatially and temporally. Figure 5.4 shows all of the unwrapped interferograms in the Ciloto landslide area. The estimation of the SCLA or DEM error and the phase ramp were subtracted from the phase unwrapped. The range of SCLA error varied from -14.2 m to 13.25 m but most PS scatters found near to the Ciloto region were not affected by this great DEM error. There are 19858 SDFP selected pixels in total and 1455 PS or 727 PS/km^2 specific to the Ciloto region. Unfortunately, we could not detect any PS in the middle of the study area since it is mostly covered by vegetation (from agricultural land use). Due to the lack of spatial distribution and the low density in middle-resolution (30 x 30)m, we can not identify the translational movement clearly that occurred at that location (Sadarviana et al., 2014).

The mean velocity of 1-2 cm/year occurred on the top of the study area as shown in Figure 5.5.a where the land use is mostly for the rural area. The PS density for this specific location is 210 PS for 0.54 km^2 where the high way, buildings, telephone and electricity pylons, and bare rocks exist.

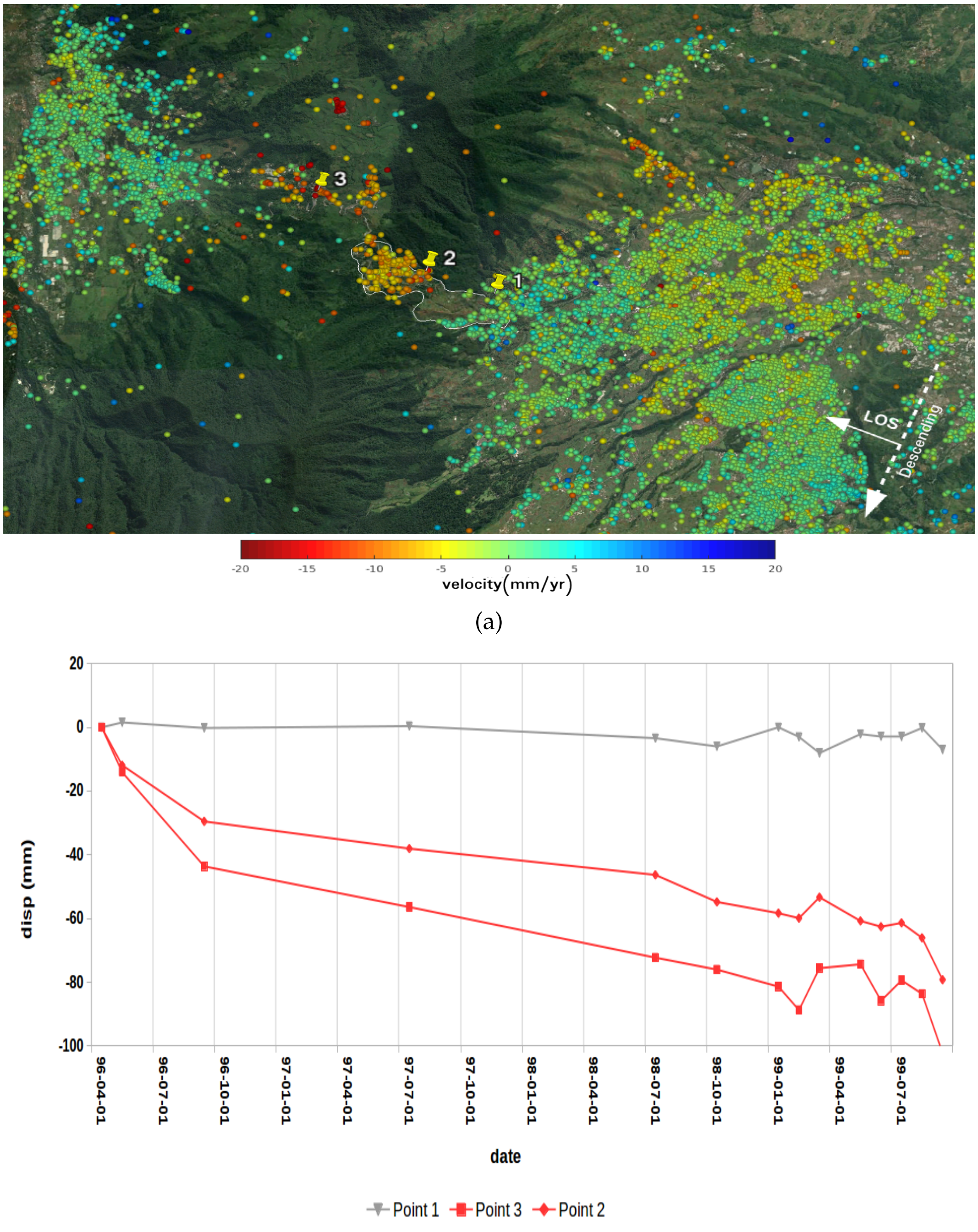

(a)

(b)

FIGURE 5.5: (a) LOS mean velocity ERS1/2 SB-SDFP result with the overlay on optical image from Google Earth (b) sample points of time series SB both on non-stable and stable area

These structures are more appropriate to a proper characteristic of radar scattering than natural terrain. For the time series result, we take 8 sample points with 100 m radius (Figure 5.6.a) to determine the trend displacement. The selected points are located on coordinates; 106.997° longitude and -6.7099° latitude. The location is close to buildings and streets which are characterized as high coherence objects. The mean LOS displacement value of 8 selected PS points can be seen in Figure 5.6.b. One time series point is identified as noise due to a large deviation from other time

TABLE 5.2: The optimized parameters in SB-SDFP processing for Ciloto area

Step	Parameter	Value
Identifying PS	DEM	SRTM
	Max DEM error	10
	Filter grid size	25
	CLAP α	0.5
Selecting PS	Spatial density	4
Weeding PS	Weed time windows	365
Phase correction	Merge resample size	50
Phase unwrapping	Unwrap grid size	50
	Unwrap time win	365
	Unwrap goldstein filter	0.4

series points. The observation from April 1996 to July 1998 detects a very slow displacement of about 1.4 cm/year.

Nonetheless, we still question to SB time series result between acquisition September 1996 and July 1998 which has only one SAR scene (07.06.1997) to connect the SB configuration for master and slave. The Doppler centroid (f_{DC} for 19960929; 19970706; 19980725 scenes = -801.87; -825.59; -469.11) of this acquisition times are also relative great which affect the quality of coherence and make these two pairs have the low signal noise ratio (SNR). We force to keep them because there are no other better chances to connect the configuration without using them. The trend of displacement for three years appears moving linearly with an exception during the dry season the displacement looks stable (Figure 5.6.c).

There is no PS point found in the middle study area as shown in Figure 5.5.a. However, the landslide and ground movement have frequently occurred in that region reported by BPBD [1] since 1984. Based on the displacement rate on the top study area, it belongs to very slow movement (Cruden et al., 1993) that could form creep and scarp on the local surface. Unfortunately, we could not compare the LOS deformation SB result in a terrestrial geodetic campaign held by PVMBG[2] due to a different geographic location of measurement.

We then estimate uncertainty in our SB result to the stable area located on the relatively flat surface and showing a high coherence signal as well (Reference area: 107.01° - 107.02° Longitude; -6.73° - -6.72° Latitude). The decision to use the location as a reference area is according to the class of the risk ground movement map produced by PVMBG, 2016. This location is categorized as one of the lowest risk areas for ground movement considering geologic and lithology conditions. Moreover, it is close to the prone landslide study area in order to avoid a different atmospheric artifact. The standard deviation of a selected point on the reference area is 3.8 mm/year. Namely, it is the estimation error value due to noise term for the sample of stable points. The high error could be propagated by time series inversion since if we see only for the time-dependent signal, it is not a constraint of specific form (Schmidt et al., 2003). In principle, even though the precision of InSAR measurement can be on the order of millimeters, the SB-SDFP result varies in precision due to various errors caused by uncorrelated atmospheric effect, noise and ground surface condition. Hence, in the future, we need to use an external source from weather data to those errors primarily related to a tropospheric error in a mountainous area.

---

[1] Regional Board for Disaster Management, West Java

[2] Centre of Volcanology and Geological Hazard Mitigation

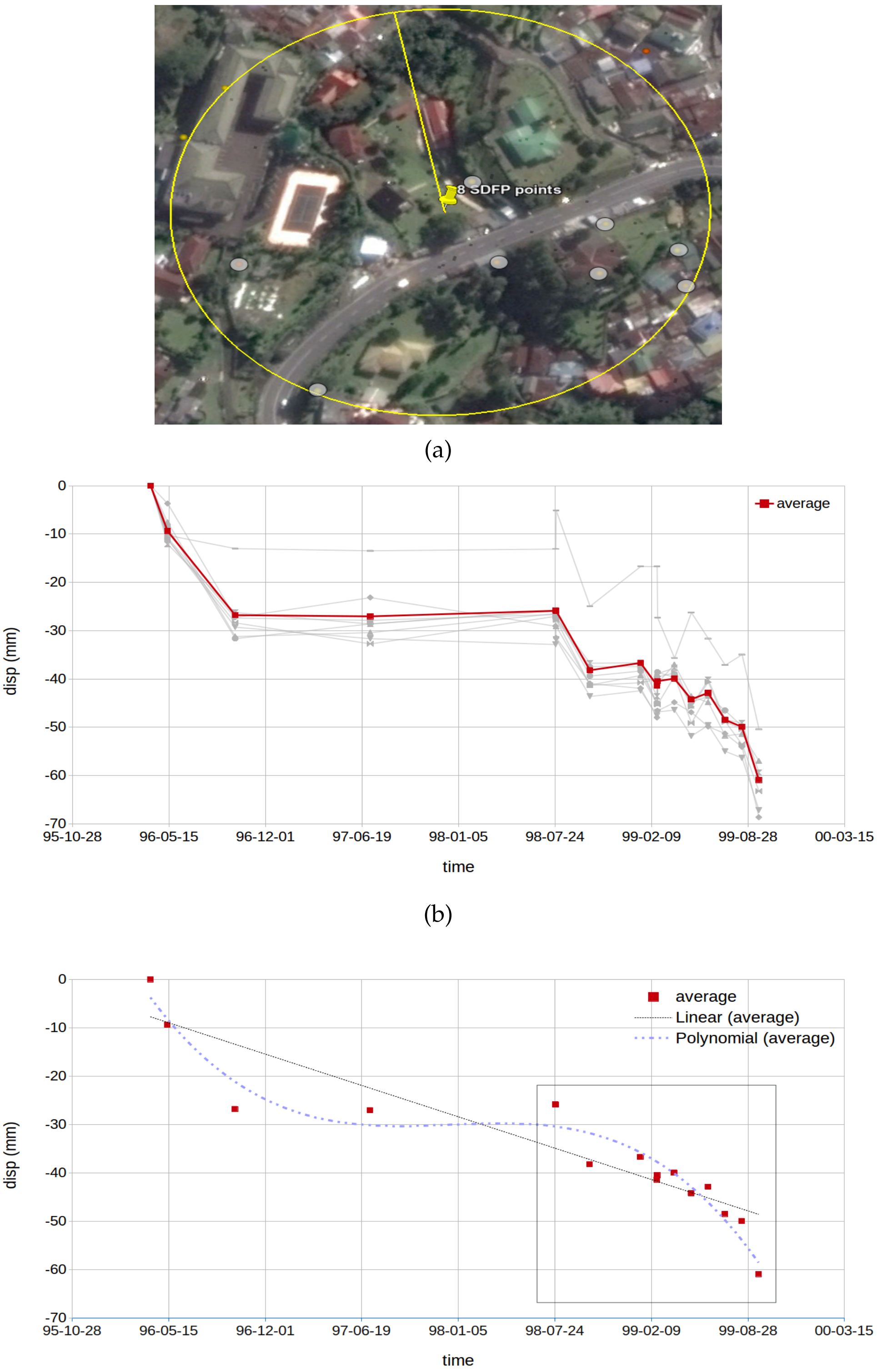

(a)

(b)

(c)

FIGURE 5.6: (a) An example of PS selected point 2 shown in Figure 5.5.a (b) SB time series from April 1996 to September 1999 (c) the linear (R^2=0.82) and polynomial (R^2=0.94) displacement model for 3 years, in which the standard deviation error is larger in the linear model than in the polynomial model.

5.2 ALOS PALSAR L-Band Data (2007 - 2009)

The SAR imagery analyzed in this study consists of 13 ascending ALOS PALSAR data sets both in Fine Beam Single (FBS) and Fine Beam Double (FBD) polarization collected between January 2007 and February 2009. The L-Band operates at a wavelength of 23.6 cm with a revisiting time of 46 days and the incidence angle approximately 38 degrees. The advantage of L-Band data is able to partially penetrate through vegetation cover reaching the ground surface. The characteristic of the ALOS sensor is suitable for the Ciloto case study where mostly the area is used as the agriculture and residential (rural) areas. Nevertheless, some parts of Ciloto are suffered for high decorrelated since the wavelength is unable to penetrate through dense vegetation adequately.

5.2.1 Configuration of Interferograms

We did the pre-processing step for ALOS data named as *focusing* because the collected data were in RAW format. FBD images were oversampled to the pixel spacing of the FBS images. A multi-look factor of 15 (3 pixels in range and 5 pixels in azimuth directions) was applied to generate InSAR images at a spatial resolution of 30 m in both directions. We selected 36 interferograms from track 437 as seen in Table 5.3 and Figure 5.7. We set the parameters of temporal and perpendicular baseline to a maximum of 365 days and 1300 m. There were three interferograms which over than 1000 m but the decorrelation's threshold is still far away (less than 10%) from the critical baseline of ALOS which is 6.5 km for the FBD2FBD and 13 km for the FBS2FBS over a flat area (Lu, 2007; Sandwell et al., 2008). A shorter baseline must be used for measuring deformation in purpose to avoid errors due to inaccurate topographic phase in the interferometric pairs. Hence, the threshold is 1/10 of critical baseline giving $\sim$ 1300 m. All of the interferograms were generated using DORIS and continuously exported to StaMPS for the SB-SDFP processing.

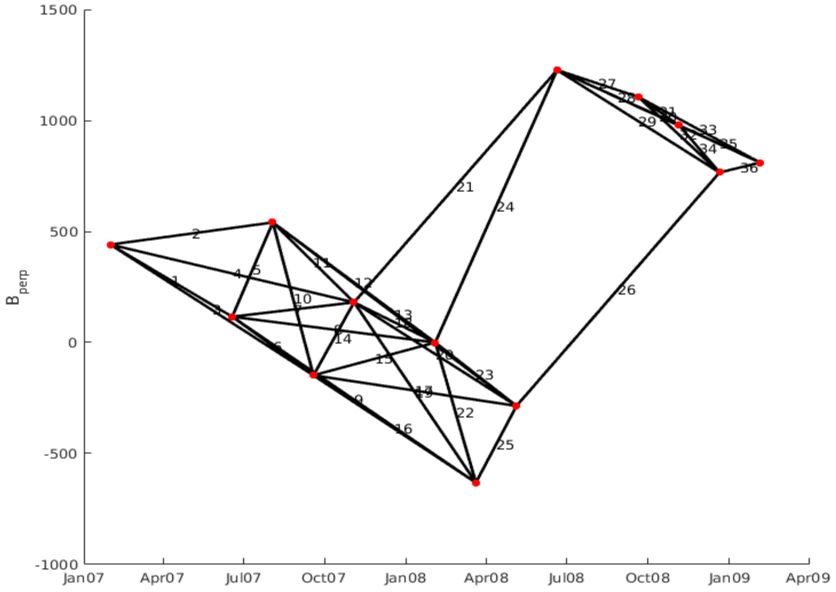

FIGURE 5.7: The SB configuration for ALOS PALSAR data sets

TABLE 5.3: ALOS PALSAR interferometric pairs

No	Master	Slave	Days	$\perp$Baseline(m)
1	20070131	20070618	138	-325
2	20070131	20070803	184	100
3	20070131	20070918	230	-589
4	20070131	20071103	276	-260
5	20070618	20070803	46	425
6	20070618	20070918	92	-264
7	20070618	20071103	138	65
8	20070618	20080203	230	-116
9	20070618	20080320	276	-747
10	20070803	20070918	46	-689
11	20070803	20071103	92	-360
12	20070803	20080203	184	-541
13	20070803	20080505	276	-826
14	20070918	20071103	46	329
15	20070918	20080203	138	148
16	20070918	20080320	184	-483
17	20070918	20080505	230	-138
18	20071103	20080203	92	-181
19	20071103	20080320	138	-812
20	20071103	20080505	184	-466
21	20071103	20080620	230	1047
22	20080203	20080320	46	-631
23	20080203	20080505	92	-286
24	20080203	20080620	138	1227
25	20080320	20080505	46	346
26	20080505	20081221	230	1051
27	20080620	20080920	92	-121
28	20080620	20081105	138	-248
29	20080620	20081221	184	-462
30	20080620	20090205	230	-417
31	20080920	20081105	46	-127
32	20080920	20081221	92	-340
33	20080920	20090205	228	-296
34	20081105	20081221	46	-213
35	20081105	20090205	92	-169
36	20081221	20090205	46	44

5.2.2 The LOS Displacement Result

We obtain the displacement rate map in the LOS direction over the Ciloto area shown in Figure 5.8.a. A total of 24504 points are identified in ROI, covering an area of 536 km^2 from the Cianjur to the Cikabuyutan regency. The scale legend is approximately from -54.5 to 48.8 mm/year. Strong phase difference signals are found in some areas. They are located at Cibulao and Cisarua-Sukawangi Village in the Sukamakmur region. We suspect these discoveries whether they are caused by deformation or unwanted noise such as atmospheric effect. PVMBG classified those areas as the zone of the high-risk landslide. Furthermore, the ground movement occurred on 12th November 2017 in Sukamakmur and it was reported by the local news that three houses were heavily damaged, seven houses were slightly damaged, and 5 Ha harvest area was destroyed. Even though the local authority confirmed that there was a ground movement event, a detail investigation should be done in the future especially to clarify that there is no effect of SAR geometry distortion. To prove no distortion effect, the slope geometry should be, at least, less than 38° considering the general ALOS look angle value.

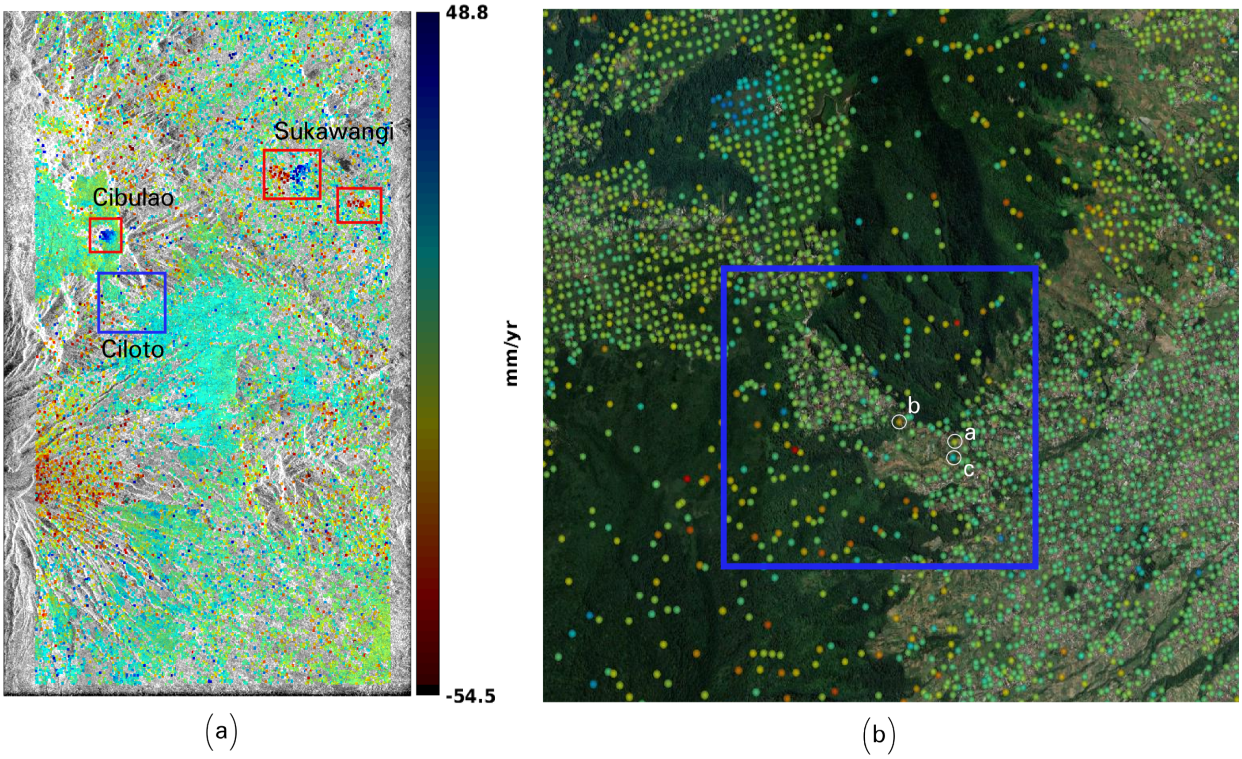

(a) (b)

FIGURE 5.8: a) Spatial Distribution of Landslide Deformation in Ciloto and its surrounding based on ALOS PALSAR processing superimposed on the mean amplitude images. b) The sample distribution of PSs in Ciloto. The points of a, b , and c are located on 107.007°; -6.714°, 107.002°; -6.712°, 107.006°; -6.715°, respectively.

The rate displacement in Ciloto is considered a very slow movement and mostly the observed points are relatively stable. The mean velocity for a whole scene in Ciloto (623 number of PSs) is about 4 mm/year. However, we found high number values (> 10 mm/year) at Puncak Highway as seen in Figure 5.8.b. Point a and b are located near to local houses and plants field whereas point c places on an open field near to Puncak-Bogor Street. Figure 5.9 shows the time series displacements detected in those areas. The mean velocities of points a, b, and c are -11.3, -25.6, and 26.7 mm/year, respectively. The detected motion from January 2007 to February 2009 cumulatively moved -34 mm, -68 mm (LOS change far from the satellite) and 51 mm (LOS change near to the satellite), respectively. The high pixel values found on a steep hill with dense vegetation cover are not considered as deformation signals since decorrelation might be leaked on the final PS processing.

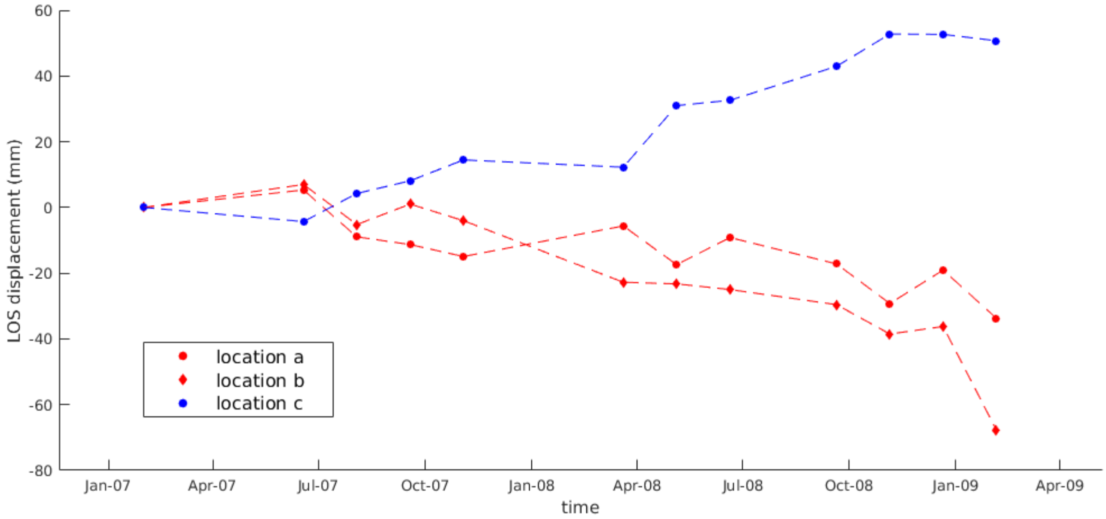

FIGURE 5.9: Time series displacement generated from ALOS PALSAR data sets from 2007 to 2009.

The highlight observation area for the Ciloto is the Puncak Pass and the Puncak Highway region. Using ALOS data sets for only two years and limited images, PS point is not detected in the Puncak Pass since the low temporal sampling of ALOS is impossible to determine the time lag at a finer temporal resolution. A few points near to the location are interpreted as stable with the mean velocity of 1.6 mm/year.

It is challenging to evaluate ERS1/2 and ALOS PALSAR result in term of showing a complex spatial pattern of motion because of the significant changes in the soil surface state, local morphology, and the vegetation inducing changes of the ground scattering properties between two consecutive image acquisitions (Schlögel et al., 2015). Moreover, ERS and ALOS PALSAR available data are limited only in one orbit preventing a complete geometrical analysis of slope movement. The next section will describe the assessment of Sentinel-1 in more detail than their previous SAR sensors due to its accessible data both in ascending and descending orbit.

5.3 Sentinel-1 C-Band Data (2014 - 2018)

5.3.1 Small Baseline Interferograms

We processed Sentinel-1 data from October 2014 until June 2018 for the ascending orbit and from November 2014 until June 2018 for the descending orbit. 341 and 349 interferograms were generated among the duration of SAR acquisitions with the threshold 100 days and 100 m for the temporal and spatial baseline as described in Figure 5.10. Since the slope aspect of the Ciloto region is mostly facing southeastern direction, ascending data are more suitable for SAR interferometry, but the use of descending data is yet acceptable because the slope aspects are not straightly facing east. Moreover, (Colesanti et al., 2006) on the assessment of suitability SAR data for the recognition of geological features through SAR image interpretation described that the steepest slope less than 67°, which the average incidence angle Sentinel-1 images in this area are 50° - 56°, does not have shadow effect and could be interpreted.

We generated the interferograms in full resolution using GMTSAR (Sandwell et al., 2011) and modified the result to be suitable for StaMPS format. Firstly, the SLC images were filtered using Gauss 5x5 windows in order to get the amplitude and preserve the spatial relationship between

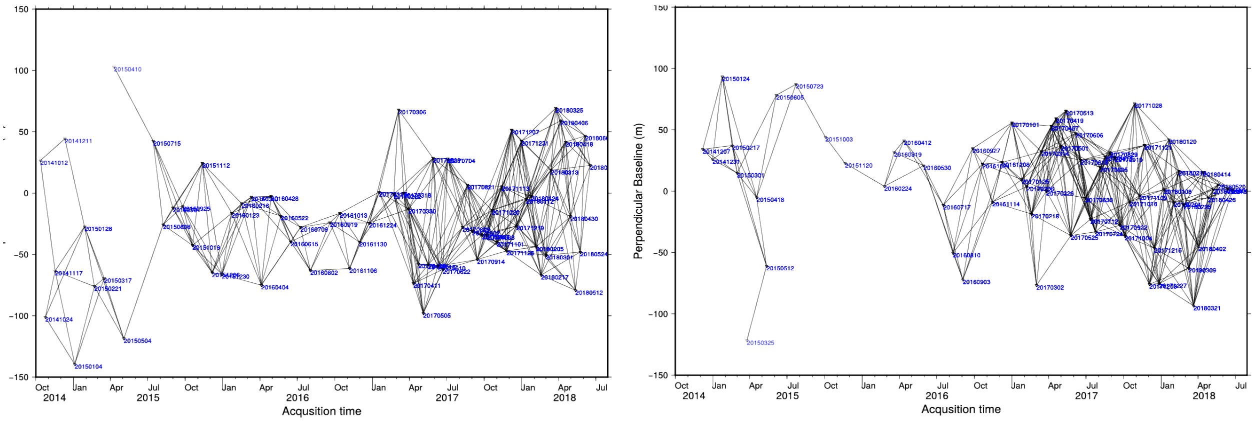

(a)

(b)

FIGURE 5.10: SB Configuration for Sentinel-1 a) ascending and b) descending orbits.

pixels. Furthermore, we calibrated each image by a weighting factor calculated from the ratio between the amplitude of each SAR image and the mean amplitude for whole set images (Lyons et al., 2003). We then calculated the amplitude difference dispersion with the same algorithm from (Ferretti et al., 2001) and (Hooper, 2008) as an indication of phase stability $(D_{\Delta A} = \frac{\sigma_{\Delta A}}{\mu_A})$ using the ratio between the mean amplitude for all master-slave pairs and the standard deviation of the difference of amplitudes. This selection of phase stability candidates was performed to reduce a big computational process for many master-slave configurations. The land use of the Ciloto area is the rural and agriculture area. Thus, most of the areas covered by heavy vegetation are decorrelated. Considering this issue, we arranged the threshold of amplitude difference dispersion to 0.5 value. Figure 5.11 describes the distribution of amplitude difference dispersion in both ascending and descending orbit. The scale bar is interpreted as; a) the value near to 0 indicating good phase stability; b) the value near to 1 indicating a low chance to be included as PS candidate. Furthermore, all of the generated interferograms were corrected using the power-law phase-based method as described in Chapter 4 (Isya et al., 2018) and processed by the SB-SDFP algorithm to identify PSs through small baseline networks.

5.3.2 The LOS Displacement Result

Figure 5.12 presents the final result of LOS time series displacements. We take samples of displacement located at the crown of Puncak-Bogor highway landslide where the previous research using GPS observation from 2002 to 2005 was conducted (Sadarviana, 2006). The trend is not straightly moving linear showing an indication of the precipitation influence regarding a greater shift in the rainy season. We discuss more the correlation between the motion and local weather in the next section. The InSAR result shows the displacements moves slower about -2 to 1 cm/year than GPS result which in certain locations could be up to -10 cm/year for the vertical and 1-25 cm/year for the horizontal motion. Furthermore, Sumaryono et al., 2015 continuously monitored the area in 2012 which describes the movement at the crown landslide's body increased from -0.3 to -2.24 cm for a vertical shift while the horizontal still moved up to 11 cm to southeast direction. Meanwhile, at the toe area, the horizontal motion was 1.32 to 13.62 cm and the dominant vertical shift from 0.19 to 21.89 cm. Since the shift movement at each benchmark had variation in motion, this GPS data indicated that the movement was formed by "multiple sliding surfaces". We can not find any reliable PS scatters at the toe since the area is used for horticulture covered by heavy vegetation causing the signal decorrelated easily. Therefore, for our processing result, we could not figure out the up-shift location and make it difficult to estimate the shear strain.

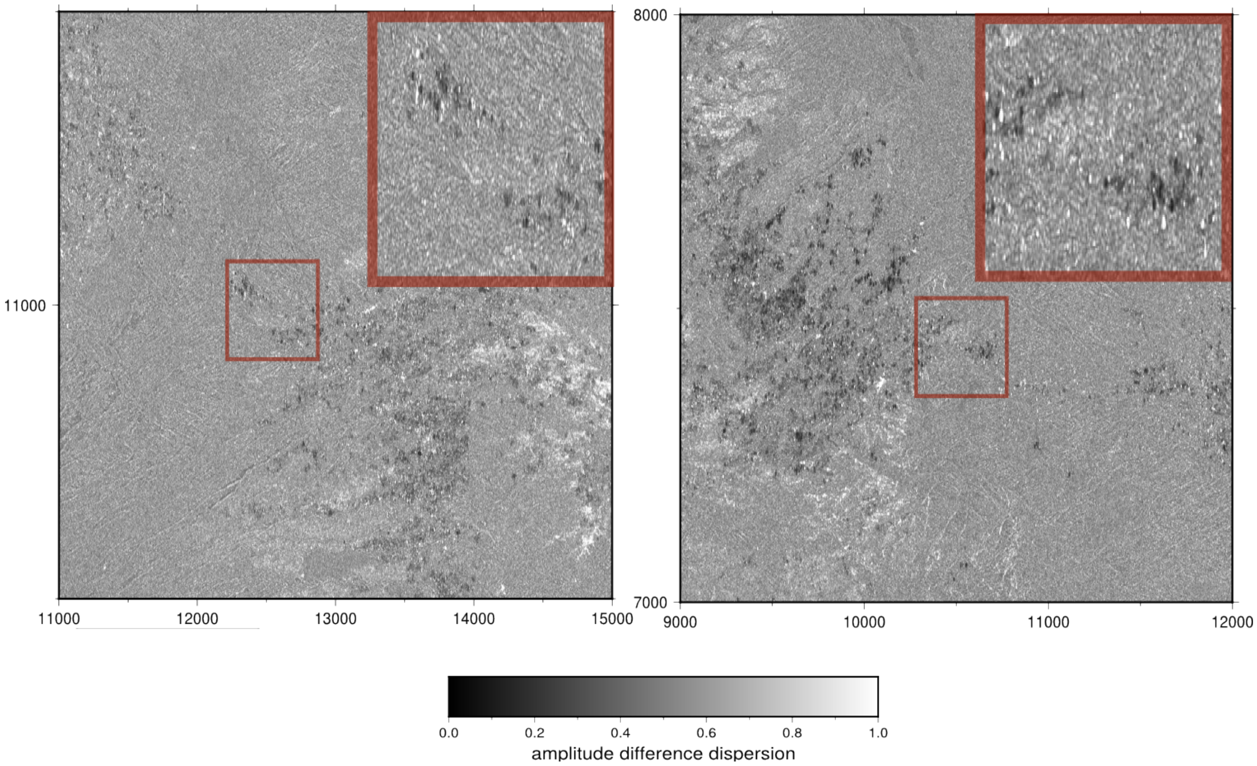

FIGURE 5.11: The scatters of amplitude difference dispersion for the ascending (left image) and descending (right image) data. The darker scale color, the higher PS candidates are selected.

Slope Geometry and Extensometer

We generally define the phase-change detection in Ciloto categorized as the extremely slow movement (Varnes, 1978) which agrees to the installed extensometer (0.7 cm/year) located on the southern part of Puncak Pass resort's hall. As noted, not all of the observed area shows extremely slow motions but a high rate displacement (cm to m unit) also exist in some regions proved by crack found on houses located on Kampung Puncak RT.6. However, we cannot detect this high rate of landslide's velocity classes due to a limit of the phase sensitivity. Moreover, we could not use the amplitude-based method as well due to the low spatial resolution hardly implemented in a small area and strongly influenced by the decorrelated signal due to dense vegetation area.

Before our result is compared to independent ground truth data, we identify it firstly whether the location of scatters is convenient in terms of detecting potential persistent scatterers based on the effect of topography on the SAR images or not. The R-Index developed by Notti et al., 2014 was calculated on each PS point selected by the SDFP algorithm. All topography effects will be presented using the ratio between the slant range as a radar geometry distance and the ground range as the earth surface distance described in Figure 5. 13 both for the ascending and the descending data. There are four main R-Index (RI) classes, which are; (1) RI$\leq$ 0 is expected to have layover, foreshortening, and shadow effects which the PSs are totally not detected; (2) 0 $<$ RI $<$ 0.3 which the location is possible to detect a few PSs; (3) 0.3 $<$ RI $<$ 0.5, the rate detection of PS is from the low to middle level, and; (4) RI $>$ 0.5 is an adequate topography and located in slopes with a good orientation to the satellite. The classes only take into account for the SAR geometry to the local topography but not for the land use. Therefore, the third and fourth classes are not totally indicating the area having a high PS distribution since the "green" land use, such as agriculture, will reduce the number of phase stability.

Considering PS scatter samples around the extensometer location (the black dots in Figure

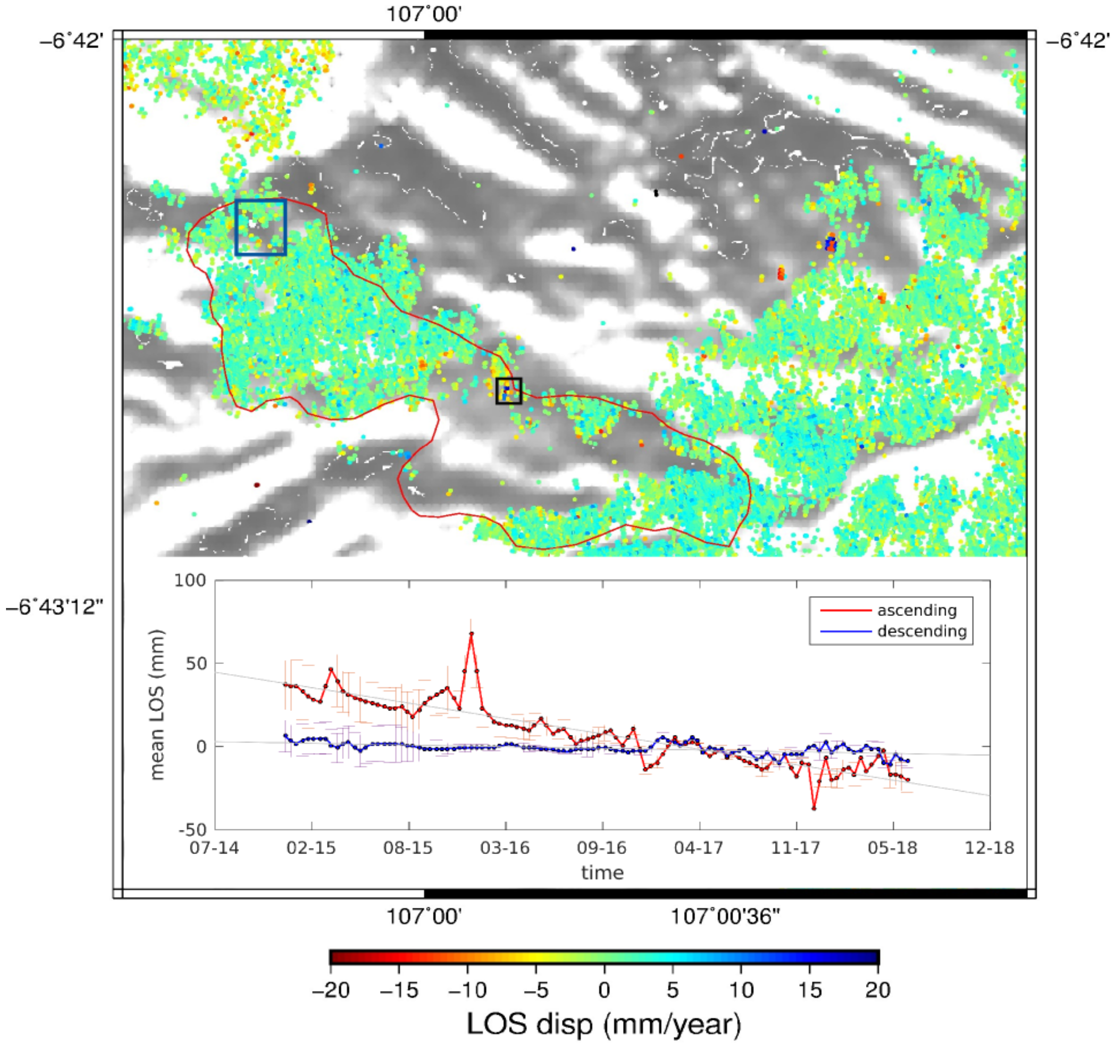

FIGURE 5.12: LOS displacement both ascending and descending data in which the black rectangle indicates a sample of time series movement (the bottom graphic) located at the Puncak-Bogor highway landslide. The blue rectangle presents the Puncak Pass landslide area which the graphic of time series is shown in Figure 5.15.b.

5.13), both orbits are categorized as the fourth class RI which is suitable to process SAR on a different look angle view from either the ascending or the descending Sentinel-1 data. The mean RI values for both tracks are 0.82 and 0.71, respectively. Since the main Ciloto region is facing south-east, the ascending SAR images are adequate to preserve good amplitude and phase stability (Colesanti et al., 2006). It is agree to the RI which shows the ascending having greater value than the descending data. The $C_{ascending}$ shows positive values for the slope aspect 90-180^{o} ($\approx$ east-south direction), which means the movement is mostly registered with no reverse direction. Hence, we use ascending data to validate the time series displacements to extensometer data (see Chapter 4.3).

The extensometer is located at the southeastern Puncak Pass Resort. We could not find any PS point both from the ascending and the descending SAR data due to the place covered by heavy vegetation. Nevertheless, some PS points from the ascending data are found at the village (houses) near to the location. They are compared to extensometer data in purpose at least to figure out whether the rate displacements both of them have a similar trend or not.

V_{slope} (V_{LOS}/C) is computed by the ratio between LOS velocity and the percentage of real detected movement (C) (see the formula on (Notti et al., 2014)). Figure 5.14 shows that neither V_{slope}

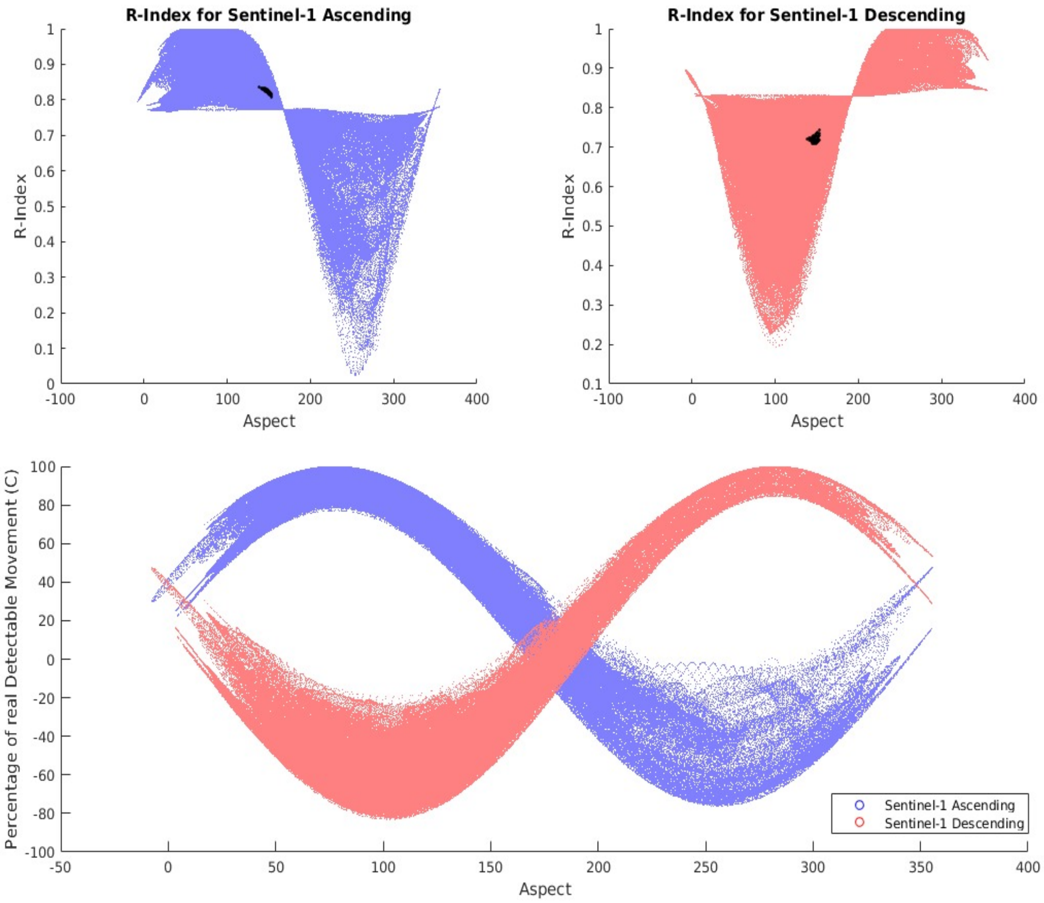

FIGURE 5.13: R-Index (top) represents the ratio between the slant range and ground range. The R-index describes the possibility of topography effect in the Ciloto area looked at by the ascending and descending tracks. The black dots locate to the area around the extensometer location. The bottom picture shows the percentage of real detected movement which is used as a coefficient to calculate the velocity projected along the slope (V_{slope}) assuming the landslide movement parallel to the slope.

ascending nor descending data have a similar trend to recorded extensometer data. However, the rate of displacement of the extensometer from October 2015 until February 2017 is close to the LOS displacement values. We do not validate quantitatively between the ground observation and InSAR result because of a different spatial location and a geometry perspective. The V_{slope} is calculated assuming that the movement is parallel to the slope and has planar slides (translational slide). Therefore, we realize that V_{slope} could be overestimated and not reliably presented the movement behavior since PVMBG and (Sugalang, 1993) classified as a compound slide which progressing indefinitely slowly (identified as a creep) but periodically generating rotational slides, fractures, and slumps. Overcoming the biased perspective using only one look-view (either LOS or planar-slope), we aim to understand more the ground movement behavior in Ciloto by generating 3D vectors displacement in the next chapter.

The Post Processing Time Series Analysis

We processed Sentinel-1 both the ascending and the descending from 11th December 2014 to 17th June 2018. Considering the noise and any anomaly through processing data, we did a post-processing procedure to avoid an incorrectly-estimated deformation model and to improve the

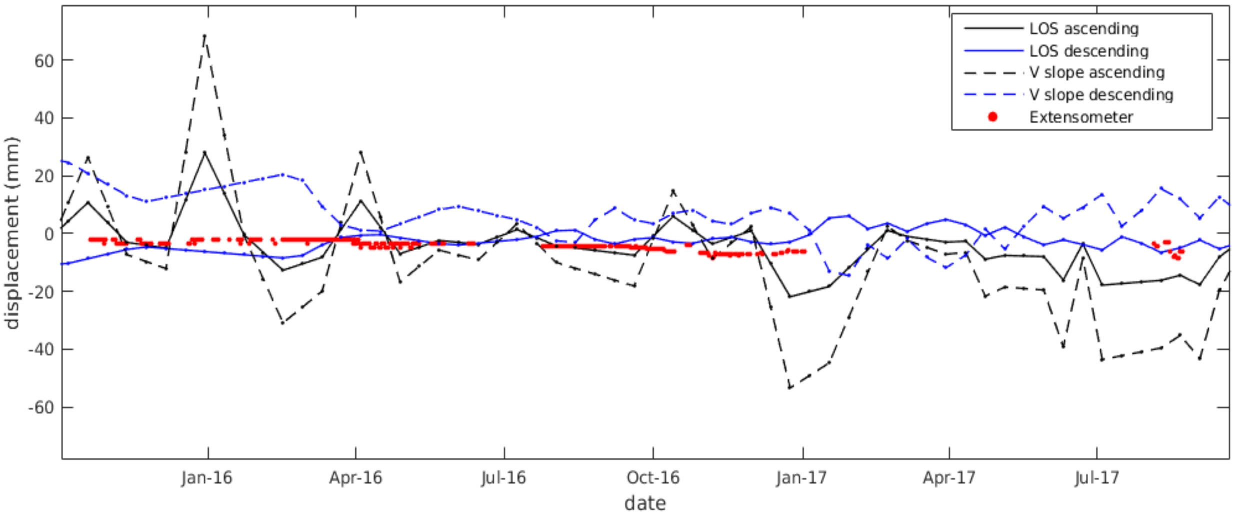

FIGURE 5.14: The comparison between extensometer, LOS and V_{slope} ascending data. PS scatters are located at -6.707933° - -6.707348 ; 106.995259° - 106.995680° while the extensometer at -6.707306° ; 106.994972°. The spatial difference between of them is 60 m since there is no scatters found at the exact location of the extensometer.

quality of InSAR data and correct possible errors especially near to the event of material's collapse in Puncak Pass. The method has been carried out by Notti et al., 2015 improving time series analysis in the landslide case study. We take into account three corrections, which are: 1) removing noise and regional trends, 2) detect and correct possible phase unwrapping errors, and 3) averaging time series.

Firstly, presuming the stratified tropospheric phase screen is only corrected the systematics component delay and yet remaining noise signal due to errors in data processing and undefined effect from the local geological process. We recognized and corrected the regional trends on ascending data identified by a selected stable area (107.014030° - 107.015197° ; -6.728465° - -6.726994°) with the high coherence sampling > 0.8. It is located on the flat terrain used as a residential area where there is no record of ground motion with the LOS average velocity ± 2.5 mm/year. We chose this sample outside the Ciloto district since the region of interest are mostly classified for either the middle or high rate ground movement. Figure 5.15.a shows the regional trend that we subtract on the LOS ascending result. As noted, the LOS descending result remains original since we do not find any significant regional trend in the stable area. Moreover, the average rate displacement of the descending result is smaller than of the ascending since there is a limitation of slope view on the descending line of sight as shown by the R-Index values. Removing a regional trend in the descending data may consequently change the real displacement value at the prone landslide area.

The possibility of phase unwrapping error due to more than a quarter of the radar wavelength motion could highly occur between two successive acquisitions (Crosetto et al., 2010) especially for a landslide study case which a rapid or sudden movement is mostly occurring several months, weeks or days before the collapse of slope failure. We applied the empirical method suggested by (Notti et al., 2015) at the Puncak Pass landslide area. We add a deviation value of ±5mm for the detection of phase ambiguity since the observed region is relatively covered by dense vegetation making it more difficult to find whether it is the real signal or local noise. This correction could be applied only for one unwrapping error and has to be validated with external source data such as local weather and ground survey measurement. The tool is limited to only one unwrapping error. Hence, if the tool finds a high absolute difference of displacement (more than + 14 mm ± 5 mm or less than - 14 mm ± 5 mm) between two consecutive acquisitions, it might be an indication of the

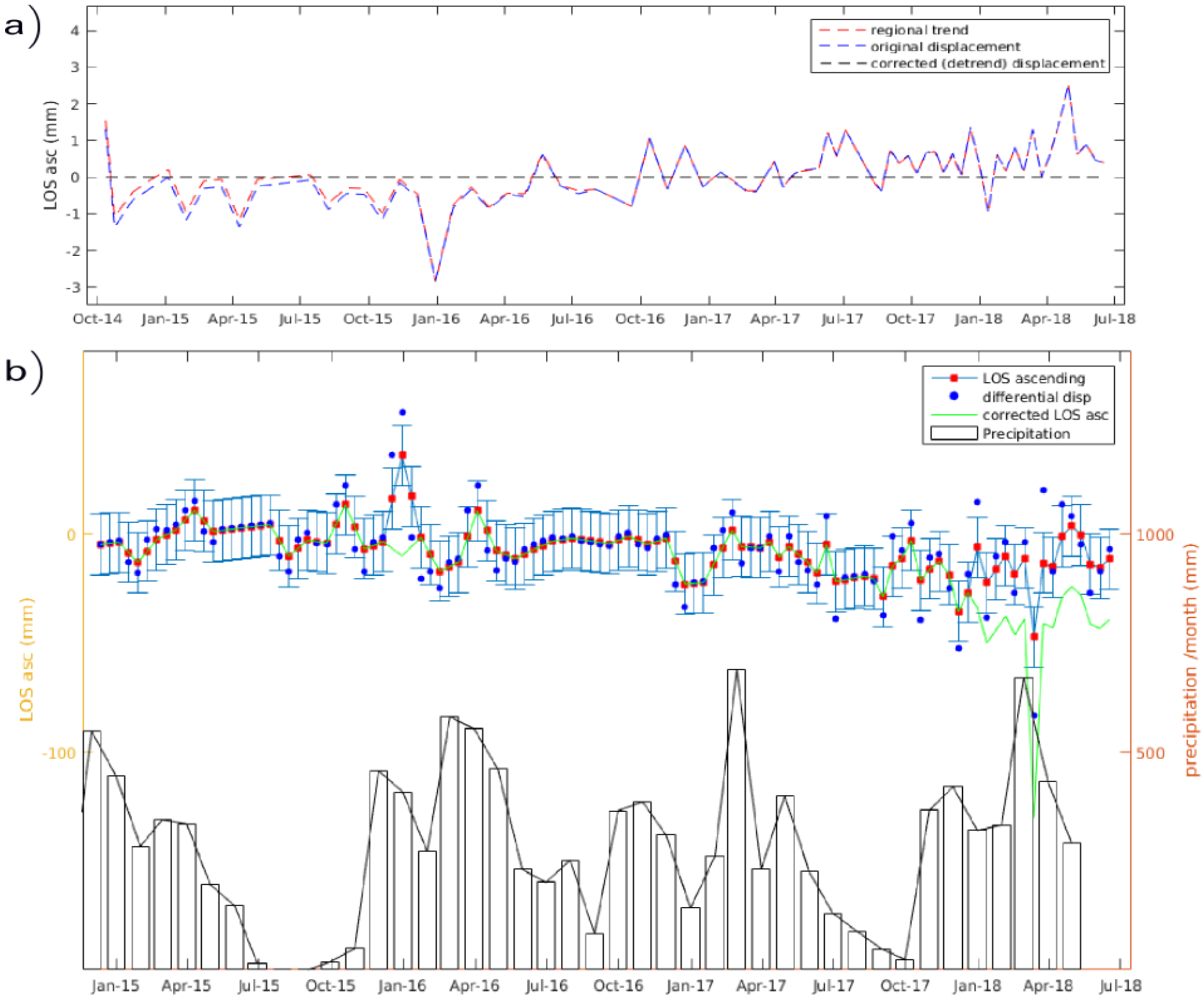

FIGURE 5.15: a) a corrected unwrapped result based on the calculated regional trend placed at stable area b) The standard time series with its error bars $\pm\lambda/4$, the blue dots represent the differential displacement between two consecutive acquisition. The corrected unwrapped error will be applied if the differential displacement (the blue dots) exceeds or outside TS error bars $|\ \lambda/4|$. The PS points are located on the top of Puncak Pass area.

break time because of the landslide collapse.

The graphic of time series displacement located at the Puncak Pass as shown in Figure 5.15.b explains trend displacements before and after the unwrapped error correction. The correction is successfully identifying both the downward motion at the crown body and the up-lift placed at the deposit zone near to the Puncak Pass resort building. A high anomaly signal has been found between 13 March and 06 April 2018. Considering the absolute difference more than 14 mm ± 5 mm, we notice this breakpoint as the range time of landslide reportedly occurred on 28 March 2018 by BPBD.

5.4 The Evaluation of Time Series Deformation From Multi-band SAR Data

We evaluate the characteristic of ground motion for long periods (1996-2018) using the time series InSAR result of multi-temporal ERS1/2, ALOS PALSAR and Sentinel-1 product. In particular, the data quality is not equivalent to compare the estimated velocity, since ERS1/2 and ALOS PALSAR results have limited numbers of interferograms. It decreases the coverage of ground points due to phase decorrelation in temporal and spatial. The number of PS for ERS1/2 descending, ALOS PALSAR ascending, Sentinel-1 ascending, and Sentinel-1 descending are 461: 426: 14037: 12918 points, respectively. The number of PS points generated by ERS and ALOS data are enormously less than by Sentinel-1 in the region of interest. Their correlations to each other are compared for 77 matching PS points in all regular grid (Fig. 5.17.a). The result shows that between ERS1/2 and ALOS points have the highest spatial correlation of 0.5328 than other correlated data. It means that both of those data are spatially distributed at a similar difference rate of movement. Meanwhile, there is no good correlation for Sentinel-1 points to other data. For the sample matching locations, we consider that their accelerations have become slower since 2007 because the rate of displacement decreases from -20 mm/year to -10 mm/year. Regarding the variation of the phase value, the mean of PS points is -7.3 for ERS data, 4.9 for ALOS data, 1.5 & -0.1 for Sentinel-1 ascending and descending data. However, the ERS result might have a high bias in the final deformation result due to the atmospheric phase delay.

We describe the deformation results generated by different geodetic measurements. To interpret them easier, we draw a profile line with its section for $\sim$ 30 m. Figure 5.16 shows a profile from point A (106.99°; -6.71°) to B (107.01°; -6.72°) which covers the Puncak Pass and the Puncak Highway area. Its line is starting from higher, 1400 m, to the lower elevation, 1200 m. We emphasize the dashed line box as the location for GPS and terrestrial measurement described in Chapter 2. The SAR data were resampled using the nearest-neighbor function with the radius of 30 m to register PS points in the regular grid. Thus, the tracking points based on the A-B profile are arranged in the same spatial resolution.

Furthermore, Figure 5.17 shows the mean velocity distribution in the Ciloto district produced by InSAR and ground measurements and the relationships of the different multi-band and temporal InSAR results. The profile length is ca. 2.8 km. We divide the section into 51 parts with their width 275 m from the ridge. The rate displacement from each observation has a different velocity. The reason are; a) their differences in temporal and spatial resolution, b) non-identical objects of observation, c) different wavelength sensor and data quantity in spaceborne monitoring, d) different geometry view and e) unlike sources of error.

The range of displacement rate generally is -20 to 20 mm/year. However, some parts have great movements especially for the location in Puncak Highway. ERS1/2 shows the highest displacement rate until -20 mm/year located at the top Ciloto area whereas the bottom part is relative stable, 1-4 mm/year from 1996 until 1999. Because the number of interferograms is limited and there is a long temporal baseline in 1997, the result might overprint to other signals such as atmospheric effect and noise due to error processing especially in co-registration and phase unwrapping. The mean velocity from 2007 until 2009 is $\pm$10 mm/year manifested by ALOS PALSAR. Nevertheless, a few PS points are detecting high downward motion to -25 mm/year found at the upper Puncak Highway area. The result from Sentinel-1 processing shows that the mean velocity is $\pm$10 mm/year. However, we found some regions have velocities >$\pm$10 mm/year. They are mostly located in the Puncak Highway area as well.

According to ground measurement points in the Puncak Highway area, we projected GPS and terrestrial vectors displacement (d_U, d_E, d_N) into LOS direction using the average incidence and azimuth angle from Sentinel-1 ascending sensor. We applied the computation into ascending SAR

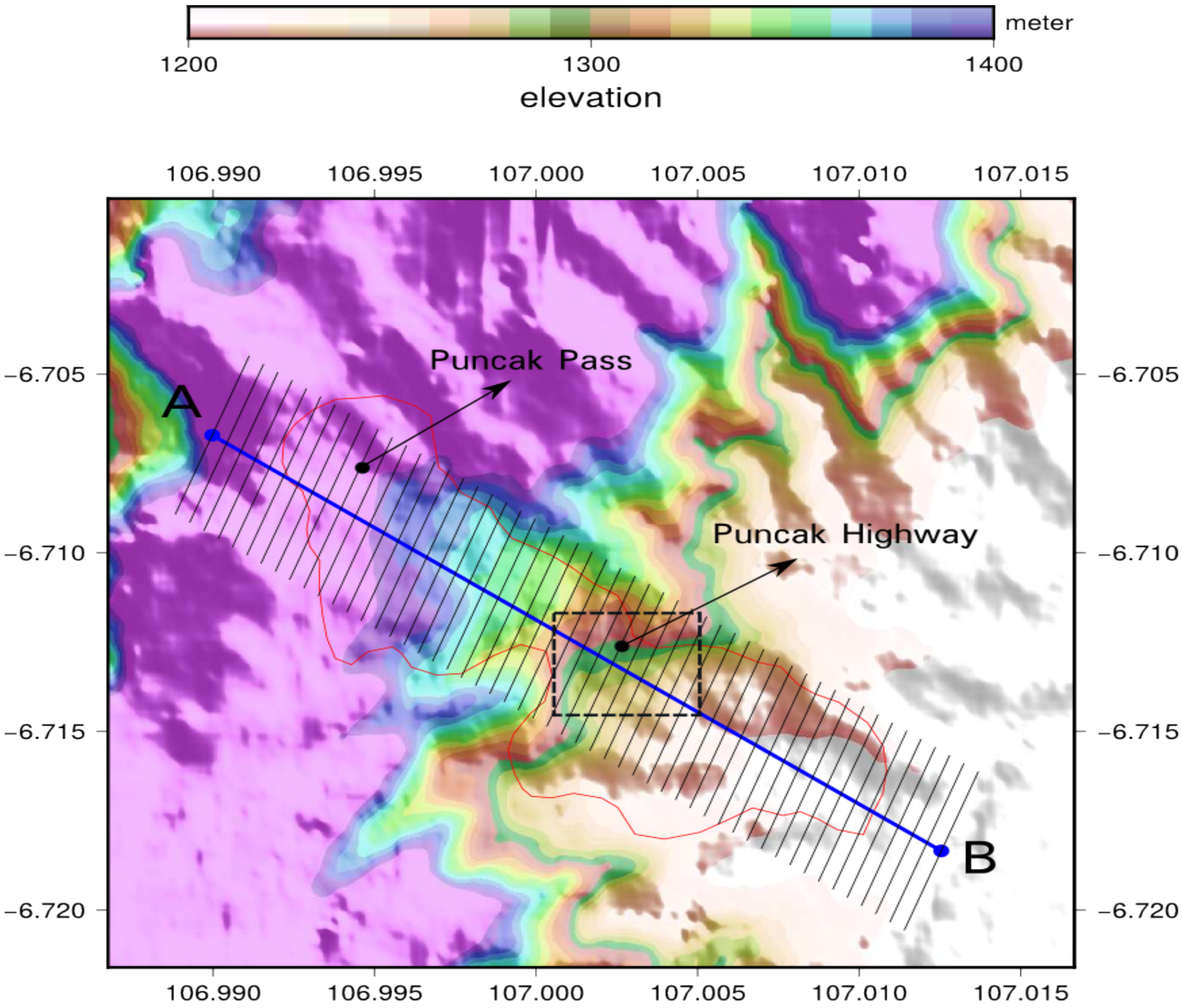

FIGURE 5.16: Ciloto area along the A-B profile which its sections are covering the deformation result as shown in Figure 5.17.b

data because the R-Index calculation revealed a better performance in the ascending orbit considering the characteristic of Ciloto slope. Although a few terrestrial benchmarks are in the range of ±10 mm/year, the rests have different high rates maximum to -95 mm/year. An important note, the terrestrial points show high rates of movement since they were located on the precarious positions along CiJimber River. PVMBG informed that erosion and ground movement intently occurred. Moreover, the technical surveying report explained that there was an accidental event and this factor was beyond the control of the surveyor. Furthermore, the displacement rate from GPS analysis is similar to InSAR results especially for ALOS and Sentinel-1 sensors. GPS2, GPS9, GP11 and GP14 moved 11.1, 20.9, -15.4 and -27.9 mm/year, respectively. Other GPS points have the mean velocity <±10 mm/year.

We found displacement rates for 3 GPS points valid from 2002 to 2005 regarding the location of ALOS and Sentinel-1 scatters as shown in Table 5.4. They have a high correlation to the ALOS result acquired from 2007 to 2009 which is covering a similar period of time. However, the GPS result does not fit to the displacement rate determined by Sentinel-1 (2014-2018) or the ERS data (1996-1999). This can be explained by the non-linearity of the slope movement triggered by physical events. For the extensometer recorded in 2016-2017, the mean velocity is -7.6 mm/year assumed as a linear movement. The displacement rate of the extensometer is slightly faster than the

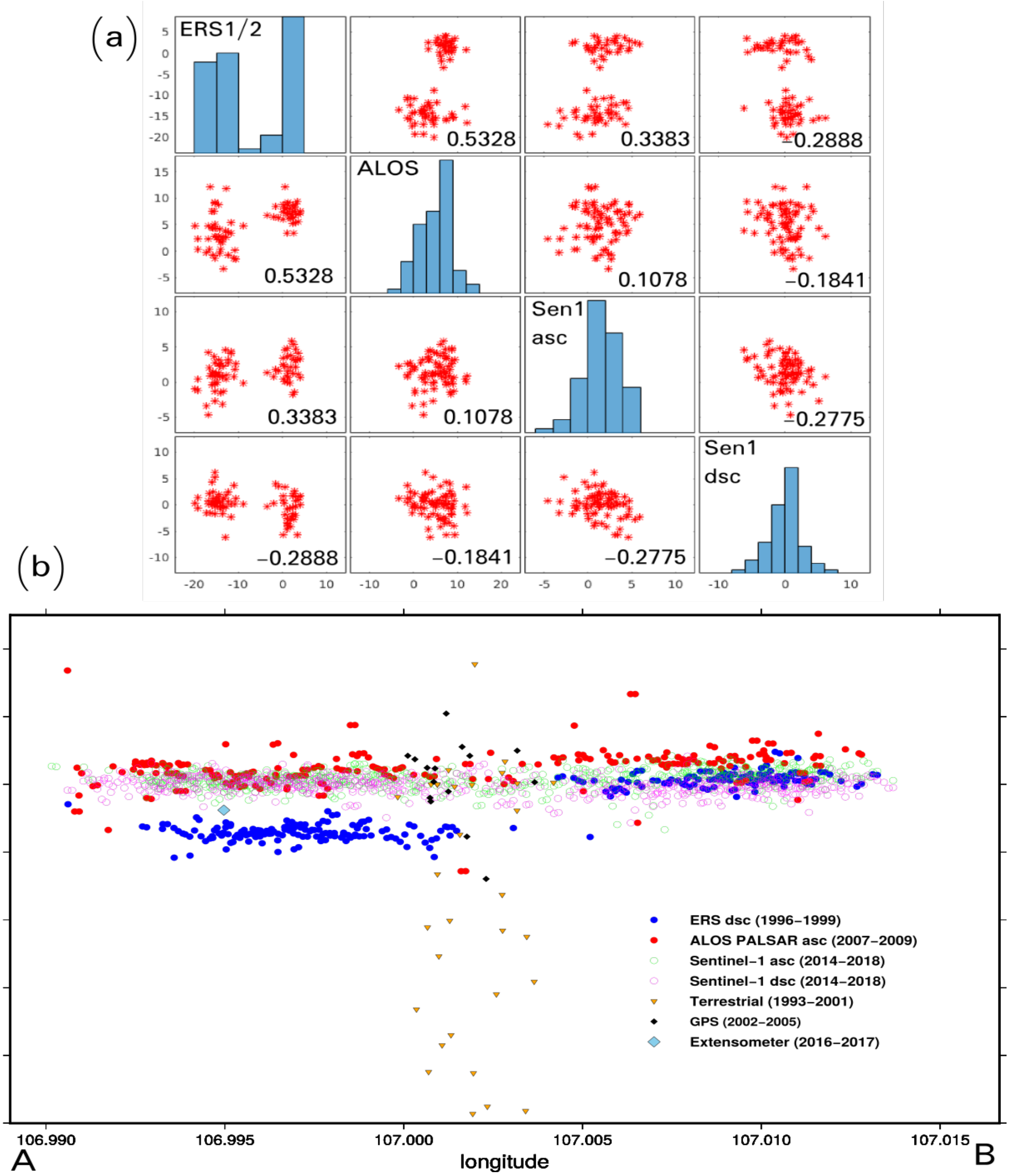

FIGURE 5.17: a) Correlation matrix between SAR data for 77 samples matching grid. b) The distribution scatters of mean velocities from all geodetic observations in Ciloto area.

Sentinel-1 result. However, as discussed in Chapter 3., the time series trend displacement between them shows a high correlation.

For both main focus areas, Puncak Pass and Puncak Highway, sufficient PS points are only found in Sentinel-1 processing. The previous sensors are suffered by decorrelation and make it unachievable to retain the time series evolution for long term periods and the whole ROI. However, near to Ciawi-Cianjur Street and Bumi Aki Restaurant, a few PSs have been detected on 3 SAR sensors. Jl. (street) Ciawi-Cianjur, which is a part of upper Puncak Highway, is located in the middle of ROI. It is a national highway connecting Jakarta and Bandung, two of Indonesia's

TABLE 5.4: The mean velocity (mm/year) of ALOS, Sentinel-1, and GPS measurement

Point	GPS	ALOS	Sen-1 Asc	Sen-1 dsc
1	8.12	2.84	-0.32	2
2	8.45	1.59	1.39	3.89
3	9.95	6.01	-0.34	-2.54

major cities. The detected deformation signal on the location cannot be neglected because it has continuously moved until present.

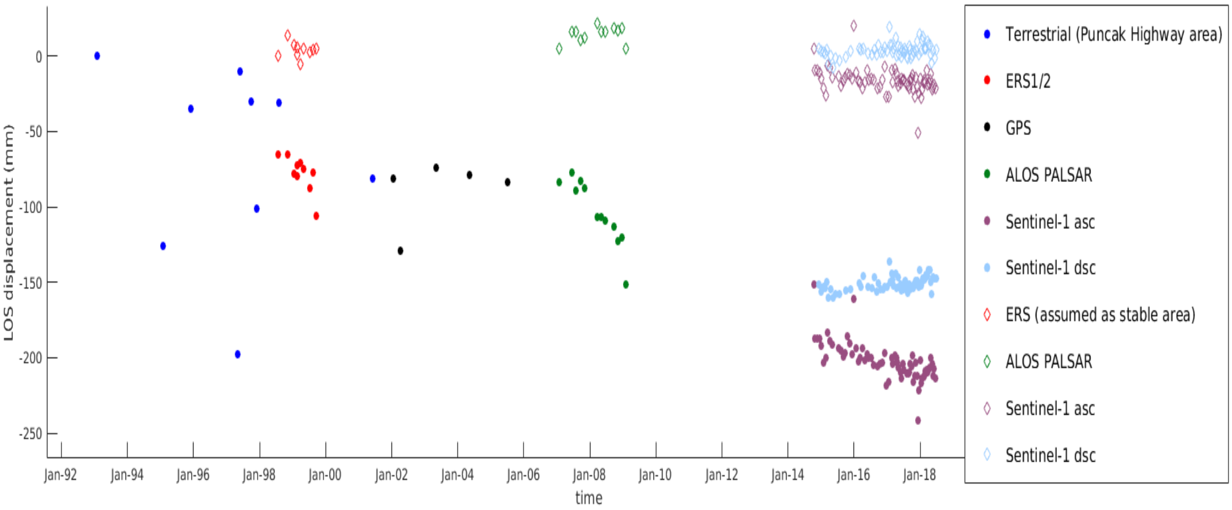

FIGURE 5.18: The time series evolution for 25 years (not considered unobserved dates) in the upper part of Puncak Highway which the location refers to the dashed box of Figure 5.16

Based on the above location, we assess time series displacements provided by all geodetic measurements as shown in Figure 5.18. Since their spatial and temporal distributions are different, we take the points nearby the location and calculate the average values of the selected points from each observation. The size area is ca. 10,000 m^2 located on 107.0015°; -6.7123°. Three points from the terrestrial survey are identified, M7, M8, and M9 while there are two points observed by GPS measurement, GPS7 and GP14. We found 1, 1, 16, 6 PS points for ERS1/2, ALOS PALSAR, Sentinel-1 ascending and descending data, respectively. We do not count GP14 in assessment because there was partly unrecorded GPS signal during surveying time. We found that the region has cumulatively displaced until -24,1 cm for 25 years. All data utilize the relative reference height based on its last displacement value from the previous survey. For terrestrial data, the reference height starts from zero (0). This time series evolution is not considering a possible ground motion that might happen during missing unobserved dates due to unavailable sources from neither ground nor space-borne measurement. If we evaluate unobserved time using an approach displacement model for expected motion, the cumulative movement will be more than -24 cm for 25 years monitoring. Regardless of this issue, the slope movement detection generated by all geodetic tools agrees to the ground evidence where on February 2017 small landslide occurred in front of the restaurant which proves that this area is unstable for long periods as shown in Figure 5.19.a with the exact area drawn by the blue rectangle.

Although the Ciloto district classified as the middle- to high-risk ground motion, there are some regions detected in the SAR sensor which tend to be stable. One of the examples is located at Jl. Raya Ciloto Puncak Km.90 placed on south-western of Ciloto, 107.003°; -6.717°. The size of the sample area is 13,200 m^2 (marked by the yellow rectangle in Figure 5.19.a). We detect 7, 4, 247, and 129 PS points from ERS1/2, ALOS PALSAR, Sentinel-1 ascending and descending result, respectively. No ground measurement has been conducted in this location and no official report and news as well about an occurrence of ground movement. The identified PS points in this area could reveal the quantity of SAR processing for each SAR sensor. The average mean velocities and its standard deviation for all distribution scatters are 1.3±1.7, 4.5±1.5, 1.2±2.6, and -1.5±2.6 mm/year, respectively. It shows that ALOS PALSAR processing is the highest possibility of noise effect still left on the final deformation result.

Our experiment confirms the capability of C-Band and L-Band SAR data for the slow-moving landslide assessment. The significant movement in the upper part Puncak Highway is described as both the non-linear and non-uniform displacement. The following are several reasons to consider the movement as a non-linear trend; a) the performance of InSAR and ground measurements depends on many factors such as the quantitative of spatial and temporal resolution, dense vegetation cover and geometric distortion in the mountainous environment, and b) the influence of periodical physical environment, such as creep behavior, ground & surface water and local precipitation, or human intervention, such as the change of land use.

5.5 The Relationship Between The InSAR Result and Ciloto Physical Environment

5.5.1 Precipitation

We exploit the relationship between the InSAR result and precipitation. The purpose is to understand whether slow-moving landslide has a direct relationship to the amount of precipitation or not. We assess the correlation between ERS1/2 result and local precipitation recorded in 5 stations near to Ciloto area. We do not calculate it for ALOS data since there is no official published precipitation data during its acquisition time. Meanwhile, we omit the assessment of the Sentinel-1 result since we will explain in the next chapter separately the relationship between the displacement trend and the rainfall intensity in a 3D vectors perspective.

The ERS1/2 InSAR result from July 1998 to September 1999 was assessed in order to figure out the relationship of slope movement to local weather which commonly the high trigger of a landslide caused by wet seasonal precipitation. The discussion only uses one-year duration densely acquisition scenes characterized by the reasonably high signal to noise ratio. The Ciloto geographic condition belongs to the noisier SAR area observation where the uncertainty of deformation estimate at the corresponding time epochs may exist. Hence, we need to have sufficient interferograms to reduce this effect (Agram et al., 2015).

There are two versions of trend displacements (Fig. 5.20.b) which are; a) the least square inversion calculates the time series deformation for three years (the red line, version 1) and; b) it calculates the time series deformation for only one year (the purple dashed line, version 2). The root means square (RMS) of those is 2.7 mm/year meaning the trend considerably still in a similar pattern. The graphic blue column is an average of rainfall intensity from 1996-1998. The source of weather information was taken from five local stations, which are; 1) SMPK Pacet 2) Pasir Saronge 3) Tri Fasung 4) ATS and 5) Darmaga. All of the stations are located in radius 30 km to the Ciloto area except to Darmaga Climatology Main Station having the distance of 70 km. Regarding the rainy season that usually occurs starting from September to April with a high rainfall intensity 300-350 mm/month, Figure 5.18 shows the downward movement or the phase change moved away from the sensor direction.

Meanwhile, it was relatively stable from May-August (summer or dry season) even though the rainfall intensity was still about 100-150 mm/month. Since we used SAR data for one year only,

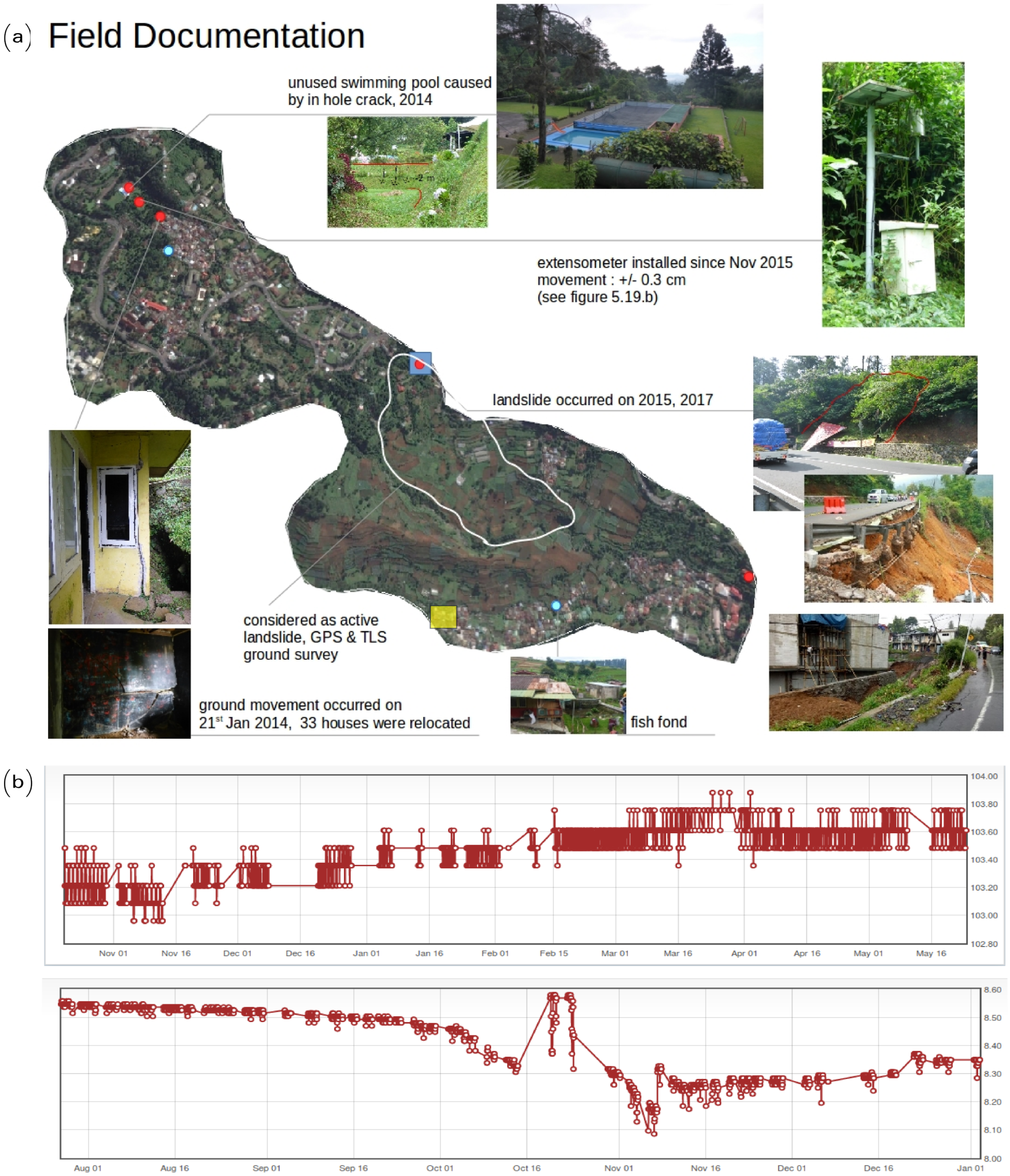

FIGURE 5.19: a) The field documentation in Ciloto conducted in 2017 with the evidence of landslide event in the Puncak Highway area. b) The relative time series displacements based on the extensometer monitoring (source: BPPTKG, 2017).

we could not interpret whether the deformation shows a seasonal oscillation similar to precipitation pattern or not. Moreover, the rainfall distribution is not correct precisely compared to the acquisition dates of SAR data either since it used the mean rainfall from 1996-1998 but missing

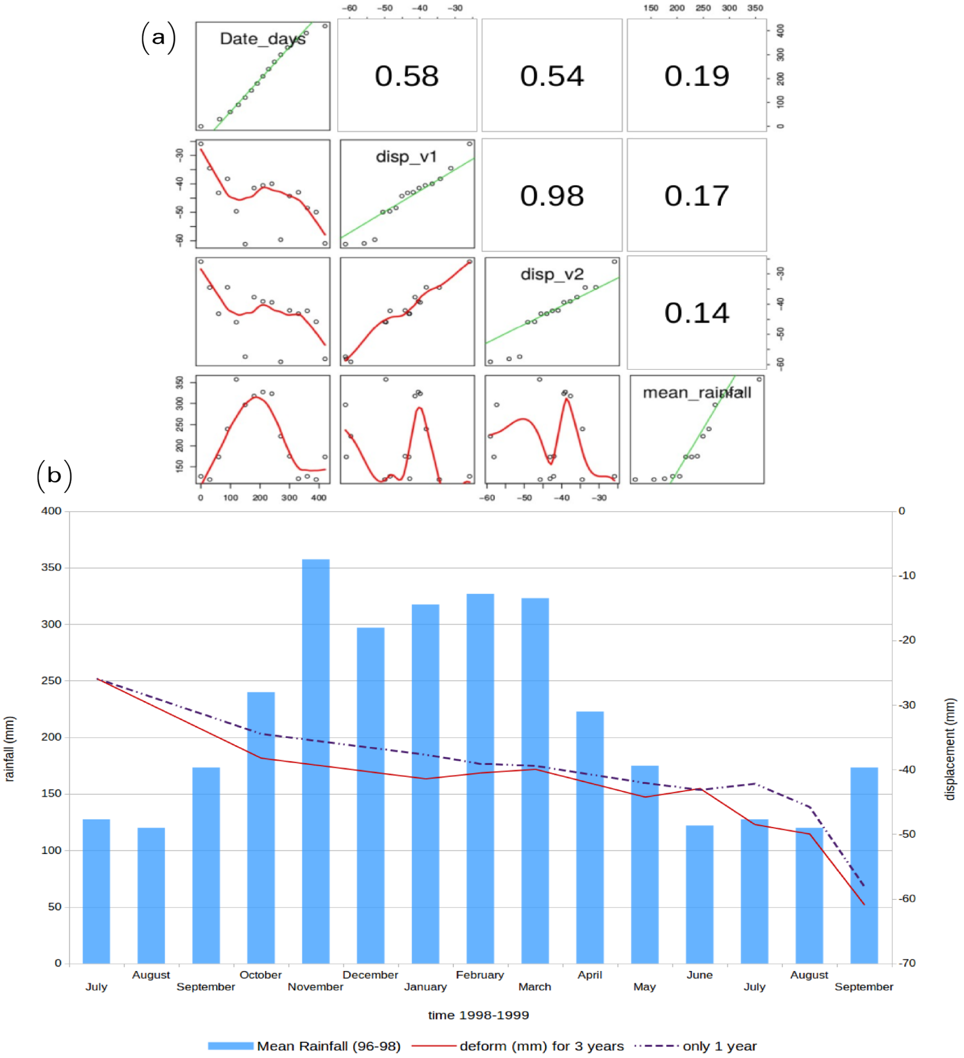

FIGURE 5.20: a) Scatterplot matrix for correlation between LOS displacement and rainfall distribution. b) the comparison between the rainfall intensity and the ERS1/2 LOS displacement. The first version represents the time series adjustment for three years while the second one is calculated only in 1 year (1998-1999).

information in 1999. Figure 5.20 presents the correlation between the ERS1/2 result and the precipitation recorded on local stations near to the Ciloto district. The smoothing panel for displacement and mean rainfall distribution shows high peak points in the same range of period (rainy season) as seen in the bottom left of Figure 5.20.a. Nevertheless, the relation between the landslide and rainfall distribution is not simple as a direct influence from the large amount of precipitation which increases pore pressure and moisture contents in soil (Fetene, 2014). This statement agrees with the Pearson bi-variate correlation method that shows a low correlated value for a direct association between the precipitation and the displacement both version 1 & version 2 with the coefficient correlations 0.17 & 0.14, respectively (see the top right of Figure 5.20.a).

The relationship between the mean precipitation and ERS result evaluates low coefficient correlations since the rainfall distribution commonly has a seasonal oscillation pattern that might be better approached by a polynomial instead of a linear trend. Although the slope failure (landslide) is commonly triggered by heavy rainfall, the very slow movement (a pre-failure process), is related to the complex geological phenomenon. The analysis needs to consider many trigger factors in investigating the slope instability, for instance, soil & rock structures, geological structures, weathering, the landslide history, and the hydrology condition (Abramson et al., 1995).

5.5.2 Physical Structures

The identified area in the upper part of Puncak Pass was measured by Piezometer (see Appendix.A) from 1995 to 2001. Sadarviana, 2006 classified the location as the main body of the landslide. GPS7 and GP14 were in the same position as CP7 in the Piezometer survey. The CP7 point was measured the pore pressure in the depth of -12 m which the lithology soil type was silty sand and silt. The pore water pressure (U), pore water pressure ratio (r_u) and subsurface soil stress (σ_u) of CP7 were 4.095, 4.085, 0.01; 0.42, 0.35, 0.57 ; 9.75, 11.77, 0.02 in January 1995, May 1995, and August 1997, respectively. The higher the pore water pressure, the greater the risk of ground motion. This theory is a part of conclusions from the laboratory investigations held by Ogawa et al., 1987. The landslide, especially for the slow rate displacement, might occur by an increment of pore water pressure at the slip surface.

The relationship between the pore water pressure, subsurface soil stress, and rainfall intensity manifests a non-linear correlation. The precipitation data recorded the increase of rainfall intensity in May - December 2007. During this period, the high precipitation partly influenced the increment of high pore pressure at some piezometer points (CP2, CP5, CP6, CP7, and CP8). However, not all of the measured points were recorded having high pore water pressure and high subsurface soil stress. It means that pore water pressure and subsurface soil stress is not only influenced by rainfall but also other factors such as the soil types in each depth level, the water infiltration flowing from the surface into groundwater runoff and trapped in the catchment, and the human activity.

According to the background of morphology, the Ciloto district lays between the mountain Gunung Lemo and the volcano Gunung Gede. The water coming from those morphologies is accumulated and flows through the area of the Ciloto (Schuler, 2015). Furthermore, considering the hydrology factor, previous research mentioned that there was surface runoff found in the ground movement area (Munarto et al., 2015). The surface runoff depends not only on rainfall intensity but also on other factors; the topography and properties of the catchment, slope gradient and length, vegetation characteristics and soil types. This runoff caused the volcanic breccias layers becoming more saturated and expanding their weight. Consequently, these layers increased their active lateral pressure.

On the other hand, groundwater runoff comes by part of the runoff which passed into the ground or infiltrated to groundwater level through soil pore space. As noted in Sadarviana, 2006, there was a high coefficient correlation, 0.92, between the change of groundwater level and the displacements of GPS points. The trend of displacement might not respond directly to the local rainfall. However, the increment of groundwater level and pore pressure is significantly induced by the local rainfall.

It is a challenge to correlate quantitatively between the InSAR result, the lithology and the hydrology factors in the Ciloto district because of the lack of available *in situ* observation either by the spatial distribution and the period of surveying time. Moreover, the relationship between the time series displacement generated by InSAR (ERS and Sentinel-1 data) and precipitation shows low coefficient correlation values. Therefore, we can not rely only on the rainfall intensity but the physical factors occurred on the surface and the ground to understand the motion's behavior. The critical note, even though landslide occurs mostly when the area has heavy rainfall or constantly rainy in a few days, the time series InSAR result is classified as a very slow movement. The slow-moving material could be interpreted as a creep in which the structure is moving continuously to a particular area. The soil and rock affected by the creep phenomenon might not always lead to the landslide event (the mass movement). However, the creep is well known as a factor of decreasing the shear strength regularly. The acceleration of creep speed will increase when the slope is close to the failure event and makes the steady slide of landslide becoming unstable. The continuous creep movement mostly occurs in the area containing clay material. This identification of creep is suitable to the geological survey of soil types reported by Sumaryono et al., 2015 described in Figure 2.5 and proved by the result of the drilling log observation in Figure 2.4.

5.6 Conclusions of Ground Motion in Ciloto

Based on ERS1/2, ALOS PALSAR and Sentinel-1 processing results, we detect the slow deformation signals in the Ciloto district. Their PS points yield distribute diversely through the area. Since the overlaid PSs from all band SAR data are limited to the upper Puncak Highway area, it is difficult to assess the motion's behavior from 1996 to 2018 for the whole observed are in detail and further inspect to Ciloto's physical factors. As noted, the ERS1/2 outcomes have a high possibility that APS might still exist on the final InSAR analysis. One of the substantiations is that the deformation map produced by ERS1/2 SAR data clearly shows significant subside values for -20 mm/year in the whole top segment of the Ciloto district.

Chapter 5 investigated in detail only for the active landslide areas. The primary object is defining the ground movement manifested both by the Ciloto's environment and the InSAR technique and interpreting the deformation result along with the LOS perspective. The description of landslide inventory, especially for the classification of the states of landslide's activities which are active; suspended; reactivated; inactive; dormant; abandoned; stabilized; and relict, do not demonstrate in our research. The suggestion, however, takes into account the next research to include an automatic classification of the states of landslide's activities based on the InSAR time series analysis for large study areas. Its classification has to meet a conditional sequence of a statistical test. Regarding this development, a prior study by Berti et al., 2013 has been conducted in which the time series PS-InSAR data are classified into distinctive predefined target trends of ground deformation such as uncorrelated, linear, quadratic, bilinear, and discontinuous. Even though the classification of landslide activity was performed by Kalia, 2018 for a mean velocity of deformation at a regional scale, the automatic classification of the states of landslide activities is not yet well-established for the result of time series InSAR.

Chapter 6

The Modelling of 3D-Displacements Using The Ascending and Descending InSAR Data

In Chapter 5, the slope movement is evaluated by LOS-displacement. It is necessary comprehension of the geometry motion in a 3D perspective to evaluate the mechanism of kinematic landslides appropriately. This chapter describes the process and result of estimating the 3D field of slow displacements, implemented on PS-DISP, both from the ascending and the descending InSAR data under the assumption that the horizontal component has a motion parallel to the downhill slope. We applied our method specifically in the Puncak Pass and the Puncak Highway region. The result shows evidence of slow deformation for three years in which two consecutive landslides occurred within the Puncak Pass area in February and March 2018. We investigated the cumulative movement geometrically using the 3D slope aspect method. Notably, we quantified motion in the depleted and accumulated zones. The linear and non-linear relationships between 3D field displacements and precipitation are calculated quantitatively to figure out whether there is a direct correlation between those variables.

6.1 The Generation of The Vertical and Horizontal Component

The spaceborne InSAR technique measures the phase difference in its LOS. It is an insensitive tool for measuring the changing displacement along the north-south direction since most satellite SAR sensors run along near-polar orbits which means the angle between flight direction and north-south axis is a relatively small amount of <12° (Ferretti, 2014). The combination of different orbit particularly can retrieve the vertical and west-east motion. However, it is not possible to generate full displacement only based on two slant-range SAR looking images (ascending and descending orbit).

According to Hanssen, 2001, the LOS projection (d_{LOS}) to d_U for vertical, d_E for west-east and d_N for north-south components is described as

$$d_{LOS} = d_U cos(\theta_{inc}) - sin(\theta_{inc})[(d_N cos(\alpha_h) + d_E sin(\alpha_h)] \tag{6.1}$$

where θ_{inc} is the incidence angle and α_h is the satellite platform heading angle - $3\pi/2$. The computation can use the ordinary least-square (OLS) solution as an inversion of the SAR geometry model. There are some solutions to generate the vertical and horizontal component described in the following methods:

- Retrieving 2D components
  This method decomposes only two components which are vertical and west-east. The retrieve neglects the north-south component. Therefore, the geometric model of d_N is assumed as zero (0). The method is commonly applied if the SAR data are present only in ascending and descending orbit without an acknowledgment of the displacement's characteristic.

$$\begin{bmatrix} cos\theta_{inc_{asc}} & -sin\theta_{inc_{asc}}.sin\alpha_{h_{asc}} \\ cos\theta_{inc_{dsc}} & -sin\theta_{inc_{dsc}}.sin\alpha_{h_{dsc}} \end{bmatrix} \cdot \begin{bmatrix} d_U \\ d_E \end{bmatrix} = \begin{bmatrix} d_{LOS_{asc}} \\ d_{LOS_{dsc}} \end{bmatrix} \tag{6.2}$$

- Retrieving 3D components using along-track information
  The decomposition of full 3D vectors displacement is calculated both from across-track (slant-range) and along-track direction. This method is the best scenario to retrieve the full 3D field. However, the application has a limitation only for the case study by having a high correlated area and an extreme deformation that can be observed in the along-track direction. Some methods to measure the deformation from along-track direction are the azimuth offset (Fialko et al., 2001), Multiple Aperture Interferometry (MAI) (Barbot et al., 2008), and the burst overlap interferometry method (Grandin et al., 2016). In my experimental research, I applied MAI to the Ciloto case study. The result is not fully convincing because, regarding the limited resolution of half the antenna length, slow movement rates can not be detected in the along-track direction.

$$\begin{bmatrix} cos\theta_{inc_{asc}} & -sin\theta_{inc_{asc}}.sin\alpha_{h_{asc}} & sin\theta_{inc_{asc}}.cos\alpha_{h_{asc}} \\ cos\theta_{inc_{dsc}} & -sin\theta_{inc_{dsc}}.sin\alpha_{h_{dsc}} & sin\theta_{inc_{dsc}}.cos\alpha_{h_{dsc}} \\ 0 & sin\alpha_{h_{asc}} & cos\alpha_{h_{asc}} \\ 0 & sin\alpha_{h_{dsc}} & cos\alpha_{h_{dsc}} \end{bmatrix} \cdot \begin{bmatrix} d_U \\ d_E \\ d_N \end{bmatrix} = \begin{bmatrix} d_{LOS_{asc}} \\ d_{LOS_{dsc}} \\ d_{AZI_{asc}} \\ d_{AZI_{dsc}} \end{bmatrix} \tag{6.3}$$

- Retrieving 3D components using many different InSAR tracks or an external observation
  The inversion model could incorporate to either utilizing constraints from the multi-geometry InSAR data fusion (Fuhrmann et al., 2019) or a ground observation which its spatial and temporal resolution is similar or close to the InSAR observation. The external information to retrieve the full 3D field could be taken from additional source data such as GPS observations (Polcari et al., 2016), Ground Radar Measurements (Carlà et al., 2018) or UAVSAR (Handwerger et al., 2019).

- Retrieving 3D components using an assumption
  The movement is assumed as having a movement characteristic in a certain direction. For example, the landslide and the glacier flow monitoring mostly are located in the mountainous area. Their motions have a geophysical behavior moving parallel to the surface (Joughin et al., 1998; Mohr et al., 1998; Sun et al., 2016).

6.1.1 The 3D Slope Aspect

The availability of Sentinel-1 both for ascending and descending at across-track view allows estimating 2D displacement vectors regarding vertical and east-west motions. However, retrieving the 3D deformation components is still challenging for a small rate movement's study because of an insensitivity observed in the along-track direction. Hence, the inversion model needs, at least, one independent observation incorporating from other geodetic data sources to estimate the third component (the north-south direction). Another possibility is to assume the characteristics of displacement whose geometric information is available as a priority (Hu et al., 2014). For the slope movement case, the motion takes into account as its direction towards downslope considering a natural characteristic of a geophysical phenomenon. This assumption was applied to the monitoring of ice-sheet motion (Joughin et al., 1998; Meyer, 2003). We also assume the same for the landslide's motion in Ciloto by having a slope-parallel surface. The north-south motion is suggested as a projection from the west-east component using the angle from the estimated slope aspect as shown in Figure 6.1. The projection only concerns the direction of movement and computes the scalar result as a *pseudo* component.

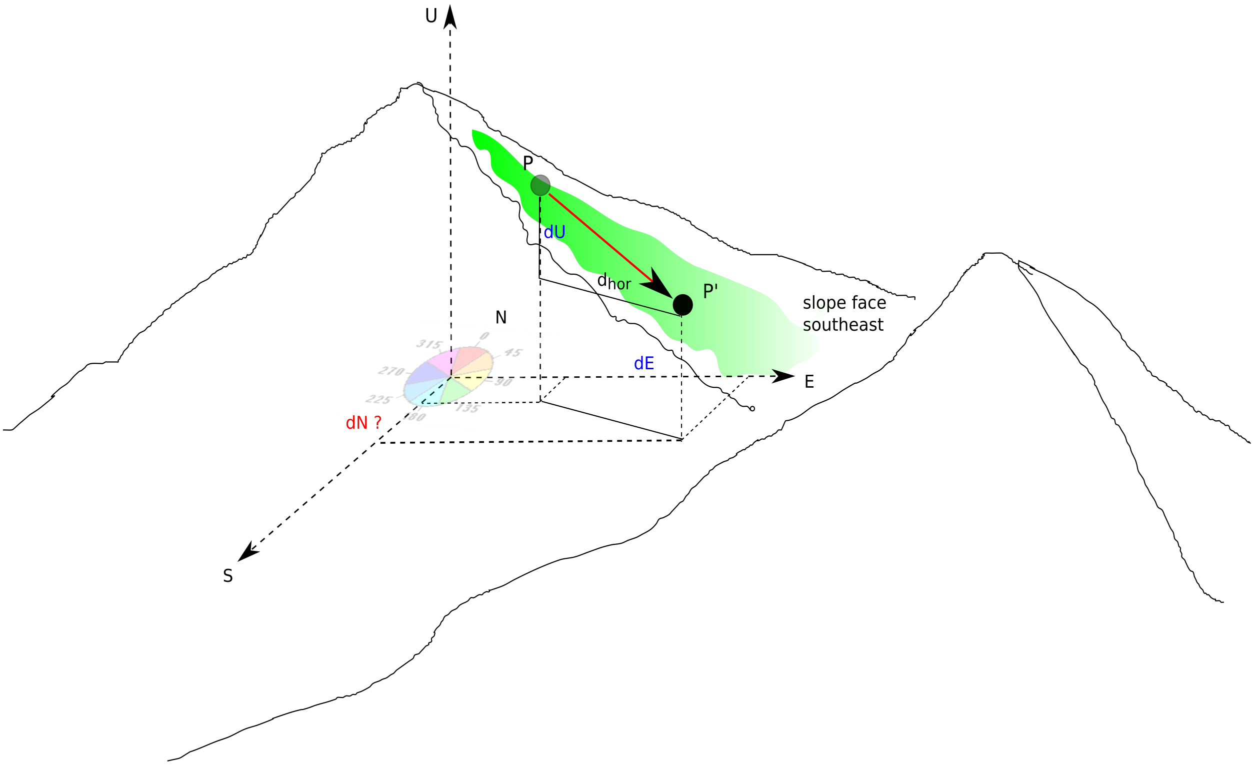

FIGURE 6.1: The illustration of ground movement occurred in a hilly area. The motion takes into account moving parallel to downhill slope direction, the aspect. The values of aspect output cells are the compass direction expressed in the positive degree (0 - 359.9).

Figure 6.1 illustrates that object P is moving down to P'. Regarding 3D coordinate, P is displaced in vertical (d_u) and in horizontal (d_{hor}; d_E,d_N). The relationship between those vectors is related to the slope angle and the slope aspect. For instance, the object of P is located in a hilly area with the slope facing the SE direction. Our assumption is that object P' displaced into the same slope direction which is the southeast also. Since we need to estimate the d_N vector, a simple way is conceding that the horizontal motion moves on the slope direction. d_E could be already inverted by two orbits data. Thus, a projection between d_E and d_N registered on a horizontal field is determined.

The motion direction is taken into account by the aspect slope information. The concept is well known on Geographic Information System (GIS) (Burrough et al., 1998; Huisman et al., 2009). The slope aspects is described as the compass direction, with 0° begin from the north, of this maximal down-slope of slope path (p) as illustrated in the right of Figure 6.2. The calculation of slope aspect could be extracted from an elevation raster (DEM) generated by a high-resolution single/dual-pass satellite interferometry, photogrammetry, or LiDAR . As the neighborhood function seen in the left of Figure 6.2, the finite differencing of 8 neighbors of a cell (but not the cell value itself) is approached to determine the true derivatives $\partial z/\partial x$ and $\partial z/\partial y$ as following

$$\begin{aligned}\frac{\partial z}{\partial x} &= ((z_{1,3} + 2 \times z_{2,3} + z_{3,3}) - (z_{1,1} + 2 \times z_{2,1} + z_{3,1}))/8\partial x \\ \frac{\partial z}{\partial y} &= ((z_{3,1} + 2 \times z_{3,2} + z_{3,3}) - (z_{1,1} + 2 \times z_{1,2} + z_{1,3}))/8\partial y\end{aligned} \tag{6.4}$$

then the slope angle (gradient) and slope aspect are determined to

$$\begin{aligned}gradient &= tan^{-1} = \sqrt{(\tfrac{\partial z}{\partial x})^2 + (\tfrac{\partial z}{\partial x})^2} \\ aspect &= tan^{-1}\left(\frac{\partial z/\partial y}{-\partial z/\partial x}\right)\end{aligned} \tag{6.5}$$

the aspect value is converted to compass direction according to the following rule

- if aspect < 0, the aspect angle = 90 - aspect;
- if aspect > 90, the aspect angle = 360 - aspect + 90;
- if 0 < aspect < 90, the aspect angle = 90 - aspect.

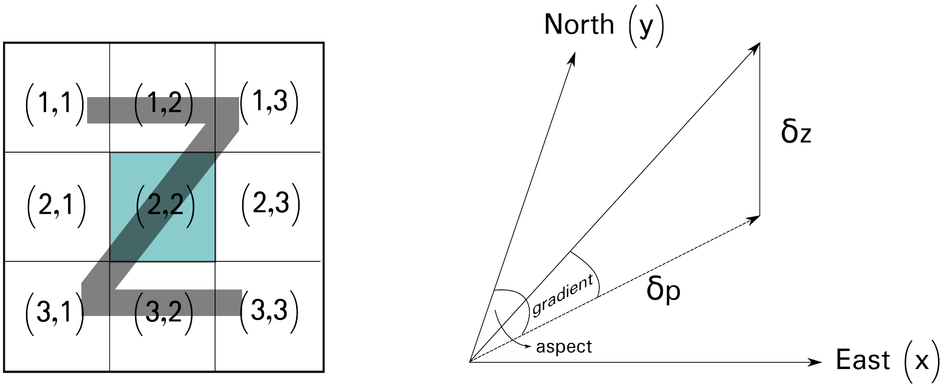

FIGURE 6.2: The definition of slope angle and slope aspect in cell

The aspect value indicates the directions of physical slopes face. Based on the slope aspect angle, the descriptive direction is commonly classified as; flat (-1), north (0 - 22.5), northeast (22.5 - 67.5), east (67.5 - 112-5), southeast (112.5 - 157.5), south (157.5 - 202.5), southwest (202.5 - 247.5), west (247.5 - 292.5), northwest (292.5 - 337.5), and north (337.5 - 360). Originally, we already get two components, vertical and east-west, retrieved by ascending and descending SAR data yet missing one component, the north-south direction. Therefore, the north-south displacement will be suggested as a projection from the west-east component using the slope aspect angle.

6.1.2 Pixel Selection from both Ascending and Descending PS Points

In the beginning, we interpolated the InSAR results in time for the further time series analysis. Since PS scatters from the ascending and descending orbit have different geometric locations, the first step was that we tried to relocate both results using either the surface (Smith et al., 1990) or the nearest-neighbor (Ebdon, 1985) gridding method. The surface function interpolates the irregular space (x,y,z) data to be gridded using *the adjustable tension continuous curvature splines*. The algorithm is an improvement of the minimum-curvature surface (Swain, 1976) that is commonly used in the earth sciences for the gridding method. Meanwhile, the nearest-neighbor function assigns an average value to each node which has at least one or more PS points within a radius centered on the node. The average value is calculated as a weighted mean of the nearest PS point from each sector inside the search radius (Wessel et al., 2019).

The gridded table data produced by the surface function were masked by the location of amplitude difference dispersion (x,y) to control the possibility of distorted interpolation on the non-value scatter pixels location. On the other hand, if we used the nearest-neighbor method, the gridded outcome created new resampled pixels at a certain radius (30 m for this case) and finally selected them with a criterion having values both from ascending and descending data process. Consequently, the number of LOS pixels generated by the surface method was higher than that of the nearest-neighbor method.

6.1.3 The Estimation of dU, dE, and dN by Means of The Inversion Model from InSAR and The Slope Aspect

The next step is estimating vertical (dU) and horizontal (dE, dN) components using a Gauss-Markov model or linear regression analysis. We firstly computed local incidence angles and heading angles based on a master SAR scene used by the earlier co-registration process. The slope aspects were computed from the DEM (i.e., SRTM 30 m) using an algorithm that incorporates the values of the cell's eight neighbors (Burrough et al., 1998). The slope aspect pixels were resampled spatially in purpose to create the similar registration of LOS grids.

Regarding the projection from LOS to ground looking geometry, the 3D vector displacement is approached by the original or ordinary least square (OLS) estimator (Niemeier, 2008). The matrix design in Equation 6.8 for the first and second rows are generated from the decomposition of the displacement vector projected to one slant-range component either viewed by ascending or descending direction (Hanssen, 2001). Meanwhile, the third row is supposed to the characteristic of landslide movement in a hilly area. Because we assumed the northern component having a motion parallel to down-slope direction, we projected the eastward to northward vector employing the slope aspect as the third equation derived by,

$$d_N = r \cdot cos(90 - \theta_{asp}) \tag{6.6}$$

with,

$$r = d_E \cdot cos(\theta_{asp}) \tag{6.7}$$

where θ_{asp} is the aspect angle, d_N and d_E are northern and eastern components, respectively and r is the related projection vector between d_N and d_E.

Furthermore, we estimated d_U, d_E, and d_N using the least square inversion as described in the following equation

$$\begin{bmatrix} cos(\theta_{inc_{asc}}) & -sin(\theta_{inc_{asc}})\, sin(\alpha_{h_{asc}}) & sin(\theta_{inc_{asc}})\, cos(\alpha_{h_{asc}}) \\ cos(\theta_{inc_{dsc}}) & -sin(\theta_{inc_{dsc}})\, sin(\alpha_{h_{dsc}}) & sin(\theta_{inc_{dsc}})\, cos(\alpha_{h_{dsc}}) \\ 0 & cos(\theta_{asp})\, cos(90 - \theta_{asp}) & -1 \end{bmatrix}$$

$$\cdot \begin{bmatrix} d_U \\ d_E \\ d_N \end{bmatrix} = \begin{bmatrix} d_{LOS_{asc}} \\ d_{LOS_{dsc}} \\ 0 \end{bmatrix} \tag{6.8}$$

where θ_{inc} is the incidence angle and α_h is the satellite platform heading angle - $3\pi/2$.

Figure 6.3.a explains the steps to generate the full 3D field with the assumption that the motion moves parallel to the downhill slope. Two options, the surface and the nearest-neighbor gridding method, could be chosen to combine two different tracks of InSAR results in the same regular pixel grids. Furthermore, two LOS measurements and one projection's model are inverted using OLS to retrieve the 3D vectors displacement. The simple projection's model between west-eastern (x axis) and north-southern (y axis) of a horizontal component is described in Figure 6.3.b.

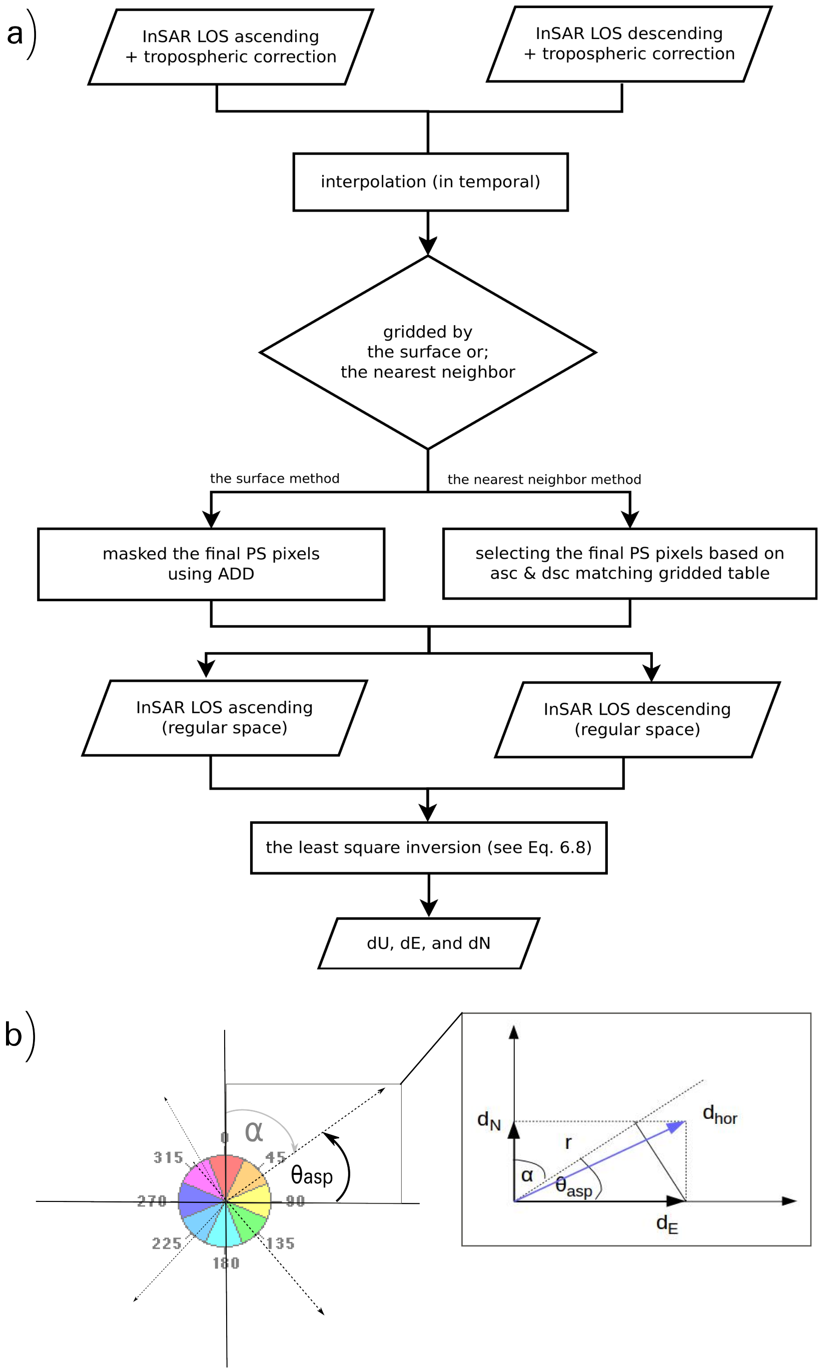

FIGURE 6.3: a) The strategy to estimate 3D vector displacements using InSAR both orbit directions and the slope aspect. b) The assumption of the northern component as a result from the eastern vector projected by aspect information

6.2 The Applications of 3D Estimation Using InSAR and The Slope Aspect Assumption

Landslides have a complex behavior of movement, and in some instances, it is difficult to determine the failure of surface geometry due to the lack of real-time (in-situ) observation. One effective technique to observe the surface's motion, in general, is radar remote sensing. The InSAR time series examination is highly recommended to comprehend Ciloto landslide's behavior. However, one of the limitations of this technology is that the interferometric phase is observed in the slant range direction. This geometry leads to displacement result in the line of sight (LOS) projection. Therefore, a combination of several different geometries is needed to generate three vector components. Two independent observations from different data tracks could fulfill this requirement and determine two vectors, the vertical and the east-west direction (Ferretti, 2014). Because the satellite orbit is close to the polar direction, it makes the detection of deformation insensitive to the north-south-component. To overcome this problem, we assume that in the case of landslide studies, the deformation will point downhill.

This sub-chapter describes the process and result of generating the 3D field of slow displacements both from the ascending and the descending InSAR data under the assumption that the horizontal component has a motion parallel in direction of slope. We applied our method specifically in the Puncak Pass and Puncak Highway region. The result shows evidence of slow deformation for three years which two consecutive landslides occurred within the area in February and March 2018. We investigated the cumulative movement geometrically using our 3D slope aspect method for three years. Notably, we quantified motion in the depleted and accumulated zones.

The Puncak Pass Area

The Puncak Pass area located at the top of the study area is classified by PVMBG as the highest potential ground movement class. This phenomenon mainly occurs due to high precipitation and affects surface and groundwater volumes. Based on the geological report, Clay and sand (weathering soil) with brown to red-brown color was found at the upper part of the Puncak Pass in 1-5 m depth. Meanwhile, the lower part is composed of igneous rocks, primarily breccias (identified as the layer of slip surface) and a mix of sand and clay. These forms are vulnerable to move if the abundance of surface and groundwater is not flowing properly. Moreover, an old movement that occurred in 2014 on the location could be re-activated and stimulate the slope instability.

Two Puncak Pass landslides occurred on Sunday, 4 February and Wednesday, 28 March 2018 after heavy rainfall events. It was located at 6° 42′ 27" S and 106° 59′ 38" E, 1450 - 1500 m above MSL near to the Puncak Pass resort hotel. The landslide has 60° gradient slope with the toe's part about 10°. PVMBG categorizes them into a type of debris slide. The landslide's geometry, for the length, width, and depth from crown to the main body, is 59 m, 50 m, and 25 m, respectively. The landslide's materials moved to the southern direction (N 182° E). The total length from the debris' source to the toe of surface rupture was 101 m. Several factors causing these landslides are; a very steep slope ($\geq 45^o$), strongly porous weathered soil, the weak shear strain due to weathering and water infiltration, a bad drainage system, and high rainfall intensity as the main trigger factor.

Concerning this event, an investigation is necessary to understand the slow movement's behavior quantitatively before these two successive landslides occurred in early 2018. Such information would help to comprehend whether particular motions occurred before the actual event. Thus, a continuous geodetic observation might help to identify possible slope failures in a similar environment and support the precautions. The InSAR technique is one of the solutions to quantify surface changes both in horizontal and vertical directions especially for a motivation to figure out depleted and accumulated landslide's zones.

The Puncak Highway Area

Slump and cracks have been found in the Puncak Highway region since 1984. Based on the previous study by Sulaeman et al., 2013, they discovered the crown of landslide with the length and height of slump 0.6-7 m and 0.3-1.9 m, respectively. The type of movement belonged to a compound slide of rotational and translational. The soft clays, one of the identified materials found in the in-situ observation, are vulnerable to become a slip plane if the saturated water contaminates the clay's layer. In December 2012, slump and crack were discovered near to the local shops located at the old Puncak Highway. The slump was 7 m along and moving down 10-15 cm. The ground truth also confirmed that they found new cracks on the side 4-6 m length and 5-10 mm width after heavy rainfall in 6 hours further monitoring in the same location. Due to creep and landslide histories, this area belongs to a high-risk spot and being monitored continuously by PVMBG. Several geodetic observations have been conducted which are terrestrial (1993-1997), GPS (2002-2015, 2013), and laser scanning (2012-2013) measurements.

6.3 Experimental Results in The Active Landslide Areas

We estimated 3D vectors displacement generated only by InSAR data under the slope aspect assumption without any external data from ground measurements since the study area was a lack of up-to-date geodetic survey information. The combination of two orbits SAR data was assessed both by the surface and nearest-neighbor method. Figure 6.4 shows the scatters comparison between these methods. The number of PS points differs between the methods: For the whole region of interest used for computation, the number of scatters selected by the surface method is 2.15 times larger than the nearest-neighbor method.

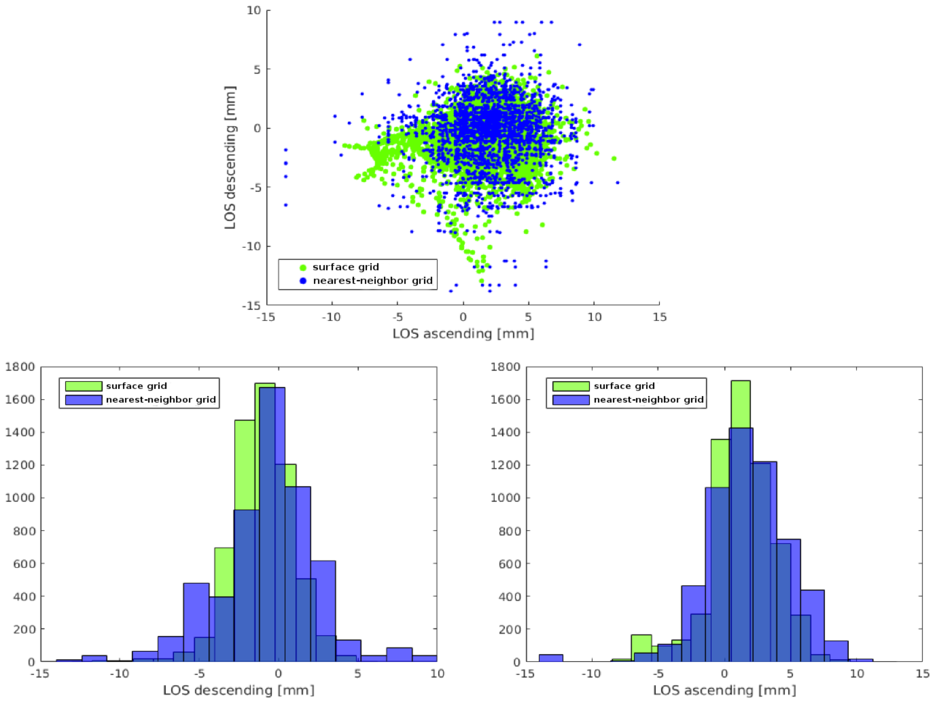

FIGURE 6.4: The top image shows a scatter distribution between nearest-neighbor and surface merging results while the bottom images show the histogram both for the ascending and the descending data. The sample of scatters was captured on the bottom part of the Ciloto district. The sample PS points are located in a stable urban area near to the Ciloto district (ca. 9 km2 area's size).

Based on Varnes, 1978, the detected deformation is classified as a creep that moves slowly and continuously to downslope. Soil and rocks sustained by either seasonal or continuous creep are not completely classified as a landslide, but it performs a significant role in the slow displacement of the landslide blocks (Terzaghi et al., 1950) as a potential factor for increasing the shear stress periodically. Van Asch, 1984 distinguished two phases in a landslide; (a) the phase of initial failure, and (b) the subsequent phase after the movement has started and the mass material runs out (Brunsden et al., 1979). Because slow creep movements could precede the initial failure of a slope, the following analysis focuses on the rate of displacement acceleration progressively.

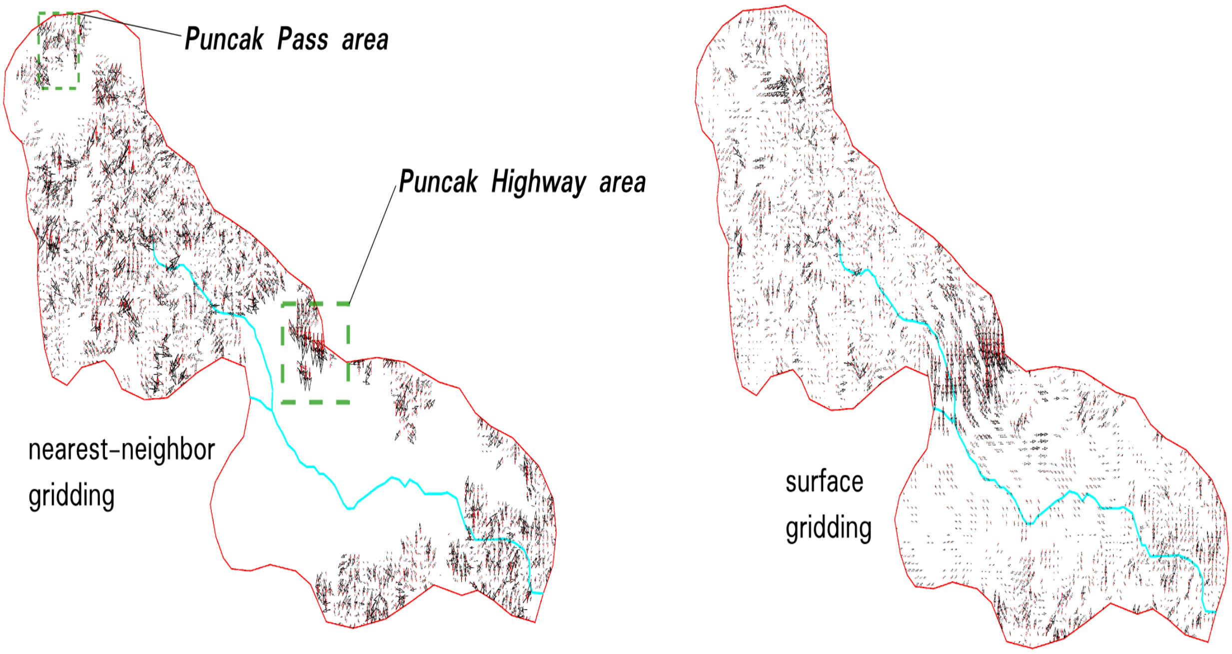

FIGURE 6.5: The gridded result from the nearest-neighbor (the top image) and surface method (the bottom image). The black arrow represents the horizontal component and the red one for the vertical component. The cyan line illustrates the CiJember river.

In general, we defined a 3D displacement field for horizontal and vertical movements in Puncak Pass and Puncak Highway, Ciloto as illustrated in Figure 6.5. As seen in the middle ROI, there is a definite movement detected by the InSAR product using the surface gridding method which explains an indication of leaking water from the CiJember river toward the bottom part of the Puncak Highway landslide observation. The previous investigation from Supriatna, 2002) explained that the main trigger of movement was the increasing of water intensity caused by rainfall and water infiltration. The issue might be worse if the streams of CiJember are not flowing correctly and leaking to vulnerable soil materials surrounding the river areas. Thus, the potential of a slope failure could occur in Puncak Pass, the residents at the south-east Puncak Pass (RW.06) and Puncak-Bogor Highway when the rate of the detected displacement accelerates progressively.

6.3.1 The Puncak Pass Landslide

Two samples of selected PS points in the Puncak Pass area were examined to comprehend the behavior of the slope movement. The zone (1) and (2) are located on the top near to the main road and the bottom close to Puncak Pass resort and hotel, respectively. Figure 6.6 represents the mean LOS time series InSAR result from ascending and descending data. An unwrapping error was detected at landslide events in February and March 2018. We applied the correction of one phase unwrapping error introduced by Notti et al., 2015. Since the differential displacement between two consecutive acquisitions (residue) from ascending data at this time exceeded $|\lambda/4|$ x 2 mm, we could not correct the error easily. Hence, we assumed this range time as a breakpoint due to largely displaced materials. In order to highlight the great motion that occurred in this period, the displacement values of this timeline are modified to be $residue \pm \lambda$. Furthermore, the trend of displacement generated by the ascending data identifies more significant deformation signals than descending data because the area has a slope facing east-southern direction (the slope aspect of 130^{o} - 160^{o}).

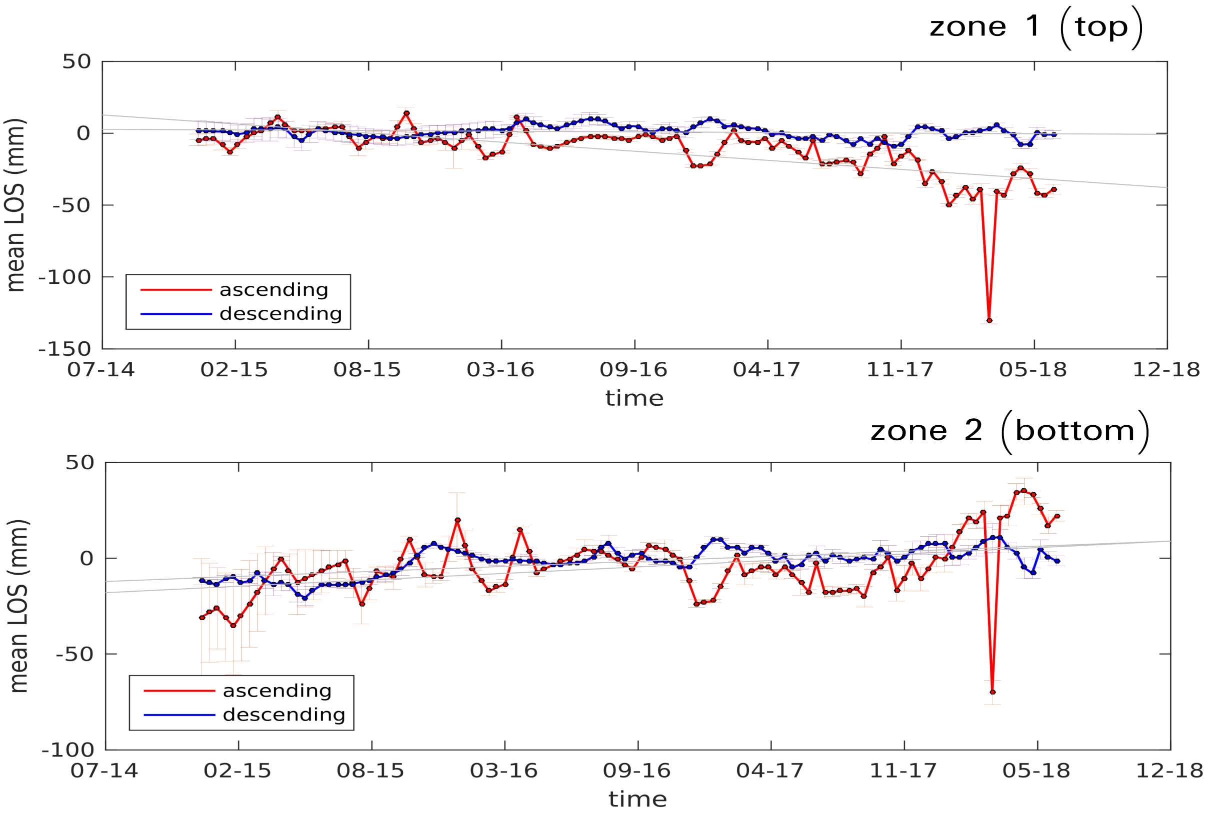

FIGURE 6.6: The mean LOS InSAR result from Sentinel-1 ascending and descending SAR data in the Puncak Pass area. The phase jump occurred during February - March 2018 due to phase unwrapping error.

We assessed the generated 3D vectors displacement specifically in the Puncak Pass landslide. A sufficient number of PS points are found at the location because high coherence objects existed there. Those are the road, permanent buildings owned by a resort hotel, local houses, and natural objects such as rocks and trunks. The temporal displacements were calculated using the time series inversion technique (Schmidt et al., 2003) producing LOS results and subsequently projecting those to the vertical (d_U) and the horizontal (d_E,d_N) component. A surface model is used further to grid the table of vertical time series displacements as a visual interpretation whereas the horizontal component is plotted by velocity vectors ($\overrightarrow{dE}$,$\overrightarrow{dN}$). Figure 6.7.b describes the cumulative vertical and horizontal displacement and identifies the top of the Puncak Pass as a crown landslide's body considering clear evidence of the pre-failure surface. The head of the landslide's body cumulatively moved down -5 cm in vertical and 1-2 cm in horizontal displacement from November 2014 to January 2018. However, the anatomy of the landslide movement cannot be identified accurately whether the materials are displaced in the term of $d_U > d_E, d_N$ for the top part, $d_E, d_N > d_U$ for the middle part, and $d_E, d_N, d_U <<<<$ for the toe part. The reason is that the PS points are not heterogenic distributed in the area especially in the middle part, no PS point is found.

As an interpretation of a typical debris slide, there should be a definite location where it was going to deposit. We found a streak of fragment assumed as the landslide deposit (expected as landslide's toe) at the southeast part. Meanwhile, the horizontal vectors show that the direction is parallel to downslope towards the southeast. Considering the east-westward perspective (the original d_E generation from InSAR data), the vectors agree to aspect's direction where the top of landslide's body takes motions toward the east and partly west while the middle of that moves to eastward and for the bottom area toward the west. In particular, the result evaluates that the

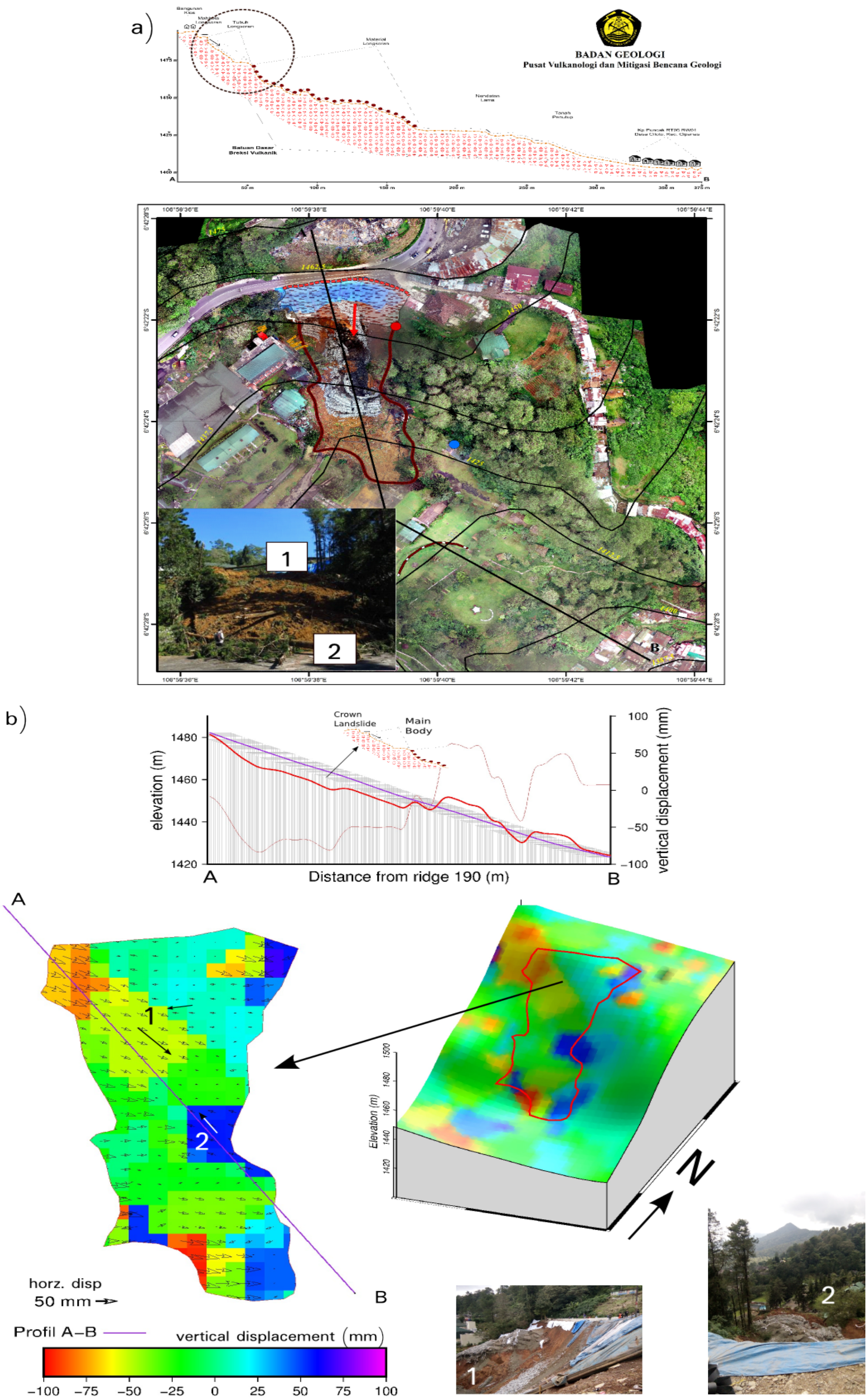

FIGURE 6.7: a) An aerial photography was taken after the landslide occurred on 28 March 2018. b) The 3D motion field generated by the InSAR from November 2014 to January 2018. The pictures show a profile of the cumulative vertical displacement occurred in Puncak Pass which the horizontal displacement moved from the road to the lower surface's elevation placed a few buildings owned by a resort hotel.

landslide began with a very slow movement (1-2 cm/year). Nevertheless, there is a possibility at certain places where a high rate movement might exist, but we could not identify on the SAR signal because of the decorrelation (e.g., a rapid change of amplitude value).

PVMBG documented the Puncak Pass landslides and assessed the aftermath. Its crown body was placed at Cianjur-Bogor Street and moved to the western hall of Puncak Pass resort (a red arrow in Fig. 6.7.a). The estimated vertical motion given by Sentinel-1 data shows a slowly subside to -5 - -10 cm in general. Due to a lack of distributed PS points on the whole sub-area, the horizontal vector is not precisely conducting a direct path to the scarp deposit but tends to move both from the south-west and the south-east direction at the top landslide's body. In the middle part, we could see an uplift displacement proving that the materials moved toward south-eastern, even though PS points are not available in the middle area which is between the change of down and uplift motion (the red and blue scale color). The line profile (black color) presents the main body and material deposit for 25 m and 76.2 m, respectively. We compared a line profile (purple color) from the InSAR model which the result is slightly different from field survey, 45 m for the zone of depletion (see number 1 from Fig. 6.7.b) and 80 m for the zone of accumulation (see number 2). Close to the toe of the surface of rupture, the PVMBG's investigation found the ponded water indicating a slip surface spot. It weakened the shear strength since there was direct contact between the layer of weathering soil (sand and clay materials) and a waterproof curtain.

Regarding the retrieving 3D motion field, we realize that the third element comes from an assumption of the slope aspect derived by a digital elevation model (DEM). If the source of DEM has a low-middle resolution, the downslope direction to its neighbors might not be computed precisely, in particular, the northward component. We used SRTM 1 arc-second (30 meters) as a DEM source which was still reliable to describe a common horizontal motion regarding the size of the area (170 x 220 m). Another issue is that PS scatters are not distributed homogeneously in the whole observed area. Considering the motion beginning from the head of main scarp to the foot part and ending at the toe, we partly dissolve the direction flow of surface failure whether straightly moved to southern part N 182° E (a red arrow in Figure 6.7.a) or started from north-west at the main body then went to south-east for the zone of accumulation. The reason for this uncertain direction is that the slow movement derived by InSAR data has a more variate direction than described by the PVMBG's report on 6 April 2018.

Additionally, another investigation to the previous landslide (4th February 2018) occurred at the same location gives a more understandable description of the western part of the landslide's body. The preceding report explained that they found a crack at the hotel's hall located in the north-west area (Figure 6.7.b) with the length ca. 5 m toward south-east N 145-148° E. It confirms that the ground movement in this area moved both from the north-west and north-east to south-east region. Moreover, a spring (the blue dot in Figure 6.7.a) was found as well in the south-east part of the sub-area. Hence, a potential of follow-up landslides in the future might occur if there are no proper precautions to prevent the surface's failure.

6.3.2 The Puncak Highway Landslide

Based on the previous observation (Sadarviana, 2006), the displacement rate from the InSAR result is slightly different from the GPS result. From 2002 to 2005, the area was reported moving about 15.5 cm/year where the material in the middle landslide zone had 70% horizontal displacement greater than the top zone (10%) and the below zone (20%). Comparing to the InSAR result which has a different scale of the spatial resolution and a different location to the GPS result, the motion is generally getting slower to millimeter rate which is -17±6 mm/year and 5±3 mm/year for vertical and horizontal, respectively in recent years as plotted in Figure 6.8 (a sample location: the white box). We calculated these mean velocities as a linear model displacement. Although we can not compare quantitatively between the GPS and InSAR results due to different spatial and temporal data, the trend of rate displacements between these two data is still achievable to describe the general motion.

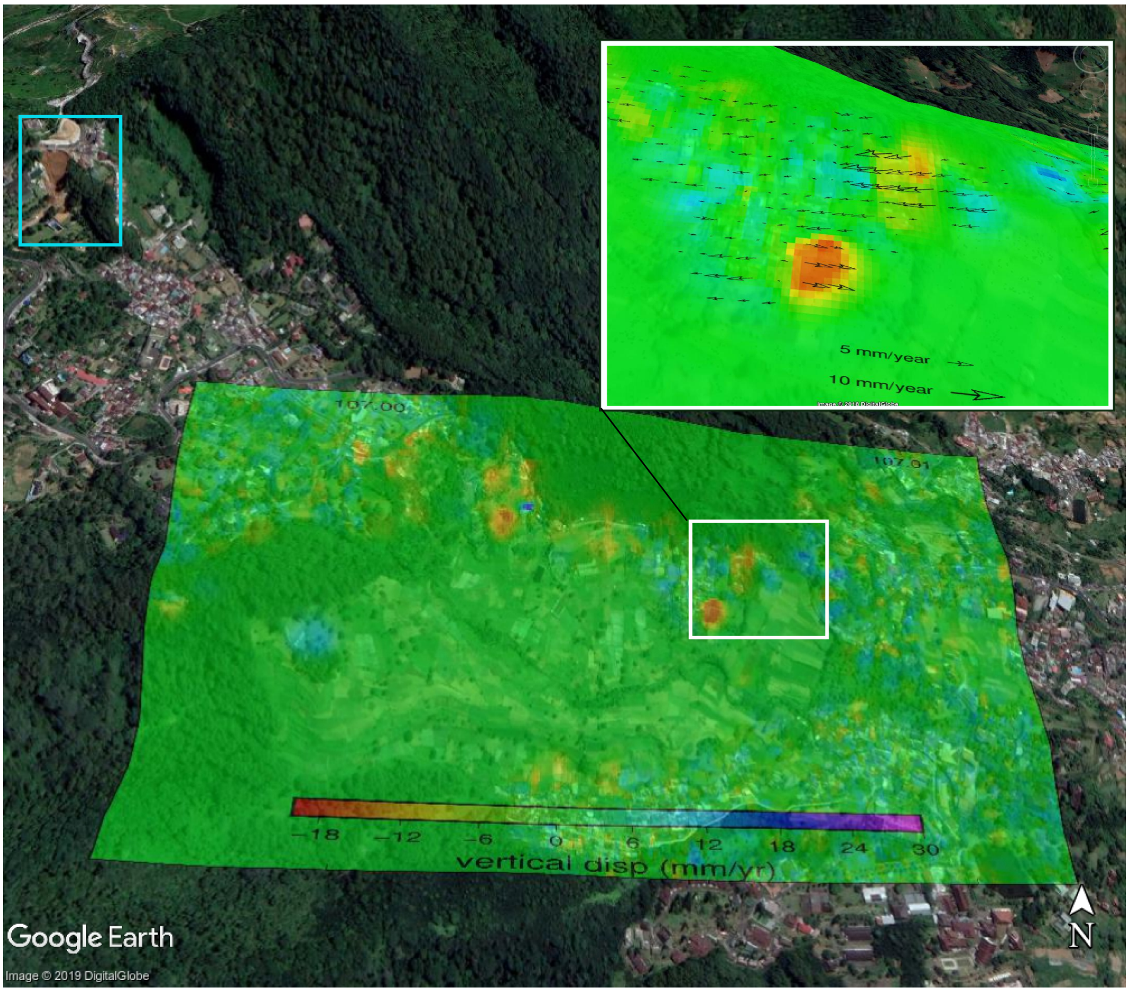

FIGURE 6.8: 3D perspective InSAR result from November 2014 to June 2018 in Puncak Highway Km.81 Bandung - Puncak - Bogor route, one of the most landslide prone area in the Ciloto district. The white box shows a significant motion detected on the location. The vertical displacement moved ±17 mm/year with the estimated horizontal ±5-10 mm/year going to the south-western direction at highway location and south-eastern at the local houses near to a planted field. Meanwhile, the cyan box is the Puncak Pass location described in Figure. 6.7.

Figure 6.9.a shows that the horizontal vector moved mostly to the west-southern place roughly defined by the location of debris material while the 3D generation SAR result headed into variant ways. Nevertheless, some regions have a similar direction to GPS horizontal vector especially near to the CiJember riverside. Figure 6.9.b describes the vertical motion observed both by InSAR and GPS observation. The interpolation points from GPS data explains that the upper elevation depleted (red color) to the lower part (blue color) examined as the deposit zone. Nonetheless, the InSAR result could detect only down lift deformation in this area (the dashed box) where the accumulated zone as shown on GPS measurement is not found around this area since it covers by dense vegetation and the persistent objects mostly not exist. Therefore, this is one of the difficulties to identify the dynamic of movement materials along the surface slide.

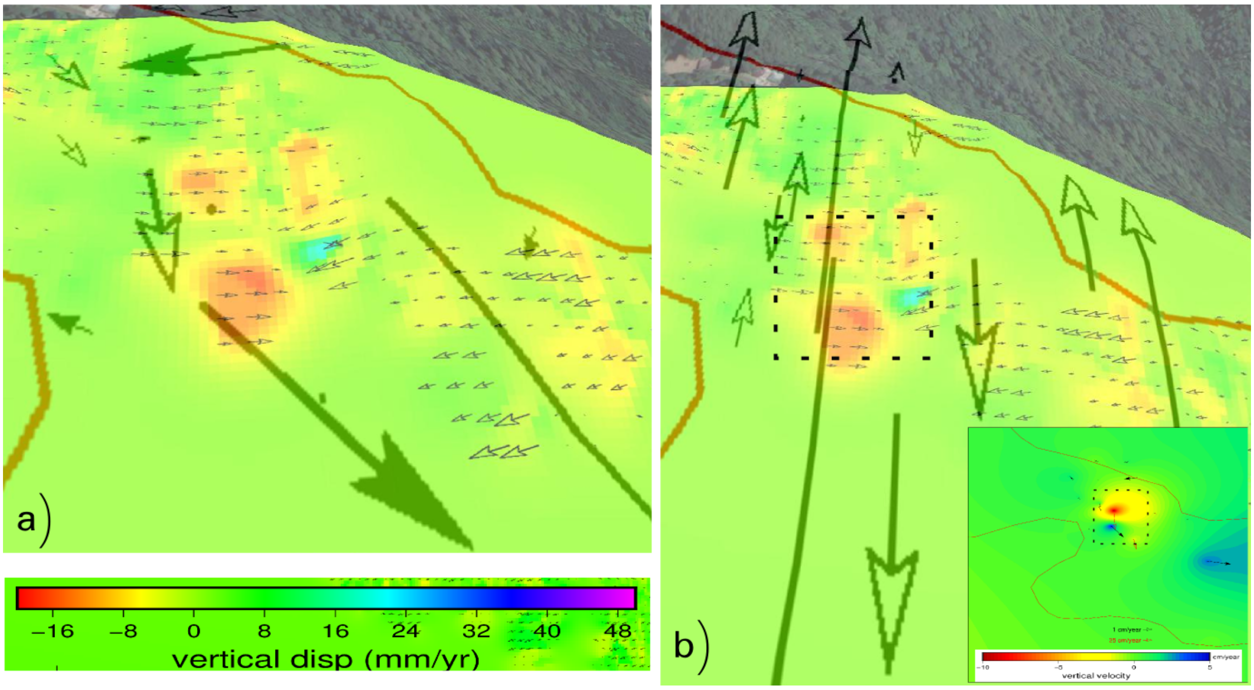

FIGURE 6.9: The overlay between 3D InSAR (2014-2018) and a) GPS horizontal vector and b) GPS vertical vector (2002-2005) with the dashed box emphasized the depleted (red color) and accumulated (blue color) zone.

Comparison between the slope aspect and the surface-parallel-flow method

The derivation of three-component velocity by means of surface-parallel-flow was applied to the monitoring of ice-flow velocity (Joughin et al., 1998; Joughin et al., 1996). The components were derived by using two non-parallel tracks (i.e., ascending and descending tracks) under the surface-parallel flow assumption. Sun et al., 2016 applied the method for the slow-moving landslide monitoring in the Zhouqu Case Study, China. The research concluded the 3D velocity as constant deformation rates. However, the deformation of extremely slow/slow landslide mostly is a not-steady motion's pattern influenced by seasonal and multi-annual weather variations and the hydrology factor with a proof of the low linear correlation as discussed in the previous sections.

We compare the result of the 3D aspect and surface-parallel-flow in the Puncak Highway region. Neither the slope aspect nor the surface-parallel-flow method is satisfied for the generation of 3D velocity component especially for the north-south direction (d_N). Although the direction of d_N parallel to the slope aspect is suitable for the landslide's geometry, the d_N scalar might result in an underestimation value because the slope aspect method is not initially showing the real displacement in Y-axis but only a scalar projection from d_E. Due to an orthogonal projection, the scalar of d_N is not reliable computed, especially for, the slope aspect close to the north-south direction which tends to have a smaller value; the closer the aspect angle to Y-axis, the more under-estimated for the d_N computation. As an important note, the generated 3D velocity from the slope aspect has a similar relative ratio to the sensitivity decomposition of a slant range deformation which the unit vectors are [0.92d_U, 0.38d_E, -0.07d_N] (Massonnet et al., 1998). Meanwhile, the surface-parallel-flow outcome is certainly not accurate for d_U and d_N component as well. The adjustment of least square combination might be overestimated computation since the accuracy of the estimation depends on the surface slopes along the corresponding LOS (the incidence angle) generated by DEM and the quality of SAR processing and the algorithm is assumed the velocity as a steady motion.

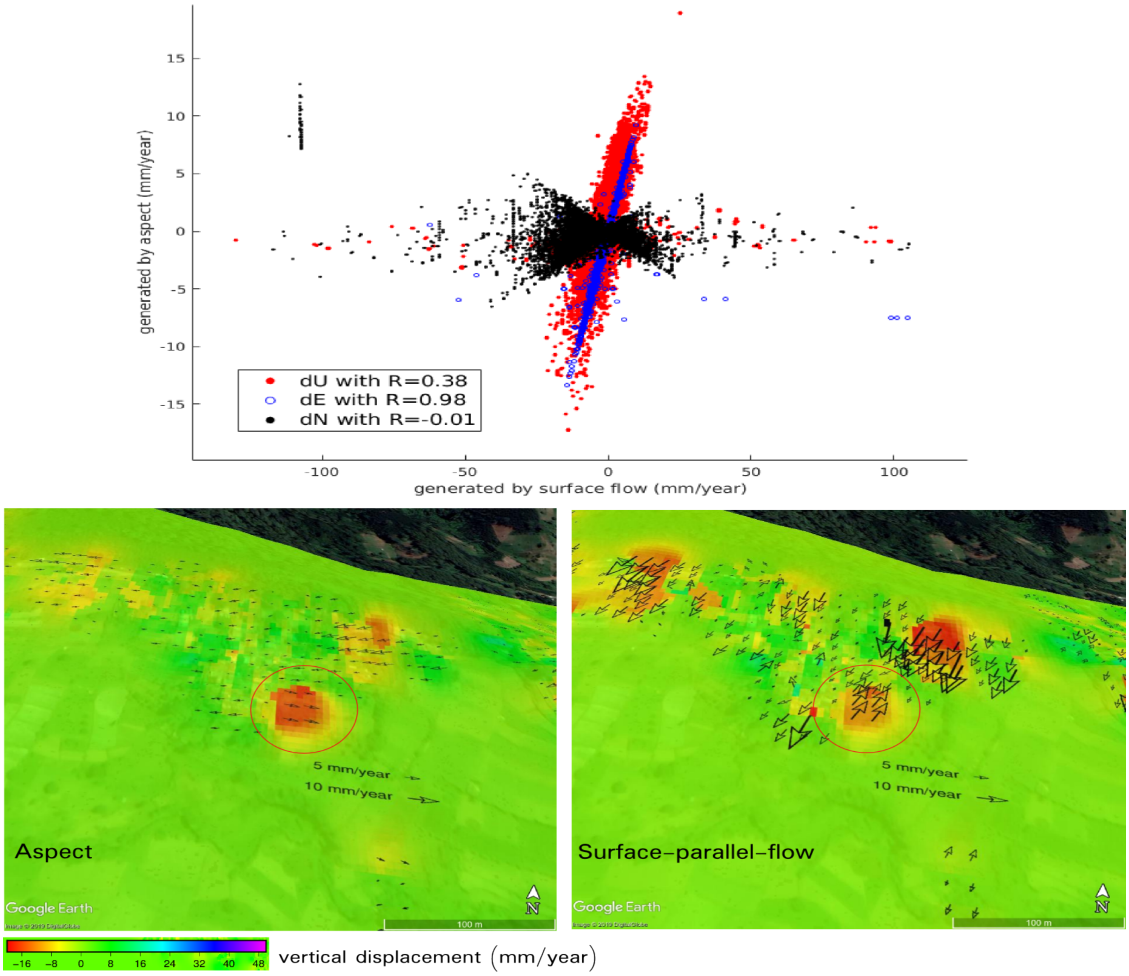

FIGURE 6.10: The scatters distribution of 3D mean velocity generated by the slope aspect and the surface-parallel-flow method in the Puncak Highway area.

Figure 6.10 shows the distribution scatters of 3D velocities between the surface-parallel-flow and the slope aspect in the Puncak Highway area. For the surface-parallel-flow result, we found that 25 points were out of expected range value (> 300 mm/year) since the points had a high noisy value either from $dLOS_{asc}$ or $dLOS_{dsc}$ pixel. Thus, we did not include these points for our computation. The coefficient correlation between those methods (R) for d_U, d_E and d_N are 0.38, 0.98, and -0.01, respectively. Regarding the value of Rd_N, the two results completely have different unit vectors of $\hat{d_N}$. There is an area showing different directions (drawn in the red circle) between two methods. If we consider the slope angle and aspect are facing south-east in the area, the d_N values generated by the surface-parallel-flow are partly in the wrong directions because the horizontal field appears towards counter the downhill surface.

6.4 The Relationship Between 3D Vectors Displacement and Precipitation

6.4.1 The Linear Relationship

The Puncak Pass

The heavy rainfall intensity and bad drainage system caused the pond water flowing along a slide surface as seen in Figure 6.7.b. It infiltrated to porous soil and accumulated among the space of grains and cracks. Since soil contains saturated water, it makes the mass weight and pore pressure increases while the shear strength decreases. Because of the possible impact of rainfall on motion's behavior, a relationship between precipitation and slope movement is necessary to be further investigated.

zone 1 (top)

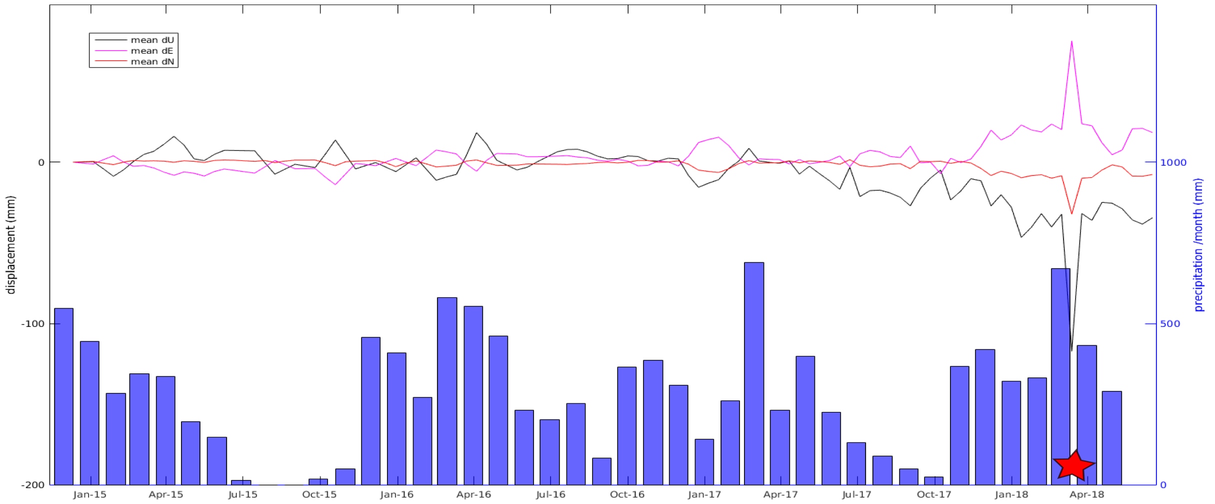

zone 2 (bottom)

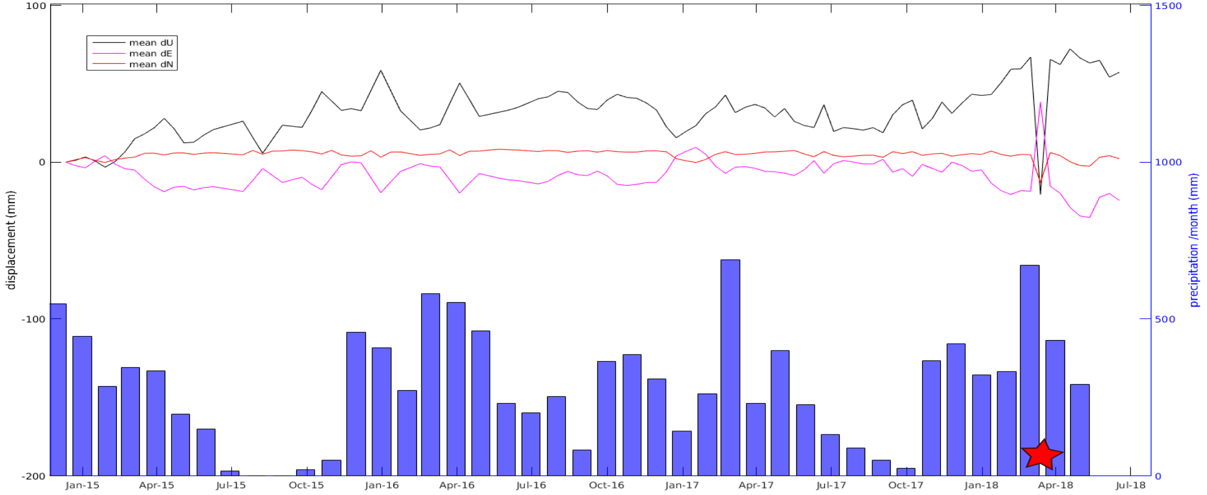

FIGURE 6.11: InSAR displacements in U, E, N directions at zone of depletion (1) and zone of accumulation (2), the Puncak Pass landslide, along with total precipitation (/month). The red star indicates the date of two consecutive landslides occurred in February and March 2018. The correlation values between displacement vectors and precipitation are -0.04, 0.25, -0.22 (zone 1) and 0.22, -0.07, -0.2 (zone 2).

3D vectors samples at zone 1 determined as the depletion area with 18 PS scatters [-6.706° - -6.705° S; 106.993° - 106.994° E]) are compared to the total precipitation (per month [mm]) recorded by Citeko Station. The total rainfall intensities recorded from October 2016 to February 2017 for five months (rainy season) are 1788 mm with the highest intensity in February 2017, 688.5 mm. Figure 6.11 (top) shows that all vectors within this time indicate maximum cumulative motion of -47 mm, 23 mm, -10 mm for dU, dE and dN, respectively. Additionally, a significant movement also occurred from December 2014 - September 2015. The vertical components denote upwards in the rainy season (December - February) while during the dry season (March - September), they point downwards. A creep phenomenon, another geological behavior, might influence on this final result because the surface soil material containing clay tends to expand during the wet season (expansive clay) and otherwise shrinks on the dry season. In total, we observed a slow motion towards downslope with the mean velocity of -10±9, 5±5, -2±2 mm/year for dU, dE and dN, respectively and its rates increase to cm/day close to the landslide's event. In that case, the SAR sensor was not able anymore to detect the rapid movement due to a limit of phase sensitivity. The RMSEs (root mean square errors) are relatively high since the model fit to calculate the mean velocity (mm/year) is using linear regression. The model, however, does not account for non-linear behavior caused by precipitation. Therefore, a non-linear model fitting is better to be used in the future for predicting the displacement trend and velocity.

Fot the accumulated zone or zone 2, the mean time series displacement of 20 PS scatters located at the southern part of ROI [-6.7065° - -6.7063° S; 106.9941° - 106.9943° E] is shown in Figure 6.11 (bottom). The cumulative displacements (dU, dE, dN) until 12 January 2018 are 43, -13, 7 mm, respectively. The samples are taken near to a building owned by the Puncak Pass hotel with the direction motion slightly towards the south-west. The mean velocities assumed as linear displacement rates of dU, dE, dN are 10±12, -1±8, -0.2±2 mm/year, respectively. The movement's acceleration has started in February 2017. The early period (December 2014 - January 2017) of the time series displacement result is relatively stable. The indication of an oscillation pattern might also take into account if we consider the influence of rainfall intensity on the slope movement's characteristic. Although this zone suffered from low coherent objects, the generated 3D vectors indicate that the vertical component is going to up-lift describing the simultaneous ground movement displaced slowly from the top to downhill. Meanwhile, it is still difficult to determine the accurate horizontal direction in this zone because of the heterogeneity of rate velocities on the dU and dE component through the observed period. The linear regression does not fit the trend velocity as well demonstrated by very low coefficient of determination ($R^2 d_U$ = 0.4266, $R^2 d_E$ = 0.0181, $R^2 d_N$ = 0.0114).

We calculated a linear correlation between the rainfall intensity, recorded at the local station 6.5 km away, and the detected displacement in Puncak Pass region. We approached both precipitation and total displacement cumulative values on each month to simplify the relationship pattern. The correlation in depleted zone (1) shows R_{d_U} = -0.04, R_{d_E} = 0.25, R_{d_N} = -0.22 while in accumulated zone (2) shows R_{d_U} = 0.22, R_{d_E} = -0.07, R_{d_N} = -0.2. The correlation values indicate that the precipitation is not a constantly main trigger factor for the slope movement. However, close to the landslide's events in February and March 2018, there were significant movements in both zones since February 2017 with the correlation rising R_{d_U} = 0.293, R_{d_E} = 0.072, R_{d_N} = -0.043 and R_{d_U} = 0.395, R_{d_E} = -0.248, R_{d_N} = 0.288, respectively. The motion relates to the increase of precipitation chat bars especially on the rainy season (November 2017 - March 2018) which the highest second record of precipitation proves the slope failure occurred on the area and makes the time series trend having an unwrapped error due to an insensitivity for detecting large deformation at a small region, namely, during the failure event. This interception is considered as a breakpoint marked by the red star in Figure 6.11.

Puncak Highway

The unstable materials are significantly moving slowly downhill towards the open-field area. We expect in the future the rate of displacement will be greater than in the past since this area is near to CiJember River where groundwater flows from up-hill to nearby regions and accumulates towards the CiJimber streams. The samples of 65 PSs at the Puncak Highway [-6.714° - -6.713° S; 107.005° - 107.006° E] in Figure 6.12 also express a very low correlation to the local precipitation (R_{d_U} = 0.04, R_{d_E} = 0.03, R_{d_N} = -0.04). Hence, the movement might happen not only on the rainy season but also on the dry season even though the rate of displacement will be different and the motion trend demonstrates as a non-linear displacement. In the case of slow movement monitoring, the condition of groundwater and surface water flow as the hydrology factor has to

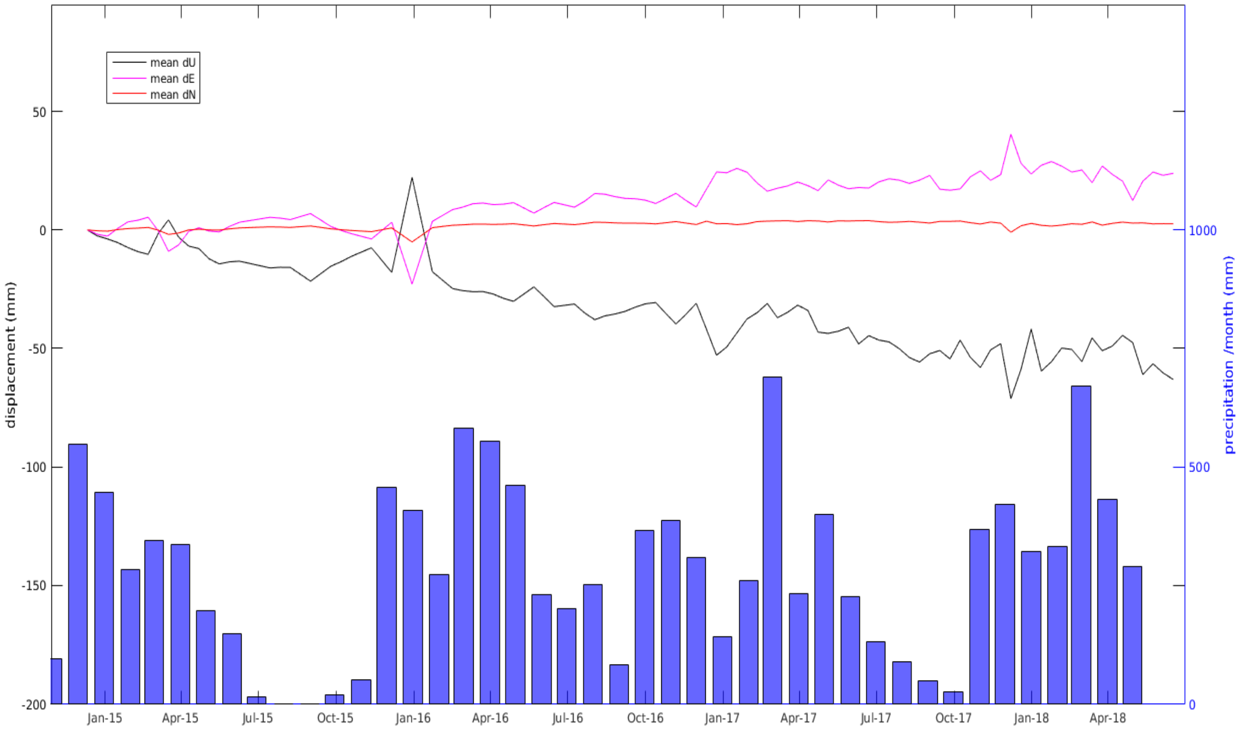

FIGURE 6.12: InSAR displacements in U, E, N directions in Puncak Highway along with total precipitation (/month) recorded at Meteorology Station Citeko [6°41′53" S, 106°56′6" E) about 6.5 km away from the location. The correlation values between displacement vectors are 0.04, 0.03, -0.04, respectively.

be considered as well instead of a direct correlation to rainfall intensity. Furthermore, regarding the moving trend in the Puncak Pass landslide, a significant correlation to rainfall intensity may increase when the shear strength of slide surface decreases close to its limit to the initial slope's failure.

6.4.2 The Non-linear Relationship

Like the previous section, we could not find a direct influence of precipitation for the detected slow movement generated by the InSAR technique in the Ciloto district except the period close to the two successive landslide's event. Therefore, we attempted to figure out the non-linear relationship between those variables.

Firstly, we created a generalization to incorporate the non-linear relationship as a sample conditional expectation. The generalized additive model (GAM) takes into account the smooth functions of our predictor variables as shown in Figure 6.13. It allows non-linear forms between the covariates, represented as $f(x = time)$ and the target variable y, represented as the displacement and precipitation values. Our data might not be defined with simple transformations of the predictors. Simple approaches, such as a logarithm or long transform and cubic polynomial regression, do not present the best-fitted result to the observed data. The approach needs higher orders and a flexible model to capture the nuances of the data. Thus, we used the GAM model to approach the fitted trend for our data. The term of GAM is originally from Generative Linear Model (GLM). The distinguish is GAM including any quadratically penalized GLM and a variety of other models estimated by a quadratically penalized likelihood type approach. For our case study, we chose the cubic regression splines to penalize the basis coefficients in order to control the degree of smoothness. The reason for the choice is that we need to have a cubic spline basis

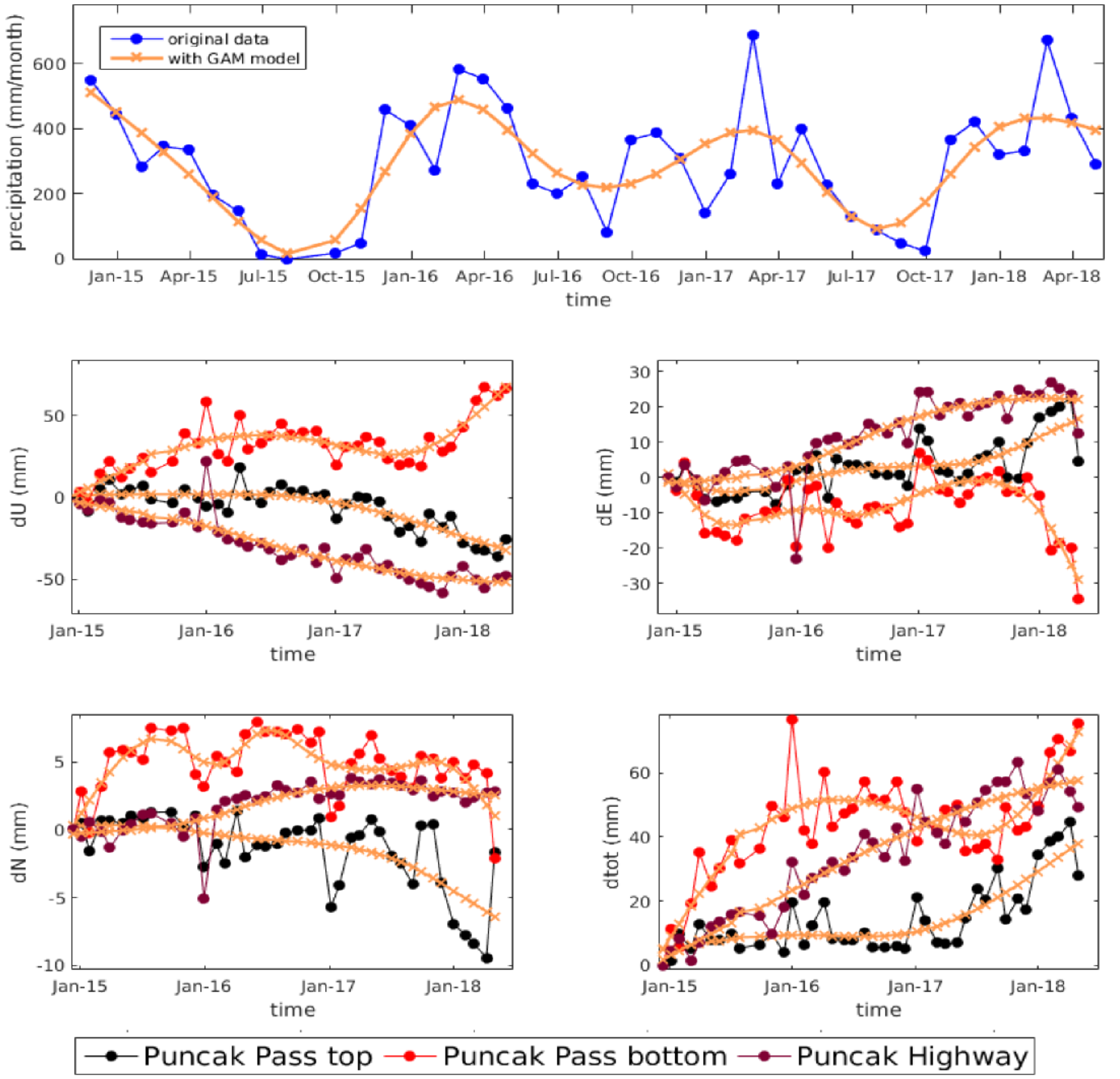

FIGURE 6.13: The non-linear model both for precipitation and the 3D vectors displacement in the Puncak Pass and the Puncak Highway area.

defined by a modest-sized of knots spreading evenly through the covariate values (Wood, 2006). GAM specifies the function following as:

$$y = f(x) + \epsilon \tag{6.9}$$

and if we choose a cubic spline for the basis to capture non-linear relationship, the above equation can be added more detail where

$$y = f(x) + \epsilon = \sum_{j=1}^{d} B_j(x)\gamma_j + \epsilon \tag{6.10}$$

each B_j is a basis function of a polynomial as

$$f(x) = \gamma_0 + \gamma 1 \cdot x^1 ... + \gamma_d \cdot x^d \tag{6.11}$$

TABLE 6.1: The correlation values between precipitation and the 3D vectors displacement

Method	d_U	d_E	d_N	d_{tot}
Puncak Pass Top (Zone 1)				
Pearson	-0.041	0.254	-0.222	0.106
Kendall	-0.039	0.129	-0.117	-0.015
Spearman	-0.031	0.189	-0.158	-0.021
Max Corr	0.069	0.554	0.661	0.49
Puncak Pass Bottom (Zone 2)				
Pearson	0.240	-0.076	-0.207	0.136
Kendall	0.166	-0.005	-0.195	0.154
Spearman	0.248	-0.034	-0.308	0.230
Max Corr	0.753	0.368	0.585	0.758
Puncak Highway				
Pearson	0.279	0.0399	-0.025	0.034
Kendall	0.049	0.051	-0.056	-0.024
Spearman	0.053	0.068	-0.064	-0.016
Max Corr	0.629	0.372	0.583	0.633

where x is depending on the type of basis considered, represented as the time for our case study and γ is the corresponding regression of coefficients.

The best fitted trend of GAM model both for the 3D vectors displacement and precipitation will be compared using the linear and non-linear relationship. If the data have either bivariate normal distribution or rank correlation, the linear relationship using the Pearson and Spearman method might be sufficient to discover the relationship. However, the InSAR and precipitation data are random variables characterized as independence completely. They have no preference for linearity or monotonicity. Moreover, the physical factors are more dependable than the rainfall intensity to arouse the ground movement directly. Table 6.1 explained that the linear correlation from *Pearson*, *Kendall*, and *Spearman* method has small values close to ~ 0. The maximal correlation could quantify the non-linear relationship and solve this issue. For the computation, we need to find the characteristic function of a random variable and define a norm on random variables (Tibshirani, 2013) as fixed points of maximal correlation. The alternating conditional expectations (ACE) algorithm is used to determine the fixed point equations of the maximal correlation. We computed the sample conditional expectations (ACE) of each best fitted smoothing GAM for the precipitation, d_U, d_E, d_N, and d_{tot} data. We took into account the maximum correlation over GAM functions of our two random variables (precipitation and the vector displacement in a function of time) to serve as an estimated value of the population parameter. If the random variables are completely independent without any relationship, then the maximal correlation equals zero.

Three sample data are taken in the Puncak Pass top (Zone 1), the Puncak Pass bottom (Zone 2) and the Puncak Highway. As described in Table 6.2, the maximal correlations have high values indicating the non-linear relationship between precipitation and the slow movement occurred in the Ciloto area.

The linear correlation of the Puncak Pass top area shows a positive value while the bottom area shows a negative value for the d_U component classified as the depleted and accumulated zone. The non-linear relationship between precipitation and ground motion does not show a high correlation even using the maximal correlation approach ($R_{d_U} = 0.069$) in the Puncak Pass top area. Hence, we approached the best fitted GAM model for our data to generalize their patterns. We found that there is a non-linear relationship between the rainfall intensity occurred in the Ciloto and the slow movement's behavior. Reshef et al., 2011 classified the relationship type based

TABLE 6.2: The correlation values between precipitation and the 3D vectors displacement with the GAM best fitted model

Method	d_U	d_E	d_N	d_{tot}
Puncak Pass Top (Zone 1)				
Pearson	-0.16	0.321	-0.228	0.106
Kendall	-0.105	0.163	-0.093	-0.015
Spearman	-0.12	0.242	-0.135	-0.021
Max Corr	0.728	0.907	0.794	0.875
Puncak Pass Bottom (Zone 2)				
Pearson	0.2	-0.072	-0.544	0.1
Kendall	0.256	0.041	-0.361	0.28
Spearman	0.365	0.024	-0.501	0.399
Max Corr	0.754	0.705	0.618	0.764
Puncak Highway				
Pearson	-0.078	0.085	0.05	0.072
Kendall	-0.056	0.049	-0.083	0.056
Spearman	-0.086	0.079	-0.085	0.087
Max Corr	0.965	0.917	0.838	0.966

on scores given to various noiseless functional relationship. The maximal correlation values for our samples area are from 0.7 to 0.96. The Puncak Pass area belongs to a sinusoidal relationship since the maximal correlation is between 0.7 and 0.8 while the Puncak Highway area has a periodic relationship with the maximal correlation value close to *0.9*. Based on the discovery of non-linear relationship, a further investigation for the pattern of rainfall intensity either using a sinusoidal or a periodic approximation needs to incorporate to other landslides trigging factors.

6.5 The Drawbacks of The 3D Slope Aspect Method

Applying the slope aspect method to particularly generate d_N vector from InSAR result should consider many factors as following

- The surface slide is assumed as a type of planar, thus, the method only works for a translational landslide case study. The generated 3D vectors of the slope aspect might have a big error deviation for the rotational and the compound slide.
- The generated d_N vector is a ***pseudo*** value of d_N. The d_N result only helps to visualize and interpret the direction of movement along y axis. The scalar of d_N, yet, remains ambiguous due to the scalar projection only depending on the slope aspect and d_E value.
- The projection of d_N might result in an exaggerated or understated scalar value. As we know $d_{aspect} \neq d_{hor}$, then these situations might appear illustrated in Figure 6.14.
  - (i) an exaggerated result, if $d_N < d_E$ and θ_{asp} close to the north direction ($\sim 90°$).
  - (ii) an understated result, if $d_N > d_E$ and θ_{asp} close to the north direction ($\sim 90°$).
  - (iii) the θ_{asp} angle gives the ambiguity of d_N scalar in term of y axis.

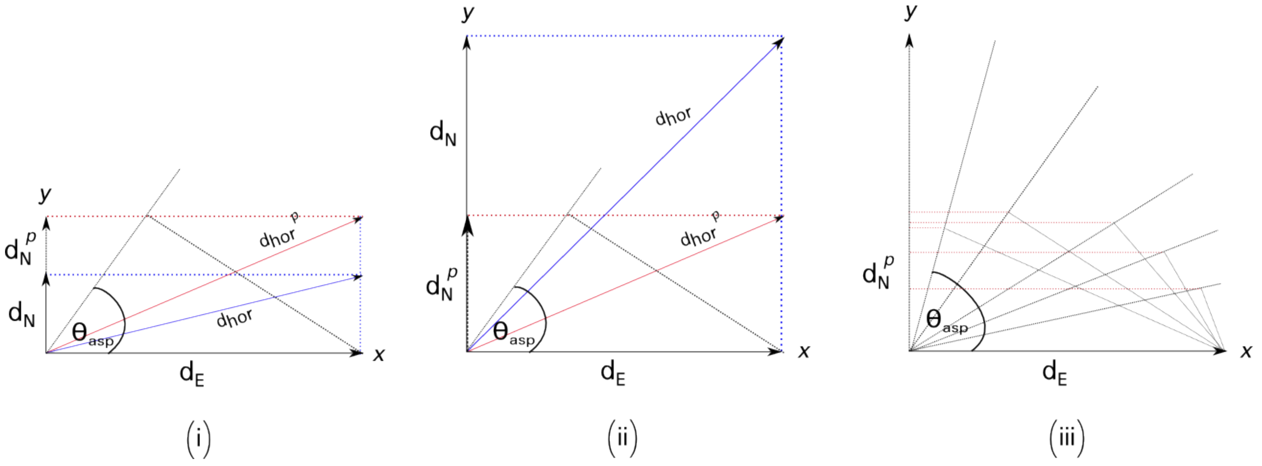

FIGURE 6.14: The ambiguities of scalar projection of d_N in y coordinate

6.6 The Fusion of Surface-Parallel-Flow and Slope Aspect

The surface-parallel-flow developed by Joughin et al., 1996 is a technique to allow the three-component ice-flow velocity field to be estimated from two SAR orbits data under an assumption of surface-flow. For the ice-dynamic studies, the three component velocity vector is defined by

$$v = v_x\hat{x} + v_y\hat{y} + v_z\hat{z} = v_h + v_z\hat{z} \tag{6.12}$$

with the estimation of velocity vector in SAR geometry under surface-parallel-flow assumption yielding to

$$\begin{bmatrix} v_x \\ v_y \end{bmatrix} = (1 - ABC)^{-1} AB \begin{bmatrix} \frac{\phi_{disp,asc}}{2k\delta T_{asc}\, sin\, \theta_{asc}} \\ \frac{\phi_{disp,dsc}}{2k\delta T_{dsc}\, sin\, \theta_{dsc}} \end{bmatrix}$$

with A, B, C are defined to

$$\begin{gathered} A = \begin{bmatrix} cos\beta & cos\,(\alpha+\beta) \\ sin\beta & sin\,(\alpha+\beta) \end{bmatrix}, \\ B = \frac{1}{sin^2_\alpha} \begin{bmatrix} 1 & -cos\alpha \\ -cos\alpha & 1 \end{bmatrix}, \\ C = \begin{bmatrix} \frac{\partial z_t}{\partial x}\, cot\theta_{asc} & \frac{\partial z_t}{\partial y}\, cot\theta_{asc} \\ \frac{\partial z_t}{\partial x}\, cot\theta_{dsc} & \frac{\partial z_t}{\partial y}\, cot\theta_{dsc} \end{bmatrix} \end{gathered} \tag{6.13}$$

then applying the surface-parallel-flow assumption from (6.13) into (6.12) with $v_z = d_U \frac{\lambda}{4\pi}\delta T$, $d_E = \frac{\partial}{\partial x} z_t(x,y)$, and $d_N = \frac{\partial}{\partial y} z_t(x,y)$, we obtain

$$d_U = v_x d_E + v_y d_N \tag{6.14}$$

with ϕ_{disp} is the phase unwrapped, δT is the time between acquisition images, β is the angle between x axis and the across track ascending direction, α is the angle between across track ascending and descending, and θ is the incidence angle. The detail explanation for this algorithm could be read on Joughin et al., 1998.

These equations were created intentionally to estimate the ice flow velocity. It is clear that the motion's materials between ice-flow and landslide study are different. However, if we neglect the characteristic motion of ice and soil, the general definition of a flow parallel to the surface could be applied to the translational landslide case study. Thus, we attempted to fusion the surface-parallel-flow taken into account for the scalar vector value and the slope aspect for the horizontal flow direction.

The strategy to generate 3D component based on the surface-parallel-flow and the slope aspect is described in the following steps

(a) Firstly, the retrieving of d_U, d_E, d_N is estimated using the OLS inversion under the surface-parallel-flow assumption.

$$\begin{bmatrix} cos\theta_{inc_{asc}} & -sin\theta_{inc_{asc}}.sin\alpha_{h_{asc}} & sin\theta_{inc_{asc}}.cos\alpha_{h_{asc}} \\ cos\theta_{inc_{dsc}} & -sin\theta_{inc_{dsc}}.sin\alpha_{h_{dsc}} & sin\theta_{inc_{dsc}}.cos\alpha_{h_{dsc}} \\ -1 & v_x & v_y \end{bmatrix} \cdot \begin{bmatrix} d_U \\ d_E \\ d_N \end{bmatrix} = \begin{bmatrix} d_{LOS_{asc}} \\ d_{LOS_{dsc}} \\ 0 \end{bmatrix} \tag{6.15}$$

(b) The generated d_N vector then is re-arranged by means of the aspect quadrant illustrated in Figure 6.15 where:

- Quadrant I & IV have y axis in (+) direction.
- Quadrant II & III have y axis in (-) direction.

(c) It considers that d_U, d_E, d_N remain in the original LOS projection by using two non-parallel tracks and surface slope either from an interferometry or an external elevation model. However, the direction of d_N is now controlled by the aspect quadrant.

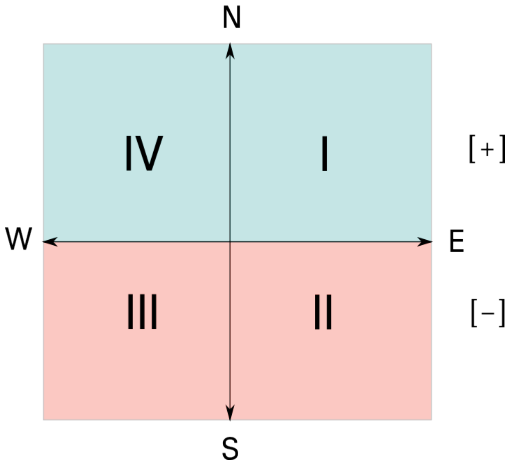

FIGURE 6.15: The aspect quadrant which defines the direction of d_N vector.

Application of The Fusion Method in Puncak Highway

We demonstrate this fusion to the time series InSAR data in Puncak Highway since the mean velocity result explained in Section 6.3.2 is insufficient to be applied concerning the non-linear velocity and the inaccuracy in three-component velocity as the result of cumulative errors from SAR processing. Thanks to the wide availability of Sentinel-1 data which reduce, at least, the common errors found on the InSAR application (González et al., 2011). A short-repeat period allows a wide range of temporal baselines for increasing the ability to measure either slowly and rapidly moving ground. Short perpendicular baselines are obtained to avoid look angle and baseline error. Hence, a more accurate estimation of movement can be achieved.

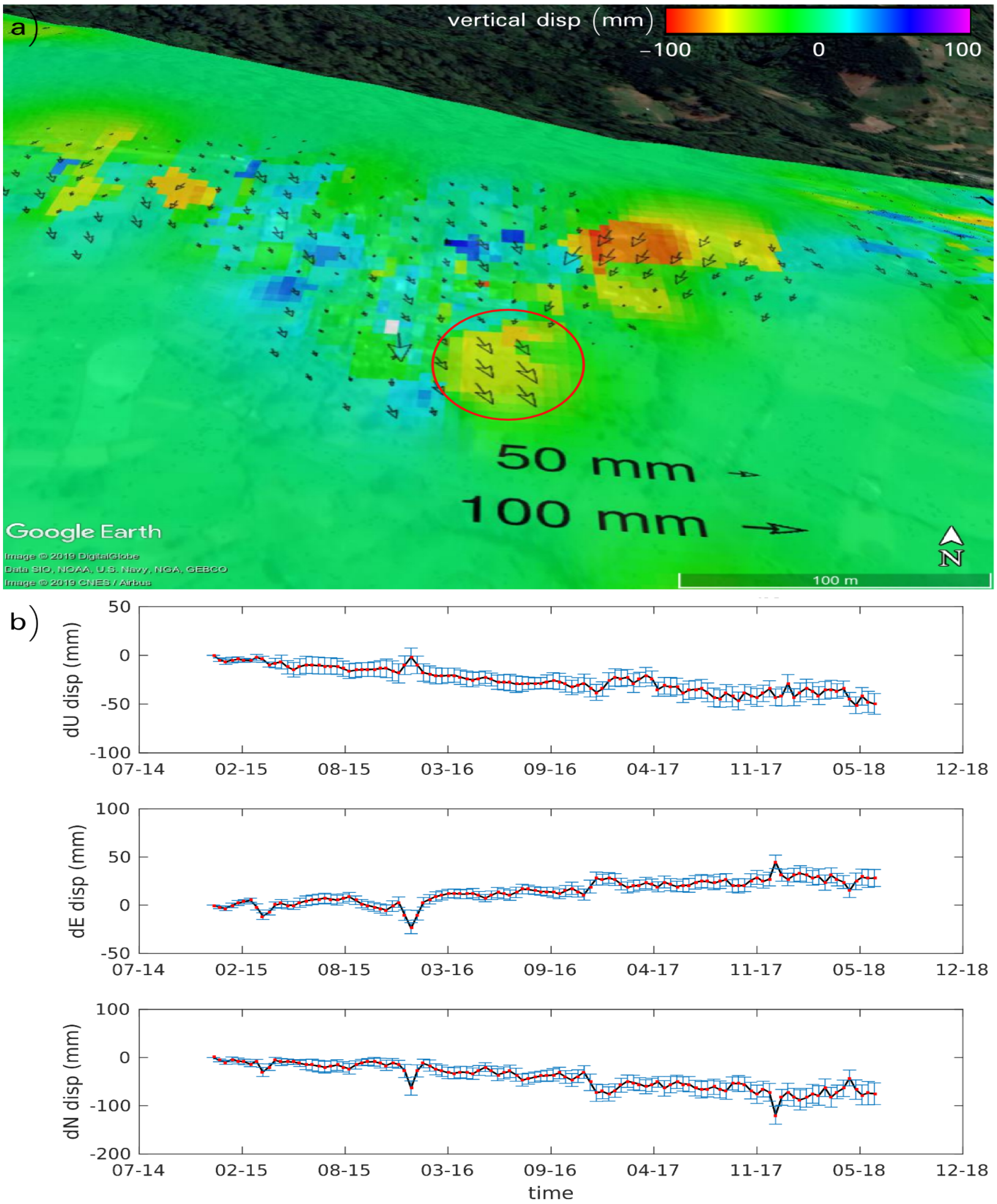

FIGURE 6.16: a) 3D cumulative displacement results from the fusion of surface-parallel-flow and slope aspect method applied to the Puncak Highway landslide. b)The time series displacement for each component with its error bar taken from 49 scatters near to local houses (the red circle).

Figure 6.16 shows the result of the combination between the surface-parallel-flow and the aspect quadrant technique. We take 49 scatters near to the local houses in Puncak Highway. The area is detected moving to -50 mm in vertical cumulatively for three years. Regarding the horizontal movement, the motion's direction agrees to the slope face toward south-eastern. The resultant of d_E and d_N at the taken sample area are 28 and -75 mm, respectively. The generated vectors based on this integration shows a better result than only appealing each method on the final time series displacements. Overcoming of the insensitivity in polar direction could be solved using the surface-parallel-flow assumption for the scalar projection and considering the slope aspect for the moving direction. Furthermore, the coefficient correlations of d_U, d_E, d_N between the original slope aspect (without the aspect quadrant control) and the fusion method significantly increase to 0.97; 1; 0.87; respectively.

The 3D field adjacent from the fusion method, however, might introduce another bias as the outcome of linear regression estimation. The *RMSE* of estimated d_U, d_E, d_N between the original slope aspect and the fusion are 15.8; 1.1; 47.2, respectively. Because d_N is intentional to create an improvement in the scalar projection, the RMSE value is expected to have a high deviation. However, we take note of the d_U value which also has high residual. This new estimation shows the decrease of cumulative vertical displacement rate from -73 to -50 mm. Unfortunately, there is no ground truth data located at the 49 scatters sample area to validate our results.

The inaccuracy in three-component displacement, in fact, is complicated to be analyzed since the characterizations of all sources of error are not yet explicitly determined (Joughin et al., 1998). Hence, it should be better in the future to implement the WLS solution to the linear system if the error sources are found. In addition, the original surface-parallel-flow was initially established for an application of rapid movement instead of slow-motion monitoring. It requires an accurate surface slope estimation as we derive it from SRTM1 with $\sim$ 30 m resolution instead of the generated high-resolution interferometric DEM for the Ciloto area.

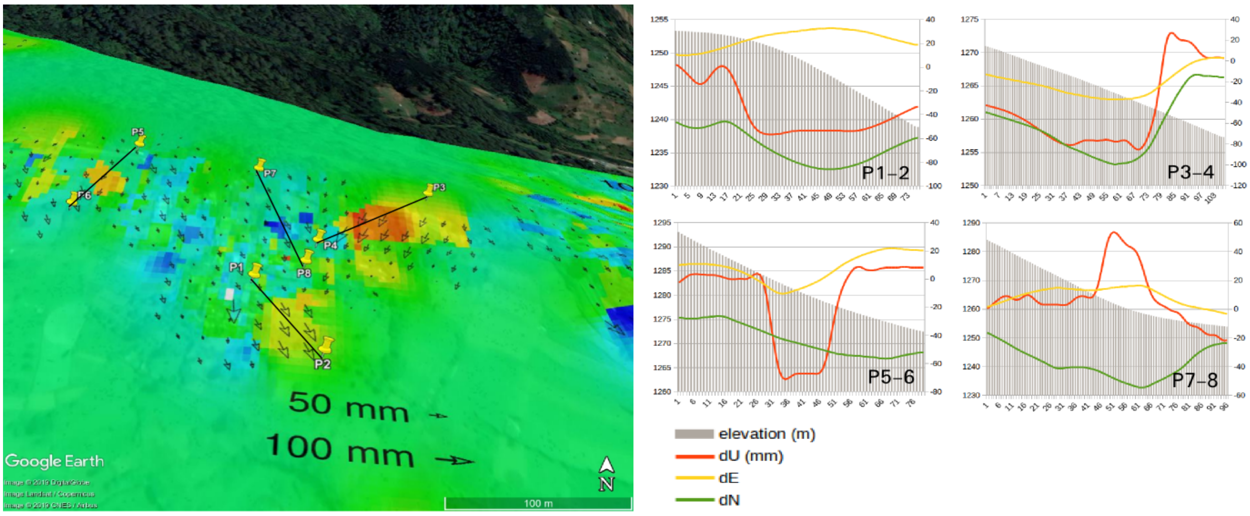

FIGURE 6.17: The characterization of slope shapes and movement's behavior in the Puncak Highway.

The morphology of identified slopes is relatively short with about 70 - 100 m yet involving a volume destabilized material. A chaotic terrain represented by short slopes, indeed, increase the vulnerability of catchment areas to slip phenomena (Mansour et al., 2015). The imaginary profile lines located in Puncak Highway are established to figure out the relationship between the short length of slopes and the 3D retrieved displacements described in Figure 6.17. Firstly, the P1-2 is identified as the convex slope which the surface was displaced up to -60 mm whereas the P3-4 and the P5-6 are generally classified as the linear slope, however, the P5-6 could be called as a linear-concave slope as well. The P3-4 profile shows that the area eroded into the maximum of -90 mm and deposed to 20 mm. On the other hand, the P5-6 was moved down to the maximum of -70 mm. It takes into account that the P5-6 area has limited PS points. Thus, the movement might be partly recognized. The P7-8 belongs to the concave slope which its motion has a lower rate displacement than the other slope profiles. The materials in the P7-8 profile were slightly eroded to -20 mm and deposed until 50 mm.

Regarding the characterization of slope shapes and maximum motion values, our result generally agrees to the laboratory study conducted by Rieke-Zapp et al., 2005. It concludes that the convex-linear slope has greater maximum erosion than the concave-linear slope. Nonetheless, a further morphometric analysis should be done since the retrieved 3D components only compare descriptively to the down-slope component but not to the cross-slope component.

This "fracturing" landslides detected by the InSAR time series technique are genuinely favored by Ciloto's lithology described in Chapter 2 and the presence of fluid circulation which the vulnerability ought to be worse due to lacking seepage control and flood drainage facilities. An opportunity of identifying parts of the landslide body could be determined based on the movement's behavior for long-temporal monitoring. Nevertheless, the challenge to fully implement the technique is that the distribution of the activity of landslides (Casale et al., 1994) is fatiguing to only rely on the distributed PS points. It needs a robust examination to determine the properties of displaced mass and rupture surface concerning the unrevealed landslide style. Relating to the imaginary profile lines, it is not yet known whether the landslide belongs to advancing, retrogressive or enlarging style. For instance, the P1-2 might be either a part of the landslide's body from the P7-P8 or a standalone classification. Hence, in-situ observation is necessary to conduct for validating these discoveries.

6.7 Conclusions of Estimation of 3D-Displacements

We evaluated the slow movement's behavior using a 3D perspective and tested the time series deformation to the real event landslide's location. Several ground movements observed in the Ciloto district, considered as the highest threatened area for landslide hazards, are classified as two types: an extremely slow displacement rate; and a slow displacement rate (several mm/year) known as creeps. However, the motion rate is simultaneously moving faster to cm or m unit close to slope's failure event. This type of movement resulted in the two successive Puncak Pass landslides occurred in February and March 2018. It was debris slide with a moderate size of landslide about 60 x 170 m. We did not find out a direct linear relationship to the recorded rainfall intensity. Nevertheless, there is a strong indication of rainfall influence from November 2017 until March 2018. The Puncak Pass area constantly moved in this range of time.

The retrievement of 3D vectors is using two independent InSAR look directions under the slope aspect assumption estimated by the OLS estimator. The north-south component is assumed as a projection from its east-west component utilizing the aspect angle. We introduce a fusion between the surface-parallel-slope and the slope aspect to improve the scalar value of d_N component. The application of our method can be further examined to other geophysical phenomena that have the characteristics of movement parallel to the down-slope, such as, monitoring of debris flow, glacier flow, and volcano activity.

Two approaches combining PSs from the ascending and the descending data are the nearest-neighbor and surface gridding method. We evaluated both methods in this case study, but the nearest-neighbor function mostly created the final results. The nearest-neighbor gridding method might lose some well-detected signals if the matched location is only found on one track. The surface method could avoid the loss of good candidate scatters utilizing the adjustable interpolation from its neighbor. Nonetheless, the control of the final matching procedure might still have a bias since its parameter is taken by the amplitude dispersion index (ADI) either from ascending or descending data. Hence, we suggest applying the R-Index computation (Notti et al., 2014) to choose correctly which orbit's direction is the best to observe the slope geometry. The slope assumption only works for a motion parallel to the down-slope direction. Even for landslide studies, the surface of rupture might be more complicated to be illustrated only based on the slope aspect generated by DEM. The landslide might occur not only on one slide surface but also on compound slides. It would be better that the third assumption is based on its local characteristics considering a local geophysical survey.

As a geo-technique application to recognize the slope instability especially for the active and suspended landslide classification, the exploitation of InSAR spaceborne is limited to the LOS view, but the problem could be overcome by applying different tracks of SAR data. Although it is better to retrieve the full 3D field displacement using incorporation from other geodetic tools, the flow assumption could be another option to interpret the missing component of d_N at least for movements along one planar slide. Nevertheless, the assessment of 3D vectors displacement is, yet, difficult to determine types and style of movement since how the landslide movement distributed from the rupture surface to the displaced mess is restricted due to lack of PS points found in the area covered by dense vegetation.

Chapter 7

Summary

The Persistent scatters (PS) has proven widely for Geo-Applications to overcome the signal decorrelation problem in conventional interferometric synthetic aperture radar (InSAR) technique. In the beginning, the PS application is limited only in the urban area, but in recent years the development of PS algorithm using the small baseline network named SB-SDFP has been improved and could be implemented in the case study located in rural and agricultural areas where human-made structures are mostly absent on the earth's surface.

This dissertation described an implementation of SB-SDFP in the Ciloto landslides application which some parts of the locations are covered by vegetation. We established the time series InSAR analysis and retrieving into 3D vectors displacement to examine geometrically the slope movement's behavior in Ciloto. This thesis is divided into several following steps for achieving the research purpose.

- Considering the potential atmospheric phase delay in the mountainous study area, we examined the tropospheric phase delay correction using the power-law phase-based method as a better option than using filtering in the spatially correlated term. This correction was applied for Sentinel-1 SAR data processing.
- The multiband and temporal SAR data from ERS1/2, ALOS PALSAR and Sentinel-1 were processed progressively for detecting the ground movement from 1996 to 2018 (noted: there are time gaps due to non-accessible SAR data).
- The retrieved 3D vectors displacement under the slope aspect assumption, implemented on `PS_DISP`, is introduced by the utilization of two non-parallel tracks and the assumption of the slope aspect, especially to generate the north-south component as a *pseudo* value.
- All of the source codes for this work are available on *github* which are: `gmtsar2stamps_sbas` is a bundled script to convert the generated interferograms from GMTSAR to the StaMPS environment to further analyze the phase stability using the SB-SDFP algorithm; `INSAR_G2S` is the automatic program to process the Sentinel-1 dataset both for the PS and SB methods; and `PS_DISP` is a bundled script written in shell and Matlab codes to estimate the 3D-field displacement (see Appendix. B).

Regarding the InSAR time series result, we conclude that generally, the Ciloto area has moved in the first and second velocity classes which are extremely slow (± 15 mm/year) and very slow (± 1.6 m/year), respectively. From the field trip's outcome, some cracks in the street and buildings were found in the Puncak Pass and the Puncak Highway area, but some permanent structures were undamaged by movement. However, those class velocities could be consistently altered to the rapid until extremely rapid velocity class (± 1.8 m/hour) if there are no proper precautions. The successive Puncak Pass landslides verified this issue that occurred in February and March 2018 which the events destroyed the local structures, possessions, and equipment. Fortunately, the escape evacuation of local netizen was still possible.

7.1 Limitations

This work also addresses the main limitations for all of the completed data processing in this research, which are:

- The power-law method is successfully applied when the interferogram has the relative delays appropriate to the power-law function. If the phase delay is subjected to the turbulent variations and local weather instead of the stratified term, the subtracted phase correction might be under or overestimation of the tropospheric phase delay.
- A rapid landslide movement exceeds the range of interferogram fringe is not detectable by the InSAR technique due to the loss of coherence between acquisitions. Although we could detect the states of the landslide's activity, especially for the active and the suspended landslide classes, and predetermine the slip surface assumed as a translational slide, it is still challenging to regulate the distribution of the landslide's activity. The reason is that some parts of areas are suffered by decorrelated signals leading to the unavailable PS distribution. Moreover, it is also a lack of ground data collection in the observed areas to validate the InSAR result.
- Regarding 3D vectors displacement, the use of two orbits SAR data and the moving assumption parallel to slope face generate a *pseudo* value for the north-south component. The assumption of movement yield is a projection of the east-west component. The scalar of the north-south vector might be under or overestimated since it depends only on the slope aspect angle. The fusion method between the surface-parallel-flow algorithm and the quadrant of the slope aspect was introduced to improve the retrieving 3D vectors displacement.

7.2 Future Directions

In this thesis, only the SB-SDFP algorithm was exploited. Although in the simulation I explored other algorithms, such as the PS algorithm by Hooper et al., 2004 and the SBAS method by Berardino et al., 2002, Schmidt et al., 2003, I did not use the result of these algorithms for the final assessment of the slope movement in Ciloto. The results from PS and SBAS algorithms were not sufficient enough to detect the PS ground points in rural and agricultural regions. However, it is recommended exploiting other algorithms that also aim to find persistent natural objects in the likely environment of Ciloto. For instance, the Coherent Pixels Technique (CPT) developed by Mora et al., 2003 then improved by Zhang et al., 2012, called the Temporarily Coherent point (TCP) InSAR. Another potential advanced InSAR method is SqueeSAR developed by Ferretti et al., 2011 which the algorithm is a jointly process PS and Distributed Scatters (DS) which takes into account their different statistical behavior.

For the APS correction, we found that a large case study is more beneficial than a small area in consideration of the subtraction of phase delay. The source of phase delay varies on each interferogram regarding the spatial and temporal term. Moreover, the complex atmospheric behavior might not only be characterized by the systematic component, for example, behaving into a stratified layer due to the different altitudes, but also the stochastic component, for example, the effect of local weather and climate. Therefore, if suitable external supporting data is available, it is better to combine the phase-based, the spectrometer, and the weather model method statistically to each interferogram in order to minimize the under or over phase delay estimation.

We exploited the Ciloto district to evaluate the slow movement's behavior and quantify the kinematics of active landslides using InSAR techniques. Generally, the results are quietly satisfying regarding the targets that I would like to achieve at the beginning of this doctoral research. The final assessments reported valuable information for the prevention and mitigation of ground instability. For instance, the surrounding area in Puncak Highway Km. 80 has constantly moved to open-field and residential areas. Hence, the local government should take precautions to hinder the landslide hazard endangering human life and destroying infrastructures. Furthermore, it is also highly recommended to monitor accurately and continuously the landslide deformation in the Ciloto district using an integration of the InSAR technique and other ground-geodetic measurements. Regarding the capability of InSAR measurement, the set-up corner reflector at prime spots such as in areas with dense vegetation cover is necessary to solve unavailable PS ground points.

Appendix A

Detail Measurement

A.1 Piezometer Measure

TABLE A.1: Piezometer Measure; Pore Water Pressure Ratio (Pangabean et al., 1998) and (Rachman et al., 2001)

Point	Lithology	Depth (m)	r_u							
			May 1993	Aug 1993	Jan 1995	May 1995	Aug 1997	Oct 1997	Dec 1997	Jun-Jul 2001
CP1	clay, sand, gravel	-4.4	0.37	0.38	0	0	0	0	0	0
CP2	shale clay (slide)	-9.3	0.33	0.37	0.39	0.409	0.59	0.62	0.64	0.58
CP3	silty sand	-7.4	0.54	0.51	0.55	0.383	0.17	0.13	0.17	0.31
CP4	silty sand, gravel	-7.35	0.16	0.38	0.39	0.356	0.57	0.49	0.54	0
CP5	silt loam	-13.5	0.48	0.48	0.49	0.43	0	0	0	0
CP6	silty sand, silt	-12	0.4	0.34	0.39	0.369	0.46	0.45	0.55	0
CP7	silty sand, silt	-12	0	0	0.42	0.347	0.57	0.55	0.64	0.55
CP8	silty sand	-8	0	0	0.42	0.356	0.61	0.52	0.52	0.52

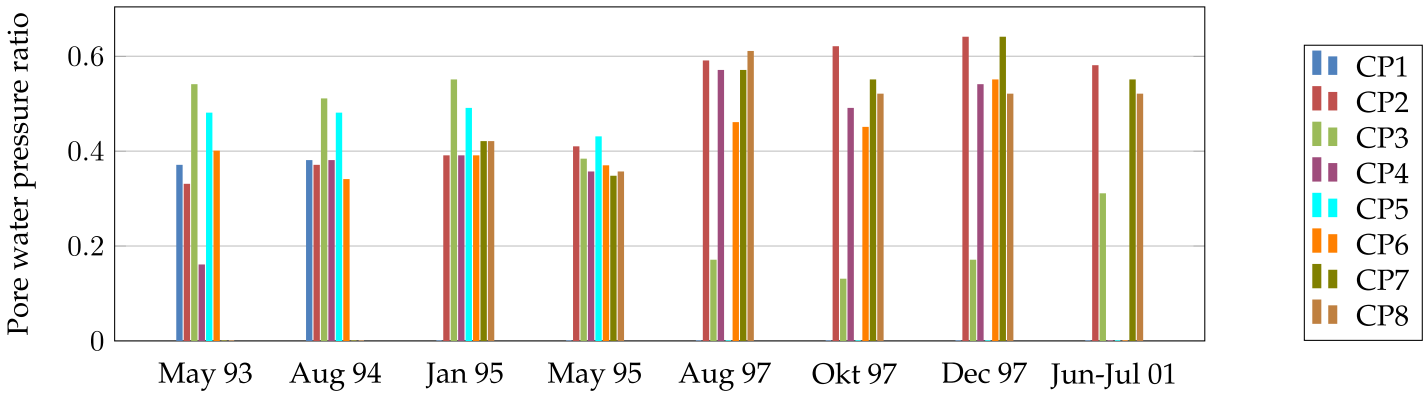

TABLE A.2: Subsurface Soil Stress (Pangabean et al., 1998) and (Rachman et al., 2001)

Point	Lithology	Depth (m)	σ_v							
			May 1993	Aug 1993	Jan 1995	May 1995	Aug 1997	Oct 1997	Dec 1997	Jun-Jul 2001
CP1	clay, sand, gravel	-4.4	3.2	0	0	0	0	0	0	0
CP2	shale clay (slide)	-9.3	5.86	6.66	6.9	7.25	0.06	0.05	0.27	8.3
CP3	silty sand	-7.4	7.726	7.19	7.86	13.56	0.54	0.13	0.2	3.9
CP4	silty sand, gravel	-7.35	2.25	5.42	5.53	6.31	0.11	0.34	0.38	0
CP5	silt loam	-13.5	12.56	12.5	12.64	7.17	0	0	0	0
CP6	silty sand, silt	-12	9.3	6.3	0.36	8.99	0.02	0.01	0.19	0
CP7	silty sand, silt	-12	0	0	9.75	11.77	0.02	0.44	0.17	11.33
CP8	silty sand	-8	0	0	9.8	6.36	0.11	0.21	0.19	6.61

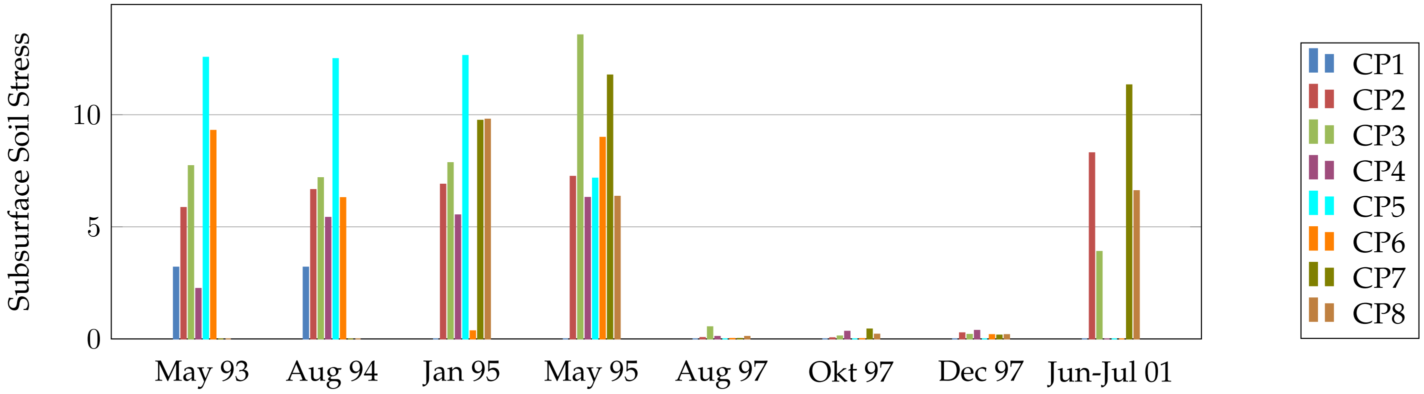
Subsurface Soil Stress
0
5
10
May 93
Aug 94
Jan 95
May 95
Aug 97
Okt 97
Dec 97
Jun-Jul 01
CP1
CP2
CP3
CP4
CP5
CP6
CP7
CP8

Appendix B

Github URL

The source codes of all my work in this doctoral thesis are available in the following links:

- `gmtsar2stamps_sbas`: https://github.com/dedetmix/gmt5sar2stamps_sbas
- `INSAR_G2S`: https://github.com/dedetmix/INSAR_G2S
- `PS_DISP`: https://github.com/dedetmix/PS_DISP

Bibliography

Abidin, H. et al. (2015). “Landslide Monitoring and Slip Surface Estimation by Geomterical Approach Case Study: Ciloto-Puncak, West Java”. *Proceedings of Slope 2015*.

Abidin, H.Z. et al. (2007). “Studying landslide displacements in the Ciloto area (Indonesia) using GPS surveys”. *Journal of Spatial Science* 52.1, pp. 55–63. DOI: `10.1080/14498596.2007.9635100`.

Abramson, L.W. et al. (1995). *Slope stability and stabilization methods*. John Wiley and Sons, New York, NY (United States).

Agram, P. S. and M. Simons (2015). “A noise model for InSAR time series”. *Journal of Geophysical Research: Solid Earth* 120.4. 2014JB011271, pp. 2752–2771. ISSN: 2169-9356. DOI: `10.1002/2014JB011271`.

Agram, Piyush Shanker (2010). “Persistent Scatterer Interferometry in Natural Terrain”. PhD thesis. Standford University.

Ahnert, Frank (1996). *Einführung in die Geomorphologie*. UTB, Stuttgart.

Aleotti, Pietro (2004). “A warning system for rainfall-induced shallow failures”. *Engineering Geology* 73.3. Rainfall-triggered landslides and debris flows, pp. 247 –265. ISSN: 0013-7952. DOI: `https://doi.org/10.1016/j.enggeo.2004.01.007`.

Allan, C. R., L. Silver, and F. G. Stehli (1960). “Agua Blanca fault, A Major Transverse Structure of Northern Baja California, Mexico”. *Geo Science World Bulletin* 71.4, pp. 457–482.

Antonello, G. et al. (2004). “Ground-based SAR interferometry for monitoring mass movements”. *Landslides* 1.1, pp. 21–28. ISSN: 1612-5118. DOI: `10.1007/s10346-003-0009-6`.

Attema, E., G. Levrini, and M. Davidson (2006). “Sentinel-1 ESA’s New European Radar Observatory”. *Proceeding of the Second International Workshop The Future of Remote Sensing, ISPRS Archives*. Ed. by J. Everaerts. Vol. XXXVI-1. W44.

Attema, Evert et al. (2010). “Sentinel-1 Mission Overview”. Vol. 1, pp. 1 –4. DOI: `10.1109/IGARSS.2009.5416921`.

Baldo, Marco et al. (2009). “LIDAR monitoring of mass wasting processes: The Radicofani landslide, Province of Siena, Central Italy”. *Geomorphology* 105.3, pp. 193 –201. ISSN: 0169-555X. DOI: `https://doi.org/10.1016/j.geomorph.2008.09.015`.

Bamler, R. and P. Hartl (1998). “Synthetic Aperture Radar Interferometry”. *Inverse Problems* 14.4, R1–54.

Barbot, Sylvain, Yariv Hamiel, and Yuri Fialko (2008). “Space geodetic investigation of the coseismic and postseismic deformation due to the 2003 Mw7.2 Altai earthquake: Implications for the local lithospheric rheology”. *Journal of Geophysical Research: Solid Earth* 113.B3. B03403, n/a–n/a. ISSN: 2156-2202. DOI: `10.1029/2007JB005063`.

Bekaert, D. P. S., A. Hooper, and T. J. Wright (2015a). “A spatially variable power law tropospheric correction technique for InSAR data”. *Journal of Geophysical Research: Solid Earth* 120.2, pp. 1345–1356. DOI: `10.1002/2014JB011558`.

Bekaert, D. P. S. et al. (2017). “Spaceborne Synthetic Aperture Radar Survey of Subsidence in Hampton Roads, Virginia (USA)”. *Scientific Reports* 7.1, pp. 14752–. ISSN: 2045-2322.

Bekaert, D.P.S. et al. (2015b). “Statistical comparison of InSAR tropospheric correction techniques”. *Remote Sensing of Environment* 170, pp. 40 –47. ISSN: 0034-4257. DOI: `https://doi.org/10.1016/j.rse.2015.08.035`.

Berardino, P. et al. (2002). “A new algorithm for surface deformation monitoring based on small baseline differential SAR interferograms”. *IEEE Transactions on Geoscience and Remote Sensing* 40.11, pp. 2375–2383. ISSN: 0196-2892. DOI: 10.1109/TGRS.2002.803792.

Berti, M. et al. (2013). “Automated classification of Persistent Scatterers Interferometry time series”. *Natural Hazards and Earth System Sciences* 13.8, pp. 1945–1958. DOI: 10.5194/nhess-13-1945-2013.

BNPB (2018). *Info Bencana - Informasi Kebencanaan Bulanan Teraktual*. Indonesian. URL: https://bnpb.go.id/uploads/24/info-bencana-november-2018.pdf.

Bovenga, F. et al. (2012). “Using COSMO/SkyMed X-band and ENVISAT C-band SAR interferometry for landslides analysis”. *Remote Sensing of Environment* 119, pp. 272 –285. ISSN: 0034-4257. DOI: https://doi.org/10.1016/j.rse.2011.12.013.

BPPTKG, Balai Penyelidikan dan Pengembangan Teknologi Kebencanaan Geologi (2017). *Extensometer Data Records*. Indonesia. Center for Investigation and Technology Development of Geological Disaster. URL: http://www.merapi.bgl.esdm.go.id/gertan/grafik.php?ids=28.

Brakke, Kenneth A. (1992). “The Surface Evolver”. *Experimental Mathematics* 1.2, pp. 141–165. DOI: 10.1080/10586458.1992.10504253.

Brunsden, D. and J. B. Thornes (1979). “Landscape Sensitivity and Change”. *Transactions of the Institute of British Geographers* 4.4, pp. 463–484. ISSN: 00202754, 14755661.

Burrough, P. A. and R. A McDonell (1998). *Principles of Geographical Information Systems*. Oxford University Press, New York.

Caine, Nel (1980). “The Rainfall Intensity - Duration Control of Shallow Landslides and Debris Flows”. *Geografiska Annaler: Series A, Physical Geography* 62.1-2, pp. 23–27. DOI: 10.1080/04353676.1980.11879996.

Canli, Ekrem et al. (2015). “Permanent 3D Laser Scanning System for Alpine Hillslope Instabilities”, pp. 1–1.

Carlà, Tommaso et al. (2018). “Integration of ground-based radar and satellite InSAR data for the analysis of an unexpected slope failure in an open-pit mine”. *Engineering Geology* 235, pp. 39 –52. ISSN: 0013-7952. DOI: https://doi.org/10.1016/j.enggeo.2018.01.021.

Casagli, N. et al. (2003). “Ground-based SAR interferometry as a tool for landslide monitoring during emergencies”. *IGARSS 2003. 2003 IEEE International Geoscience and Remote Sensing Symposium. Proceedings (IEEE Cat. No.03CH37477)*. Vol. 4, 2924–2926 vol.4. DOI: 10.1109/IGARSS.2003.1294633.

Casale, R. et al. (1994). *Temporal Occurrence and Forecasting of Landslides in the European Community: Final Report. Part 1, Methodology (reviews) for the Temporal Study of Landslides. Part 2, Case Studies of the Temporal Occurrence of Landslides in the European Community*. European Commission.

Cascini, Leonardo, Gianfranco Fornaro, and Dario Peduto (2010). “Advanced low- and full-resolution DInSAR map generation for slow-moving landslide analysis at different scales”. *Engineering Geology* 112.1, pp. 29 –42. ISSN: 0013-7952. DOI: https://doi.org/10.1016/j.enggeo.2010.01.003.

Casu, F., M. Manzo, and R. Lanari (2006). “A quantitative assessment of the SBAS algorithm performance for surface deformation retrieval from DInSAR data”. *Remote Sensing of Environment* 102.3, pp. 195 –210. ISSN: 0034-4257. DOI: https://doi.org/10.1016/j.rse.2006.01.023.

Chen, C. W. and H. A. Zebker (2002). “Phase unwrapping for large SAR interferograms: statistical segmentation and generalized network models”. *IEEE Transactions on Geoscience and Remote Sensing* 40.8, pp. 1709–1719. ISSN: 0196-2892. DOI: 10.1109/TGRS.2002.802453.

Chen, Curtis and Howard Zebker (2001). “Two-dimensional phase unwrapping with use of statistical models for cost functions in nonlinear optimization”. *J. Opt. Soc. Am. A* 18.2, pp. 338–351. DOI: 10.1364/JOSAA.18.000338.

Chen, Curtis W. and Howard A. Zebker (2000). "Network approaches to two-dimensional phase unwrapping: intractability and two new algorithms". *J. Opt. Soc. Am. A* 17.3, pp. 401–414. DOI: 10.1364/JOSAA.17.000401.

Chen, Jingyi et al. (2016). "Confined aquifer head measurements and storage properties in the San Luis Valley, Colorado, from spaceborne InSAR observations". *Water Resources Research* 52.5, pp. 3623–3636. DOI: 10.1002/2015WR018466.

Cheung, P.Y., M.C. Wong, and H.Y. Yeung (2006). "Application of Rainstorm Nowcast to Real-time Warning of Landslide Hazards in Hong Kong". *WMO PWS Workshop on Warnings of Real-Time Hazards by Using Nowcasting Technology*, pp. 9–13.

Cigna, Francesca, Silvia Bianchini, and Nicola Casagli (2013). "How to assess landslide activity and intensity with Persistent Scatterer Interferometry (PSI): the PSI-based matrix approach". *Landslides* 10.3, pp. 267–283. ISSN: 1612-5118. DOI: 10.1007/s10346-012-0335-7.

Colesanti, Carlo and Janusz Wasowski (2006). "Investigating landslides with space-borne Synthetic Aperture Radar (SAR) interferometry". *Engineering Geology* 88.3, pp. 173 –199. ISSN: 0013-7952. DOI: https://doi.org/10.1016/j.enggeo.2006.09.013.

Corsini, A. et al. (2009). "Coupling geomorphic field observation and LIDAR derivatives to map complex landslides". *Proceedings of the landslide processes conference, 6–7 February 2009, Strasbourg*.

Costantini, M. and P. A. Rosen (1999). "A generalized phase unwrapping approach for sparse data". *IEEE 1999 International Geoscience and Remote Sensing Symposium. IGARSS'99*. Vol. 1, 267–269 vol.1. DOI: 10.1109/IGARSS.1999.773467.

Costantini, Marine (1998). "A novel phase unwrapping method based on network programming". *Geoscience and Remote Sensing, IEEE Transactions on* 36, pp. 813 –821. DOI: 10.1109/36.673674.

Crosetto, M. et al. (2010). "Persistent Scatterer Interferometry". *Photogrammetric Engineering & Remote Sensing* 76.9, pp. 1061–1069. ISSN: 0099-1112. DOI: doi:10.14358/PERS.76.9.1061.

Crosetto, Michele et al. (2016). "Persistent Scatterer Interferometry: A review". *ISPRS Journal of Photogrammetry and Remote Sensing* 115. Theme issue 'State-of-the-art in photogrammetry, remote sensing and spatial information science', pp. 78 –89. ISSN: 0924-2716. DOI: https://doi.org/10.1016/j.isprsjprs.2015.10.011.

Crosta, G. B. and P. Frattini (2001). "Rainfall thresholds for triggering soil slips and debris flow". *Proceedings of the 2nd EGS Plinius Conference on Mediterranean Storms. Siena, Italy*, pp. 463–487.

Cruden, D.M. and D.J. Varnes (1993). *Landslide Investigation and Mitigation, Chapter 3. Landslide Types and Processes*. Transportation and Road research board, National Academy of Science, Washington D.C.

Cummins, Phil R. (2017). "Geohazards in Indonesia: Earth science for disaster risk reduction – introduction". *Geological Society, London, Special Publications* 441.1, pp. 1–7. ISSN: 0305-8719. DOI: 10.1144/SP441.11.

Dabbiru, Lalitha, James Aanstoos, and N.H. Younan (2014). "Comparison of L-band and X-band polarimetric SAR data classification for screening earthen levees". DOI: 10.1109/IGARSS.2014.6947038.

Dai, F.C and C.F Lee (2001). "Frequency–volume relation and prediction of rainfall-induced landslides". *Engineering Geology* 59.3, pp. 253 –266. ISSN: 0013-7952. DOI: https://doi.org/10.1016/S0013-7952(00)00077-6.

Day, Robert W. (2010). *Foundation Engineering Handbook 2/E*. McGraw-Hill's AccessEngineering. McGraw-Hill Education. ISBN: 9780071740104.

Dietrich, WE, D. Bellugi, and Real de Asua R. (2001). "Land use and watersheds: human influence on hydrology and geomorphology in urban and forest areas, Water Science and Application". Ed. by Burges SJ Wigmosta MS. Wiley Online Library. Chap. 2, pp. 195–227.

Dixon, Timothy et al. (2002). “Seismic cycle and rheological effects on estimation of present-day slip rates for the Agua Blanca and San Miguel-Vallecitos faults, northern Baja California, Mexico”. *Journal of Geophysical Research: Solid Earth* 107.B10, ETG 5–1–ETG 5–23. DOI: `10.1029/2000JB000099`.

Doin, M.-P. et al. (2009). “Corrections of stratified tropospheric delays in SAR interferometry: Validation with global atmospheric models”. *Journal of Applied Geophysics* 69.1. Advances in SAR Interferometry from the 2007 Fringe Workshop, pp. 35 –50. ISSN: 0926-9851. DOI: `https://doi.org/10.1016/j.jappgeo.2009.03.010`.

Doin, Marie-Pierre et al. (2011). “Presentation of the small baseline NSBAS processing chain on a case example: The Etna deformation monitoring from 2003 to 2010 using Envisat data”.

Ebdon, David (1985). *Statistics in Geography*. Blackwell.

ERDAS (2010a). *Radar Interferometry - User's Guide*. ERDAS, Inc. USA.

— (2010b). *SAR Interferometry*. ERDAS. URL: `ftp://ftp.ecn.purdue.edu/jshan/ERDAS_Library/2011help/html/insar/wwhelp/wwhimpl/js/html/wwhelp.htm?href=INSAR_Wizard_SpectralShift.html`.

Eriksen, Harald Øverli et al. (2017). “Visualizing and interpreting surface displacement patterns on unstable slopes using multi-geometry satellite SAR interferometry (2D InSAR)”. *Remote Sensing of Environment* 191, pp. 297 –312. ISSN: 0034-4257. DOI: `https://doi.org/10.1016/j.rse.2016.12.024`.

ESA, European Space Agency (2019a). *Envisat Mission Summary*. European Space Agency. URL: `https://earth.esa.int/web/guest/missions/esa-eo-missions/envisat/mission-summary`.

— (2019b). *ERS Design for SAR Image Mode*. European Space Agency. URL: `https://earth.esa.int/web/guest/missions/esa-operational-eo-missions/ers/instruments/sar/design`.

— (2019c). *ERS Mission Summary*. English. European Space Agency. URL: `https://earth.esa.int/web/guest/missions/esa-eo-missions/ers/mission-summary`.

— (2019d). *Sentinel-1 Mission*. English. European Space Agency. URL: `https://earth.esa.int/web/guest/missions/esa-operational-eo-missions/sentinel-1`.

Fattahi, Heresh and Falk Amelung (2015). “InSAR bias and uncertainty due to the systematic and stochastic tropospheric delay”. *Journal of Geophysical Research: Solid Earth* 120.12, pp. 8758–8773. DOI: `10.1002/2015JB012419`.

Ferretti, A., C. Prati, and F. Rocca (2001). “Permanent scatterers in SAR interferometry”. *IEEE Transactions on Geoscience and Remote Sensing* 39.1, pp. 8–20. ISSN: 0196-2892. DOI: `10.1109/36.898661`.

Ferretti, A. et al. (2011). “A New Algorithm for Processing Interferometric Data-Stacks: SqueeSAR”. *IEEE Transactions on Geoscience and Remote Sensing* 49.9, pp. 3460–3470. ISSN: 0196-2892. DOI: `10.1109/TGRS.2011.2124465`.

Ferretti, Alessandro et al. (2007). *InSAR Principles: Guidelines for SAR Interferometry Processing and Interpretation*. Ed. by Karen Fletcher. ESA Publications.

Ferretti, Allesandro (2014). *Satellite InSAR Data. Reservoir Monitoring from Space*. European Association of Geoscientist and Engineers.

Fetene, Fasil Beyene (2014). “Landslide monitoring in mountainous regions based on high resolution and differential radar interferometry and GIS methods”. PhD thesis. Technische Universität Clausthal.

Fialko, Yuri, Mark Simons, and Duncan Agnew (2001). “The complete (3-D) surface displacement field in the epicentral area of the 1999 MW7.1 Hector Mine Earthquake, California, from space geodetic observations”. *Geophysical Research Letters* 28.16, pp. 3063–3066. DOI: `10.1029/2001GL013174`.

Fuhrmann, Thomas and Matthew C. Garthwaite (2019). “Resolving Three-Dimensional Surface Motion with InSAR: Constraints from Multi-Geometry Data Fusion”. *MDPI Journal of Remote Sensing* 11.3, p. 241. DOI: `https://doi.org/10.3390/rs11030241`.

Funning, Gareth J. et al. (2005). “Surface displacements and source parameters of the 2003 Bam (Iran) earthquake from Envisat advanced synthetic aperture radar imagery”. *Journal of Geophysical Research: Solid Earth* 110.B9. DOI: `10.1029/2004JB003338`.

Gabriel, Aandrew K. and Richard M. Goldstein (1988). “Crossed orbit interferometry: theory and experimental results from SIR-B”. *International Journal of Remote Sensing* 9.5, pp. 857–872. DOI: `10.1080/01431168808954901`.

Gabriel A. K., R. M. Goldstein and H. A. Zebker (1989). “Mapping Small Elevation Changes over Large Areas: Differential Radar Interferometry”. *Journal of Geophysical Research* 94.b7, 9183 – 91.

Gatelli, F. et al. (1994). “The wavenumber shift in SAR interferometry”. *IEEE Transactions on Geoscience and Remote Sensing* 32.4, pp. 855–865. ISSN: 0196-2892. DOI: `10.1109/36.298013`.

Godt, Jonathan W., Rex L. Baum, and Alan F. Chleborad (2006). “Rainfall characteristics for shallow landsliding in Seattle, Washington, USA”. *Earth Surface Processes and Landforms* 31.1, pp. 97–110. DOI: `10.1002/esp.1237`.

Goldstein, R. M., H. A. Zebker, and C. L. Werner (1988). “Satellite radar interferometry: Two-dimensional phase unwrapping”. *Radio Science* 23.4, pp. 713–720. ISSN: 1944-799X. DOI: `10.1029/RS023i004p00713`.

Goldstein, R. M., H. A. Zebker, and T. P. Barnett (1989). “Remote Sensing of Ocean Currents”. *Science* 246.4935, pp. 1282–1285. ISSN: 0036-8075. DOI: `10.1126/science.246.4935.1282`.

Goldstein, Richard M. and Charles L. Werner (1998). “Radar interferogram filtering for geophysical applications”. *Geophysical Research Letters* 25.21, pp. 4035–4038. DOI: `10.1029/1998GL900033`.

Gong, Wenyu et al. (2016). “Comparison of Small Baseline Interferometric SAR Processors for Estimating Ground Deformation”. *Remote Sensing* 8.4. ISSN: 2072-4292. DOI: `10.3390/rs8040330`.

González, Pablo J. and José Fernández (2011). “Error estimation in multitemporal InSAR deformation time series, with application to Lanzarote, Canary Islands”. *Journal of Geophysical Research: Solid Earth* 116.B10. DOI: `10.1029/2011JB008412`.

Graham, L. C. (1974). “Synthetic interferometer radar for topographic mapping”. *Proceedings of the IEEE* 62.6, pp. 763–768. ISSN: 0018-9219. DOI: `10.1109/PROC.1974.9516`.

Grandin, R. et al. (2016). “Three-dimensional displacement field of the 2015 Mw8.3 Illapel earthquake (Chile) from across- and along-track Sentinel-1 TOPS interferometry”. *Geophysical Research Letters* 43.6, pp. 2552–2561. DOI: `10.1002/2016GL067954`.

Guzzetti, F. et al. (2007). “Rainfall thresholds for the initiation of landslides in central and southern Europe”. *Meteorology and Atmospheric Physics* 98.3, pp. 239–267. ISSN: 1436-5065. DOI: `10.1007/s00703-007-0262-7`.

Guzzetti, Fausto et al. (2008). “The rainfall intensity–duration control of shallow landslides and debris flows: an update”. *Landslides* 5.1, pp. 3–17. ISSN: 1612-5118. DOI: `10.1007/s10346-007-0112-1`.

Hamazaki, T. (1999). *PALSAR Performance*. Doc. NBF99019. Nat. Space Develop. Agency Japan (NASDA).

Handwerger, Alexander L. et al. (2019). “A shift from drought to extreme rainfall drives a stable landslide to catastrophic failure”. *Scientific Reports* 9.1, pp. 1569–. ISSN: 2045-2322.

Hanssen, R. and R Bamler (1999). “Evaluation of Interpolation Kernels for SAR interferometry”. *Geoscience and Remote Sensing, IEEE Transactions* 37.1, pp. 318–321.

Hanssen, R.F. (2001). *Radar Interferometry: Data Interpretation and Error Analysis*. Remote Sensing and Digital Image Processing. Springer Netherlands. ISBN: 9780792369455.

Hardiyatmo, Hary Christady (2012). *Tanah Longsor dan Erosi - Kejadian dan Penanganan*. Gadjah Mada University Press.

Herrera, G. et al. (2009). “Mapping and monitoring geomorphological processes in mountainous areas using PSI data: Central Pyrenees case study”. *Natural Hazards and Earth System Sciences* 9.5, pp. 1587–1598. DOI: `10.5194/nhess-9-1587-2009`.

Herrera, Gerardo et al. (2011). “Analysis with C- and X-band satellite SAR data of the Portalet landslide area”. *Landslides* 8.2, pp. 195–206. ISSN: 1612-5118. DOI: `10.1007/s10346-010-0239-3`.

Hetland, E et al. (2012). “Multiscale InSAR Time Series (MInTS) analysis of surface deformation”. *Journal of Geophysical Research (Solid Earth)* 117, pp. 2404–. DOI: `10.1029/2011JB008731`.

Hooper, A., P. Segall, and H. Zebker (2007a). “Persistent scatterer interferometric synthetic aperture radar for crustal deformation analysis, with application to Volcán Alcedo, Galápagos”. *Journal of Geophysical Research: Solid Earth* 112.B7. B07407, n/a–n/a. ISSN: 2156-2202. DOI: `10.1029/2006JB004763`.

Hooper, Andrew (2008). “A multi-temporal InSAR method incorporating both persistent scatterer and small baseline approaches”. *Geophysical Research Letters* 35.16. L16302, n/a–n/a. ISSN: 1944-8007. DOI: `10.1029/2008GL034654`.

Hooper, Andrew et al. (2004). “A new method for measuring deformation on volcanoes and other natural terrains using InSAR persistent scatterers”. *Geophysical Research Letters* 31.23. DOI: `10.1029/2004GL021737`.

Hooper, Andrew and Howard A. Zebker (2007b). “Phase unwrapping in three dimensions with application to InSAR time series”. *J. Opt. Soc. Am. A* 24.9, pp. 2737–2747. DOI: `10.1364/JOSAA.24.002737`.

Hooper, Andrew et al. (2012). “Recent advances in SAR interferometry time series analysis for measuring crustal deformation”. *Tectonophysics* 514-517, pp. 1 –13. ISSN: 0040-1951. DOI: `https://doi.org/10.1016/j.tecto.2011.10.013`.

Hooper, Andrew John (2006). “Persistent Scatterer Radar Interferometry for Crustal Deformation Studies and Modeling of Volcanic Deformation”. PhD thesis. Stanford University.

Hu, J. et al. (2014). “Resolving three-dimensional surface displacements from InSAR measurements: A review”. *Earth-Science Reviews* 133, pp. 1 –17. ISSN: 0012-8252. DOI: `https://doi.org/10.1016/j.earscirev.2014.02.005`.

Huisman, Otto and Rolf A. de By (2009). *Principles of Geographic Information Systems*. Ed. by Otto Huisman and Rolf A. de By. The International Institute for Geo-Information Science and Earth Observation (ITC).

Hunt, B. R. (1979). “Matrix formulation of the reconstruction of phase values from phase differences”. *J. Opt. Soc. Am.* 69.3, pp. 393–399. DOI: `10.1364/JOSA.69.000393`.

Isya, N. H. et al. (2018). “Comparison of Power Law Tropospheric Correction for Time Series InSAR Application”. *Wissenschaftlich-Technische Jahrestagung der DGPF und PFGK18 Tagung in München*. 27. Deutschen Gesellschaft für Photogrammetrie,Fernerkundung und Geoinformation e.V., pp. 483 –507.

Isya, Noorlaila, W Niemeier, and Markus Gerke (2019). “3D Estimation of Slow Ground Motion Using InSAR and The Slope Aspect Assumption, A Case Study: The Puncak Pass Lanslide, Indonesia”. *ISPRS Annals of Photogrammetry, Remote Sensing and Spatial Information Sciences* IV-2/W5, pp. 623–630. DOI: `10.5194/isprs-annals-IV-2-W5-623-2019`.

Isya, Noorlaila H. and Muhammad Taufik (2014). “Optimization of DInSAR Results Using Geographic Information System in Potential Landslide Areas”. *Proceedings of International Conference Data Mining, Civil and Mechanical Engineering*.

Jaboyedoff, M. et al. (2004). “Toward preliminary hazard assessment using DEM topographic analysis and simple mechanical modeling by means of sloping local base level”. *Proceedings of Symposium 1st Advances in Geomorphological Mapping and 9th International Symposium of Landslides RiO 2004*.

Jaboyedoff, Michel et al. (2009). “Use of terrestrial laser scanning for the characterization of retrogressive landslides in sensitive clay and rotational landslides in river banks”. *Canadian Geotechnical Journal* 46.12, pp. 1379–1390. DOI: `10.1139/T09-073`.

Jaboyedoff, Michel et al. (2012). “Use of LIDAR in landslide investigations: a review”. *Natural Hazards* 61.1, pp. 5–28. ISSN: 1573-0840. DOI: `10.1007/s11069-010-9634-2`.

Joughin, I. R., R. Kwok, and M. A. Fahnestock (1998). “Interferometric estimation of three-dimensional ice-flow using ascending and descending passes”. *IEEE Transactions on Geoscience and Remote Sensing* 36.1, pp. 25–37. ISSN: 0196-2892. DOI: `10.1109/36.655315`.

Joughin, Ian, Ron Kwok, and Mark Fahnestock (1996). “Estimation of ice-sheet motion using satellite radar interferometry: method and error analysis with application to Humboldt Glacier, Greenland”. *Journal of Glaciology* 42.142, 564–575. DOI: `10.3189/S0022143000003543`.

Jung, J., D. Kim, and S. Park (2014). “Correction of Atmospheric Phase Screen in Time Series InSAR Using WRF Model for Monitoring Volcanic Activities”. *IEEE Transactions on Geoscience and Remote Sensing* 52.5, pp. 2678–2689. ISSN: 0196-2892. DOI: `10.1109/TGRS.2013.2264532`.

Kalia, Andre (2018). “Classification of Landslide Activity on a Regional Scale Using Persistent Scatterer Interferometry at the Moselle Valley (Germany)”. *Remote Sensing* 10, p. 1880. DOI: `10.3390/rs10121880`.

Kampes, Bert M. (2006). *Radar Interferometry ; Persistent Scatterer Technique*. Vol. 12. Springer Netherlands.

Kampes, Bert M., Ramon F. Hannsen, and Zbigniew Perski (2003). “Radar interferometry with public domain tools”. *Proceedings of FRINGE 2003 Workshop, Fracasti, Italy*. European Space Agency, SP–550.

Klooster, C.G.M. van ’t (2011). “ERS-1, European Remote-Sensing Satellite Was Launched 20 Years Ago”.

Kotchoni, D. O. Valerie et al. (2019). “Relationships between rainfall and groundwater recharge in seasonally humid Benin: a comparative analysis of long-term hydrographs in sedimentary and crystalline aquifers”. *Hydrogeology Journal* 27.2, pp. 447–457. ISSN: 1435-0157. DOI: `10.1007/s10040-018-1806-2`.

Lanari, Riccardo et al. (2007). “An Overview of the Small BAseline Subset Algorithm: A DInSAR Technique for Surface Deformation Analysis”. *Deformation and Gravity Change: Indicators of Isostasy, Tectonics, Volcanism, and Climate Change*. Ed. by Detlef Wolf and José Fernández. Basel: Birkhäuser Basel, pp. 637–661. ISBN: 978-3-7643-8417-3.

Lee, Jong-Sen et al. (2003). “Speckle filtering and coherence estimation of polarimetric SAR interferometry data for forest applications”. *IEEE Transactions on Geoscience and Remote Sensing* 41.10, pp. 2254–2263. ISSN: 0196-2892. DOI: `10.1109/TGRS.2003.817196`.

Li, F.K. and R.M. Goldstein (1990). “Studies of Multibaseline Spaceborne Interferometric Synthetic Aperture Radars”. *Geoscience and Remote Sensing, IEEE Transactions* 1.28, pp. 88–97.

Li, Zhengxiao and James Bethel (2008). “Image Coregistration in SAR Interferometry”. *The International Archives of the Photogrammetry, Remote Sensing and Spatial Information Science* XXXVII.Part B1.

Li, Zhenhong et al. (2009). “Advanced InSAR atmospheric correction: MERIS/MODIS combination and stacked water vapour models”. *International Journal of Remote Sensing* 30.13, pp. 3343–3363. DOI: `10.1080/01431160802562172`.

Liu, Peng et al. (2015). “Land Subsidence over Oilfields in the Yellow River Delta”. *Remote Sensing* 7.2, pp. 1540–1564. ISSN: 2072-4292. DOI: `10.3390/rs70201540`.

Lu, Zhong (2007). “ALOS PALSAR Interferometric Synthetic Aperture Radar (InSAR)”. *Alaska Satellite Facility News and Notes* 4.4.

Lyons, Suzanne and David Sandwell (2003). “Fault creep along the southern San Andreas from interferometric synthetic aperture radar, permanent scatterers, and stacking”. *Journal of Geophysical Research: Solid Earth* 108.B1. DOI: `10.1029/2002JB001831`.

Mansour, Zaagane et al. (2015). “Morphometric analysis of landslides in the Ouarsenis area (west Algeria): implications for establishing a relationship between tectonic, geomorphologic, and hydraulic indexes”. *Arabian Journal of Geosciences* 8.9, pp. 6465–6482. ISSN: 1866-7538. DOI: 10.1007/s12517-014-1711-5.

Marinkovic, P. and Y. Larsen (2015). “On Resolving the Local Oscillator Drift Induced Phase Ramps in ASAR and ERS1/2 Interferometric Data - The Final Solution”. *Fringe 2015 workshop (ESA SP-731), Poster Session*.

Martinez, M.L. and N. P. Psuty (2007). *Coastal Dunes: Ecology and Conservation. Ecological Studies*. 301-308. Springer Berlin Heidelberg.

Massonnet, D. et al. (1993). “The Displacement Field of the Landers Earthquake mapped by Radar Interferometry”. *Nature* 364, pp. 138–142.

Massonnet, Didier, Pierre Briole, and Alain Arnaud (1995). “Deflation of Mount Etna monitored by spaceborne radar interferometry”. *Nature* 375.6532, pp. 567–570. ISSN: 1476-4687.

Massonnet, Didier and Kurt L. Feigl (1998). “Radar interferometry and its application to changes in the Earth’s surface”. *Reviews of Geophysics* 36.4, pp. 441–500. DOI: 10.1029/97RG03139.

Meyer, Franz Josef (2003). “Simultane Schaetzung von Topographie und Dynamik polarer Gletscher aus multi-temporalen SAR Interferogrammen”. PhD thesis. Institut fuer Photogrammetrie und Kartographie, Technische Universitaet Muenchen.

Mohr, Johan J., Niels Reeh, and Søren N. Madsen (1998). “Three-dimensional glacial flow and surface elevation measured with radar interferometry”. *Nature* 391, pp. 273–.

Monti-Guarnieri, A. and P. Guccione (2001). “Optimal "focusing" for low resolution ScanSAR”. *IEEE Transactions on Geoscience and Remote Sensing* 39.3, pp. 479–491. ISSN: 0196-2892. DOI: 10.1109/36.911107.

Mora, O., J. J. Mallorqui, and A. Broquetas (2003). “Linear and nonlinear terrain deformation maps from a reduced set of interferometric SAR images”. *IEEE Transactions on Geoscience and Remote Sensing* 41.10, pp. 2243–2253. ISSN: 0196-2892. DOI: 10.1109/TGRS.2003.814657.

Munarto, Eddie Sunaryo, Herry Vaza, and Rudy Febrijanto (2015). “Landslide Evidence Problem Solving on National Road Bandung - Jakarta at KM 18+000 in Ciloto – Puncak Pass Regions”. *Proceedings of Slope 2015*. Ed. by Paulus P. Rahardjo and Adrin Tohari. Parahyangan Catholic University.

Niemeier, W. (2008). *Ausgleichungsrechnung: Statistische Auswertemethoden*. De Gruyter.

Notti, D. et al. (2010). “Assessment of the performance of X-band satellite radar data for landslide mapping and monitoring: Upper Tena Valley case study”. *Natural Hazards and Earth System Sciences* 10.9, pp. 1865–1875. DOI: 10.5194/nhess-10-1865-2010.

Notti, Davide et al. (2014). “A methodology for improving landslide PSI data analysis”. *International Journal of Remote Sensing* 35.6, pp. 2186–2214. DOI: 10.1080/01431161.2014.889864.

Notti, Davide et al. (2015). “A User-Oriented Methodology for DInSAR Time Series Analysis and Interpretation: Landslides and Subsidence Case Studies”. *Pure and Applied Geophysics* 172.11, pp. 3081–3105. ISSN: 1420-9136. DOI: 10.1007/s00024-015-1071-4.

Ogawa, Shoji et al. (1987). “Influence of Pore Water Pressure on Landslide Occurrence”. *Landslides* 24.2, pp. 2–9. DOI: 10.3313/jls1964.24.2.

Pangabean, J and Agoes Darsoatmodjo (1998). *Hasil Pemantauan Bencana Alam Gerakan Tanah di Daerah Ciloto dan Cianjur Selatan, Daerah Tingkat II Kabupaten Cianjur Propinsi Jawa Barat*. Tech. rep. Direktorat Geologi Tata Lingkungan, Direktorat Jenderal Geologi dan Sumberdaya Mineral, Departemen Pertambangan dan Energi.

Polcari, Marco et al. (2016). “3D displacement field retrieved by integrating Sentinel-1 InSAR and GPS data: the 2014 South Napa earthquake”. *European Journal of Remote Sensing* 49.1, pp. 1–13. DOI: 10.5721/EuJRS20164901.

Purnomo, H (1993). *Hasil Pemantauan Gerakan Tanah Daerah Ciloto, Kabupaten DATI II Cianjur Jawa Barat*. Tech. rep. Direktorat Geologi Tata Lingkungan, Direktorat Jenderal Geologi dan Sumberdaya Mineral, Departemen Pertambangan dan Energi.

PVMBG (2016). *Susceptibility to landslide zone map of Cianjur Regeny, West Java Province*. Tech. rep. Centre of Volcanology, Geological Hazard Mitigation (PVMBG), Geological Agency: Ministry of Energy, and Mineral Resources.

— (2018). *The map of potential ground movement areas in Indonesia*. Indonesia. URL: `http://www.vsi.esdm.go.id/index.php/kegiatan-pvmbg/download-center/doc_details/3614-peta-prakiraan-maret-2018`.

Rachman, S. et al. (2001). *Pemantauan Bencana Alam Tanah Longsor di Kecamatan Pacet, Kabupaten Cianjur, Propinsi Jawa Barat*. Tech. rep. Direktorat Vulkanologi dan Mitigasi Bencana Geologi, Direktorat Jenderal Geologi dan Sumberdaya Mineral, Departemen Energi dan Sumber Daya Mineral.

Rafferty, J.P. (2011). *The Living Earth: Lakes and Wetlands*. Vol. 5. 132-156. Britannica Educational Publishing.

Reichenbach, P. et al. (1998). "Regional hydrological thresholds for landslides and floods in the Tiber River Basin (central Italy)". *Environmental Geology* 35.2, pp. 146–159. ISSN: 1432-0495. DOI: `10.1007/s002540050301`.

Reshef, David N. et al. (2011). "Detecting Novel Associations in Large Data Sets". *Science* 334.6062, pp. 1518–1524. ISSN: 0036-8075. DOI: `10.1126/science.1205438`.

Riedel, A. et al. (2018). "Bestimmung der Erdoberflächenbewegung mittels Radarinterferometrie nahe der Agua Blanca Störung, Baja California". *Wissenschaftlich-Technische Jahrestagung der DGPF*. Vol. 27. TU Munich.

Rieke-Zapp, D. H. and M. A. Nearing (2005). "Slope Shape Effects on Erosion". 69, pp. 1463–1471.

Rosen, P. A. et al. (2000). "Synthetic aperture radar interferometry". *Proceedings of the IEEE* 88.3, pp. 333–382. ISSN: 0018-9219. DOI: `10.1109/5.838084`.

Rosen, Paul A. et al. (2004). "Updated repeat orbit interferometry package released". *Eos, Transactions American Geophysical Union* 85.5, pp. 47–47. ISSN: 2324-9250. DOI: `10.1029/2004EO050004`.

Rosenqvist, Ake et al. (2007). "ALOS PALSAR: A Pathfinder mission for global-scale monitoring of the environment". *Geoscience and Remote Sensing, IEEE Transactions on* 45, pp. 3307 –3316. DOI: `10.1109/TGRS.2007.901027`.

Rosi, A. et al. (2013). "Landslide Characterization Using Satellite Interferometry (PSI), Geotechnical Investigations and Numerical Modelling: The Case Study of Ricasoli Village (Italy)". *International Journal of Geosciences* 4.5. DOI: `10.4236/ijg.2013.45085`.

Sadarviana, V. et al. (2010). "Karakteristik, Tipe dan Bidang Gelincir pada Zona Longsor Ciloto, Jawa Barat Berdasarkan Estimasi Metode Geodetik". *Geo-Dynamics JSDG* 20.2, pp. 117–130.

Sadarviana, Vera (2006). "Pemanfaatan Metode Geodetik untuk Mengestimasi Karakteristik Tipe dan Bidang Gelincir pada Zona Longsor, Wilayah Studi: Zona Longsor Ciloto-Puncak, Jawa Barat". PhD thesis. Institut Teknologi Bandung.

Sadarviana, Vera et al. (2014). "The GPS Data Campaign for the Slip Surface Estimation Ciloto Landslide Zone Case Study, West Java, Indonesia". *The XXV FIG International Congress 2014*. International Federation of Surveyors.

Sanchez, J. I. and H. Laur (1997). "The ERS-SAR performances, products systems". *Third ERS Symposium on Space at the service of our Environment*. Ed. by T.-D. Guyenne and D. Danesy. Vol. 414. ESA Special Publication, p. 1753.

Sandwell, David et al. (2011). *GMTSAR: An InSAR Processing System Based on Generic Mapping ToolsGMTSAR: An InSAR Processing System Based on Generic Mapping Tools*. Tech. rep. Scripps Institution of Oceanography.

Sandwell, David T. et al. (2008). "Accuracy and Resolution of ALOS Interferometry: Vector Deformation Maps of the Father's Day Intrusion at Kilauea". *IEEE Transactions on Geoscience and Remote Sensing* 46.11, pp. 3524–3534.

Scharroo, Remko and Pieter Visser (1998). "Precise orbit determination and gravity field improvement for the ERS satellites". *Journal of Geophysical Research: Oceans* 103.C4, pp. 8113–8127. ISSN: 2156-2202. DOI: `10.1029/97JC03179`.

Schlögel, Romy et al. (2015). "Landslide deformation monitoring with ALOS/PALSAR imagery: A D-InSAR geomorphological interpretation method". *Geomorphology* 231, pp. 314 –330. ISSN: 0169-555X. DOI: `https://doi.org/10.1016/j.geomorph.2014.11.031`.

Schmidt, David A. and Roland Buergmann (2003). "Time-dependent land uplift and subsidence in the Santa Clara valley, California, from a large interferometric synthetic aperture radar data set". *Journal of Geophysical Research: Solid Earth* 108.B9. 2416, n/a–n/a. ISSN: 2156-2202. DOI: `10.1029/2002JB002267`.

Schuler, Martin (2015). "Mass movement modelling over Ciloto area based on integrated GNSS and TLS observations". MA thesis. Technische Universität Wien.

Segoni, S. et al. (2009). "Towards a definition of a real-time forecasting network for rainfall induced shallow landslides". *Natural Hazards and Earth System Sciences* 9.6, pp. 2119–2133. DOI: `10.5194/nhess-9-2119-2009`.

Segoni, Samuele et al. (2015). "Integration of rainfall thresholds and susceptibility maps in the Emilia Romagna (Italy) regional-scale landslide warning system". *Landslides* 12.4, pp. 773–785. ISSN: 1612-5118. DOI: `10.1007/s10346-014-0502-0`.

Smith, E. K. and S. Weintraub (1953). "The Constants in the Equation for Atmospheric Refractive Index at Radio Frequencies". *Proceedings of the IRE* 41.8, pp. 1035–1037. ISSN: 0096-8390. DOI: `10.1109/JRPROC.1953.274297`.

Smith, W. H. F. and P. Wessel (1990). "Gridding with continuous curvature splines in tension". *Geophysics* 55.3, pp. 293–305. ISSN: 0016-8033. DOI: `10.1190/1.1442837`.

Sudrajat, Ajat and Aditia Aulia Rohman (2019). *Jawa Barat hadapi 544 bencana tanah longsor sepanjang 2018*. Indonesia. Antara. URL: `https://www.antaranews.com/berita/783233/jawa-barat-hadapi-544-bencana-tanah-longsor-sepanjang-2018`.

Sugalang (1989). "Landslide in Ciloto Area, West Java, Indonesia". MA thesis. Lulea University of Technology.

Sugalang, Sugalang (1993). "Landslide in Ciloto Area, West Java, Indonesia (Review)". *Bulletin of the Directorate of Environment Geology*. Ed. by P.H. Silitonga Ida Bagus Sudjana Adjat Sudrajat. 7. Directorate of Environmental Geology, Directorate General of Geology, Mineral Resources, Ministry of Mines, and Energy, pp. 1–9.

Sulaeman, Cecep et al. (2013). "Analisis regangan pada area gerakan tanah di Ciloto, Jawa Barat". *Jurnal Lingkungan dan Bencana Geologi* 4.2, pp. 89–99.

Sumaryono, S. T. et al. (2015). "Landslide Investigation and Monitoring at Ciloto, West Java, Indonesia". *Engineering Geology for Society and Territory - Volume 2: Landslide Processes*. Ed. by Giorgio Lollino et al. Cham: Springer International Publishing, pp. 1089–1096. ISBN: 978-3-319-09057-3. DOI: `10.1007/978-3-319-09057-3-193`.

Sun, Qian et al. (2016). "Towards Slow-Moving Landslide Monitoring by Integrating Multi-Sensor InSAR Time Series Datasets: The Zhouqu Case Study, China". *Remote Sensing* 8.11. ISSN: 2072-4292. DOI: `10.3390/rs8110908`.

Supriatna, Atip (2002). "Kajian Spasial Gerakan Tanah di KP. Baru, Desa Ciloto, Kab. Cianjur". MA thesis. Department of Geodetic Engineering, Bandung Institute of Technology.

Swain, C. J. (1976). "A FORTRAN IV program for interpolating irregularly space data using the difference equations for minimum curvature". *Coumputers and Geosciences* 1, pp. 231–240.

Tao, Qiuxiang et al. (2018). "Optimal selection and application analysis of multi-temporal differential interferogram series in StaMPS-based SBAS InSAR". *European Journal of Remote Sensing* 51. DOI: `10.1080/22797254.2018.1542977`.

Tarchi, Dario et al. (2003). "Monitoring landslide displacements by using ground-based synthetic aperture radar interferometry: Application to the Ruinon landslide in the Italian Alps". *Journal of Geophysical Research: Solid Earth* 108.B8. DOI: `10.1029/2002JB002204`.

Terzaghi, K. and Geological Society of America (GSA) (1950). *Mechanism of Landslides*. Harvard University, Department of Engineering.

Teshebaeva, Kanayim et al. (2015). "ALOS/PALSAR InSAR Time-Series Analysis for Detecting Very Slow-Moving Landslides in Southern Kyrgyzstan". *Remote Sensing* 7.7, pp. 8973–8994. ISSN: 2072-4292. DOI: `10.3390/rs70708973`.

Thayer, Gordon D. (1974). "An improved equation for the radio refractive index of air". *Radio Science* 9.10, pp. 803–807. DOI: `10.1029/RS009i010p00803`.

Tibshirani, Ryan (2013). "Data Mining: Spring 2013 - Statistics". Dept. of Statistics, Baker Hall. Chap. 11 Correlation analysis 2: Measures of correlation.

Tiebes, B. and T. Glade (2016). "Landslide early warning systems – fundamental concepts and innovative applications". *Proceeding of International Symposium on Landslides 2016, Naples, Italy*.

Usai, Stefania (2001). "A new approach for long term monitoring of deformations by differential SAR interferometry". PhD thesis. Delft University.

USGS (2004). *Landslide Types and Processes*. USGS.

Van Asch, Th. W. J. (1984). "Creep processes in landslides". *Earth Surface Processes and Landforms* 9.6, pp. 573–583. DOI: `10.1002/esp.3290090611`.

Varnes, David J. (1978). "Slope movement types and processes". Ed. by R.L Schuster and R.J Krizek. Vol. In Special Report 176: Landslides: Analysis and control. Transportation and Road research board, National Academy of Science, Washington D.C. Chap. 2, pp. 11–33.

Wegmuller, U., C. Werner, and T. Strozzi (1998). "SAR interferometric and differential interferometric processing chain". *IGARSS '98. Sensing and Managing the Environment. 1998 IEEE International Geoscience and Remote Sensing. Symposium Proceedings. (Cat. No.98CH36174)*. Vol. 2, 1106–1108 vol.2. DOI: `10.1109/IGARSS.1998.699687`.

Wei, Meng, David Sandwell, and Bridget Smith-Konter (2010). "Optimal combination of InSAR and GPS for measuring interseismic crustal deformation". *Advances in Space Research* 46.2. GNSS Remote Sensing-1, pp. 236 –249. ISSN: 0273-1177. DOI: `https://doi.org/10.1016/j.asr.2010.03.013`.

Wessel, P. et al. (2019). *The Generic Mapping tools (GMT) Man Pages*. Release 5.4.5.

Wieczorek, G. F. and T. Glade (2005). "Climatic factors influencing occurrence of debris flow". *Debris-flow Hazards and Related Phenomena*, pp. 325–362.

Wood, Simon N. (2006). *Generalized Additive Models: an introduction with R*. Chapman & Hall/CRC.

Yu, Chen, Zhenhong Li, and Nigel T. Penna (2018). "Interferometric synthetic aperture radar atmospheric correction using a GPS-based iterative tropospheric decomposition model". *Remote Sensing of Environment* 204, pp. 109 –121. ISSN: 0034-4257. DOI: `https://doi.org/10.1016/j.rse.2017.10.038`.

Zebker, Howard A. and Richard M. Goldstein (1986). "Topographic mapping from interferometric synthetic aperture radar observations". *Journal of Geophysical Research: Solid Earth* 91.B5, pp. 4993–4999. DOI: `10.1029/JB091iB05p04993`.

Zebker H. A., P. A. Rosen R. M. Goldstein A. Gabriel and C. L. Werner (1994). "On the Derivation of Coseismic Displacement-fields using Differential Radar Interferometry - the Landers Earthquake". *Journal of Geophysical Research* 99.B10, pp. 617–634.

Zhang, Lei et al. (2012). "Mapping ground surface deformation using temporarily coherent point SAR interferometry: Application to Los Angeles Basin". *Remote Sensing of Environment* 117. Remote Sensing of Urban Environments, pp. 429 –439. ISSN: 0034-4257. DOI: `https://doi.org/10.1016/j.rse.2011.10.020`.